Some Fundamental Mechanisms of Hydraulic Fracturing

A Dissertation
Presented To
The Academic Faculty

by

Ruiting Wu

In Partial Fulfillment
of the Requirements for the Degree
Doctor of Philosophy in the
School of Civil and Environmental Engineering

Georgia Institute of Technology
May 2006

Some Fundamental Mechanisms of Hydraulic Fracturing

Approved by:

Dr. Leonid N. Germanovich, Advisor
School of Civil and Environmental Engineering
Georgia Institute of Technology

Dr. Jianmin Qu
School of Mechanical Engineering
Georgia Institute of Technology

Dr. Arash Yavari
School of Civil and Environmental Engineering
Georgia Institute of Technology

Dr. José I. Adachi
Engineering Applications Department
Schlumberger Oilfield Services

Dr. Robert Lowell
School of Earth and Atmospheric Sciences
Georgia Institute of Technology

Dr. Larry C. Murdoch
Department of Geological Sciences
Clemson University

Date Approved: November 17, 2005

ACKNOWLEDGEMENT

First of all I would like to thank my thesis advisor, Dr. Leonid Germanovich, for his guiding and support throughout my research and study at Georgia Tech. Without his endless encouragement, support and trust at all levels I could not have accomplished the research projects reported in this dissertation. His ingenious perspective into the scientific research and optimistic attitude towards the challenges in daily life has set up a good example for me to follow in my future career.

I would like also to thank for serving in my thesis committee: Dr. José I. Adachi, Dr. Robert Lowell, Dr. Larry C. Murdoch, Dr. Jianmin Qu, and Dr. Arash Yavari. I benefited a lot from their valuable comments and suggestions.

The completion of this research was possible due to the contributions of many other persons. Specifically, I really appreciate Dr. Peter Van Dyke for his invaluable inspiration, encouragement and support during the preparation process of this dissertation. I thank Mr. Mike Sorenson and Mr. Kenneth Thomas for providing timely assistance in the experimental set-ups. I greatly appreciate the assistance and encouragement from past and present graduate students of the Rock and Fracture Mechanics Group at Georgia Institute of Technology: Dr. Dmitry Astakhov, Dr. Hong Chang, Dr. Rajesh Chanpura, Jongwon Choi, Gence Genc, Charlie George, Devon Gwaba, Robert Hurt, Sihyun Kim, Cem Ozan, Pierre Ramondenc, Chanin Ruangthaveekoon, Dr. Youngjong Sim, and Kasemchart Sriwalai. I am also very grateful to Robert Hurt and Gence Genc for their help on conducting some experiments reported in Chapter 3. I am particularly in debt to Pierre Ramondenc for his kind help with editing the manuscript of this dissertation.

I can not forget to thank my husband, Tianyi Yi, for his love, encouragement, trust, and support. I should also express my deep gratitude to my beloved parents, Wanye Wu and Yufeng Zhou, my dear sister and brother, Tingting Wu and Jian Wu, for their continuous encouragement and support.

Finally, I would like to thank the financial support provided by Schlumberger (2003 and 2005 Summer Internships), National Science Foundation (grants CMC-9896136, CMC-0421090, and OCE-0242163), and Georgia Tech Foundation during the years of my Ph.D. study.

TABLE OF CONTENTS

Acknowledgement…..…… ..iii

List of Tables……...x

List of Figures……..…...xi

Summary…….....xx

Chapter 1 Introduction 1

References 11

Chapter 2 A Laboratory Technique for Controlling Hydraulic Fractures 16

2.1 Introduction 16

2.2 Experimental Procedure 20

2.3 Fracture Orientation Controlled by Thermal Stresses..... 21

2.4 Starter Fracture..... 27

2.5 Fracture Size 30

2.6 Applications 37

2.6.1 Mixed Mode Hydraulic Fracture Propagation..... 37

2.6.2 Visualization of Residual Permeability in Natural Fractures 40

2.7 Conclusions 42

Acknowledgement..... 44

References 45

Chapter 3 Mixed-mode I+III Fracture Propagation and Segmentation 49

3.1 Introduction 50

3.2 Laboratory Set-up..... 60

3.3 Experimental Results 62

3.3.1 Mode I+III Fracture Geometry at Low K_{III}/K_I 62

3.3.2 Types of Intersection 70

3.3.3 Twist Angle 71

3.4 Mode III Component of Non-Planar Fractures 73

3.5 Theoretical Model 79

3.5.1 Effect of Interaction in Segmented Fracture 79

3.5.2 Pressurized Segmented Circular Fracture 85

3.6 Discussion 93

3.7 Conclusions 96

Nomenclature 97

References 100

Chapter 4 Effects of Crack Tip Plasticity on Hydraulic Fracturing in Cohesionless Materials 104

4.1 Introduction 105

4.1.1 Hydraulic Fracturing in Particulate Material 105

4.1.2 Cohesive and Cohesionless Particulate Materials 107

4.1.3 *Chang*'s [2004] Laboratory Experiments 111

4.1.4 Theoretical Models for Crack Tip Plasticity 112

4.2 A Model of the Localized Process Zone 118

4.2.1 Problem Descriptions and Main Assumptions 118

4.2.2 Stresses inside the Process Zone 120

4.2.3 Stresses outside the Process Zone 122

4.2.4 Size of the Process Zone 125

4.2.5 Discussion 126
4.3 Shear Band Model 128
4.3.1 Numerical Modeling 129
4.3.2 Super-dislocation Model 136
4.4 Conclusions 145
Nomenclature 146
References 149
Chapter 5 A Super-dislocation Model of Crack-tip Plasticity in Mohr-Coulomb Materials 153
5.1 Introduction 153
5.2 The Super-dislocation Model 156
5.2.1 Mathematical Background 156
5.2.2 Dislocation Stability and Main Equations 170
5.3 Parametric Study 178
5.3.1 Frictionless Material 178
5.3.2 Cohesionless Material 186
5.3.3 Cohesive-Frictional Material 193
5.4 Maximum Shear Stress Criterion 196
5.5 Conclusions 201
Nomenclature 201
References 204
Chapter 6 Discrete Element Simulation of Fluid Injection into Particulate Materials ... 208
6.1 Introduction 209
6.2 Numerical Model 211

6.2.1 *PFC* Background 211

6.2.2 Model Set-up 215

6.3 Results of Numerical Simulation 221

6.4 Fluidization Mechanism of Cavity Initiation 225

6.5 Closed-Form Solution for Pressure Distribution 230

6.5.1 Exact Solution for Darcy Flow 230

6.5.2 Approximate Solution for Darcy flow 232

6.5.3 Approximate Solution for non-Darcy flow 235

6.6 Stress and Strain Distributions 238

6.6.1 Radial flow 238

6.6.2 1-D flow 241

6.6.3 Matched solution 243

6.6.4 Fluidization Criterion 244

6.6.5 Comparison with Numerical Experiments 249

6.7 Parametric Analysis 251

6.8 Conclusions 256

Acknowledgement 257

Nomenclature 257

References 261

Chapter 7 Conclusions and Recommendations 264

7.1 Conclusions 264

7.2 Recommendations for Future Work 268

Appendix A Design of the Syringe Pump 271

Appendix B Upper Estimate of the Volume Change due to Tubing Deformation ….. ..274

Appendix C Discussion on Fracture Size Controlling ……..…….……. ...276

Appendix D Laboratory Setup for Mode I+III Fracture Propagation ….…….. 278

LIST OF TABLES

Table 2.1. Nomenclature of notation…….22

Table 3.1. Summary of the initial fractures and experimental parameters 61

Table 3.2. Summary on the observed segmented fractures 69

Table 3.3. Data for numerical simulation with FRANC3D 76

Table 3.4. Summary on the fitting parameters..... 92

LIST OF FIGURES

Figure 2.1. Non-ideal orientations of hydraulic fractures created by injecting fluid into a cased hole in arbitrarily stressed PMMA. On both pictures, the outer diameter of the casing is 0.32 cm. 19

Figure 2.2. Starter notch (yellow) created by using a bent, sharpened rod to scratch out PMMA material, and the subsequent fracture propagated hydraulically [*Germanovich et al.*, 1999]. The drill hole diameter is 0.71 cm. 19

Figure 2.3. A sample with hydraulically created fracture. The sample has a diameter of 10.2 cm and a length of 30.5 cm. The stainless steel casing tubing has outer and inner diameters of 0.32 and 0.22 cm, respectively. The fracturing fluid is a dark-green, oil-based liquid dye with a dynamic viscosity of 48 cp. No proppant was pumped into the hydraulic fracture. 20

Figure 2.4. The schematic drawing of the stress state created by the transient heating the surface of a cylinder: (a) horizontal and (b) vertical cross sections. (c) Normalized temperature and thermal stresses along the cylinder radius for a dimensionless time of $\tau = 0.076$, and (d) normalized thermal stresses at the center, $\rho = 0$, of the cylinder as the function of dimensionless time (the maximum values of s_{zz} and $s_{\theta\theta}$ occur at $\tau = 0.076$). 22

Figure 2.5. Hydraulic fracture (diameter = 1.8 cm) perpendicular to the axis of a cylindrical PMMA sample: (a) side and (b) end views. The sample has a length of 30.5 cm and a diameter of 7.62 cm. The drilled hole has a diameter of 0.36 cm and a length of 15.2 cm. Stainless steel casing has an outside diameter of 0.32 cm and a wall thickness of 0.05 cm. The measured peak pressure was 32 MPa. 26

Figure 2.6. Hydraulic fracture (diameter = 2.0 cm) parallel to the axis of a cylindrical PMMA sample. The sample has a length of 15.2 cm and a diameter of 5.08 cm. The drilled hole has a diameter of 0.36 cm and a length of 7.6 cm. Stainless steel casing has an outside diameter of 0.32 cm and a wall thickness of 0.05 cm. 27

Figure 2.7. Hydraulic fracture perpendicular to the axis of a cylindrical sample: (a) small starter fracture, (b) propagated hydraulic fracture, and (c) injection pressure during fracture propagation. The starter fracture of the diameter of 0.8 cm was created by applying a load of 1.5 kN. The diameter of the propagated hydraulic fracture is 3.0 cm. The sample has a length of 15.2 cm and a diameter of 5.08 cm. The drilled hole has a diameter of 0.36 cm and a length of 7.6 cm. Stainless steel casing has an outside diameter of 0.32 cm and a wall thickness of 0.05 cm. Note that the peak pressure, p_1 = 20.7 MPa, is significantly smaller than that for the hydraulic fracture

shown in Figure 2.5 because of the starter fracture. 29

Figure 2.8. (a) Initial and (b) final instances of fracture propagation. Volume V_0 represents the injection fluid "between" the pump and the fracture, i.e., the volume of the drill hole (inside the casing, if any) plus connecting tubing. 30

Figure 2.9. Normalized volume of the injection fluid in the sample versus normalized radius of the propagated fracture for different initial fracture radii. 35

Figure 2.10. Hydraulic fracture under mixed-mode I + III loading: (a) initial circular fracture created with thermal technique (i.e., sample pre-heating), (b) side view of mode III segmentation of the propagated fracture, (c) end view of the propagated fracture, and (d) injection pressure curve. The sample has a length of 30.5 cm and a diameter of 10.2 cm. The drilled hole has a length of 15.24 cm. 36

Figure 2.11. (a) Fracture fully opened by the pressure of the flowing fluid (at $5.0 \cdot 10^{-3}$ ml/min), and (b) residual fracture opening after the fluid flow was interrupted and the pressure declined to atmospheric. Fracture diameter is 9 cm. The inflow is along the vertical drill hole casing, and the outflow is at the left side of the sample boundary. The initial fracture parallel to the axis of the cylindrical PMMA sample was created by sample pre-cooling, and then propagated hydraulically to the size shown. Higher color (i.e., darker gray scale) intensity indicates larger fracture aperture. White color corresponds to contact zones (i.e., resting on mismatched asperities). 41

Figure 3.1. (a) Outcrop of segmented magmatic dike [*Delaney*, 1996]; (b) dike segmentation due to rotation of least principal stress axis during upward propagation [after *Delaney and Pollard*, 1981]. 51

Figure 3.2. Segmented hydraulic fracture observed in the laboratory experiments of (a) *Hubbert and Willis* [1957] and (b) *Abass et al.* [1996]..... 51

Figure 3.3. Three modes of fractures: (a) mode I – opening mode, (b) mode II – sliding (in-plane shear) mode, and (c) mode III – tearing (out-of-plane shear) mode [*Kanninen and Popelar*, 1985]. 53

Figure 3.4. Schematic illustration of fracture propagation path: (a) pure mode I, (b) mixed-mode I+II, and (c) mixed-mode I+III [after *Pollard and Aydin*, 1988]. 53

Figure 3.5. Mixed mode I+III fracture surface in a cylindrical glass rods conducted by *Sommer* [1969]. 56

Figure 3.6. Mixed mode I+III fatigue surface in low pressure steam turbine rotor steel

[*Yates and Miller*, 1989]. 57

Figure 3.7. Mixed mode I+III fracture surface in rectangular plexiglass specimen conducted by *Cooke and Pollard* [1996]: (a) testing machine setup, (b) oblique view of fracture surface, and (c) view of en-echelon twisting fractures along crack plane and in the propagation direction. Numbers in (b) refer to the propagation sequence. 58

Figure 3.8. Experimental set-up for mode I+III fracture initiation and propagation. 60

Figure 3.9. Initial hydraulic fracture in sample 4-10: (a) side and (b) end views. 62

Figure 3.10. Segmented fracture of type *A* in sample 4-2: (a) side view (perpendicular to the axis of the sample), and (b) end view (along the axis of the sample). The numbers in (b) show the sequence of segments appearance. 64

Figure 3.11. Schematic drawing of the segmented fracture geometry: (a) end and (b) side views. 65

Figure 3.12. Segmented fracture of type *B* in sample 4-5: (a) side and (b) end views. 66

Figure 3.13. Segmented fracture of type *A* in sample 4-7: (a) side and (b) end views. 67

Figure 3.14. Schematic of the geometry of the intersection between the parent fracture and the segments: (a) perspective and (b) front views. 70

Figure 3.15. Segmented fracture of type *A* in sample 4-10: (a) side and (b) end views. The segments propagated toward the parent fracture plane and contacted with it. 71

Figure 3.16. The observed relationship between the twist angle and the ratio of K_{III}/K_I. Sample numbers are shown above the bars that indicate the range of twist angles observed for each sample. $\nu = 0.38$. 73

Figure 3.17. FRANC3D model of the mixed mode I+III fracture. The propagated fracture is shown in Figure 3.18. 75

Figure 3.18. Results of the numerical simulation with FRANC3D model. 77

Figure 3.19. A 2-D model of segmented fracture: (a) geometric configuration of three closely spaced overlapping fractures, (b) opening of the overlapping fractures, and (c) opening of the single (effective) fracture of the same total length (the sketch is not scaled). 80

Figure 3.20. Beam model of the ligament between the overlapping fractures in Figures 3.21a and 3.21b. 81

Figure 3.21. Equivalent fracture loaded by resistance forces, F_n, generated at the ligament ends (Figures 3.21b and 3.22) and by internal pressure, p. 81

Figure 3.22. Function f in (3.10) versus b/a for $s/(2c) = 0.1$, 0.2 and 0.3. 85

Figure 3.23. (a) Pressurized "effective" circular fracture, and (b) cross section perpendicular to the fracture plane. 86

Figure 3.24. The measured injection pressure curve for sample 4-10 and the fitting $p(t)$ curve obtained with (3.20) and (3.16). 89

Figure 3.25. The measured injection pressure curve for sample 4-7 and the fitting $p(t)$ curve obtained with (3.20) and (3.16). 89

Figure 3.26. Type *A* fracture: (a) segmented fracture geometry; (b) measured injection pressure curve for sample 4-13 and the fitting $p(t)$ curve obtained with (3.20) and (3.16). 90

Figure 3.27. Type *B* fracture: (a) segmented fracture geometry; (b) measured injection pressure curve for sample 4-11 and the fitting $p(t)$ curve obtained with (3.20) and (3.16). 91

Figure 3.28. The injection pressure curves during fracture segmentation in (a) sample 4-2 shown in Figure 3.10 and (b) sample 4-5 shown in Figure 3.12. 94

Figure 3.29. (a) Field observed fracture injection pressure curve and inferred fracture geometry, and (b) typical hydraulic fracture injection pressure curve and interpretations of this curve based on the conventional theory [*Economides and Nolte*, 2000] 96

Figure 4.1. Effect of over-pressured zones on the decrease of the pressure margin at a SWF site in the Gulf of Mexico [*Ostermeier et al.*, 2000]. 106

Figure 4.2. Trench formed by SWF [*Ostermeier et al.*, 2000]. 106

Figure 4.3. Stress distribution at the fracture tip in cohesive material with a non-zero tensile strength, σ_t. The dashed line indicates the singular stress distribution for a discontinuity in ideally elastic material. 108

Figure 4.4. Schematic of stress distribution at fracture tip in a cohesionless material. The stress near the fracture tip is less than the ambient value. The Mohr-Coulomb diagram illustrates that yielding near the fracture front occurs as a result of decreasing stresses compared to remote in-situ stresses. 111

Figure 4.5. Observed three typical fracture fronts of hydraulic fractures in particulate material [*Chang*, 2004]: (a) beveled front (in silica flour); (b) fingered front (in Georgia Red Clay); (c) round front (in silica flour). 112

Figure 4.6. A model of the localized process zone: (a) Dugdale-Barenblatt model applied to cohesionless material, and (b) a representative element in the process zone in a state of compression. Grey areas indicate the process zones at the crack tips. 120

Figure 4.7. Localized process zone model: fracture loaded by σ_{yy}^{0} in the process zone and $p(x)$ inside the crack in addition to the remote load, σ_1 and σ_3. 122

Figure 4.8. Auxiliary problems for the localized process zone model: (a) remote stress problem, and (b) crack loaded by σ_0 in the process zone and $\sigma(x)$ inside the crack. Note that different (translated) coordinate set (compared to that in Figure 4.7). Also note that stress σ_0 closes the crack at the process zone. 123

Figure 4.9. Shear band model. Here, p is the injection pressure inside the fracture, θ is the angle of the shear band with respect to the fracturing direction, and Δa is the incremental advance of the fracture in the fracturing direction. 129

Figure 4.10. (a) Overview of the grid fragment, and (b) magnified view of the grid fragment in the vicinity of the fracture front. 131

Figure 4.11. (a) Plastic zone (red color; green color shows elements that are currently elastic, but were plastic in the past), and (b) contour of maximum shear strain increment. Elements 1, 2, 3, and 4 are also shown in Figure 4.12 and described in the text. 133

Figure 4.12. (a) Stress distribution of σ_{xx} and σ_{yy} ahead of the fracture tip, and (b) Mohr circles for elements 1, 2, 3, and 4 shown in Figure 4.11a. 134

Figure 4.13. Single superdislocation model. 139

Figure 4.14. Dependence of the normalized fluid pressure at the crack tip on ϕ_2 for ϕ_1 = 10º, 20º, 30º, and $c = 0$. 144

Figure 5.1. Schematic representation of the super-dislocation model (modified after *PA*). 154

Figure 5.2. Auxiliary problems: (a) remote stress problem, (b) crack with internal pressure, and (c) crack interacting with dislocations. 159

Figure 5.3. An elastic problem of an unloaded crack interacting with a single dislocation of a given strength, b. 163

Figure 5.4. The dependence of $f_1(\theta)$ and $f_2(\theta)$ on θ. 168

Figure 5.5. The dependence of $f(\theta) = f_1(\theta) + \tan\phi f_2(\theta)$ on θ for several values of ϕ. 173

Figure 5.6. Frictionless material, $\phi = 0$: the dependence of the value of θ, which maximizes δ, on the loading parameter, $\lambda = (\sigma_1 - \sigma_3)/(2c)$. 180

Figure 5.7. Frictionless material, $\phi = 0$: the dependence of the critical fluid pressure at the fracture tip on the loading parameter, λ. 182

Figure 5.8. Frictionless material, $\phi = 0$: (a) normalized dislocation length versus dislocation angle, and (b) normalized CTOD versus dislocation angle for different loading parameters, $\lambda = 0$, 0.3, 0.6, and 0.9. 183

Figure 5.9. Frictionless material, $\phi = 0$: dependence of normalized dislocation length and CTOD on loading parameter, λ. 184

Figure 5.10. Cohesionless material, $c = 0$, $\phi = 10°$: normalized dislocation length versus dislocation angle for different loading parameters, λ, $\Delta p = 2.82$ MPa, and $p(0) = p(x) = 15$ MPa. 188

Figure 5.11. Cohesionless material, $c = 0$, $\phi = 10°$: normalized shear stress on the dislocation versus dislocation angle for different loading parameters, λ, $\Delta p = 2.82$ MPa, and $p(0) = p(x) = 15$ MPa. 189

Figure 5.12. Cohesionless material, $c = 0$, $\phi = 10°$: normalized CTOD versus dislocation angle (in the range satisfying conditions (5.28), (5.29), and (5.34)) for different loading parameters, λ, $\Delta p = 2.82$ MPa, and $p(0) = p(x) = 15$ MPa. 189

Figure 5.13. Cohesionless material, $c = 0$, $\phi = 10°$: dependence of dislocation angle on the loading parameter, λ, for $\Delta p = 2.82$ MPa and $p(0) = p(x) = 15$ MPa. 190

Figure 5.14. Cohesionless material, $c = 0$, $\phi = 10°$: dependence of the normalized dislocation length and CTOD on the loading parameter, λ, for $\Delta p = 2.82$ MPa and $p(0) = p(x) = 15$ MPa. 190

Figure 5.15. Cohesionless material, $c = 0$, $\phi = 40°$: normalized dislocation length versus dislocation angle for loading parameters, λ, for $\Delta p = 2.82$ MPa and $p(0) = p(x) = 15$ MPa. 192

Figure 5.16. Cohesionless material, $c = 0$, $\phi = 40°$: normalized shear stress on the dislocation versus dislocation angle for loading parameters, λ, for $\Delta p = 2.82$ MPa and $p(0) = p(x) = 15$ MPa. 192

Figure 5.17. Cohesionless material, $c = 0$, $\phi = 40°$: normalized CTOD versus dislocation angle (in the range satisfying the conditions (5.28), (5.29), and (5.34)) for different loading parameters, λ, $\Delta p = 2.82$ MPa, and $p(0) = p(x) = 15$ MPa. 193

Figure 5.18. The dependence of $F(\theta) = [f_1(\theta) + \tan\phi f_2(\theta)]/\cos(\theta/2)$ on θ for several values of ϕ. 195

Figure 5.19. Cohesionless material, $c = 0$, $\phi = 10°$: dependence of θ on the loading parameter, λ ($0 \le \lambda < \cos\phi = 0.98$), for $\Delta p = 2.82$ MPa and $p(0) = p(x) = 15$ MPa. Solid and dashed lines are obtained by maximizing τ and δ, respectively. 197

Figure 5.20. Cohesionless material, $c = 0$: dependence of θ on the loading parameter, λ ($0 \le \lambda < \cos\phi$) for different values of ϕ, $\Delta p = 2.82$ MPa, and $p(0) = p(x) = 15$ MPa. . 198

Figure 5.21. Cohesive-frictional material, $\phi = 40°$: dependence of θ on the loading parameter, λ ($0 \le \lambda < \cos\phi$). Curves plotted for $c/\Delta p = 0$, 0.35, and 1.06 are hardly distinguishable. 199

Figure 5.22. Cohesive-frictional material, $c = 1$ MPa: dependence of θ on the loading parameter, λ ($0 \le \lambda < \cos\phi$) for different values of ϕ, $\Delta p = 2.82$ MPa, and $p(0) = p(x) = 15$ MPa. Curves $\phi = 0.1°$ and $0.01°$ are not distinguishable, which indicates the convergence at $\phi \to 0$. 200

Figure 6.1. *PFC*^{2D}: the assembly is discretized by circular or spherical particles interacting through contacts. 213

Figure 6.2. Boundary conditions in *PFC*^{2D} simulations. 216

Figure 6.3. Fluid cells (solid lines) and the assembly of particles (circles) employed in the *PFC*^{2D} simulation. 217

Figure 6.4. Cavity formation at the injection velocity $v_{in} = 123$ m/s in the (a) fine mesh ($c = 3$ mm) and (b) coarse mesh ($c = 6$ mm). 219

Figure 6.5. Pressure history at the first five fluid cell along the x-axis in the (a) fine mesh (c = 3 mm) and (b) coarse mesh (c = 6 mm)..... 220

Figure 6.6. Observed stages of cavity propagation: (a) "fixed bed flow" during the cavity initiation stage, (b) stable cavity development, and (c) unstable cavity propagation. 222

Figure 6.7. Pressure history curve for the base combination of parameters and the injection velocities, v_{in} = 135 m/s, 154m/s, 230 m/s, 338m/s, 395 m/s, and 445 m/s. 223

Figure 6.8. Stabilized particle positions near the injection point just (a) before and (b) after the cavity initiation. The fluid velocities at these moments are 135 m/s and 154 m/s, respectively, and correspond to the first two steps in Figure 6.7. 224

Figure 6.9. Dependence of the critical initiation velocity on fluid viscosity for the base combination of material parameters..... 225

Figure 6.10. Distribution of contact forces between the particles for (a) low fluid velocity (v_{in} = 1 m/s) and (b) critical fluid velocity (v_{in} = 5 m/s). In this PFC^{2D} simulation, the fluid viscosity is 10^4 cp. The thickness of the black lines indicates the relative scale of contact force magnitude..... 227

Figure 6.11. Cavity initiation mechanism: (a) the "liquefied" and plastic zones, and (b) Mohr-Coulomb diagram showing the state of three representative volume elements located in the elastic zone (element 1), plastic zone (element 2) and liquefied zone (element 3), respectively. 229

Figure 6.12. Simplified model: a point source in a finite rectangular plate..... 231

Figure 6.13. Contour plot of pressure distributions (6.13) in a finite, rectangular plate. 232

Figure 6.14. Source in a rectangular plate: normalized pressure distribution along the x-axis. The solid and dash lines represent the approximate (6.23) and exact (6.13) solutions, respectively. 235

Figure 6.15. The dependence of dimensionless injection velocity v_{cr}^* on the dimensionless fluid viscosity μ_f^*. 246

Figure 6.16. Cavity shape for different fluid viscosities: (a) μ_f = 100 cp, and (b) μ_f = 10,000 cp. 248

Figure 6.17. The dependence of dimensional injection velocity v_{cr} on the dimensional fluid viscosity, μ_f. The dots show the critical injection velocity obtained from PFC^{2D} simulations (Figure 6.8). 249

Figure 6.18. The pressure distribution along x-axis: comparison between the approximate solution (6.34) and PFC^{2D} simulation results for the case of μ_f = 10 cp and Q = 0.96 m^2/s. 250

Figure 6.19. Cavity shape and pressure history for different group parameters: (a) ρ_p = 2650 kg/m^3, ρ_p = 1000 kg/m^3, μ_f = 100 cp, $K_n = K_s$ = 50 MN/m σ_1' = 0.2 MPa, σ_3' = 0.1 MPa; (b) all parameters are doubled compared to case (a), that is, ρ_p = 5300 kg/m^3, ρ_p = 2000 kg/m^3, μ_f = 200 cp, $K_n = K_s$ = 100 MN/m, σ_1' = 0.4 MPa, σ_3' = 0.2 MPa. In both cases, v_{in} = 242 m/s. 253

Figure 6.20. Cavity shape and pressure history for different particle densities, (a) ρ_p = 2650 kg/m^3 and (b) ρ_p = 5300 kg/m^3, in the case of μ_f = 100 cp and the injection velocity v_{in} = 242 m/s. In the pressure history figures, the curves from top to bottom are in the first five cells close to the injection point along the x-axis. 255

Figure A.1. Pump used in our experiments: (a) schematics of the design and (b) actual pump……272

Figure C.1. A crack loaded on one side, which simulates creating a starter fracture by pushing a rod inside the drill hole (section 2.4)……...277

Figure D.1. Laboratory set-up: (a) general view, (b) sketch of back-view, and (c) sketch of the level-weight system in the cross section A-A in (b) (the dashed line and solid line are the positions of the level before and after hanging the weights, respectively). In photograph (a), the stepping gear motor, which is used to drive the hex-head bolt (Figure A.1), is placed inside an aluminum box to eliminate the effect of electromagnetic radiation…….279

SUMMARY

During recent decades, hydraulic fracturing has been widely used for the stimulation of petroleum and geothermal reservoirs, remediation of soil and groundwater aquifers, injection of wastes, and measurement of in-situ stresses. Hydraulic fractures, induced by fluid pressurized in a solid host material, are also observed in nature as joints, veins, and dikes. Due to the heterogeneity of material properties, rock structure, and in-situ stress state, hydraulic fracturing processes are highly complex, and many open questions still exist. This work focuses mainly on three topics: (1) mixed-mode branching and segmentation of hydraulic fractures in quasi-brittle materials, (2) hydraulic fracture propagation in particulate materials, and (3) hydraulic fracturing in water flooding conditions.

Mixed-mode loading is one of the primary causes of fracture branching and segmentation in brittle materials. We conducted systematic laboratory experiments on the mixed mode I+III hydraulic fracturing. We found that a ratio of mode III to mode I stress intensity factors as small as a few percent is sufficient for fracture front segmentation. In reality, such a small mode III component is always expected, for example, due to the small deviations of the fracture shape from planar. Thus, we concluded that fracture segmentation is likely to accompany growth of most, if not all, real fractures. We also proposed a theoretical model of a multi-segmented mode I+III fracture propagating in conditions of a low level mode III loading. The model captures the main features of experimental observations and indicates the importance of the hydraulic effect of segmentation.

Most, if not all, particulate materials exhibit pronounced non-linear behavior and

yielding even at relatively small strains. Therefore, in order to adequately describe hydraulic fracturing in particulate materials with low or no cohesion, plasticity at the crack tip needs to be explicitly considered. In this work, we investigated the shear band mechanism of strain localization at the fracture front in strain softening material. This mechanism takes into account the fact that cohesionless material can not bear tension, and is in compression everywhere, including near the fracture front. To test the shear band hypothesis, we conducted numerical simulations of the plastic deformation at the tip of a fracture in particulate material with strain softening. We also developed an analytical model that describes the shear bands by properly placed and oriented dislocations. The model results are consistent with experimental observations.

The mechanisms of water flooding, an extreme case of industrial hydraulic fracturing (i.e., very low viscosity, long injection time, and exceptionally high fluid leak-off), are poorly understood by currently available theoretical models. To investigate the fracture initiation mechanism in water flooding conditions, we conducted a numerical simulation of fluid injection into particulate material by using the discrete element method. The simulation results show that due to the effects of drag forces, particles tend to move away from the injection point. As a result, the particulate material becomes unloaded near the injection point, which causes a tensile volumetric strain in its vicinity. This phenomenon is similar to liquefaction or fluidization of particle-fluid mixtures. Hence, we considered an analytical model of cavity initiation based on the fluidization mechanism. The model takes into account the non-Darcy effect of fluid flow through porous medium. Despite the fact that in the normalized form the model has no fitting parameters, the model results agree remarkably well with the numerical simulations.

CHAPTER 1
INTRODUCTION

During recent decades, the process of hydraulic fracturing has been widely used for the stimulation of petroleum and geothermal reservoirs [*Sasaki*, 1998; *Berumen et al.*, 2000], remediation of soil and groundwater aquifers [*Murdoch and Slack*, 2002], injection of wastes [*Hunt et al.*, 1994; *Hainey et al.*, 1999], and measurement of in-situ stresses [*Hayashi et al.*, 1997; *Raaen et al.*, 2001]. Hydraulic fractures, induced by fluid pressurized in a solid host material, are also observed in nature as joints [*Pollard and Aydin*, 1988; *Lacazette and Engelder,* 1992], veins [*Srivastava and Engelder,* 1991; *Al-Aasm et al.*, 1995], and dikes [*Pollard*, 1987; *Rubin*, 1995]. Due to the heterogeneity of material properties, rock structure and in-situ stress state, hydraulic fracturing processes are highly complex [e.g., *Germanovich et al.*, 1997]. As a result, it is difficult to predict or even measure the behavior of hydraulic fractures in field conditions. Currently, there are still many open questions and uncertainties related to hydraulic fracturing, including fluid lag at the tip zone [*Advani et al.*, 1997; *Adachi*, 2001; *Detournay*, 2004], interaction between multiple fractures [*Delaney and Pollard*, 1981; *Germanovich and Astakhov*, 2004a, 2004b], and proppant effects [*Kovscek et al.*, 1995].

This dissertation focuses on three topics: (1) hydraulic fracture branching and segmentation in quasi-brittle materials, (2) hydraulic fracture propagation in particulate materials, and (3) hydraulic fracturing in water flooding conditions.

Fracture branching and segmentation is a phenomenon frequently observed in

nature, such as segmented dike outcrops [e.g., *Pollard et al.*, 1975; *Delaney and Pollard*, 1981; *Pollard et al.*, 1982] and multisegmented veins [e.g., *Vermilye and Scholz*, 1995]. In laboratory tests, splitting of the fracture front is observed even in very homogeneous materials [e.g., *Hubbert and Willis*, 1957; *Abass et al.*, 1996; *Bakala*, 1997]. Fracture branching and segmentation not only represents a mechanism that is important for understanding fractures in nature, but it also has important applications in the engineering field. For example, complex nonplanar hydraulic fractures are generally modeled as a single planar fracture. This simplification may overestimate net pressure, underestimate the propped length and the width of individual fractures with an increased potential for screen-outs, and further cause an overestimate of fluid leak-off and an underestimate of the reliable fracture confinement within a pay zone [e.g., *Germanovich et al*., 1998; *Mahrer*, 1999; *Economides* and *Nolte*, 2000]. In practice, such inaccurate conclusions may result in a poor design of hydrofrac jobs and loss of well productivity [e.g., *Hallam and Last*, 1991].

Two main conditions may trigger branching and segmentation of hydraulic fractures: material heterogeneity and stress heterogeneity [e.g., *Germanovich et al*., 1997]. In this work, we were particularly interested in fracture branching and segmentation caused by mixed-mode loading, which is considered as one of the primary causes for fracture segmentation in geomaterials [e.g., *Germanovich et al.*, 1997; *Delaney and Pollard*, 1981; *Pollard and Fletcher*, 2005]. Our main objectives were to investigate the particular features of segmentation in hydraulic fracture (i.e., injection pressure) and the geometry of the segmented fracture. First, we conducted laboratory experiments on mixed-mode I+III hydraulic fracture propagation with a small K_{III}/K_I ratio in transparent

geomaterial analogues. Second, based on the experimental observations, we developed a simple theoretical model to describe the features of the segmented fractures, particularly, the segment sizes and the injection pressure.

The second topic of this dissertation is hydraulic fracturing in particulate materials. For the last decade, hydraulic fracturing has been widely used as an alternative method for sand control in weak rock reservoirs, especially in unconsolidated or poorly consolidated formations [*Abass et al.*, 2003; *Abou-Sayed et al.*, 2004]. Hydraulic fracturing in particulate materials is responsible for many cases of rupture during pressure grouting [*Warner*, 1997], failure of dams [*Penman*, 1977], and shallow-water flow problems when drilling petroleum boreholes [*Ostermeier et al.*, 2000].

Most of the publications on the fracture initiation and propagation criteria in hydraulic fracturing target cohesive particulate materials [*Bjerrum et al.*, 1972; *Lo and Kaniaru*, 1990; *Andersen et al.*, 1993; *Economides and Nolte*, 2000]. To date, little work has been done to describe these processes in unconsolidated, cohesionless particulate materials [*Chang*, 2004; *Hurt et al.*, 2005]. Propagation criteria for cohesive particulate materials are typically based on conventional fracture mechanics that assumes non-zero tensile strength of the material in the fracture tip zone [e.g., *Murdoch*, 1993a, 1993b, 1993c, and 2002]. This presumption, however, cannot be used to describe the fracturing in cohesionless particulate materials. While some conceptual mechanisms have recently been suggested [*Chang*, 2004; *Hurt et al.*, 2005], new quantitative models have not yet been developed. This work is an attempt to make a step in this direction.

Most, if not all, particulate materials often exhibit pronounced non-linear behavior

and yielding even at relatively small strains. Therefore, in order to adequately describe the hydraulic fracturing in cohesionless particulate materials, the plasticity at the crack tip needs to be explicitly included in the modeling. To this end, we evaluated two different models. One model is based on the Dugdale-Barenblatt concept of a thin localized process zone, which is oriented along the fracture and describes plastic yielding at the fracture tip. The other model utilizes the shear band mechanism of strain localization, which is commonly observed in particulate materials with strain-softening behaviour. Both models take into account that all parts of the cohesionless particulate material, including the process zone itself, are in compression.

An important practical application related to hydraulic fracturing in particulate materials is water flooding. Water flooding is one of the most common methods used worldwide for improving oil recovery [*Mayerhofer et al.*, 1997; *Azeemuddin*, 2002; *Sommerauer and Petersen*, 2003; *Souza et al.*, 2005]. Hydraulic fracturing during some water flooding operations is undesirable because it creates permeable channels that limit the pressure in the formation undergoing water flooding treatment. On the other hand, the waterfrac method of hydraulic fracturing (that is, essentially using water as a fracturing fluid), also often referred to as water flooding, is becoming increasingly popular [*Mayerhofer et al.*, 1997; *Sommerauer and Petersen*, 2003; *Zhao et al.*, 2005]. Its advantages, such as relatively low cost, increased near-borehole permeability, fracture extension, and easy cleanup, are very attractive. However, the mechanisms of this extreme case of industrial hydraulic fracturing (i.e., very low viscosity, long injection time, and exceptionally high fluid leak-off) are poorly understood by currently available theoretical models. Furthermore, due to the aforementioned features of water flooding, it

is difficult, if not impossible, to simulate this process in the laboratory. This is why we conducted a numerical simulation of fluid injection into particulate material by using the discrete element method, which allows the simulation of particle flow. We also considered a fluidization criterion to identify a critical fluid velocity corresponding to fracture initiation. This work may aid our understanding of the water flooding mechanisms.

To present the work introduced above, this dissertation is organized into five relatively independent chapters. Each chapter is prepared in the format of a paper intended for future publishing and has its own list of references. Chapters 2 and 3 are devoted to the first discussed topic, chapters 4 and 5 are devoted to the second topic, and chapter 6 is devoted to the third topic. An overview of each chapter follows.

Chapter 2 "*A laboratory technique for controlling hydraulic fractures*" [*Wu et al.*, 2006]. This chapter introduces a simple technique to control the orientation and size of hydraulic fractures in laboratory samples. This is achieved by heating or cooling samples prior to injecting the fracturing liquid, so that the induced thermal stresses control the fracture orientation. We developed a simple theoretical model to parameterize experiments in laboratory settings and for materials that are different from ours. We also illustrate the utility of the technique with two examples: (i) mixed mode I+III hydraulic fracture propagation, and (ii) visualization of the fluid flow in the created fracture.

Chapter 3 "*Mixed-mode I+III fracture propagation and segmentation*" [*Wu and Germanovich*, 2006a]. Out-of-plane fracture propagation is usually a characteristic of mixed mode fractures. In particular, mixed-mode I+III loading is one of the primary

causes of fracture front segmentation. Such segmented fractures have been observed both in nature and in laboratory experiments. Many brittle materials (e.g., rock, concrete, ceramic) have relatively low resistance to tensile fracture. In quasi-brittle materials, even a small mode III component may cause fracture segmentation due to the creation of a tensile stresses near the fracture front. In this chapter, we experimentally studied not only the effect of mode III loading on the onset of fracture segmentation but also the effect of segmentation on the subsequent fracture growth when the K_{III}/K_I ratio was rather small (1-10%).

We used transparent, cylindrical PMMA samples with circular internal fractures perpendicular to the sample axis. Fracture orientation was controlled by thermoelastic stresses induced in each sample by preheating it before creating a fracture. In order to apply mode III loading to the initial fracture, a constant torque was applied to the specimen while fluid was injected into the fracture at a constant rate to pressurize it and to induce mode I loading. In spite of a small magnitude of the mode III component, we observed segmented fracture fronts in all the tested samples. The segments had similar dimensions and an elongated shape. When the fractures were further pressurized by injecting additional fluid into the sample, second-order segments developed along the fronts of the first-order segments.

We also developed a simple asymptotic model of a multi-segmented mode I+III fracture propagating in conditions of a low level mode III loading, which takes into account mechanical interaction between the segments and the parent fracture. The model shows good agreement with the experimental observations.

The obtained results indicate that a K_{III}/K_I ratio as small as a few percent is sufficient for fracture front segmentation even in materials as homogeneous and fracture resistant as PMMA. In reality, a small component of mode III is always expected, for example, due to slight deviations of a three-dimensional fracture from a planar shape or interaction with boundaries or other fractures. As a result, front segmentation (at an appropriate scale) is likely to accompany the growth of most (if not all) real fractures, at least in quasi-brittle materials.

Chapter 4 "*Effects of crack tip plasticity on hydraulic fracturing in cohesionless materials*" [*Wu and Germanovich*, 2006b]. In this chapter, we consider two models of hydraulic fracturing in uncemented sediments. We first introduce a model of a simple localized plastic band to describe the process zone at the tip of a fracture in cohesionless particulate material in the Dugdale-Barenblatt manner. Even though the physical nature of the localized plastic zone appearing in compression and the mechanism of localized fluid flow into cohesionless materials are unclear, the model still results in a stress state that is compressive everywhere, including the fracture tip zone. Since cohesionless materials cannot bear tensile stress, this model is appealing and yields a simple and convenient approach for modeling fracture propagation. The other model utilizes the physical mechanism of shear banding, which is characteristic for particulate materials with strain-softening behaviour. It explicitly describes the fracture front and the fluid flow mechanism. The model is consistent with experimental observations and is based on modeling the shear bands by properly oriented and positioned dislocations. To test the shear band hypothesis, we also conducted numerical simulations of the localized plastic deformation at the tip of a fracture in the particulate material with strain softening.

Chapter 5 "*On representation of crack-tip plasticity in Mohr-Coulomb materials*" [*Germanovich and Wu*, 2006]. The super-dislocation model is an important tool to model crack-tip plasticity in different settings. In this chapter, we reassess the super-dislocation model recently developed by *Papanastasiou and Atkinson* [2000] for simple representation of plastic deformation at the tip of hydraulic fractures in such pressure sensitive materials as soft sediments in hydrocarbon reservoirs. We show that in the case of the small scale yielding, the conventional approach of determining the dislocation angle by maximizing the crack opening displacement, dislocation strength, or dislocation length is only effective for frictionless materials as originally suggested by *Atkinson and Kanninen* [1977]. As an alternative, we propose a criterion based on the maximum shear stress at the dislocation position. We show that maximizing the shear stress on the dislocation makes the super-dislocation model consistent for a wide range of pressure sensitive cohesive-frictional materials.

Chapter 6 "*Discrete element simulation of fluid injection into particulate materials*" [*Wu et al.*, 2006]. To investigate the fracture initiation mechanism in water flooding conditions, we conducted a numerical simulation of fluid injection into particulate material using the discrete element method. We observed three distinct stages in the cavity evolution as the injection velocity increases: (1) cavity initiation in the vicinity of the injection point when the velocity of fluid reaches a certain critical value; (2) stable cavity development when the cavity propagates incrementally in response to each increment of velocity increase; and (3) unstable cavity propagation after the injection velocity reaches a second critical value (usually much higher than the critical velocity of cavity initiation).

These stages can be explained by considering the drag forces applied to the particles by the fluid continuously seeping through the particle assembly. Due to the drag forces, particles tend to move away from the injection point. As a result, the particulate material is unloaded near the injection point, which causes a positive volumetric strain in its vicinity. Once the strain reaches a critical value corresponding to the loss of contact between the particles in all directions, a cavity forms. This critical strain value corresponds to the "fluidization" of the particle-fluid mixture. When the injection velocity increases, the cavity begins propagating until it reaches the stable state. Once the resultant magnitude of the drag forces exceeds the reaction on the boundary of the entire particle assembly (at the second critical velocity), the body equilibrium is not possible any more and the cavity begins developing in an unstable manner, that is, without further increase in the injection velocity.

We considered a poroelastic model of cavity initiation based on the fluidization mechanism. This model suggests that the critical fluid velocity is *proportional* to the fluid viscosity if the latter is not too high. However, if the fluid viscosity is sufficiently large, the critical velocity is *inversely proportional* to the fluid viscosity. From the physical standpoint, such dependence of the injection velocity on the fluid viscosity corresponds to two different flow regimes: inertial governing regime and viscosity governing regime. The inertial governing regime occurs with low fluid viscosity when the energy dissipation is mainly due to the second term in the nonlinear Darcy law. When fluid viscosity increases, the first linear term gradually becomes dominant, and the energy dissipates mainly through the fluid viscosity. Even though the developed model is oversimplified and does not result in the correct state of stress near the injection point, the critical

velocity, estimated based on this model, fits remarkably well the values obtained from numerical simulations with PFC^{2D}.

References

Abass, H.H., A.H. Habbtar, A. Shebatalhamd, and S. Aramco (2003), Sand control during drilling, perforation, completion and production, SPE 81492, paper presented at *the SPE 13th Middle East Oil Show & Conference*, Bahrain, 9-12 June.

Abass, H.H., S. Hedayati, and D.L. Meadows (1996), Nonplanar fracture propagation from a horizontal wellbore: Experimental study, *SPE Prod. Facil.*, *11*, 133-137.

Abou-Sayed, A., K. Zaki, G. Wang, F. Meng, and M. Sarfare (2004), Fracture propagation and formation disturbance during injection and frac-pack operations in soft compacting rocks, SPE 90656, paper presented at *the SPE Annual Technical Conference and Exhibition*, Houston, TX, USA, 26-29 September.

Adachi, J. (2001), Fluid-driven fracture in permeable rock, Ph.D. thesis, University of Minnesota, MN.

Advani, S.H., T.S. Lee, R.H. Dean, C.K. Pak, and J.M. Avasthi (1997), Consequences of fluid lag in three-dimensional hydraulic fractures, *Int. J. Numer. Anal. Met.*, *21*, 229-240.

Al-Aasm, I.S., M. Coniglio, and A. Desrochers (1995), Formation of complex fibrous calcite veins in Upper Triassic strata of Wrangellia Terrain, British Columbia, Canada, *Sediment. Geol.*, *100*, 83-95.

Andersen, K.H., T.A. Lunne, C.G. Rawlings, and T.H. By (1993), Hydraulic fracture as a criterion for conductor setting depth in silt-clay, *Proceedings of the 4th Canadian Conference in Marine Geotechnical Engineering, St. Johns*, *7*, 4-26.

Atkinson, C., and M.F. Kanninen (1977), A simple representation of crack tip plasticity: The inclined strip-yield superdislocation model, *Int. J. Fracture*, *13*, 151-163.

Azeemuddin, M., S.G. Ghori, S. Saner, and M.N. Khan (2002), Injection-induced hydraulic fracturing in a naturally fractured carbonate reservoir: A case study from Saudi Arabia, SPE 73784, paper presented at *the 2002 SPE International Symposium and Exhibition on Formation Damage Control*, Lafayette, LA, USA, 20-21 Feb, p 789-799

Bakala, M. (1997), Fracture propagation in sediment-like materials, M.S. thesis, 83 pp., Univ. of Oklahoma, OK.

Berumen, S., D. Tiab, and F. Rodriguez (2000), Constant rate solutions for a fractured well with an asymmetric fracture, *J. Petrol. Sci. Eng.*, *25*, 49-58.

Bjerrum, L., J.K.T.L. Nash, R.M. Kennard, and R.E. Gibson (1972), Hydraulic fracturing in field permeability testing, *Geotechnique*, *22*, 319-332.

Chang, H. (2004), Hydraulic fracturing in particulate materials, Ph.D. thesis, 267 pp., Georgia Institute of Technology, GA.

Delaney, P.T., and D.D. Pollard (1981), Deformation of host rocks and flow of magma during growth of minette dikes and breccia-bearing intrusions near ship rock, New Mexico. *Geological Survey Professional Paper 1202, U.S. Government Printing Office, WA*.

Detournay, E. (2004), Propagation regimes of fluid-driven fractures in impermeable rocks, *Int. J. Geomech.*, *4*, 35-45.

Economides, M.J., and K.G. Nolte (2000), *Reservoir Stimulation*, 3rd Edition, John Wiley & Sons, LTD.

Germanovich, L.N., D.K. Astakhov, M.J. Mayerhofer, J. Shlyapobersky, and L.M. Ring (1997), Hydraulic fracture with multiple segments - I: Observations and model formulation*, Int. J. Rock Mech. Min. Sci.*, *34*, 471.

Germanovich, L.N., D.K. Astakhov, J. Shlyapobersky, M.J. Mayerhofer, C. Dupont, and L.M. Ring (1998), Modeling multisegmented hydraulic fracture in two extreme cases: No leakoff and dominating leakoff, *Int. J. Rock Mech. Min. Sci.*, *35*.

Germanovich, L.N., and D. Astakhov (2004a), Fracture closure in extension and mechanical interaction of parallel joints, *J. Geophys. Res.*, *109*, B02208, doi: 10.1029/2002JB002131.

Germanovich, L.N., and D. Astakhov (2004b), Stress-dependent permeability and fluid flow through parallel joints, *J. Geophys. Res.*, *109*, B09203, doi: 10.1029/2002JB002133.

Germanovich, L.N., and R. Wu (2006), On representation of crack-tip plasticity in Mohr-Coulomb materials, *Int. J. Fracture*, to be submitted.

Hainey, B.W., R.G. Keck, M.B. Smith, K.W. Lynch, and J.W. Barth (1999), On-site fracturing disposal of oilfield-waste solids in Wilmington field, California, *SPE Prod. Facil.*, *14*, 88-93.

Hallam, S.D., and N.C. Last (1991), Geometry of hydraulic fractures from modestly deviated wellbores, *J. Petrol. Techol.*, *43*, 742-748.

Hayashi, K., A. Sato, and T. Ito (1997), In situ stress measurements by hydraulic fracturing for a rock mass with many planes of weakness, *Int. J. Rock Mech. Min. Sci.*, *34*, 45-58.

Hubbert, M.K., and D.G. Willis (1957), Mechanics of hydraulic fracturing, *J. Petrol. Techol.*, *9*, 153-166.

Hunt, J.L., K. Frazier, B.P. Pendergraft, and M.Y. Soliman (1994), Evaluation and

completion procedure for produced brine and waste-water disposal wells, *J. Petrol. Sci. Eng.*, *11*, 51-60.

Hurt, R.S., R. Wu, L.N. Germanovich, H. Chang, and P. van Dyke (2005), On mechanisms of hydraulic fracturing in cohesionless materials, *EOS Trans. AGU*, *86*(*52*), *Fall Meet. Suppl.*, *Abstract H41B-0416*.

Kovscek, A.R., D.C. Tretheway, P. Persoff, and C.J. Radke (1995), Foam flow through a transparent rough-walled rock fracture, *J. Petrol. Sci. Eng.*, *13*, 75-86.

Lacazette, A., and T. Engelder (1992), Fluid-driven cyclic propagation of a joint in the Ithaca siltstone, Appalachian Basin, New York, in *Fluid Mechanics and Transport Properties of Rocks*, B. Evans and T-F. Wong eds, Academic Press Ltd., London, 297-324.

Lo, K.Y., and K. Kaniaru (1990), Hydraulic fracture in earth and rock-fill dams, *Can. Geotech. J.*, *27*, 496-506.

Mahrer, K.D. (1999), A review and perspective on far-field hydraulic fracture geometry studies, *J. Petrol. Sci. Eng.*, *24*, 13-28.

Mayerhofer, M.J., M.F. Richardson, R.N. Walker Jr., D.N. Meehan, M.W. Oehler, and R.R. Browning Jr. (1997), Proppants? We don't need no proppants, SPE 38611, *Proceedings of the 1997 SPE Annual Technical Conference and Exhibition*, *part Delta*, *Drilling and Completion*, San Antonio, TX, USA, 5-8 Oct, 457-464.

Murdoch, L.C. (1993a), Hydraulic fracturing of soil during laboratory experiments, Part I Methods and observations, *Geotechnique*, *43*, 255-265.

Murdoch, L.C. (1993b), Hydraulic fracturing of soil during laboratory experiments, Part II Propagations, *Geotechnique*, *43*, 267-276.

Murdoch, L.C. (1993c), Hydraulic fracturing of soil during laboratory experiments, Part III Theoretical analysis, *Geotechnique*, *43*, 277-287.

Murdoch, L.C. (2002), Mechanical analysis of idealized shallow hydraulic fracture, *J. Geotech. Geoenviron.*, *128*, 488-495.

Murdoch, L.C., and W.W. Slack (2002), Forms of hydraulic fractures in shallow fine-grained formations, *J. Geotech. Geoenviron.*, *128*, 479-487.

Ostermeier, R.M., J.H. Pelletier, C.D. Winker, J.W. Nicholson, F.H. Rambow, and K.M. Cowan (2000), Dealing with shallow-water flow in the deepwater Gulf of Mexico, *Proceedings of the Annual Offshore Technology Conference*, *1,* 75-86.

Papanastasiou, P., and C. Atkinson (2000), Representation of crack-tip plasticity in pressure sensitive geomaterials, *Int. J. Fracture*, *102*, 271-286.

Penman, A.D.M. (1977), Failure of Teton Dam, *Ground Eng.*, *10*, 18-20, 23-27.

Pollard, D.D. (1987), Elementary fracture mechanics applied to the structural interpretation of dykes, in *Mafic Dyke Swarms*, edited by H.C. Halls and W.F. Fahrig, *Geological Association of Canada Special Paper 34*, 5-24.

Pollard, D.D., and A. Aydin (1988), Progress in understanding jointing over the past century, *Geol. Soc. Am. Bull.*, *100*, 1181-1204.

Pollard, D.D., and R.C. Fletcher (2005), *Fundamentals of Structural Geology*, Cambridge University Press, Cambridge, 500 pp.

Pollard, D.D., O.H. Muller, and D.R. Dockstader (1975), The form and growth of fingered sheet intrusions, *Geol. Soc. Am. Bull.*, *86*, 351-363.

Pollard, D.D., P. Segall, and P.T. Delaney (1982), Formation and interpretation of dilatant echelon cracks, *Geol. Soc. Am. Bull.*, *93*, 1291 – 1303.

Raaen, A.M., E. Skomedal, H. Kjorholt, P. Markestad, and D. Okland (2001), Stress determination from hydraulic fracturing tests: The system stiffness approach, *Int. J. Rock Mech. Min. Sci.*, *38*, 529-541.

Rubin, A.M. (1995), Propagation of magma-filled cracks, *Annu. Rev. Earth Pl. Sci*., *23*, 287-336.

Sasaki, S. (1998), Characteristics of microseismic events induced during hydraulic fracturing experiments at the Hijiori hot dry rock geothermal energy site, Yamagata, Japan, *Tectonophysics*, *289*, 171-188.

Sommerauer, G., and R. Petersen (2003), Implementation of pressure maintenance in Seria Field using limited entry fractured water injection, SPE 84884, paper presented at *the SPE International Improved Oil Recovery Conference in Asia Pacific*, Kuala Lumpur, Malaysia, 20-21 Oct.

Souza, A.L.S., P.D. Fernandes, R.A. Mendes, A.J. Rosa, C.J.A. Furtado, and S.A. Petrobras (2005), The impact of injection with fracture propagation during waterflooding process, SPE 94704, paper presented at *the SPE Latin American and Caribbean Petroleum Engineering Conference*, Rio de Janeiro, Brazil, 20-23 June.

Srivastava, D.C., and T. Engelder (1991), Fluid evolution history of brittle-ductile shear zones on the hanging wall of Yellow Spring Thrust, Valley and Ridge Province, Pennsylvania, USA, *Tectonophysics*, *198*, 23-34.

Vermilye, J.M., and C.H. Scholz (1995), Relation between vein length and aperture, *J. Struc. Geo.*, *17*, 423-434.

Warner, J. (1997), Compaction grouting mechanism – What do we know? *Grouting: Compaction/Remediation/Testing*, Geotechnical Special Publication, *66*, ASCE,

New York, 1-17.

Wu, R., L.N. Germanovich, P. van Dyke, and R.P. Lowell (2006), A laboratory technique for controlling hydraulic fractures, *J. Geophys. Res.*, accepted.

Wu, R., and L.N. Germanovich (2006a), Mixed-mode I+III fracture propagation and segmentation, *J. Geophys. Res.*, to be submitted.

Wu, R., and L.N. Germanovich (2006b), Effects of crack tip plasticity on hydraulic fracturing in cohesionless materials, *Eng. Fract. Mech.*, to be submitted.

Wu, R., H. Huang, and L.N. Germanovich (2006), Discrete element simulation of fluid injection into particulate materials, *J. Geophys. Res.*, to be submitted.

Zhao, Z., D. Liu, W. Liu, L. Chai, and H. Zhou (2005), Development of systematic hydraulic fracturing technology for a natrally fractured reservoir, SPE 94101, paper presented at *the SPE Europec/EAGE Annual Conference*, Madrid, Spain, 13-16 June.

CHAPTER 2
A LABORATORY TECHNIQUE FOR CONTROLLING HYDRAULIC FRACTURES

Abstract. A simple technique is introduced to control the orientation and size of hydraulic fractures in laboratory samples. This is achieved by heating or cooling samples prior to injecting the fracturing liquid, so that the induced thermal stresses control the fracture orientation. We developed a simple theoretical model to parameterize experiments in laboratory settings and for materials that are different from ours. We also illustrate the utility of the technique with two examples: (i) mixed mode I+III hydraulic fracture propagation, and (ii) visualization of the fluid flow in the created fracture.

2.1 Introduction

During past decades the process of hydraulic fracturing has been widely used for the stimulation of petroleum and geothermal reservoirs [*Sasaki*, 1998; *Berumen et al.*, 2000], the remediation of soil and groundwater aquifers [*Murdoch and Slack*, 2002], the injection of waste [*Hunt et al.*, 1994; *Hainey et al.*, 1999], and the measurement of in-situ stress [*Hayashi et al.*, 1997; *Raaen et al.*, 2001]. Hydraulic fractures induced by fluid pressurized inside a solid host material also occur in nature as joints [*Lacazette and Engelder,* 1992], veins [*Srivastava and Engelder,* 1991; *Al-Aasm et al.*, 1995], and dykes [*Pollard*, 1987; *Rubin*, 1995]. Due to the heterogeneity of the material properties, rock structure and in-situ stress state, the hydraulic fracturing process is highly complex [see review in *Germanovich et al.*, 1997]. As a result, it is difficult to measure and predict the

behavior of hydraulic fractures in field conditions. Currently, there are still many open questions and uncertainties related to hydraulic fracturing, including fluid lag at the tip zone [*Desroches et al.*, 1994; *Garagash and Detournay*, 2000], interaction between multiple fractures [*Delaney and Pollard*, 1981; *Germanovich and Astakhov*, 2004a, 2004b], principal stresses off the axis of the borehole [*Engelder,* 1993], and proppant effects [*Kovscek et al.*, 1995].

The majority of experimental studies on hydraulic fracturing were conducted in rock and sediment samples [e.g., *Hanson et al.*, 1982; *Medlin and Masse*, 1984; *Murdoch*, 1993a, 1993b, 1993c], cement paste [e.g., *de Pater et al.*, 1994; *Groenenboom and van Dam*, 2000], and gypsum cement [e.g., *Abass et al.*, 1996]. A common difficulty with these tests is the observation and measurement of the hydraulic fractures that develop inside the opaque materials. Generally, the induced fracture geometry is measured by cutting the sample after the test [e.g., *Murdoch*, 1993a; *de Pater et al.*, 1994; *Abass et al.*, 1996], or by using an acoustic monitoring system [e.g., *de Pater et al.*, 1994; *Groenenboom and van Dam*, 2000]. Although these methods produce valuable results, they have important limitations. By cutting the samples after the test, only the final results are observed. The resolution of the acoustic method is currently insufficient to capture details of the fracture propagation process.

As a result, laboratory experiments on hydraulic fracturing in transparent materials have also been performed. These studies allowed the visualization in real time of the developing geometry of the fracture [e.g., *Rummel*, 1987; *Bunger et al.*, 2004] and the direction of fracture propagation [e.g., *Hubbert and Willis*, 1957; *Takada*, 1990;

Bakala, 1997]. Commonly used transparent geo-material analogues for fracturing are polymethylmethacrylate (PMMA, acrylic) [e.g., *Rummel*, 1987; *Cooke and Pollard*, 1996; *Germanovich and Dyskin*, 2000], polycarbonate [e.g., *Rittel*, 2000], silica glass [e.g., *Sommer*, 1969; *Germanovich et al.*, 1994], polyester resin [e.g., *Sahouryeh et al.*, 2002], gelatin [e.g., *Hubbert and Willis*, 1957; *Takada*, 1990; *Bakala*, 1997], and acrylic resin [e.g., *Rummel*, 1987; *Matsunaga et al.*, 1993].

Control of fracture orientation is important for the interpretation of laboratory results. Two examples are shown in Figure 2.1 where the fractures are inclined with respect to the drilled hole. The desired orientation was perpendicular to the hole, so that the results from these tests were of limited value. Several methods have been utilized to improve the control of the fracture orientation. For example, a starter fracture was sometimes implemented to reduce the fracture initiation pressure. *Bunger et al.* [2004] created a starter fracture by inserting a rod into the injection tube and striking it firmly with a hammer. *Germanovich et al.* [1999] created an initial notch by rotating a bent, sharpened rod inside the drill hole to scratch out PMMA material (see Figure 2.2); however, this technique is laborious and inefficient.

(a) (b)

Figure 2.1. Non-ideal orientations of hydraulic fractures created by injecting fluid into a cased hole in arbitrarily stressed PMMA. On both pictures, the outer diameter of the casing is 0.32 cm.

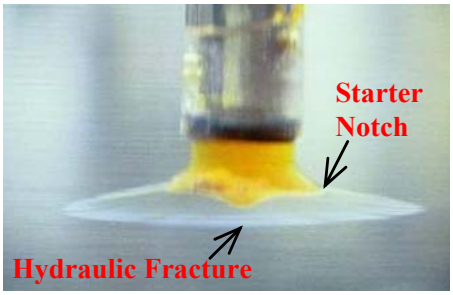

Figure 2.2. Starter notch (yellow) created by using a bent, sharpened rod to scratch out PMMA material, and the subsequent fracture propagated hydraulically [*Germanovich et al.*, 1999]. The drill hole diameter is 0.71 cm.

In this thesis, a simple but effective laboratory technique is introduced to produce hydraulic fractures with controlled orientation. The resulting fractures can be used as the basis for further studying hydraulic fracture propagation, fracturing in compression, flow of fluids in fractures and fracture networks, or other processes. While we illustrate this technique using PMMA samples, it can also be applied to other materials.

2.2 Experimental Procedure

The employed PMMA samples have a cylindrical shape (Figure 2.3). A hole with a small diameter is drilled along the central axis of each cylinder. The diameter of the drill hole is minimized to reduce boundary effects. Metal tubing can also be used as the drill hole casing. To initiate and propagate hydraulic fractures, a fracturing liquid is injected into the cylinder through the drill hole. The liquid is colored to maximize the contrast between the hydraulic fracture and the enveloping material (Figure 2.3).

Figure 2.3. A sample with hydraulically created fracture. The sample has a diameter of 10.2 cm and a length of 30.5 cm. The stainless steel casing tubing has outer and inner diameters of 0.32 and 0.22 cm, respectively. The fracturing fluid is a dark-green, oil-based liquid dye with a dynamic viscosity of 48 cp. No proppant was pumped into the hydraulic fracture.

We are not describing this experimental procedure in more detail since its implementation is fairly standard and straightforward [*Rummel*, 1987; *Abass et al.*, 1996; *Bunger et al.*, 2004]. Obviously, regardless of fracture orientation, this procedure is applicable only if a sufficiently stiff pump is available (otherwise, the fracture size is not

controllable). The pump used in our setup is described in Appendix A and is similar to that used by *Chernov and Kyu* [1996] and *Kyu and Tsygankov* [2003]. In our experiments the diameters of cylindrical PMMA samples and drilled holes varied from 5.08 to 20.32 cm and from 0.36 to 0.72 cm, respectively. Deviations from these dimensions, however, represent no principal difficulty and are only constrained by the available equipment and supplies, and the experimental goals. Specific dimensions of samples used in each tests described below are given in the figure captions.

2.3 Fracture Orientation Controlled by Thermal Stresses

To initialize a circular, planar fracture perpendicular or parallel to the central axis of the cylinder, thermal stresses are induced in the sample by heating or cooling its outer surface. This results in a temperature gradient inside the cylinder during transient state. The deformation resulting from thermal expansion or contraction is non-uniform along the radial and axial directions. This induces the thermal stresses in the sample. For example, under heating condition, the material close to the surface tends to expand more than that closer to the center of the sample. Consequently, this produces an outer ring of compression and an inner core of tension (Figures 2.4a and 2.4b). The induced thermal stresses can be utilized to control the orientation of hydraulic fractures.

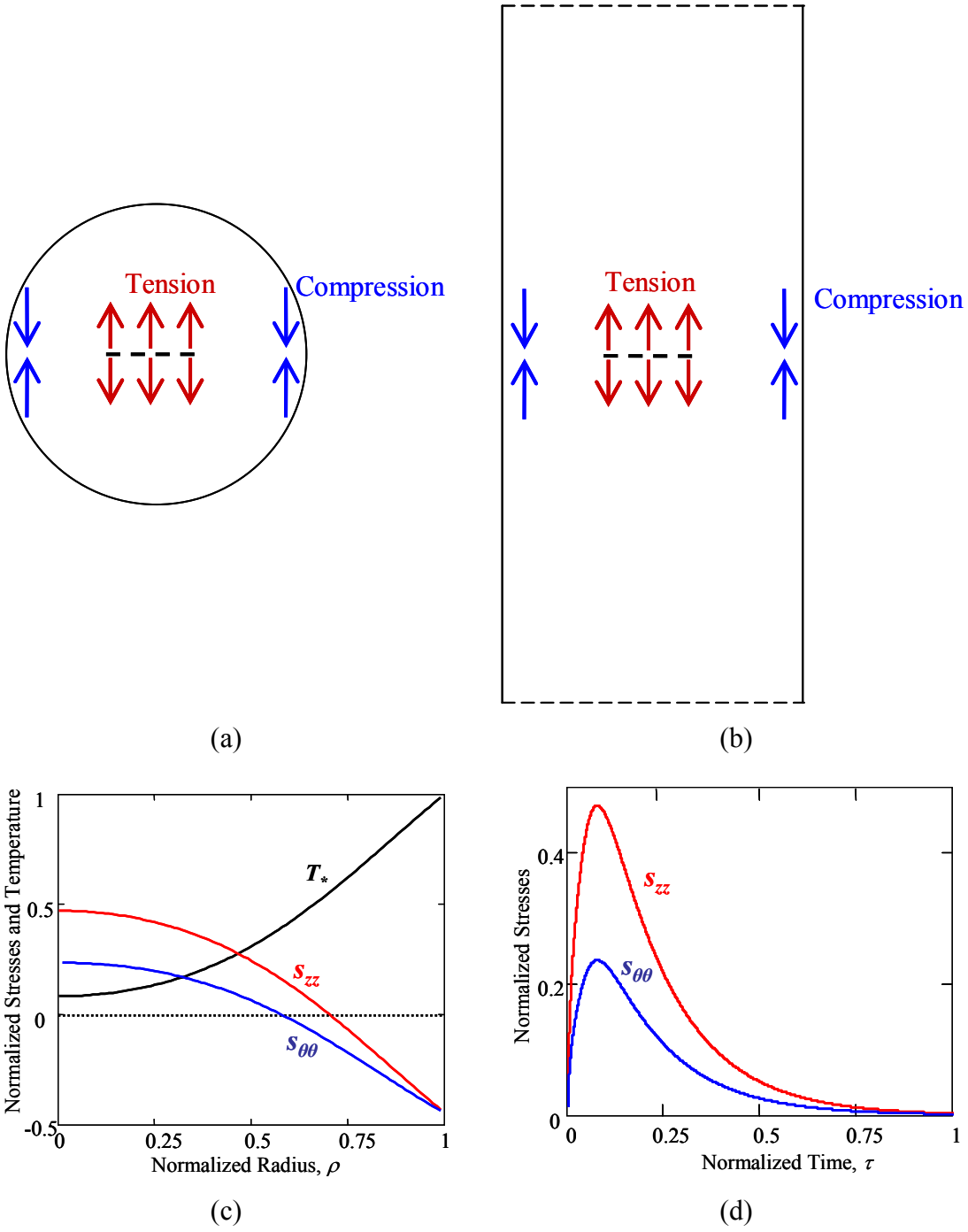

Figure 2.4. The schematic drawing of the stress state created by the transient heating the surface of a cylinder: (a) horizontal and (b) vertical cross sections. (c) Normalized temperature and thermal stresses along the cylinder radius for a dimensionless time of τ = 0.076, and (d) normalized thermal stresses at the center, ρ = 0, of the cylinder as the function of dimensionless time (the maximum values of s_{zz} and $s_{\theta\theta}$ occur at τ = 0.076).

Due to the symmetry about the central axis, z, of an elongated cylinder (*i.e.*, $R<<L$, where R and L are the radius and the length of the cylinder, respectively), the geometry of the problem reduces to a single spatial dimension, *i.e.*, the radial coordinate, r. Initially, the entire cylinder has a temperature of T_0. At time $t = 0$, the lateral surface of the cylinder is exposed to a constant temperature of T_1. The distribution of the normalized temperature inside the cylinder at $t > 0$ is given by [e.g., *Timoshenko and Goodier*, 1970]

$$T_* = \frac{T - T_0}{T_1 - T_0} = 1 - \sum_{n=1}^{\infty} \frac{2J_0(\beta_n \rho)}{\beta_n J_1(\beta_n)} e^{-\beta_n^2 \tau} \tag{2.1}$$

where $\rho = r/R$, $\tau = ta/R^2$, a is the thermal diffusivity, $J_0(x)$ and $J_1(x)$ are the zero- and first-order Bessel functions of the first kind, respectively, and β_n are the roots of $J_0(\beta) = 0$. Notations used in this paper are summarized in Table 2.1.

The corresponding dimensionless thermal stresses can be expressed as [e.g., *Timoshenko and Goodier*, 1970]

$$\begin{cases} s_{zz} = \dfrac{\sigma_{zz}(1-\nu)}{\alpha E(T_1 - T_0)} = -2\displaystyle\sum_{n=1}^{\infty} e^{-\beta_n^2 \tau} \left[\frac{2}{\beta_n^2} - \frac{J_0(\beta_n \rho)}{\beta_n J_1(\beta_n)} \right] \\ s_{\theta\theta} = \dfrac{\sigma_{\theta\theta}(1-\nu)}{\alpha E(T_1 - T_0)} = -2\displaystyle\sum_{n=1}^{\infty} e^{-\beta_n^2 \tau} \left[\frac{1}{\beta_n^2} + \frac{J_1(\beta_n \rho)}{\beta_n^2 \rho J_1(\beta_n)} - \frac{J_0(\beta_n \rho)}{\beta_n J_1(\beta_n)} \right] \end{cases} \tag{2.2}$$

where σ_{zz} and $\sigma_{\theta\theta}$ are the dimensional axial and tangential stresses, respectively, α is the coefficient of thermal expansion, E is Young's modulus, and ν is Poisson's ratio. In (2.2), the axial stresses are not uniform along the radial coordinate, $\rho = r/R$. The distributions of temperature and stresses along the radius are shown in Figure 2.5c. In the adopted sign convection, compressive stresses are negative.

Table 2.1. Nomenclature of notation

Latin Symbols

a	thermal diffusivity
a	fracture radius
a_1	initial fracture radius
a_2	final fracture radius
c	radius of the drill hole
C	$16K_f(1\text{-}\nu^2)/(3E)$
E	Young's modulus
F	force applied to the rod when creating the starter fracture
$J_0(x)$	zero-order Bessel functions of the first kind
$J_1(x)$	first-order Bessel functions of the first kind
K_I	mode I stress intensity factor
K_{III}	mode III stress intensity factor
K_{Ic}	material fracture toughness
K_f	bulk modulus of the injection liquid
L	cylinder (sample) length
L_t	tubing (casing) length
p	pressure inside the fracture
p_0	equivalent stress applied by the rod to the bottom of the drill hole
p_1	peak fluid pressure
p_2	residual fluid pressure
r	radial coordinate
r_1, r_2	inner and outer radii of drill hole casing (metal tubing)

R	cylinder (sample) radius
s_{rr}, $s_{\theta\theta}$, s_{zz}	dimensionless thermal stresses
t	time
T_0	initial temperature
T_1	temperature at the lateral surface of the cylinder (sample)
T_*	normalized temperature inside the cylinder
V_0	volume of the injection fluid inside the tubing
V_1	initial fluid volume
V_2	final fluid volume
z	coordinate along the axis of the cylinder

Greek Symbols

α	coefficient of linear thermal expansion
β_n	roots of $J_0(\beta) = 0$
θ	polar angle
ν	Poisson's ratio
ρ	dimensionless radius
σ_{rr}, $\sigma_{\theta\theta}$, σ_{zz}	dimensional thermal stresses
τ	dimensionless time

Because the diameter of the drill hole is much smaller than the sample diameter and because the fracture initiates at the drill hole, we need to know the stresses near the sample axis. As follows from expressions (2.2), at the center, $\rho = 0$, of the cylinder, $|\sigma_{zz}| = 2|\sigma_{\theta\theta}|$, i.e., at any given time the magnitude of the axial stress is twice as large as that of the tangential stress. Dependences of the thermal stresses on time at the cylinder center are shown in Figure 2.4d.

In the case of heating ($T_1 > T_0$), both the axial and tangential stresses are tensile at $\rho = 0$ (per (2.2) and Figure 2.4d). Since fractures in tensile stress fields tend to grow in a plane that is perpendicular to the maximum principal stress, it is expected that loading the sample hydraulically (after preheating, e.g., at the time $\tau = 0.076$ when the stresses reach their maximum value) would create a fracture that is oriented perpendicular to the sample axis. Indeed, Figure 2.5 shows an example of such a fracture.

(a) (b)

Figure 2.5. Hydraulic fracture (diameter = 1.8 cm) perpendicular to the axis of a cylindrical PMMA sample: (a) side and (b) end views. The sample has a length of 30.5 cm and a diameter of 7.62 cm. The drilled hole has a diameter of 0.36 cm and a length of 15.2 cm. Stainless steel casing has an outside diameter of 0.32 cm and a wall thickness of 0.05 cm. The measured peak pressure was 32 MPa.

In contrast, by cooling the cylinder ($T_1 < T_0$), both the axial stress and the

tangential stress at ρ = 0 are compressive. In compressive stress fields, fractures propagate in the direction perpendicular to the minimum compressive stress [e.g., *Hubbert and Willis*, 1957]. Therefore, loading the sample hydraulically after pre-cooling will create a fracture oriented parallel to the sample axis (i.e., along the drill hole). An example of such fracture is shown in Figure 2.6.

(a) (b)

Figure 2.6. Hydraulic fracture (diameter = 2.0 cm) parallel to the axis of a cylindrical PMMA sample. The sample has a length of 15.2 cm and a diameter of 5.08 cm. The drilled hole has a diameter of 0.36 cm and a length of 7.6 cm. Stainless steel casing has an outside diameter of 0.32 cm and a wall thickness of 0.05 cm.

2.4 Starter Fracture

Our preliminary tests revealed that fractures created with sample pre-cooling were indeed parallel to the sample axis (because the axis compressive stress exceeds the radial stress). Note that in this case, all the components of the thermal stresses are compressive. Fractures created with sample pre-heating are less controllable, probably due to the tensile nature of the thermal stress field in this case. In tensile stress field, fracture generally propagates in an unstable manner, that is, without changing the magnitudes of the external loads. Because of the dynamic character of the initial stage of fracture propagation, the fractures frequently deviate from the desired orientation (i.e.,

perpendicular to the sample axis) by an angle of the order of 10°. However, further improvement is readily achieved by using a small starter fracture (Figures 2.2a and 2.7a).

To create a starter fracture, we applied a static load to the bottom of the drill hole by slowly pushing a rod, placed inside the hole, with a loading machine. This is similar to the work of *Bunger et al.* [2004], who employed dynamic loading by forcefully hitting a rod with a hammer. The static loading is more controllable and results in small starter fractures that are circular and perpendicular to the drill hole (Figure 2.7a).

The size of the obtained starter fracture is limited by the non-elastic deformation caused by the contact loading. Furthermore, the subsequent hydraulic loading of the starter fracture may still occasionally lead to hydraulic fractures that deviate from the plane normal to the drill hole. Therefore, after creating the starter fracture, we usually also applied the thermal-stress technique to increase the size of the starter fracture. This combined technique is robust and yields a very consistent fracture orientation. Figure 2.7b shows an example of a fracture propagated hydraulically from a small starter fracture (Figure 2.7a) in a pre-heated sample. Because the diameter of the starter crack is of the order of the drill hole diameter, which is much smaller than the sample diameter, the fracture orientation is defined rather by the enveloping stress than the cavity/flaw shape.

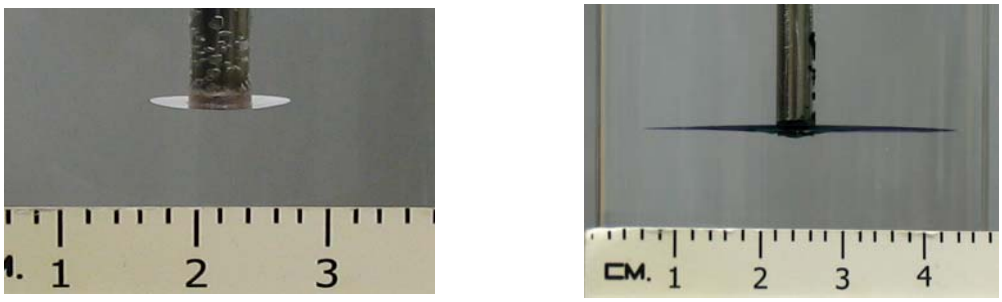

(a) (b)

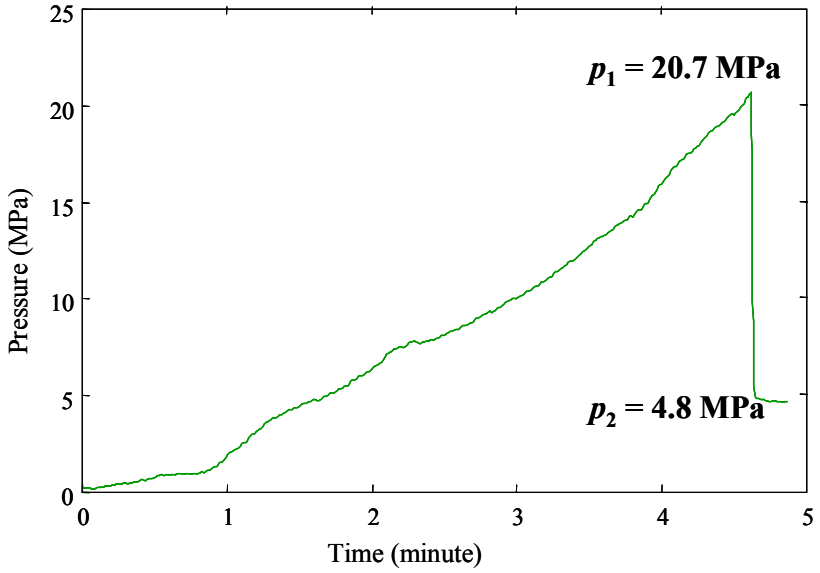

(c)

Figure 2.7. Hydraulic fracture perpendicular to the axis of a cylindrical sample: (a) small starter fracture, (b) propagated hydraulic fracture, and (c) injection pressure during fracture propagation. The starter fracture of the diameter of 0.8 cm was created by applying a load of 1.5 kN. The diameter of the propagated hydraulic fracture is 3.0 cm. The sample has a length of 15.2 cm and a diameter of 5.08 cm. The drilled hole has a diameter of 0.36 cm and a length of 7.6 cm. Stainless steel casing has an outside diameter of 0.32 cm and a wall thickness of 0.05 cm. Note that the peak pressure, p_1 = 20.7 MPa, is significantly smaller than that for the hydraulic fracture shown in Figure 2.5 because of the starter fracture.

2.5 Fracture Size

The fracture size can be controlled by varying volume V_0 of the injection fluid "between" the pump and the fracture, i.e., the volume of the drill hole (inside the casing, if any) plus connecting tubing (Figure 2.8). Even for an ideally stiff pump, the liquid occupying this volume is compressed and accumulates elastic strain energy before the fracture occurs at the peak pressure (Figure 2.7c). This energy is released (which is appropriate for not too high pressures) during the fracture propagation until the pressure drops sufficiently and the fracture stops propagating. While a few trial tests may be required, the final fracture size can be estimated based on the following simple model.

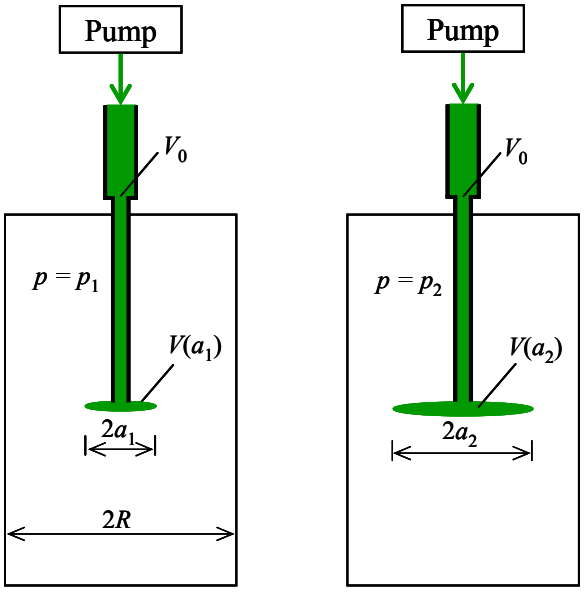

Figure 2.8. (a) Initial and (b) final instances of fracture propagation. Volume V_0 represents the injection fluid "between" the pump and the fracture, i.e., the volume of the drill hole (inside the casing, if any) plus connecting tubing.

Consider the *initial* and *final* instances of fracture propagation starting from a small starter fracture as shown in Figure 2.8. The fluid pressure reaches the peak, p_1, and

the starter fracture begins to grow at the onset of propagation. The fracture stops propagating when the fluid pressure drops to some value, p_2. Because the period of fracture growth is rather short (e.g., Figure 2.7), the additional amount of fluid injected by the pump during this period will be neglected. This assumption is practical in the case of a low injection rate and high pump stiffness. Then, the total mass of the fluid inside the injection system, which includes both the tubing and the fracture (but not the pump) remains constant during fracture propagation. Therefore, the specifics of the pump design are not important for our model. For simplicity, below we consider a drill hole, which is fully cased with rigid metal tubing (i.e., tubing deformation is ignored, Appendix B). Generalization of this model to the case of no casing, partial casing, or deformable casing is straightforward.

For simplicity, in this section, we only consider fracture propagation in an unloaded sample with uniform temperature, i.e., the fluid pressure is the only load applied to the crack. In other words, we consider the case when the magnitude of the thermal stresses acting on the sample (Figure 2.4a) are much smaller than the fluid pressure in the crack. This has been the case in all of our experiments, i.e., the thermal stresses estimated based on (2.2) (Figures 2.4c and 2.4d) have not exceeded 5% of the fluid pressure at fracture propagation.

We adopt the simplest fracture growth criterion [e.g., *Rice*, 1968]

$$K_I = K_{Ic} \tag{2.3}$$

where K_I is the mode I stress intensity factor, and K_{Ic} is the material fracture toughness.

Here K_I can be estimated by that for a uniformly pressurized, circular fracture perpendicular to the axis of an infinite long elastic cylinder:

$$K_I = \frac{2}{\pi} p\sqrt{\pi a} F(a/R) \tag{2.4}$$

where p is the pressure inside the fracture, a is the fracture radius, R is the radius of the cylinder, and

$$F(a/R) = \frac{1 - 0.5(a/R) + 0.148(a/R)^3}{\sqrt{1 - a/R}} \tag{2.5}$$

is given by *Tada et al.* [1985].

From (2.3) and (2.4), the fluid pressure in the fracture in mobile equilibrium [e.g., *Barenblatt*, 1962] can be expressed as

$$p(a) = \frac{\sqrt{\pi} K_{Ic}}{2\sqrt{R} F(a/R)} \sqrt{\frac{R}{a}} \tag{2.6}$$

The corresponding volume of the pressurized fracture is

$$V(a) = \frac{16(1-\nu^2)}{3E} p a^3 G(a/R) \tag{2.7}$$

where E is Young's Modulus, ν is Poisson's ratio, and function $G(a/R)$ is also given by *Tada et al.* [1985]. Comparing $G(a/R)$ and $F(a/R)$, it appears that for $a/R < 0.9$ (i.e., fractures that do not approach the sample boundary), the difference between $G(a/R)$ and $F(a/R)$ is less than 5%. Therefore, with an accuracy sufficient for our purposes, $G(a/R)$ =

$F(a/R)$. Then, combining expressions (2.6) and (2.7) results in

$$V(a) = \frac{8\sqrt{\pi}(1-\nu^2)K_{Ic}a^{5/2}}{3E} \tag{2.8}$$

To the first order, we can ignore the influence of the drill hole on fracture propagation. In addition, expressions (2.4) and (2.5) imply that during fracture propagation, the fluid fills the entire fracture, while in reality there could be a lag zone between the fracture and fluid fronts. Hence, $p(a)$ in (2.6) should be interpreted as an effective pressure in the sense that it maintains the same $K_I = K_{Ic}$ as in the fracture with the fluid lag.

Since the fluid mass in the sample remains constant during the fracture propagation period, the fluid volume changes only because of its compressibility. Hence,

$$p_1 - p_2 = K_f \frac{V_2 - V_1}{V_1} \approx K_f \frac{V(a_2) - V(a_1)}{V_0} \tag{2.9}$$

where K_f is the bulk modulus of the injection liquid, a_1 and a_2 are the initial and final fracture radii, $V_1 = V_0 + V(a_1)$ and $V_2 = V_0 + V(a_2)$ are the initial and final fluid volumes, V_0 is the volume of fluid inside the tubing (i.e., injection system; see Figure 2.8), and we took into account the fact that the initial fracture volume is small, i.e., $V(a_1) << V_0$.

Because $p_1 = p(a_1)$ and $p_2 = p(a_2)$, expression (2.9) can be rewritten as

$$V_0 = K_f \frac{V(a_2) - V(a_1)}{p(a_1) - p(a_2)} \tag{2.10}$$

Substituting (2.6) and (2.8) into (2.10), we obtain the volume

$$V_0 = CR^3\left[\left(\frac{a_2}{R}\right)^{5/2} - \left(\frac{a_1}{R}\right)^{5/2}\right]\left[\frac{R/a_1}{F(a_1/R)} - \frac{R/a_2}{F(a_2/R)}\right]^{-1} \tag{2.11}$$

that corresponds to a fracture of final radius, a_2. Here, the constant

$$C = \frac{16K_f(1-\nu^2)}{3E} \tag{2.12}$$

combines all relevant material properties and is independent of the fracture toughness, K_{Ic}.

Expressions (2.11) and (2.12) show that for the required loading conditions (i.e., low injection rate and high pump stiffness), the created fracture size depends upon the fluid compressibility, K_f, volume of the injection system, V_0, sample radius, R, and the radius, a_1, of the initial starter fracture. By varying these parameters (Appendix C), one can obtain the desired fracture size, a_2. In most cases, volume V_0 is readily changeable (i.e., by simply changing the casing and/or connecting tubing). The relationship between V_0 and a_2 is shown in Figure 2.9. As expected, V_0 decreases as a_2 decreases. Therefore, a smaller V_0 should be implemented in the experimental setup to achieve a smaller a_2.

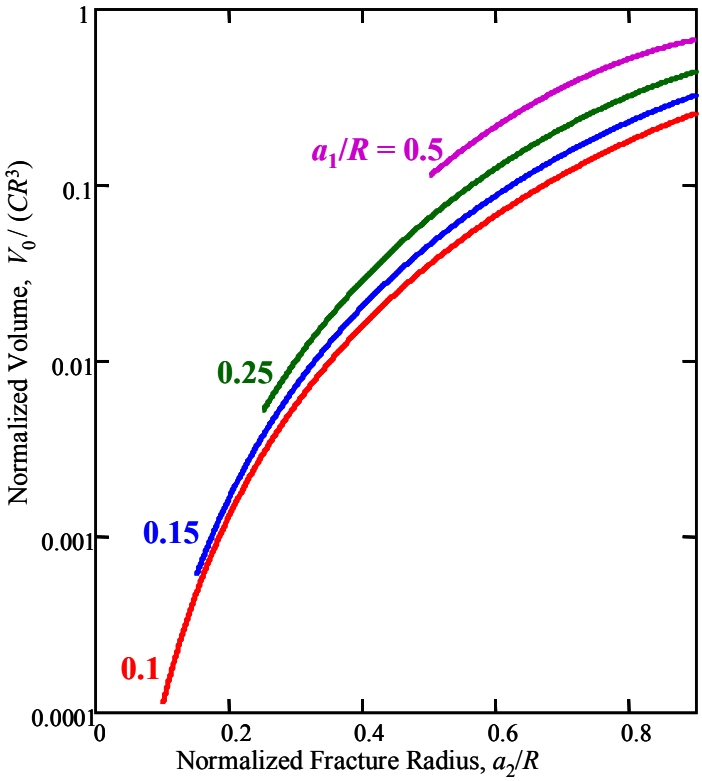

Figure 2.9. Normalized volume of the injection fluid in the sample versus normalized radius of the propagated fracture for different initial fracture radii.

Constant C in (2.11) is directly computed from expression (2.12) if the fluid and sample material properties can be determined from independent tests; although K_f can also be determined from the pressure log, e.g., from Figure 2.7, if the flow rate, Q, is measured during the pressurization stage (i.e., $dp/dt = \partial p/\partial V \times dV/dt$, where $\partial p/\partial V = 1/K_f$ and $dV/dt = Q$). Alternatively, this constant can be calibrated by a trial test. In the test shown in Figure 2.7, we had $V_0 = 2.46$ ml, which includes 0.28 ml inside the casing and 2.18 ml in the tubing connecting the casing with the pump. The fracture propagated from $a_1 = 0.4$ cm to $a_2 = 1.5$ cm. The sample radius was $R = 2.54$ cm, so expression (2.11) yields $C = 0.80$. This value can now be used for further experimental design to estimate a priori the required volume, V_0, of the injection system.

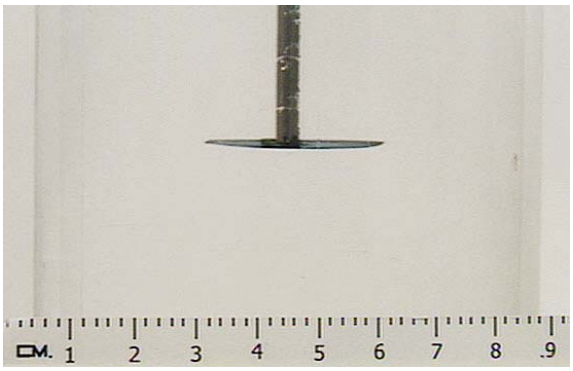

(a)

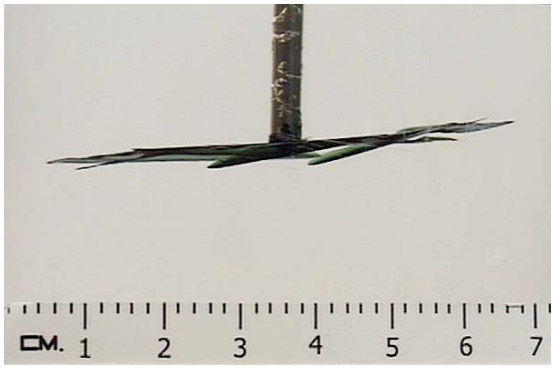

(b)

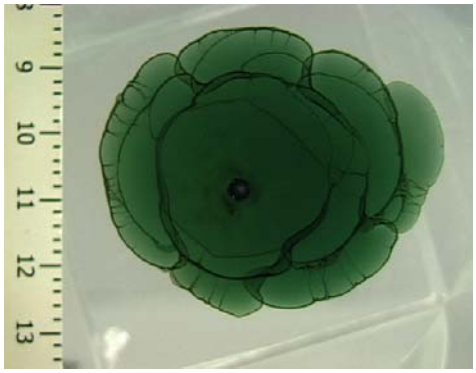

(c)

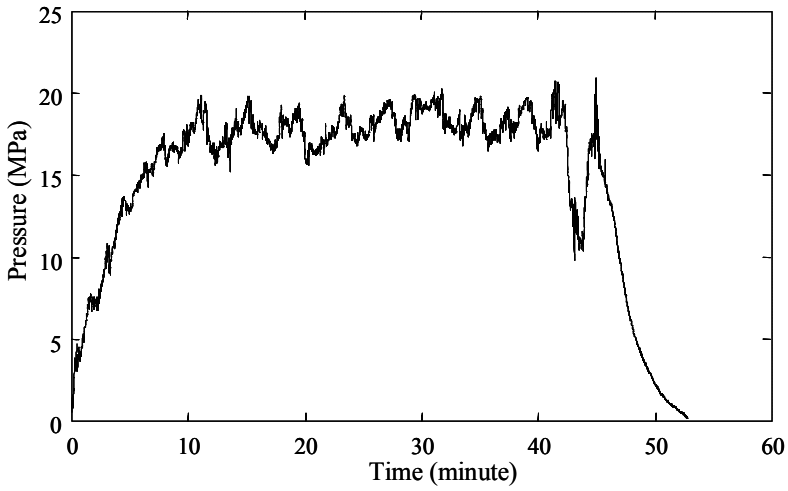

(d)

Figure 2.10. Hydraulic fracture under mixed-mode I + III loading: (a) initial circular fracture created with thermal technique (i.e., sample pre-heating), (b) side view of mode III segmentation of the propagated fracture, (c) end view of the propagated fracture, and (d) injection pressure curve. The sample has a length of 30.5 cm and a diameter of 10.2 cm. The drilled hole has a length of 15.24 cm.

For example, consider a cylindrical sample that has a radius of R = 5.08 cm (such as shown in Figure 2.3). If a_1 = 0.4 cm and the desired radius of the final fracture $a_2 \approx 1.4$ cm, according to (2.11) V_0 should be 2.37 ml. We used 15.24-cm deep drill hole (ending in the center of the sample) and an inner casing diameter of 0.22 cm. A total volume V_0 = 2.37 ml corresponds to the volume of 1.81 ml in the connecting tubing between the pump and the hole, which is easy to implement. These parameters were tested in the experiment shown in Figure 2.10a, which indeed resulted in a final fracture radius a_2 of approximately 1.4 cm.

2.6 Applications

2.6.1 Mixed Mode Hydraulic Fracture Propagation

To illustrate the application of the pre-heating technique, we consider an example of hydraulic fracture propagation under the mixed-mode loading that combines mode I (i.e., open mode) and mode III (i.e., out-of-plane shear) displacements at the fracture front. Mode I is due to fracture opening by liquid pressure, whereas mode III results from various factors such as three-dimensional fracture geometry (i.e., a small deviation from the planar shape [e.g., *Pollard and Fletcher*, 2005]), or interaction with the boundaries or with other fractures. Mode III induces inclined tensile stresses in the vicinity of the fracture front [e.g., *Rice*, 1968; *Pollard et al.*, 1982], so it may result in segmentation at the leading edge of a fracture. Such segmented fractures have been observed both in nature [e.g., *Delaney and Pollard*, 1981; *Hoek*, 1994] and in laboratory experiments [e.g., *Knauss*, 1970; *Murdoch*, 1993a; *Cooke and Pollard*, 1996; *Germanovich et al.*, 1997]. The example below shows one effect of mode III segmentation that is specific to

hydraulic fractures.

The developed technique is especially useful when the geometry of the crack in the mixed mode test needs to be accurately defined at the start of the test (i.e., circular crack; orientation nearly perfectly perpendicular to the borehole). In order to apply mixed-mode I+III loading to the initial fracture that is oriented perpendicular to the sample axis (Figure 2.10a), we applied a constant torque to the sample ends while the fracturing fluid was simultaneously injected into the drill hole. The mode III stress intensity factor, K_{III}, induced by the applied torque was only 2.2% of K_I. A constant injection rate of $3.7 \cdot 10^{-3}$ ml/min was maintained throughout the test.

In spite of a small magnitude of the mode III component, we observed segmented fracture fronts in the tested sample. The segments feature an elongated shape and comparable dimensions. The incline of the segments is noticeable (i.e., the twist angle is up to 14°), which results in the point-like connections between the segments and the initial fracture (Figure 2.10b). In general, these fracture segments spread along the perimeter of the parent fracture front, like a "flower petal" (Figure 2.10c). These segments do not form simultaneously. Instead, they form sequentially with localized fluid injection at the points where they are connected to the parent fracture.

The injection pressure was relatively constant during fracture propagation (Figure 2.10d). Yet, the overall radial fracture geometry (Figure 2.10c) implies that the pressure should have declined considerably with time [e.g., *Economides and Nolte*, 2000]. It is the fracture segmentation that changed the fluid flow pattern and consequently affected the pressure-time dependence. This can be explained by point-like connections between the

fracture segments that are inclined with respect to the initial fracture (Figure 2.10b). The small openings of these connections represent restrictions (i.e., "bottlenecks") to the fluid flow and raise the pressure in the drill hole.

Taking into account the effect of mixed mode segmentation during field-scale hydraulic fracturing can be quite important, because the geometry of the created fracture is invisible and usually has to be inferred from the pressure curves or other indirect observations. For example, relatively constant injection pressure dependence shown in Figure 2.10d is considered to be characteristic of very elongated fractures [e.g., *Economides and Nolte*, 2000]. Therefore, the inferred fracture geometry may be rather different from the real geometry, if the effects of fracture segmentation are ignored. Misinterpretation of fracture geometry is likely to significantly affect the evaluation and subsequent design of the hydraulic fracturing treatment. Furthermore, the observed effect can be at least of the same order as that of the "competition" between the rock toughness and fluid viscosity on the resistance to the fracture growth [*Detournay* 2004 and references therein].

Except our experiment, we are only familiar with the test of *Sommer* [1969] and *Cook and Pollard* [1996] who also used low K_{III}/K_I ratio (2.5% and 3%, respectively). While the experimental data is limited, it indicates that a K_{III}/K_I ratio as small as ~1% is sufficient for fracture front segmentation even in materials as homogeneous and fracture resistant as PMMA. In reality, a small component of mode III is always expected, for example, due to slight deviations of a three-dimensional fracture from a planar shape. As a result, front segmentation may accompany the process of growth of most (if not all) of

real fractures (hydraulic or not).

2.6.2 Visualization of Residual Permeability in Natural Fractures

To illustrate the application of the pre-cooling technique, we now consider an example of visualization of fluid flow in a fracture. Details of flow and transport in fractured rock are important for understanding groundwater remediation, subsurface waste disposal, and exploitation of geothermal or petroleum reservoirs. Characterizing these details is challenging in part because of a lack of direct observations [e.g., *Berkowitz*, 2002]. The fluid flow between the sides of two *rigid* plates (simulating fracture surfaces) has been described in many publications [e.g., *Berkowitz*, 2002]. The experiment described below is probably the first attempt to directly visualize the effect of pressure on the distribution of aperture of an entire "natural" fracture with flowing fluid in *elastic* material. However, the focus of this experiment is not the residual aperture distribution, but rather the tortuosity (i.e., preferential paths) of the fluid flow in the fracture (and also fracture intersections for multiple fractures) as a function of the aperture distribution.

For this purpose, we injected dyed water into an initial fracture, oriented parallel to the axis of a PMMA cylinder. Cylindrical samples are most readily available and convenient for many mechanical experimental procedures. However, for better visualization of fluid flow in the fracture, it is important to control the fracture orientation. More specifically, to avoid light reflections and hidden features, it is highly preferable to have the fracture oriented along the cylinder axis. This is why the fracture was created by sample pre-cooling (section 3), and then propagated hydraulically to a diameter of 9 cm

(Figure 2.11). The casing was removed after creating the hydraulic fracture, and before injecting the dyed liquid. Consequently, no casing is present in the photograph in Figure 2.11. The fracture is not symmetrical about the sample axis, and only the left side of the fracture breaches the sample boundary. The inflow is along the vertical drill hole casing. The outflow is through the left side sample boundary. The dyed water was continuously injected into the fracture at a rate of $5.0 \cdot 10^{-3}$ ml/min until the fracture was *fully* opened by the pressure of the flowing fluid (Figure 2.11a). After the fluid flow is interrupted and the pressure declines to atmospheric, the fracture remains *partially* open (Figure 2.11b).

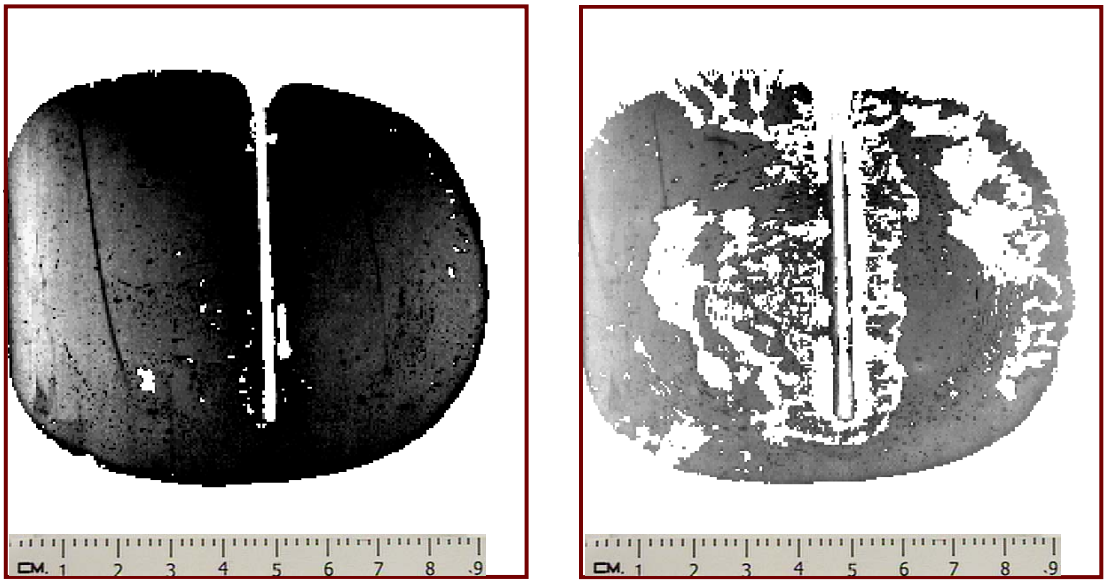

(a) (b)

Figure 2.11. (a) Fracture fully opened by the pressure of the flowing fluid (at $5.0 \cdot 10^{-3}$ ml/min), and (b) residual fracture opening after the fluid flow was interrupted and the pressure declined to atmospheric. Fracture diameter is 9 cm. The inflow is along the vertical drill hole casing, and the outflow is at the left side of the sample boundary. The initial fracture parallel to the axis of the cylindrical PMMA sample was created by sample pre-cooling, and then propagated hydraulically to the size shown. Higher color (i.e., darker gray scale) intensity indicates larger fracture aperture. White color corresponds to contact zones (i.e., resting on mismatched asperities).

The photographs in Figure 2.11 depict the color intensity of the dyed water in gray scale that characterizes the fracture aperture. Higher color (i.e., darker gray) intensity indicates larger fracture aperture. Translucent color (i.e., white gray intensity) corresponds to contact zones (i.e., resting on mismatched asperities). The contact area in the vicinity of the drill hole is due to the misalignment of the rough edges of the drill hole. Additional roughness may be due to the fact that the initial fracture propagation was perhaps dynamic and subsequently slowed down to create a smoother fracture surface [*Fineberg and Marder*, 1999].

This experiment demonstrates that because of the mismatch of asperities on the fracture sides, the fracture is open not only during water injection but even after interrupting the flow. This is an opening mode fracture that has well-matched surfaces at the onset. The resulting contact areas are broad surfaces that are either in good contact or open. They do not resemble highly localized, uniformly distributed contact points. It may seem intuitive that mode I fractures should close up completely, but this is not what happens, even in nearly perfectly homogeneous, isotropic material. Consequently, our experiment indeed shows that the fracture does not close completely. While more detailed experiments are required to describe the distribution of apertures and mismatched asperities, our results once again confirm that the simplification of the modeling of transport phenomena in fractures and fracture networks by ignoring the residual permeability should proceed with care.

2.7 Conclusions

A simple technique is introduced to control the orientation and size of hydraulic

fractures in laboratory samples. This is achieved by heating or cooling the samples to induce thermal stresses that control the fracture orientation. We developed a simple theoretical model to parameterize experiments in laboratory settings and for materials that are different from ours. We also illustrate the utility of the technique with two examples: (*i*) mixed mode I+III hydraulic fracture propagation, and (*ii*) visualization of fluid flow in the created fracture.

Except our experiment, we are only familiar with the test of *Sommer* [1969] and *Cook and Pollard* [1996] who also used low K_{III}/K_I ratio (2.5% and 3%, respectively). While the experimental data is limited, it indicates that such a low level of mode III component is sufficient for fracture front segmentation even in materials as homogeneous and fracture resistant as PMMA. Since in reality, a small K_{III} is always expected (for example, due to slight deviations of a three-dimensional fracture from a planar shape), front segmentation may accompany the process of growth of most (if not all) of real fractures.

Our fluid flow experiment (*ii*) is probably the first attempt to directly visualize the effect of pressure on the distribution of aperture of an entire "natural" fracture with flowing fluid in *elastic* material. While more detailed experiments are required to describe the distribution of apertures and mismatched asperities, our results strongly suggest that even in such nearly perfectly homogeneous and isotropic materials as PMMA, mode I fractures do not close up completely after the fluid flow stops.

Acknowledgement

This work was supported by NSF grants CMC-9896136, CMC-0421090, and OCE-0242163. The authors are grateful to D. Astakhov, J.C. Santamarina, K. Thomas, and T. Yi for their valuable assistance in developing the pump and the initial experimental setup employed for the mixed mode experiments. The authors also thank L.C. Murdoch, T. Engelder, and the associate editor for thorough review of this paper and many useful comments.

References

Abass, H.H., S. Hedayati, and D.L. Meadows (1996), Nonplanar fracture propagation from a horizontal wellbore: Experimental study, *SPE Prod. Facil.*, *11*, 133-137.

Al-Aasm, I.S., M. Coniglio, and A. Desrochers (1995), Formation of complex fibrous calcite veins in Upper Triassic strata of Wrangellia Terrain, British Columbia, Canada, *Sediment. Geol.*, *100*, 83-95.

Bakala, M. (1997), Fracture propagation in sediment-like materials, M.S. thesis, 83 pp., Univ. of Oklahoma, OK.

Barenblatt, G.I. (1962), The mathematical theory of equilibrium cracks in brittle fracture, *Adv. Appl. Mech.*, *7*, 55-129.

Berkowitz, B. (2002), Characterizing flow and transport in fractured geological media: A review, *Adv. Water Resour.*, *25*, 861-884.

Berumen, S., D. Tiab, and F. Rodriguez (2000), Constant rate solutions for a fractured well with an asymmetric fracture, *J. Petrol. Sci. Eng.*, *25*, 49-58.

Bunger, A.P., R.G. Jeffrey, and E. Detournay (2004), Toughness-dominated near-surface hydraulic fracture experiments, paper presented at *Gulf Rocks 2004, 6th NARMS: Rock Mechanics across Borders and Disciplines, ARMA*, Houston, TX, 5-9 June.

Chenov, O.I., and N.G. Kyu (1996), Oriented repture of solids by highly viscous fluid, *J. Min. Sci.*, *32*, 362-367.

Cooke, M.L., and D.D. Pollard (1996), Fracture propagation paths under mixed mode loading within rectangular blocks of polymethyl methacrylate, *J. Geophys. Res.*, *101*, 3387-3400.

Delaney, P.T., and D.D. Pollard (1981), Deformation of host rocks and flow of magma during growth of minette dikes and breccia-bearing intrusions near ship rock, New Mexico, *Geological Survey Professional Paper 1202, U.S. Government Printing Office, WA*.

Desroches, J., E. Detournay, B. Lenoach, P. Papanastasiou, J.R.A. Pearson, M. Thierchlin, and A. Cheng (1994), The crack tip region in hydraulic fracturing, *Proc. R. Soc. Lond. A*, *447*, 39-48.

Detournay, E. (2004), Propagation regimes of fluid-driven fractures in impermeable rocks, *Int. J. Geomech.*, *4*, 35-45.

de Pater, C.J., L. Weijers, M. Savic, K.H.A.A. Wolf, P.J. van den Hoek, and D.T. Barr (1994), Experimental study of nonlinear effects in hydraulic fracture propagation, *SPE Prod. Facil.*, *9*, 239-246.

Economides, M.J., and K.G. Nolte (2000), *Reservoir Stimulation*, 3rd ed., John Wiley & Sons, LTD, Chichester, UK.

Engelder, T. (1993), *Stress Regimes in the Lithosphere*, Princeton University Press, Princeton, NJ.

Fineberg, J., and M. Marder (1999), Instability in dynamic fracture, *Physics Reports*, *313*, 1-108.

Garagash, D.I., and E. Detournay (2000), The tip region of a fluid-driven fracture in an elastic medium, *Trans. ASME: J. Appl. Mech.*, *67*, 183-192.

Germanovich, L.N., and D. Astakhov (2004a), Fracture closure in extension and mechanical interaction of parallel joints, *J. Geophys. Res.*, *109*, B02208, doi: 10.1029/2002JB002131.

Germanovich, L.N., and D. Astakhov (2004b), Stress-dependent permeability and fluid flow through parallel joints, *J. Geophys. Res.*, *109*, B09203, doi: 10.1029/2002JB002133.

Germanovich, L.N., and A.V. Dyskin (2000), Fracture mechanisms and instability of openings in compression, *Int. J. Rock Mech. Min. Sci.*, *37*, 263-284

Germanovich, L.N., R.L. Salaganik, A.V. Dyskin, and K.K. Lee (1994), Mechanisms of brittle fracture of rock with multiple pre-existing cracks in compression, *Pure Appl. Geophys.*, *143*(13), 117-149.

Germanovich, L.N., D.K. Astakhov, M.J. Mayerhofer, J. Shlyapobersky, and L.M. Ring (1997), Hydraulic fracture with multiple segments - I: Observations and model formulation*, Int. J. Rock Mech. Min. Sci.*, *34*, 471.

Germanovich, L.N., D. Astakhov, J. Shlyapobersky, L. Ring, and M. Mayerhofer (1999), Multisegmented hydraulic fractures, paper presented at *Workshop in Memory of Jacob Shlyapobersky: Latest Advances in Hydraulic Fracturing*, Vail, CO, 5-6 June.

Groenenboom, J., and D.B. van Dam (2000), Monitoring hydraulic fracture growth: Laboratory experiments, *Geophysics*, *65*, 603-611.

Hainey, B.W., R.G. Keck, M.B. Smith, K.W. Lynch, and J.W. Barth (1999), On-site fracturing disposal of oilfield-waste solids in Wilmington field, California, *SPE Prod. Facil.*, *14*, 88-93.

Hanson, M.E., G.D. Anderson, R.J. Shaffer, and L.D. Thorson (1982), Some effects of stress, friction, and fluid flow on hydraulic fracturing, *Soc. Petrol. Eng. J.*, *22*, 321-332.

Hayashi, K., A. Sato, and T. Ito (1997), In situ stress measurements by hydraulic fracturing for a rock mass with many planes of weakness, *Int. J. Rock Mech. Min.*

Sci., *34*, 45-58.

Hoek, H. (1994), Mafic dykes of the Vestfold Hills, East Antarctica: An analysis of the emplacement mechanism of tholeiitic dyke swarms and of the role of dyke emplacement during crustal extension, Ph.D. dissertation, Univ. of Utrecht, The Netherlands.

Hubbert, M.K., and D.G. Willis (1957), Mechanics of hydraulic fracturing, *J. Petrol. Techol.*, *9*, 153-166.

Hunt, J.L., K. Frazier, B.P. Pendergraft, and M.Y. Soliman (1994), Evaluation and completion procedure for produced brine and waste-water disposal wells, *J. Petrol. Sci. Eng.*, *11*, 51-60.

Knauss, W.G. (1970), An observation of crack propagation in anti-plane shear, *Int. J. Fract. Mech.*, *6*, 183-187.

Kovscek, A.R., D.C. Tretheway, P. Persoff, and C.J. Radke (1995), Foam flow through a transparent rough-walled rock fracture, *J. Petrol. Sci. Eng.*, *13*, 75-86.

Kyu, N.G., and D.A. Tsygankov (2003), Method for directional failure of rocks by plastic substances, *J. Min. Sci.*, *39*, 573-578.

Lacazette, A., and T. Engelder (1992), Fluid-driven cyclic propagation of a joint in the Ithaca siltstone, Appalachian Basin, New York, in *Fluid Mechanics and Transport Properties of Rocks*, edited by B. Evans and T-F. Wong, Academic Press Ltd., London, 297-324.

Matsunaga, I., H. Kobayashi, S. Sasaki, and T. Ishida (1993), Studying hydraulic fracturing mechanism by laboratory experiments with acoustic emission monitoring, *Int. J. Rock Mech. Min. Sci. Geomech. Abstr.*, *30*, 909-912.

Medlin, W.L., and L. Masse (1984), Laboratory experiments in fracture propagation, *Soc. Petrol. Eng. J.*, *24*, 256-268.

Murdoch, L.C. (1993a), Hydraulic fracturing of soil during laboratory experiments, Part I Methods and observations, *Geotechnique*, *43*, 255-265.

Murdoch, L.C. (1993b), Hydraulic fracturing of soil during laboratory experiments, Part II Propagations, *Geotechnique*, *43*, 267-276.

Murdoch, L.C. (1993c), Hydraulic fracturing of soil during laboratory experiments, Part III Theoretical analysis, *Geotechnique*, *43*, 277-287.

Murdoch, L.C., and W.W. Slack (2002), Forms of hydraulic fractures in shallow fine-grained formations, *J. Geotech. Geoenviron.*, *128*, 479-487.

Pollard, D.D. (1987), Elementary fracture mechanics applied to the structural

interpretation of dykes, in *Mafic Dyke Swarms*, edited by H.C. Halls and W.F. Fahrig, *Geological Association of Canada Special Paper 34*, 5-24.

Pollard, D.D., P. Segall, and P.T. Delaney (1982), Formation and interpretation of dilatant echelon cracks, *Geol. Soc. Am. Bull.*, *93*, 1291-1303.

Pollard, D.D., and R.C. Fletcher (2005), *Fundamentals of Structural Geology*, Cambridge University Press, Cambridge, 500 pp.

Raaen, A.M., E. Skomedal, H. Kjorholt, P. Markestad, and D. Okland (2001), Stress determination from hydraulic fracturing tests: The system stiffness approach, *Int. J. Rock Mech. Min. Sci.*, *38*, 529-541.

Rice, J.R. (1968), Mathematical analysis in the mechanics of fracture, *Fracture*, *An Advanced Treatise*, edited by H. Liebowitz, Academic, New York, II, 3, 191-311.

Rittel, D. (2000), Experimental investigation of transient thermoplastic effects in dynamic fracture, *Int. J. Solids Struct.*, *37*, 2901-2913.

Rubin, A.M. (1995), Propagation of magma-filled cracks, *Annu. Rev. Earth Pl. Sci*., *23*, 287-336.

Rummel, F. (1987), Fracture mechanics approach to hydraulic fracturing stress measurements, *Fracture Mechanics of Rock*, edited by B.K. Atkinson, Academic Press, London, UK, 217-239.

Sahouryeh, E., A.V. Dyskin, and L.N. Germanovich (2002), Crack growth under biaxial compression, *Eng. Fract. Mech.*, *69*, 2187-2198.

Sasaki, S. (1998), Characteristics of microseismic events induced during hydraulic fracturing experiments at the Hijiori hot dry rock geothermal energy site, Yamagata, Japan, *Tectonophysics*, *289*, 171-188.

Sommer, E. (1969), Formation of fracture 'Lances' in glass, *Eng. Fract. Mech.*, *1*, 539-546.

Srivastava, D.C., and T. Engelder (1991), Fluid evolution history of brittle-ductile shear zones on the hanging wall of Yellow Spring Thrust, Valley and Ridge Province, Pennsylvania, USA, *Tectonophysics*, *198*, 23-34.

Tada, H., P.C. Paris, and G.R. Irwin (1985), *The Stress Analysis of Cracks Handbook*, 2nd ed., Paris Productions Incorporated, St. Louis, MO.

Takada, A. (1990), Experimental study on propagation of liquid-filled crack in gelatin: Shape and velocity in hydrostatic stress condition, *J. Geophys. Res.*, *95*, 8471-8481.

Timoshenko, S.P., and J.N. Goodier (1970), *Theory of Elasticity*, McGraw-Hill, New York, NY.

CHAPTER 3
MIXED-MODE I+III FRACTURE PROPAGATION AND SEGMENTATION

Abstract. Out-of-plane fracture propagation is usually a characteristic of mixed mode fractures. In particular, mixed-mode I+III loading is one of the primary causes of fracture front segmentation. Such segmented fractures have been observed both in nature and in laboratory experiments. Many brittle materials (e.g., rock, concrete, ceramic) have relatively low resistance to tensile fracture. In quasi-brittle materials, even a small mode III component may cause fracture segmentation due to the tensile stresses induced near the fracture front. In this work, we experimentally studied not only the effect of mode III loading on the onset of fracture segmentation but also the effect of segmentation on the subsequent fracture growth when the K_{III}/K_I ratio was rather small (1-10%).

We used transparent, cylindrical PMMA samples with circular internal fractures perpendicular to the sample axis. Fracture orientation was controlled by thermoelastic stresses induced in each sample by preheating it before creating a fracture. In order to apply mode III loading to the initial fracture, a constant torque was applied to the specimen while fluid was injected into the fracture at a constant rate to pressurize it and to induce mode I loading. In spite of the small magnitude of the mode III component, we observed segmented fracture fronts in all tested samples. The segments had similar dimensions and an elongated shape. When the fractures were further pressurized by injecting additional fluid into the sample, second-order segments developed along the fronts of the first-order segments.

We also developed a simple asymptotic model of a multi-segmented mode I+III fracture propagating in conditions of a low level mode III loading, which takes into account mechanical interaction between the segments and the parent fracture. The model shows good agreement with the experimental observations.

The obtained results indicate that a K_{III}/K_I ratio as small as a few percent is sufficient for fracture front segmentation even in materials as homogeneous and fracture resistant as PMMA. In reality, a small component of mode III is always expected, for example, due to slight deviations of a three-dimensional fracture from a planar shape or interaction with boundaries or other fractures. As a result, front segmentation (at an appropriate scale) is likely to accompany the growth of most (if not all) real fractures, at least in quasi-brittle materials.

3.1 Introduction

Hydraulic fracture branching and segmentation is a phenomenon extensively observed in nature [e.g., *Roering*, 1968; *Pollard et al.*, 1982; *Pollard and Aydin*, 1988; *Rubin*, 1995; *Abelson and Agnon*, 1997]. An example is given in Figure 3.1a, which shows a segmented dike outcrop. In laboratory tests, splitting of the hydraulic fracture front is observed even in homogeneous materials [e.g., *Hubbert and Willis*, 1957; *Knauss*, 1970; *Hallam and Last*, 1991; *Abass et al.*, 1996; *Bakala*, 1997]. In the first published laboratory hydraulic fracture experiment conducted by *Hubbert and Willis* [1957], we can see the segmented nature of their fracture (Figure 3.2a). *Abass et al.* [1996] tested rectangular blocks made of hydrostone (gypsum cement) that were confined in a tri-axial loading vessel. They observed multiple fracture segments when the drill hole was

inclined with respect to the maximum horizontal stress direction (Figure 3.2b).

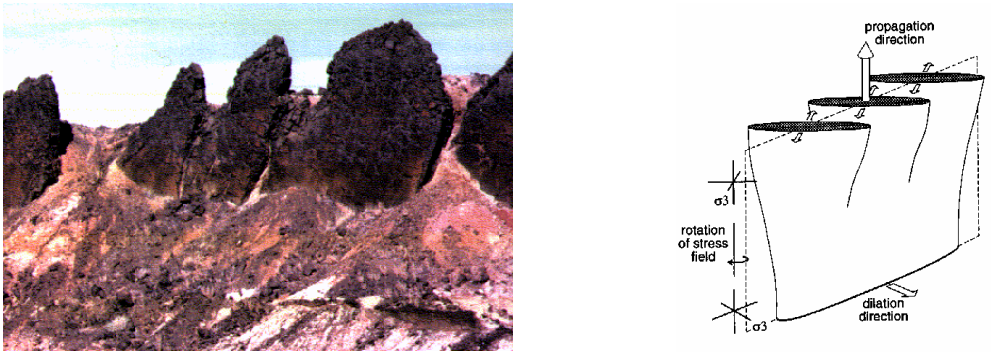

(a) (b)

Figure 3.1. (a) Outcrop of segmented magmatic dike [*Delaney*, 1996]; (b) dike segmentation due to rotation of least principal stress axis during upward propagation [after *Delaney and Pollard*, 1981].

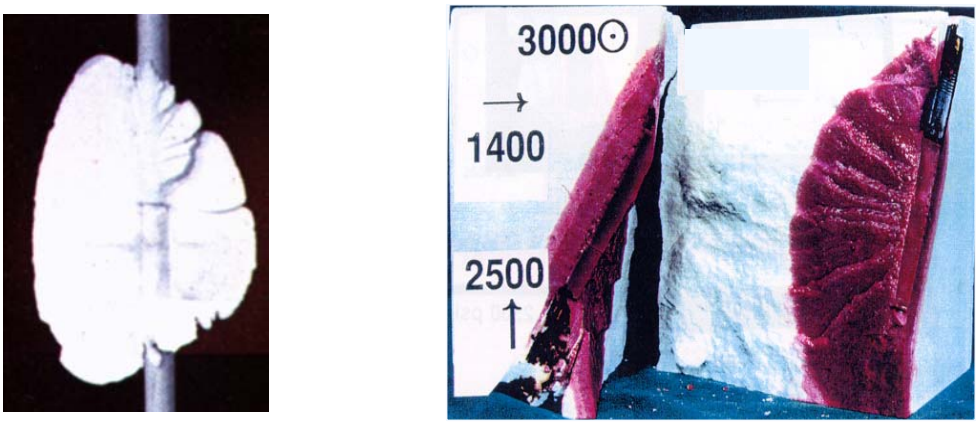

(a) (b)

Figure 3.2. Segmented hydraulic fracture observed in the laboratory experiments of (a) *Hubbert and Willis* [1957] and (b) *Abass et al.* [1996].

Conventionally, complex nonplanar segmented hydraulic fractures are generally treated as a single planar fracture. In engineering applications, this simplification may overestimate net pressure and underestimate the propped length and the width of individual fractures, which further cause an overestimate of fluid leak-off and an

underestimate of the reliable fracture confinement within the pay zone [e.g., *Germanovich et al*., 1998; *Mahrer*, 1999; *Economides* and *Nolte*, 2000]. In practice, these inaccurate predictions may result in a poor design of hydrofrac jobs and loss of well productivity [e.g., *Hallam and Last*, 1991].

In general, two main conditions contribute to fracture branching and segmentation: heterogeneity of material properties and stress heterogeneity [*Germanovich et al.*, 1997 and references herein]. In particular, stress heterogeneity is often considered to be a primary cause of fracture segmentation in geomaterials [*Delaney and Pollard*, 1981; *Cooke and Pollard*, 1996; *Germanovich et al.*, 1997]. Once the fracture grows sufficiently large, the in-situ stresses can often be considered heterogeneous (e.g., Figure 3.1b) since the fracture size becomes comparable to the typical scale of stress change [e.g., *Germanovich et al.*, 1997].

Three modes of deformation can be distinguished near a fracture front [*Kanninen and Popelar*, 1985]. In mode I, the displacements of the fracture surface are perpendicular to the fracture plane (Figure 3.3a). Mode II occurs when the displacements of the fracture surface are in the plane of the fracture and perpendicular to the fracture front (Figure 3.3b). Mode III is caused by the shear displacement of the fracture surfaces, which are parallel to the fracture front (Figure 3.3c). A fracture can be loaded under each of the above pure-mode loading or combinations of these modes (Figure 3.4). The latter case is called mixed mode loading.

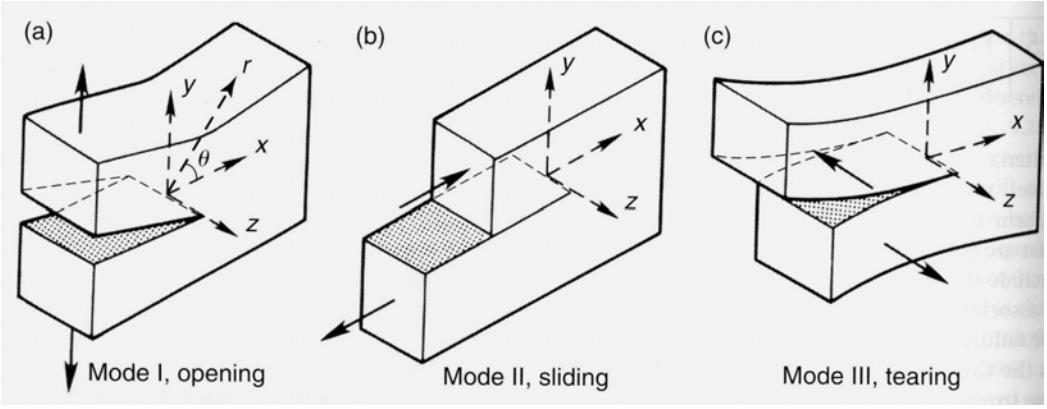

Figure 3.3. Three modes of fractures: (a) mode I – opening mode, (b) mode II – sliding (in-plane shear) mode, and (c) mode III – tearing (out-of-plane shear) mode [*Kanninen and Popelar*, 1985].

A characteristic of mixed mode fractures is that they usually produce out-of-plane propagation [*Pollard and Aydin*, 1988] (Figure 3.4). Even in relatively homogeneous media, in-plane shear (i.e., mixed-mode I+II) results in curved fractures or sharp kinks (Figure 3.4b), while out-of-plane shear (i.e., mixed-mode I+III) results in segmented fracture fronts (Figure 3.4c). In other words, modes I, II and III are "responsible" for fracture propagation, direction, and segmentation, respectively. Accordingly, fracture growth is a mechanism of relieving mode I, while mode II is relieved by changing fracture propagation direction. Fracture segmentation occurs due to the accumulation of mode III, which is relieved as a result of the segmentation.

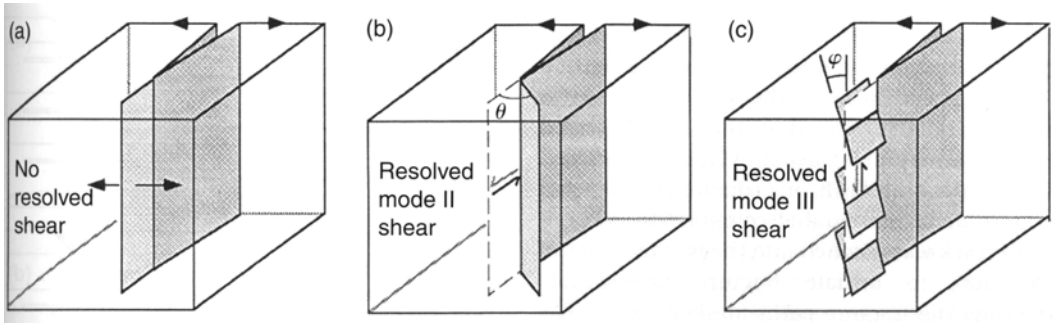

Figure 3.4. Schematic illustration of fracture propagation path: (a) pure mode I, (b) mixed-mode I+II, and (c) mixed-mode I+III [after *Pollard and Aydin*, 1988].

Mixed mode I+II fracture initiation and propagation has received considerable attention. A number of criteria, including the maximum circumferential tensile stress theory [*Erdogan and Sih*, 1963], the minimum strain energy density theory [*Sih*, 1974], and the maximum energy release rate theory [*Hussain et al*., 1974] has been proposed for crack initiation and crack growth under mixed-mode I+II loading. Laboratory experiments [e.g., *Mahajan and Ravi-Chandar*, 1989; *Thomas and Pollard*, 1993; *Roy et al.*, 1999; *Shi et al.*, 2000] and numerical simulations [e.g., *Ingraffea and Heuze*, 1980; *Crouch and Starfield*, 1983; *Maji et al.*, 1991; *Shimamoto et al.*, 1994; *Alfaiate et al.*, 2002] have also been carried out for mixed-mode I+II loading conditions. Since, to a large degree, the mixed mode I+II fracture propagation is a two-dimensional process (Figure 3.4b), while varying in details for different materials and experimental setups, in general, this phenomenon can be considered as relatively well understood (at least, for brittle fracture).

The growth of fractures under mixed-mode I+III loading has also attracted extensive attention. Laboratory tests include experiments on brittle materials such as glass [e.g., *Sommer*, 1969], polymethylmethacrylate (PMMA, acrylic) [e.g., *Ueda et al.*, 1983; *Richard and Kuna*, 1990; *Davenport and Smith*, 1993; *Cooke and Pollard*, 1996], ceramic [e.g., *Petrovic*, 1985], concrete [e.g., *Song et al.*, 2004], and rock [e.g., *Cox and Scholz*, 1988; *Chang et al.*, 2002], as well as on ductile materials such as various types of steel [e.g., *Pook*, 1985; *Yates and Miller*, 1989; *Kamat and Hirth*, 1996; *Yates and Mohammed*, 1996; *Li et al.*, 1998; *Srinivas et al.*, 2004].

The experimental studies mentioned above focused mainly on the onset of

fracture propagation. Several proposed empirical criteria for mixed mode I+III crack propagation are based on the stress intensity factors [e.g., *Petrovic*, 1985; *Davenport and Smith*, 1993; *Yates and Mohammed*, 1996; *Song et al.*, 2004]. However, empirical criteria are typically suitable only for a certain material type, loading conditions, and specimen geometry. Moreover, only a few works were devoted to the fracture geometry, such as the twist angles (the angles between the parent crack surface and the echelon fracture surfaces) [e.g., *Sommer*, 1969; *Ueda et al.*, 1983; *Yates and Miller*, 1989; *Cooke and Pollard*, 1996] and the number of echelon fractures [e.g., *Cooke and Pollard*, 1996].

In his pioneering work, *Sommer* [1969] applied fluid pressure to the notches on the lateral surface of a round alkaline resistant glass (AR-glass) rod and simultaneously superimposed a small amount of torsion. In his tests, the fracture front was broken into multiple separate segments (Figure 3.5). The mean twist angle of fracture initiation was about 3.3° for an average breaking pressure of 827 kgf/cm^2 (81.1 MPa) and a torsion stress at the rod periphery of 32 kgf/cm^2 (3.1 MPa) (K_{III}/K_I = 2.5%.). Based on his test results, *Sommer* [1969] suggested that the formation of segments was due to the local adjustment of the crack plane to the changes in the direction of maximum principal stress.

Ueda et al. [1983] conducted mode I+III experiments on the cruciform PMMA specimens. They suggested that, for brittle materials, the maximum energy release rate criterion was able to predict the direction of initial crack propagation and the fracture strength under mixed-mode loading. In their tests, the facture propagated from all portions of the notch front when $0 < K_{III}/K_I < 0.58$. In contrast, when $0.58 < K_{III}/K_I < 2.75$, the crack propagation initiated only from one point of the notch front.

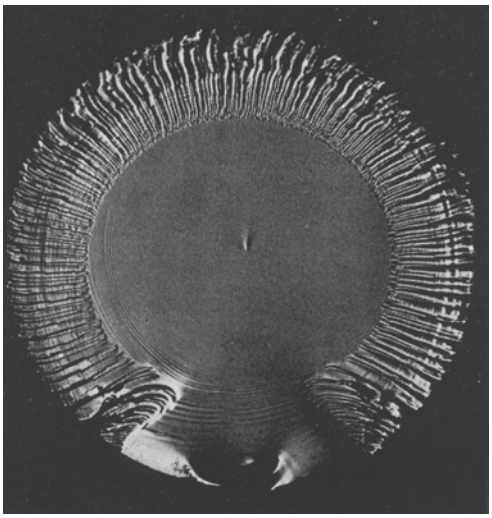

Figure 3.5. Mixed mode I+III fracture surface in a cylindrical glass rods conducted by *Sommer* [1969].

Yates and Miller [1989] performed mixed mode I+III fatigue test on a low pressure steam turbine rotor steel. The specimens tested were 25-mm diameter round bars with a 5-mm deep circumferential slit machined by electric discharge. Cracked specimens were examined by optical and scanning electron microscopy. All fracture surfaces consisited of radial facets (Figure 3.6). The inclined angle of the facet varied with the initial K_{III}/K_I ratio. When K_{III}/K_I = 2.2, discrete facets were formed in such a large angle that they did not link up. In contrast, when K_{III}/K_I = 0.4, facets were initialized at shallower inclined angles and they eventually merged into a large, continuous crack front inclined to the slit plane. The observed twist angle varied from 45° to 25° as the initial K_{III}/K_I ratio reduced from 2.0 to 0.4. Based on their test, *Yates and Miller* [1989] suggested that the maximum principal stress criterion gave a better estimate of the twist angle than the criterion of the maximum energy release rate.

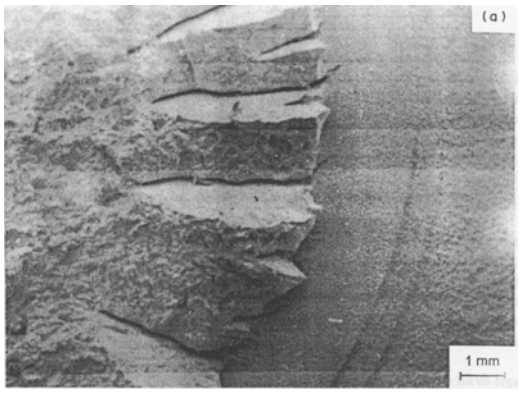

Figure 3.6. Mixed mode I+III fatigue surface in low pressure steam turbine rotor steel [*Yates and Miller*, 1989].

Cooke and Pollard [1996] tested rectangular plexiglass blocks under mixed-mode I+III loading by employing a biaxial loading system (Figure 3.7a) with independently controlled vertical and horizontal hydraulic actuators. The observed fracture twist angles (Figures 3.7b and 3.7c) were found to be significantly lower (one-third to one-half) than the theoretical prediction based on the maximum principal stress criterion. Their test results also indicated that the number of en-echelon fractures on which the fracture front split into was dependent on the ratio of stress intensity factors. This number was determined from visual inspection and, therefore, was likely underestimated [*Cooke and Pollard*, 1996]. In their work, K_{III}/K_I varied from 0.03 to 1.02.

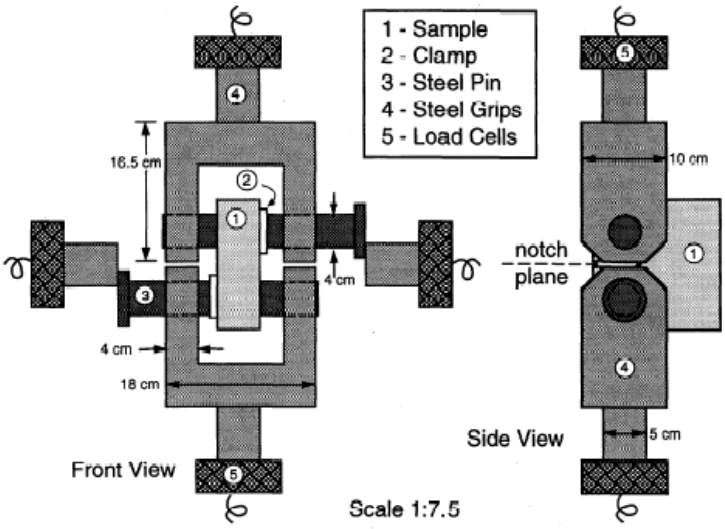

(a)

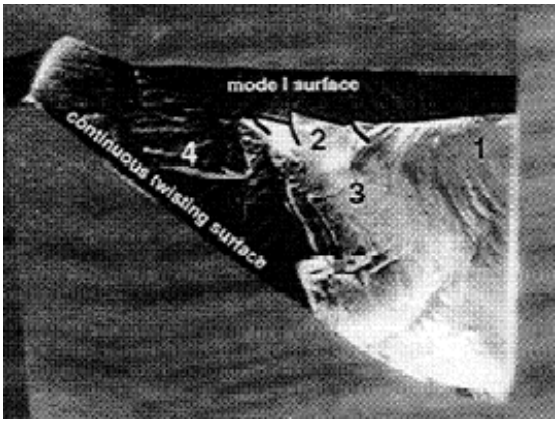

(b)

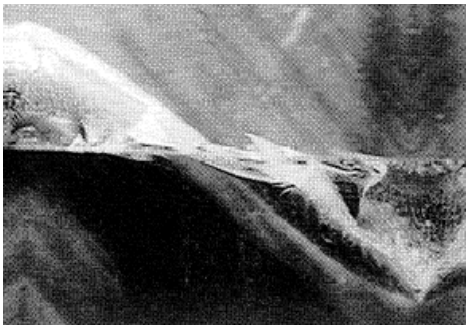

(c)

Figure 3.7. Mixed mode I+III fracture surface in rectangular plexiglass specimen conducted by *Cooke and Pollard* [1996]: (a) testing machine setup, (b) oblique view of fracture surface, and (c) view of en-echelon twisting fractures along crack plane and in the propagation direction. Numbers in (b) refer to the propagation sequence.

Our literature review indicates that although some studies have been conducted on the fracture propagation and segmentation under mixed-mode I+III loading, few publications describe branching and segmentation of hydraulic fractures [e.g., *Delaney and Pollard*, 1981; *Murdoch*, 1993; *Hoek*, 1994]. In the industrial applications of hydraulic fracturing as well as in nature, fracture size is quite often comparable to the typical spatial scale of stress change (e.g., Figure 3.1b). Furthermore, fractures are frequently three-dimensional and non-planar. Hence, in the real world, pure mode I loading is the exception rather than a rule, and mixed-mode loading condition is almost always the actual case. However, one usually ignores the existence of mixed-mode loading when the shear component is small and assumes pure mode I loading. While mode II shear is released during fracture propagation by adjusting fracture direction (e.g., Figure 3.4b), mode III is accumulated during the growth of a non-planar fracture. Yet, in brittle materials, even a small mode III component may cause fracture segmentation because it induces a tensile stress field near the fracture front, and many brittle materials (e.g., rock, concrete, and ceramic) have relatively low resistance to tensile fracture. This is why the goal of this work is to study systematically the effect of mode III loading on the fracture behavior when the component of mode III loading is small, that is, K_{III}/K_I = 1-10%. By now, such a low level of mode III loading has been utilized only in two known experiments, that is, by *Sommer* [1969] (K_{III}/K_I = 2.5%) and *Cook and Pollard* [1996] (K_{III}/K_I = 3%).

Below, we first describe the laboratory experiments on the mixed mode hydraulic fracture propagation with a small K_{III}/K_I ratio in transparent PMMA samples. Then, we discuss a simple theoretical model describing the segmented mixed mode I+III hydraulic

fractures observed in our experiments. We attempt to study not only the onset of fracture segmentation, but also the effect of segmentation on the subsequent fracture growth.

3.2 Laboratory Set-up

We used transparent, cylindrical PMMA samples with circular internal cracks. A schematic drawing of the experimental setup is shown in Figure 3.8. A hole with a diameter of 0.36 cm is drilled along the central axis of the cylinder. Metal tubing is used as the drill hole casing. An initial fracture perpendicular to the borehole axis is created by employing the preheating technique developed by *Wu et al.* [2006] and described in Chapter 2 of this dissertation. The fracturing fluid is an oil-based liquid dye with a dynamic viscosity of 50×10^{-3} Pa·s and is colored in dark green to highlight details of the hydraulic fracture. In order to apply mode III loading to the initial fracture, a constant torque is applied to the specimen while fluid is injected into the hole to induce the hydraulic fracture (Appendix D). The K_{III}/K_I ratio along the fracture front is uniform.

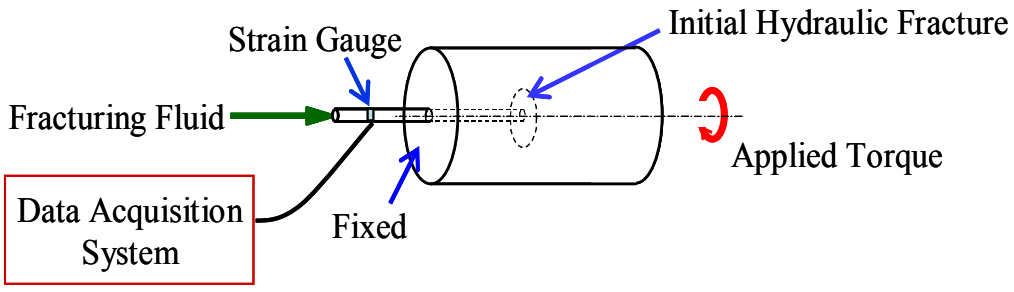

Figure 3.8. Experimental set-up for mode I+III fracture initiation and propagation.

More than 50 samples with three different diameters (5.08 cm, 7.62 cm, and 10.16 cm) have been prepared in order to develop the experimental set-up, determine the typical

magnitudes of loading, calibrate the mini pump parameters, and observe the fracture propagation and segmentation. Altogether, 19 specimens have been tested under mixed-mode I+III loading. Here, we report the result of 10 tests during which it was possible to record the fracture propagation process. All ten samples had a diameter of 10.16 cm. The designation of the specimens and the description of the parent (initial) fractures induced with the pre-heating method [*Wu et al.*, 2006; see also Chapter 2] are summarized in Table 3.1.

Table 3.1. Summary of the initial fractures and experimental parameters

Sample	Diameter of initial fracture $2a$ (cm)	Applied torque (N·m)	Injection rate (10^{-3} ml/min)	Testing time (minutes)
4-2	2.6	600	3.7	46
4-3	2.8	600	4.1	120
4-4	2.4	400	3.3	105
4-5	2.4	525	3.0	96
4-7	2.3	400	4.0	115
4-10	4.2	300	3.0	200
4-11	3.5	400	6.0	180
4-12	3.0	350	6.1	48
4-13	3.4	500	6.1	166
4-14	3.5	300	6.1	144

Ideally, the initial fracture should be a planar, circular fracture that is centered in the specimen and perpendicular to the axis of the sample. However, we found that while all of the initial fractures were planar, perpendicular to the axis of the cylinder, and relatively circular, in three samples (i.e., 4-3, 4-7 and 4-12), they were planar and circular,

but not centered in the specimen because the technique of *Wu et al.* [2006] (Chapter 2) was employed only partially. Such eccentrically placed initial fractures cause the mixed I+III loading to become asymmetrical along the fracture fronts, which, in turn, may affect the fracture propagation. One example of the initial fracture is given in Figure 3.9.

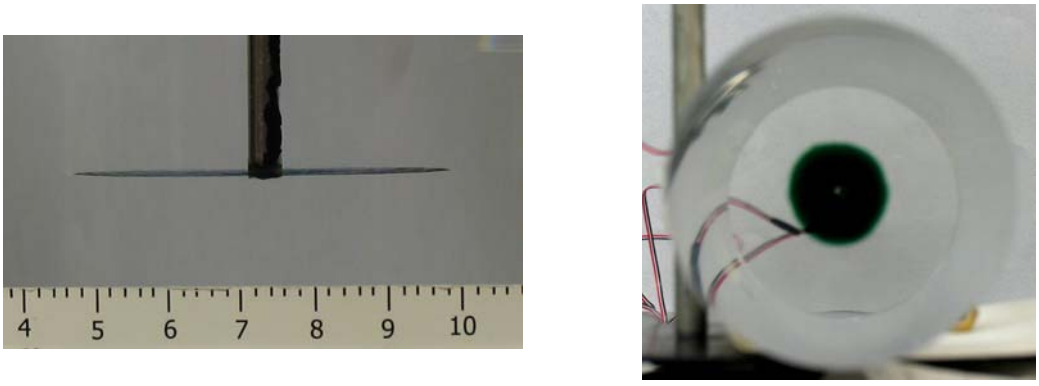

(a) (b)

Figure 3.9. Initial hydraulic fracture in sample 4-10: (a) side and (b) end views.

After the initial fractures were created, the samples were further loaded by simultaneously injecting fluid and applying static torque. To study the effect of *small* mode III component, the torque value was chosen to keep K_{III}/K_I in the range of a few percent (see the next section). The applied torque values, injection rate, and testing time of the samples are summarized in Table 3.1.

3.3 Experimental Results

3.3.1 Mode I+III Fracture Geometry at Low K_{III}/K_I

In some samples (i.e., 4-2, 4-5, 4-7, 4-12, and 4-14), the fracture appeared to initially propagate in its own plane, whereas in other samples (i.e., 4-3, 4-4, 4-10, 4-11,

and 4-13), the segmentation appeared immediately when the fracture started growing. Since there is no systematic dependence of this effect on the K_{III}/K_I ratio, we attribute it to small initial irregularities of fracture shape and/or loading conditions. In any event, fracture segmentation eventually occurred in all samples. According to our observations, segmentation always starts at a point on the fracture front while the final segmented fracture usually has a rather complex geometry (e.g., Figure 3.10). As a rule, the segments feature an elongated shape and comparable dimensions. In general, these fracture segments spread along the perimeter of the parent fracture front, like "flower petals" (Figure 3.10b). These segments do not form simultaneously; instead, they form one by one with localized fluid injection at the points where they are connected to the parent fracture. In addition, when the fluid injection is continued into the sample, some segment fronts further split into several small segments (Figure 3.10). In such cases, we call the large segments "first-order segments" and the small segments "second-order segments." A schematic illustration of the segmented fracture geometry is shown in Figure 3.11.

After the first-order segments surround the entire perimeter of the initial crack, further fracture growth features two patterns, which are shown in Figure 3.10 and Figure 3.12, and called type *A* and *B*, respectively. Propagation of the type *A* fracture occurs by starting new first-order segments from already existing (e.g., segment 6 in Figure 3.10b) although at this stage it becomes asymmetrical (Figure 3.13). In our experimental setup, this happens, most likely, due to the relatively small sample diameter. Because of this, by the moment the second "echelon" of first-order segments initiates, the fracture is already rather large (Figures 3.11 and 3.13), and its interaction with the sample boundaries makes

the quasi-symmetrical shape (e.g., fracture in Figure 3.10 just before segment 6 propagates) unstable.

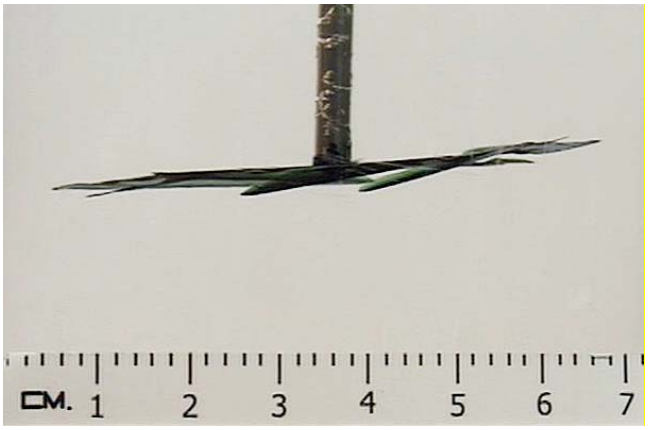

(a)

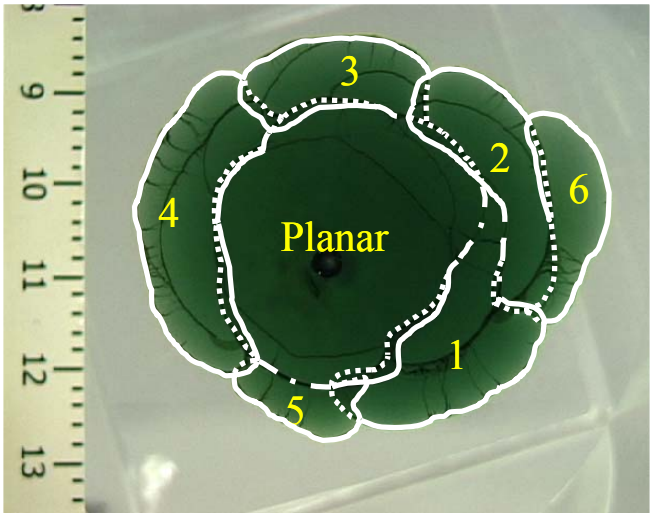

(b)

Figure 3.10. Segmented fracture of type *A* in sample 4-2: (a) side view (perpendicular to the axis of the sample), and (b) end view (along the axis of the sample). The numbers in (b) show the sequence of segments appearance.

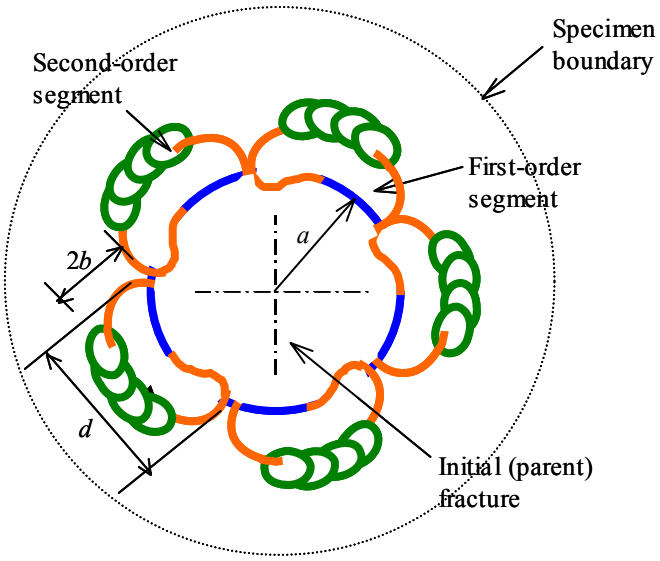

(a)

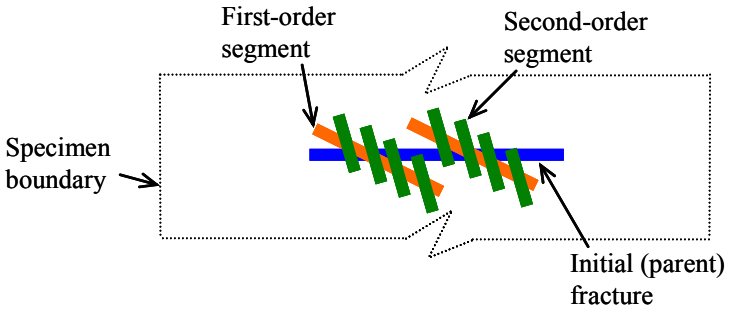

(b)

Figure 3.11. Schematic drawing of the segmented fracture geometry: (a) end and (b) side views.

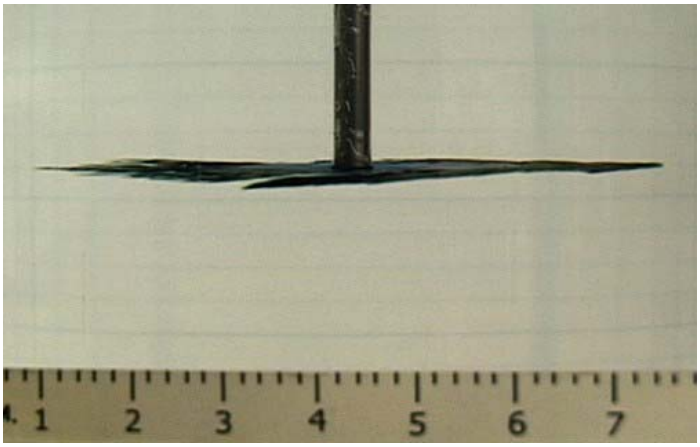

(a)

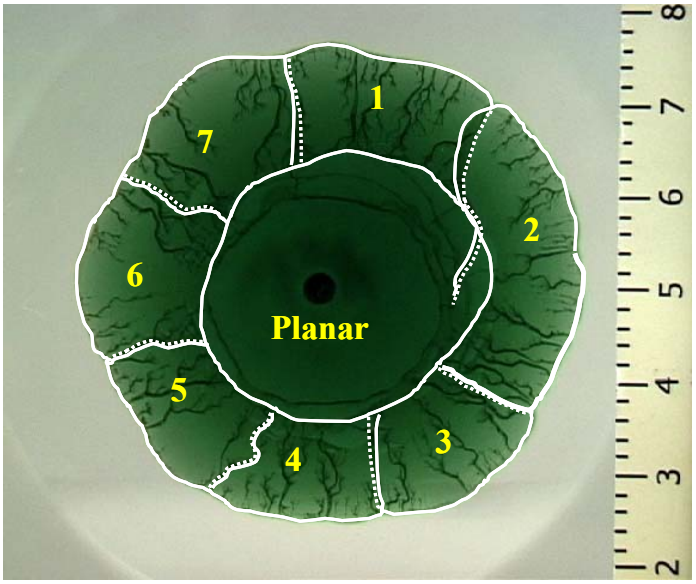

(b)

Figure 3.12. Segmented fracture of type *B* in sample 4-5: (a) side and (b) end views.

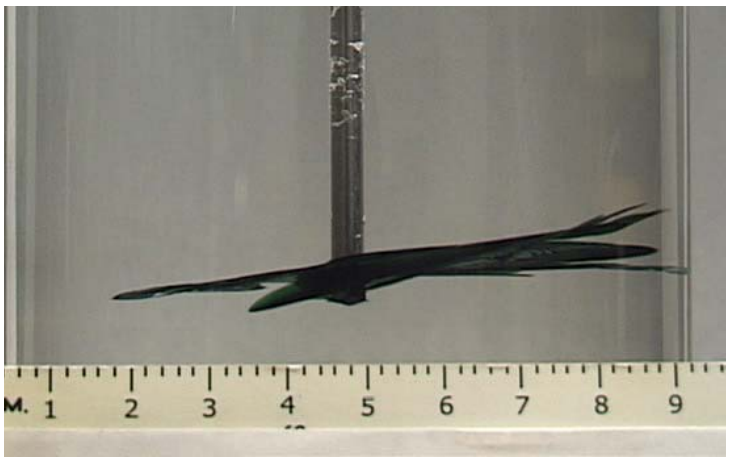

(a)

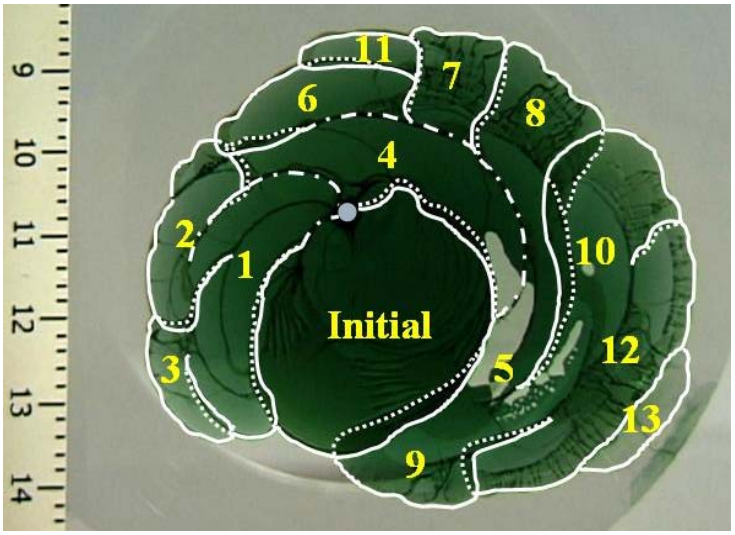

(b)

Figure 3.13. Segmented fracture of type *A* in sample 4-7: (a) side and (b) end views.

The pattern of propagation of type *B* fractures is somewhat different. Similar to type *A* fractures, the first-order segments split into many second-order segments. However, after the first-order segments cover the entire perimeter of the front of the initial fracture, as the fluid is further injected into the sample, instead of the appearance of new fracture segments, all the existing closely spaced small second-order segments grow simultaneously (Figure 3.13). As a result, the overall circular shape of the fractures persists.

To quantitatively describe the fracture geometry, the observed twist angles of the segments and the segment sizes are summarized in Table 3.2, Here, the twist angle, α, refers to the angle between the initial fracture plane and the segment plane (Figure 3.14b). The twist angles range from 4° to 18° (Table 3.2). To the first order, the segment shape can be approximated by an elongated oval that has two main dimensions (Figure 3.11): 2*b*, along the propagation direction (small size) and *d*, parallel to the fracture front (large size). The ratio of 2*b*/*a*, where *a* is the radius of initial fracture, is also given in Table 3.2.

The mode I and mode III stress intensity factors, K_I and K_{III}, of the initial fracture can be estimated by the expression for a circular fracture with the radius, *a* [*Tada et al.*, 1985]:

$$K_I = \frac{2}{\pi} p\sqrt{\pi a}, \quad K_{III} = \frac{4}{3\pi}\tau\sqrt{\pi a} \tag{3.1}$$

where *p* is the injection pressure (assumed to be uniform) and τ is the shear stress applied to the fracture plane. Since in our experiments $a < R/2$, considering a fracture in the infinite space instead of in the long cylinder of radius *R* does not introduce significant

error (based on the expressions from *Tada et. al.* [1985], no more than 7%).

Table 3.2. Summary on the observed segmented fractures

Sample	Twist angle	Segment dimensions			Number of segments	K_{III}/K_I (%)
		$2b$ (cm)	d (cm)	$2b/a$		
Type *A* fractures						
4-2	11°-14°	0.4-0.8	0.8-3.4	0.31-0.62	6	2.2
4-3	13°-16°	0.3-0.8	0.9-2.7	0.21-0.57	7	5*
4-4	10°-17°	0.4-0.9	1.6-2.8	0.33-0.75	5	4.0
4-7	5°-17°	0.2-0.6	0.7-2.4	0.17-0.52	13	2.8
4-10	7°-9°	0.9-1.7	0.7-2.2	0.43-0.81	6	5.6
4-12	5°-10°	0.3-0.8	2.5-3.5	0.20-0.53	2	3.1
4-13	8°-18°	0.8-1.3	3.6-5.0	0.47-0.76	3	6.4
Type *B* fractures						
4-5	3°-5°	0.5-0.7	0.8-3.2	0.42-0.58	7	3.5
4-11	5°-7°	0.4-0.6	0.3-2.2	0.22-0.34	6	5.4
4-14	4°-6°	1.4-2.4	4.4-6.2	0.80-1.37	4	5.3

* Pressure curve is not available due to strain gauge failure. However, based on the twist angle and other parameters, we estimeated it as 5%.

Note that expressions (3.1) are only applicable before the segments appear. After the segments form, the stress field around the fracture is no longer in simple mode I or mode III condition, and thus, the calculations for the stress intensity factors become much more complicated. Table 3.2 also lists the calculated K_{III}/K_I ratios of stress intensity factors for all the samples, which vary from 2.2 to 6.4%.

3.3.2 Types of Intersection

Figure 3.14 shows a schematic drawing of the geometry of the intersection between the parent fracture and the segments based on our experimental observations. Since the segments are inclined with respect to the parent crack, only a small opening connects each segment to the parent crack.

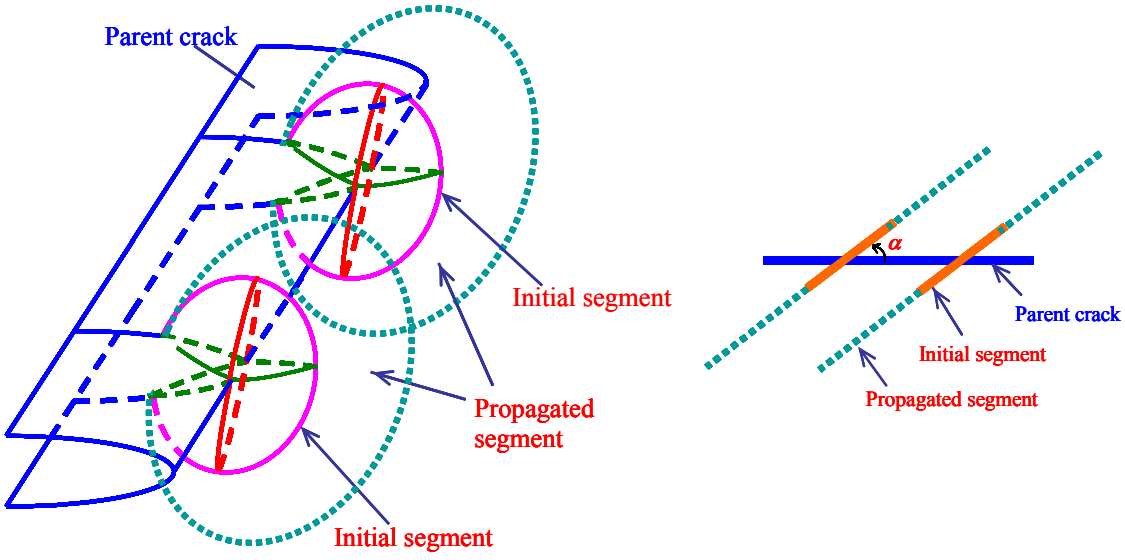

Figure 3.14. Schematic of the geometry of the intersection between the parent fracture and the segments: (a) perspective and (b) front views.

In our experiments, we also occasionally observed (i.e., in sample 4-10) that the segment fronts curved along the growth direction and propagated towards the plane of the parent fracture (Figure 3.15). Some segments finally contacted with the parent fracture. Thus, the connections between the parent fracture and the segments were no longer small. Since the topology of this type of fracture segmentation is the exception in our experiments, in the following discussion, we mainly focus on more typical geometry

shown in Figure 3.14.

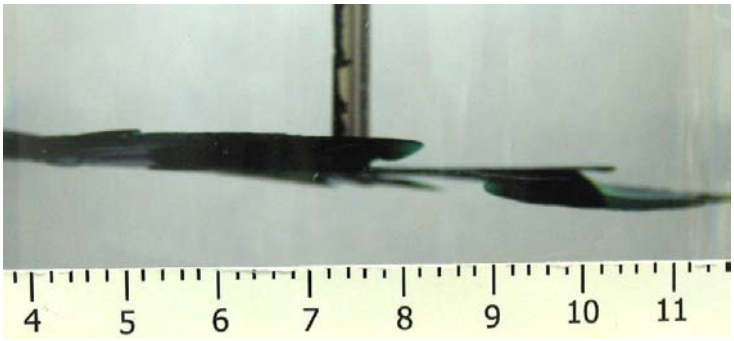

(a)

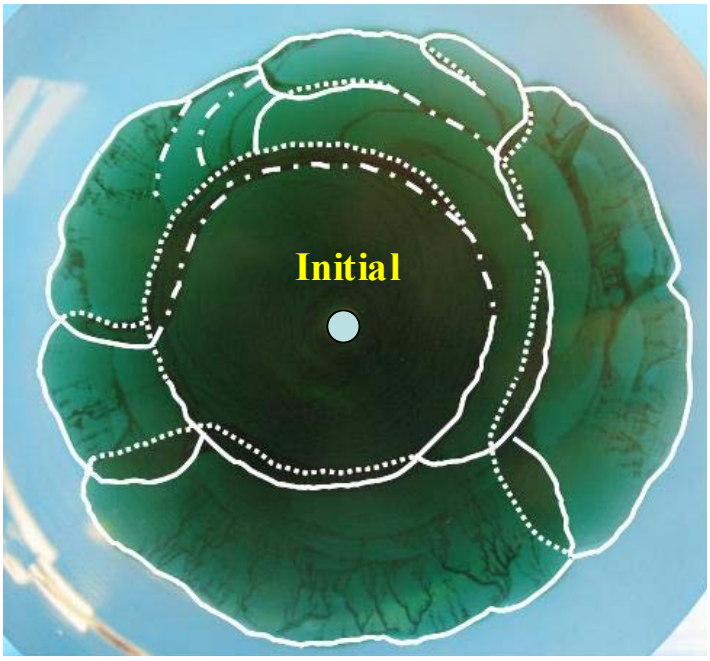

(b)

Figure 3.15. Segmented fracture of type *A* in sample 4-10: (a) side and (b) end views. The segments propagated toward the parent fracture plane and contacted with it.

3.3.3 Twist Angle

An important issue when describing fracture branching and segmentation is the

change in crack growth direction under the mixed-mode loading. Various criteria [e.g., reviewed by *Cooke and Pollard*, 1996; *Qian and Fatemi*, 1996] have been proposed to predict the twist angle. Among them, the maximum principle stress criterion, which assumes that fracture under mixed-mode I+III loading will grow within a plane which is perpendicular to the local maximum tensile stress [*Pollard et al.*, 1982], is the most often used. In this case, the relationship between the twist angle, ϕ, and the SIF ratio, K_{III}/K_I, is given by [e.g., *Pollard et al.*, 1982]

$$\phi = \frac{1}{2}\operatorname{atan}\left[\frac{2K_{III}}{K_I(1-2\nu)}\right] \qquad (K_I \geq 0) \qquad (3.2)$$

Our test results show that the twist angle is rather small (4° to 18°) when K_{III}/K_I is low (Figure 3.16). We do not intend to look in details for the relationship between the twist angle and the K_{III}/K_I ratio since the K_{III}/K_I values used in our tests concentrated in a small range (from 2.2% to 6.4%), and the accuracy of the angle measurements is not sufficient for this purpose. Yet, we computed the maximum principle stress criterion (3.2) and plotted the twist angles in Figure 3.16 (dashed line). We used Poisson's ratio, ν, as a fitting parameter and obtained the best fit for ν = 0.38. Given the low accuracy of the angle measurements at low values of K_{III}/K_I, the agreement with the experimental results appears to be reasonable.

However, generally speaking, "there is no single criterion which gives satisfactory predictions under all loading conditions" [*Qian and Fatemi*, 1996]. For example, *Cooke and Pollard* [1996] found that the observed twist angles in their tests were significantly lower (one-third to one-half) than the theoretical prediction based on the maximum

principal stress criterion. Similar discrepancy was also observed in the experiments of *Yates and Miller* [1989]. One possible reason for this discrepancy is that the mechanical interaction between adjacent segments may have significant effects on the behavior of mixed mode fractures [*Cooke and Pollard,* 1996].

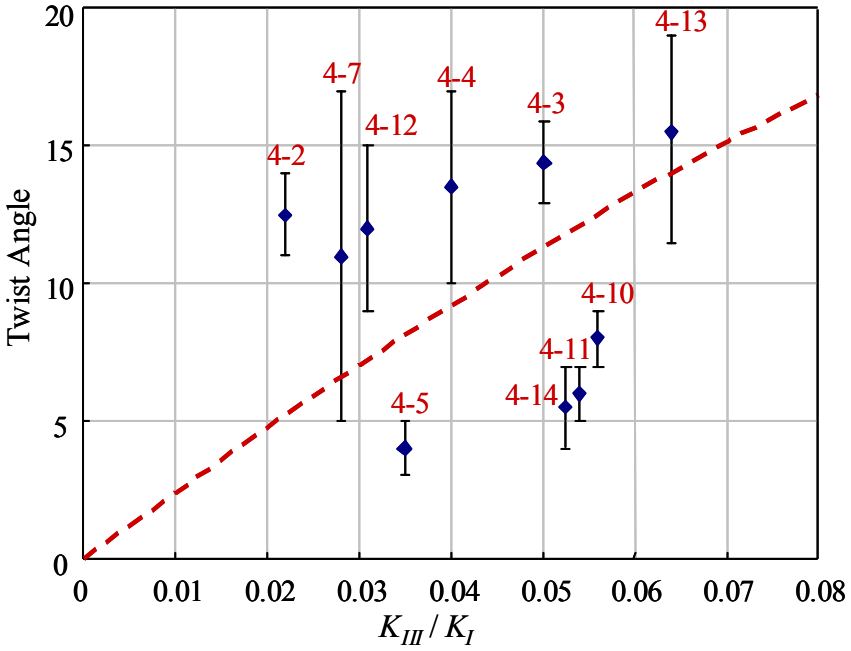

Figure 3.16. The observed relationship between the twist angle and the ratio of K_{III}/K_I. Sample numbers are shown above the bars that indicate the range of twist angles observed for each sample. ν = 0.38.

3.4 Mode III Component of Non-Planar Fractures

As mentioned before, in real non-planar three-dimentional fractures, mode III component accumulates as fractures propagate. To better understand the experimental observations in the fracture process and how low or high the ratio K_{III}/K_I may become, we used a 3D boundary element code, FRANC3D [e.g., *Gerstle and Ingraffea*, 1986; *Carter et al.*, 2000] and conducted a numerical simulation that resembles our laboratory

experiments (section 3.3). In FRANC3D, the fracture propagation criterion is $K_I = K_{Ic}$, and the code calculates the stress intensity factors using a displacement correlation technique. The schematic of the simulated problem and the model mesh are shown in Figure 3.17. Because FRANC3D does not allow applying internal tractions to the fracture sides, internal pressure in the fracture is replaced by the corresponding remote tensile stress. In linear elastic fracture mechanics, this does not affect propagation and opening of planar fractures, while the geometry of curved fractures generally will be different. Yet this numerical experiment is quite informative to quantify the K_{III}/K_I ratio of non-planar propagating fractures. The model geometry, material properties, and boundary conditions are summarized in Table 3.3. In this simulation, we were interested in the increment (accumulation), ΔK_{III}, of the mode III SIF. The fact that the initial K_{III}/K_I was not small is not too important.

The applied stress field (Table 3.3) was kept constant during the fracture propagation process. We used the maximum tangential stress criterion [*Erdogan and Sih*, 1963] to determine the fracture propagation direction. The maximum crack increment in each step was 0.04 m (two elements). After the numerical simulation was carried out for seven steps, a negative value of K_I was reported at the crack front, and the numerical simulation stopped. The final radius of the crack was 0.32 m, more than three times the size of the initial fracture.

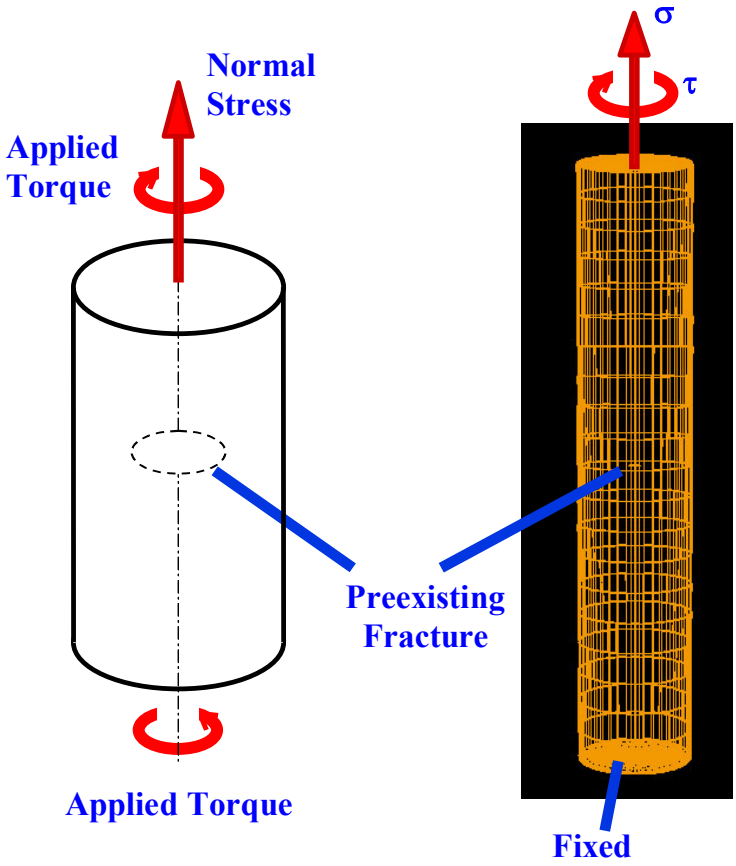

Figure 3.17. FRANC3D model of the mixed mode I+III fracture. The propagated fracture is shown in Figure 3.18.

Table 3.3. Data for numerical simulation with FRANC3D

Geometric parameters	Cylinder length	L = 10.0 m
	Cylinder radius	R = 1.0 m
	Radius of initial crack	a = 0.1 m
	Position of initial crack	z = 5.0 m
Material properties	Poisson's ratio	ν = 0.38
	Young's modulus	E = 780 MPa
	Fracture toughness	K_{Ic} = 1 MPa·m$^{1/2}$
Boundary conditions	Bottom surface	Fixed: $u_x = u_y = u_z = 0$
	Top surface	Tensile stress: σ = 3.4 MPa Shear stress: τ = 5.6 MPa
	Lateral surface	Free surface

Figure 3.18 shows the top and lateral views of the crack shape after seven steps of propagation. This figure shows that under mixed-mode I+III loading, the initial circular planar crack propagates into a non-planar shape. Due to the mode III effect, the crack front curves along the tangential direction and forms a wavy shape. In pure mode I regime, the fracture would grow in its own plane, slightly fluctuating around the front due to such factors as numerical heterogeneity of the stress field and finite size of numerical discretization. In other words, the shape of the mode I fracture is stable with respect to small out-of-plane deviations. In contrast, deviations of the mode I+III fracture from the initial plane are systematic (i.e., occur at the angle of the same sign due to the presence of mode III) and develop with the fracture propagation resulting in a wave-like fracture front (Figure 3.18).

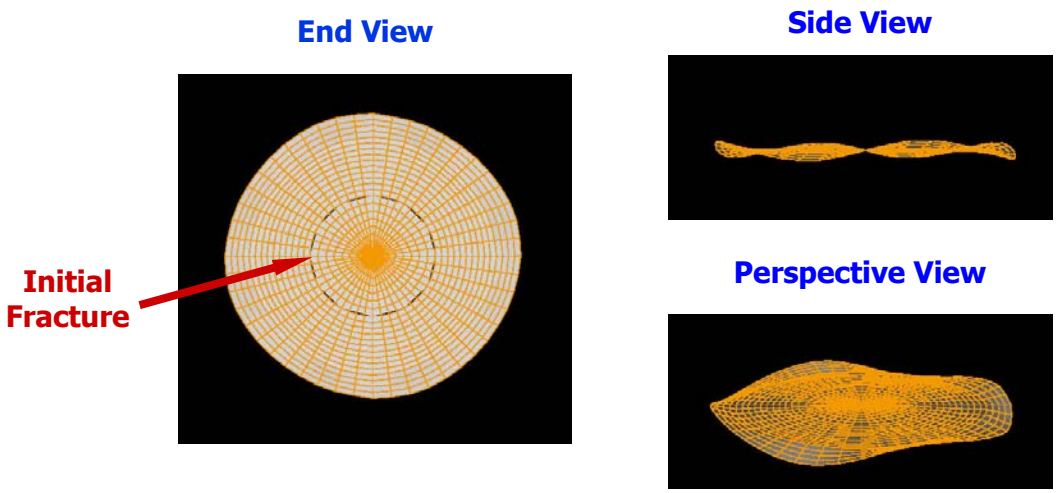

Figure 3.18. Results of the numerical simulation with FRANC3D model.

From the conventional standpoint, the fracture is supposed to propagate in such a direction that it relieves K_{II} (e.g., Figure 3.3b). Since numerically FRANC3D utilizes the finite size of the propagation increment, the propagation criterion does not relieve K_{II} completely. In particular, at the final state, K_{II} varies along the fracture front from $-1.2K_{Ic}$ to $1.2K_{Ic}$ depending upon the position on the fracture front. It should be noticed, though, that the range of K_{II} can be decreased by reducing the element size. At the same time, K_{III} changes along the front from $3.6K_{Ic}$ to $5.6K_{Ic}$. Given that the initial value of K_{III} was $1.0K_{Ic}$, we see that during the fracture growth K_{III} increased by ΔK_{III} that varies along the fracture front from 2.6 K_{Ic} to $4.6K_{Ic}$.

This result indicates that K_{II} accumulates considerably slower (if at all, since its average value on the front is still zero) than K_{III}, which has no other mechanism of relaxation, but fracture front segmentation (e.g., Figure 3.4c). With fracture propagation, K_{III} grows, and so does the maximum principal stress, which acts on the elementary area inclined to the fracture front. Eventually, this stress breaks the quasi-brittle host material

resulting in fracture segmentation and relieving mode III (Figure 3.4c).

Therefore, although the numerical simulation does show the non-planar fracture geometry at the fracture front under mixed-mode I+III loading, such important fracture features as branching and segmentation could not be captured by our numerical analysis due to the geometrical complexity of fracture intersection in 3-D (Figure 3.14). While in principle, it is possible to create the corresponding mesh [e.g., *Germanovich et al.*, 1996], currently the computations are rather inaccurate since the new geometry (Figure 3.14) invokes new singularities that have not been studied with respect to numerical calculations. Accordingly, the fracture segmentation capability has not yet been implemented in FRACN3D. To the best of our knowledge, no other fracture propagation code has this capability, so accurate numerical simulation of mode I+III segmentation still remains to be done. This is why in the next section we discuss a simple theoretical model that illustrates some fracture features observed in the laboratory tests reported in this work.

Note that the deviation of the fracture shape from planar in Figure 3.18 is rather insignificant (which can be observed from the fracture side view in Figure 3.18). While this observation is somewhat subjective, it is still worth commenting that the shown shape causes $\Delta K_{III}/K_I \sim 1$. Thus, since in the case of real three dimentional propagating fractures some deviation of shape from planar is almost always expected, it is also expected that the corresponding K_{III}/K_I will be at least in the order of a few percent (probably greater). At the same time, the obtained results indicate that such a small K_{III}/K_I ratio is sufficient for fracture segmentation even in materials as homogeneous and

fracture resistant as PMMA. Therefore, we conclude that front segmentation is likely to accompany the growth of most, if not all, real fractures, at least, in quasi-brittle materials.

3.5 Theoretical Model

3.5.1 Effect of Interaction in Segmented Fracture

In this analysis, we only consider the final stage of fracture segmentation. Based on the experimental observations, in the vertical cross section, the parent fracture and first-order segments can be viewed as closely spaced, parallel, overlapping fractures (e.g., Figure 3.11). For simplicity, we first consider a 2-D model. After we discuss the underlying principles of segment interaction, we apply them to the 3-D fracture geometry observed in our experiments.

Figures 3.23a and 3.23b show a schematic diagram of three closely spaced overlapping fractures. The lengths of the central (parent) fracture and the side fractures (segments) are $2a$ and $2b$, respectively. The overlap length is $2c$ and the spacing between the fractures is s. Following *Sim* [2004], we consider this set of overlapping fractures as an "effective" or "equivalent" single fracture (Figure 3.19c). *Sim* [2004] showed that if the spacing, s, is much smaller than the overlap, $2c$, the resistance of the thin ligament "connecting" the fractures at the overlap can be evaluated asymptotically by modeling it as a beam (plate) and by computing the beam deflection (Figure 3.20). As a result, the stress intensity factor at the tips of the segments can be estimated by considering a single fracture of the same total length, $2a + 4b - 4c$, loaded by four concentrated forces, F_n, simulating the resistance from the ligament in addition to the internal fluid pressure, p

(Figure 3.21).

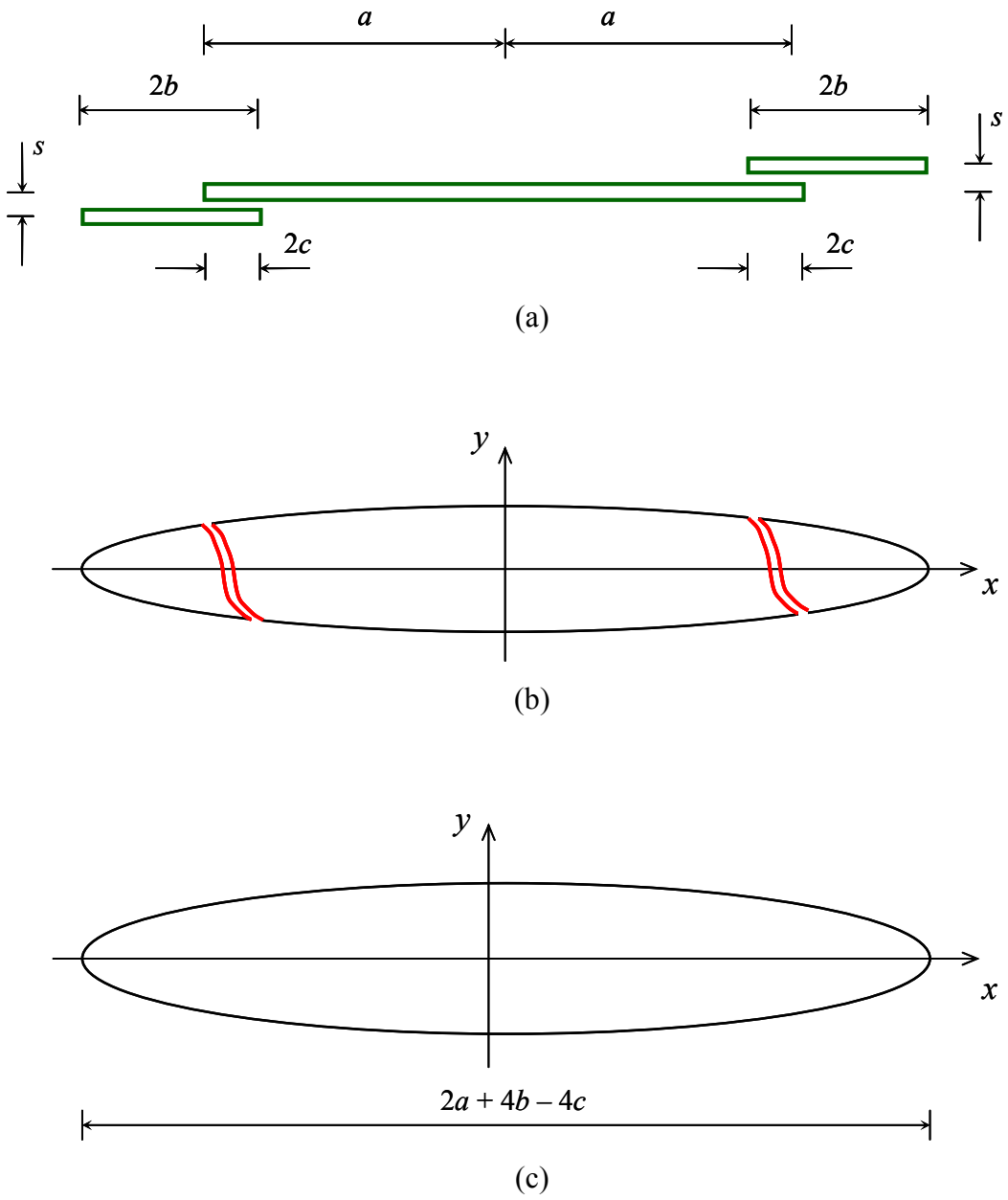

Figure 3.19. A 2-D model of segmented fracture: (a) geometric configuration of three closely spaced overlapping fractures, (b) opening of the overlapping fractures, and (c) opening of the single (effective) fracture of the same total length (the sketch is not scaled).

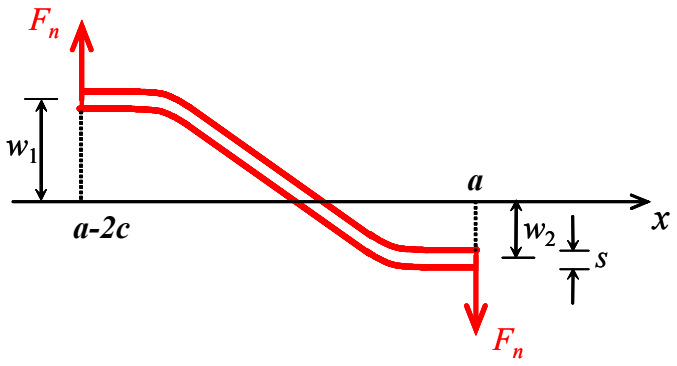

Figure 3.20. Beam model of the ligament between the overlapping fractures in Figures 3.21a and 3.21b.

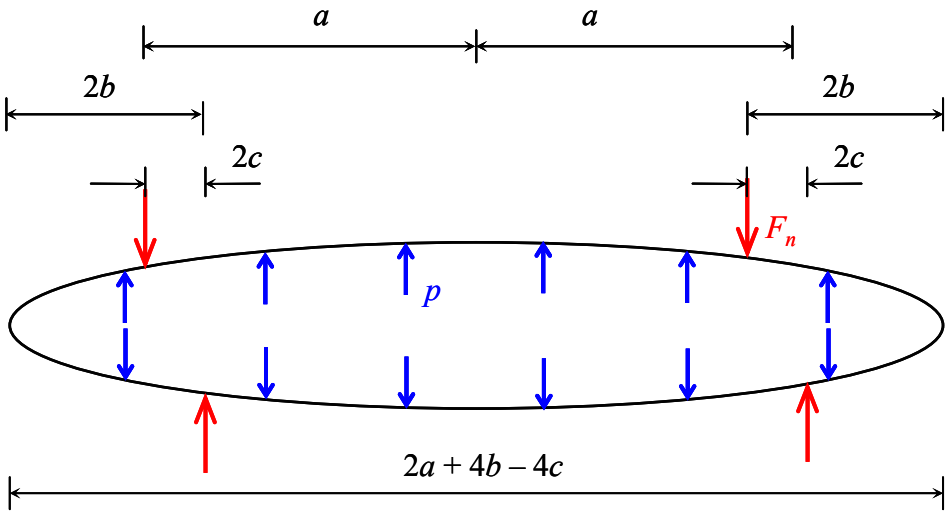

Figure 3.21. Equivalent fracture loaded by resistance forces, F_n, generated at the ligament ends (Figures 3.21b and 3.22) and by internal pressure, p.

Ignoring the longitudinal load along the beam (Figure 3.20) that results from the horizontal displacements of the fracture sides, the resistance force generated at the end of the beam is given by

$$F_n = 3E'I\frac{w_1 + w_2}{c^3} \tag{3.3}$$

where w_1 and w_2 are the deflections at the ends of the beam, and in plane strain, $I = s^3/12$, $E' = E/(1- \nu^2)$. Since the ligament (beam) is thin, in the first-order approximation, we ignore the effect of the ligament on the crack opening shape. Then, w_1 and w_2 are equal to the aperture of a single fracture with the length of $2a + 4b - 4c$ at the positions $x = a - 2c$ and $x = a$, respectively (Figures 3.24 and 3.25).

In the global coordinate system with the origin at the center of the effective crack (Figure 3.19c), the crack side displacements are

$$v^{\pm}(x) = \pm\frac{2(1-\nu^2)}{E}(a+2b-2c)p\sqrt{1-\frac{x^2}{(a+2b-2c)^2}}, \quad |x| \le a+2b-2c \tag{3.4}$$

where "+" and "–" denote the displacements of the upper and lower sides of the fracture, respectively. Accordingly,

$$w_1 = v^{+}(a-2c), \quad w_2 = -v^{-}(a) \tag{3.5}$$

The stress intensity factor, K_I, of the effective fracture (Figure 3.21) is the summation of two problems: (*A*) fracture loaded by the internal pressure, p, and (*B*) fracture loaded by four concentrated forces, F_n. The solutions to these two problems are

readily available [e.g., *Tada et al.*, 1985]:

$$K_I^A = p\sqrt{\pi(a+2b-2c)} \tag{3.6}$$

$$K_I^B = \frac{-F_n}{2\sqrt{\pi(a+2b-2c)}}\left[\sqrt{\frac{(a+b-2c)^2+b^2}{b(a+b-2c)}}+\sqrt{\frac{(a+b-c)^2+(b-c)^2}{(b-c)(a+b-c)}}\right] \tag{3.7}$$

Substituting (3.3) – (3.5) into (3.7) and adding the result to (3.6), we obtain the stress intensity factor in the problem under consideration (Figure 3.21):

$$\begin{aligned} K_I = K_I^A\Bigg\{1-\frac{s^3}{8\pi c^3}\left[\sqrt{1-\frac{(a-2c)^2}{(a+2b-2c)^2}}+\sqrt{1-\frac{a^2}{(a+2b-2c)^2}}\right] \\ \times\left[\sqrt{\frac{(a+b-2c)^2+b^2}{b(a+b-2c)}}+\sqrt{\frac{(a+b-c)^2+(b-c)^2}{(b-c)(a+b-c)}}\right]\Bigg\} \end{aligned} \tag{3.8}$$

Considering that in our case the overlap is small and the ligament is thin (e.g., Figure 3.11c), that is,

$$c << a, \quad c << b, \quad s << c \tag{3.9}$$

to the first order, we can keep in (3.8) only the leading term. Then,

$$K_I = K_I^A f\left(\frac{s}{2c},\ \frac{b}{a}\right) \tag{3.10}$$

where

$$f\left(\frac{s}{2c},\ \frac{b}{a}\right) = \left[1-\frac{4}{\pi}\left(\frac{s}{2c}\right)^3\sqrt{1-\frac{1}{(1+2b/a)^2}}\sqrt{\frac{(1+b/a)^2+(b/a)^2}{b/a\ (1+b/a)}}\right] \tag{3.11}$$

takes into account the effect of ligaments closing the fracture.

We adopt the simplest fracture growth criterion [e.g., *Broberg*, 1999]

$$K_I = K_{Ic} \tag{3.12}$$

where K_{Ic} is the material fracture toughness. Inserting (3.10) into (3.12), we obtain the equation for b:

$$f\left(\frac{s}{2c},\ \frac{b}{a}\right)K_I^A = K_{Ic} \tag{3.13}$$

Since both square roots in (3.11) are positive, function $f < 1$. On the other hand, $f > 0$ because $s/(2c) << 1$. Since $s/(2c) << 1$, function $f \approx 1$, which can also be seen from Figure 3.22, where the dependence of function f on b/a is plotted for different values of $s/(2c)$. This figure shows that as the fracture propagates, f increases with b, but this increase is insignificant and f remains practically constant and equal to 1.

Therefore, the effect of mechanical interaction between the segments and the parent fracture can be accounted for by employing the model of an effective (equivalent) fracture (Figure 3.19c), loaded by the same pressure, while the closing effect of the thin ligaments can be ignored. Their hydraulic effect, however, may still be very important in the case of hydraulic fracturing because they affect the fluid flow inside the fracture [*Wu et al.*, 2006]. In the 2-D model, they may represent a restriciton to the fluid flow, so that the segments can be considered underpressured compared to the parent fracture. Nevertheless, in the next section, we consider the simplest mode of uniformly loaded

fracture but account for the mechanical interaction between the parent fracture and the segments.

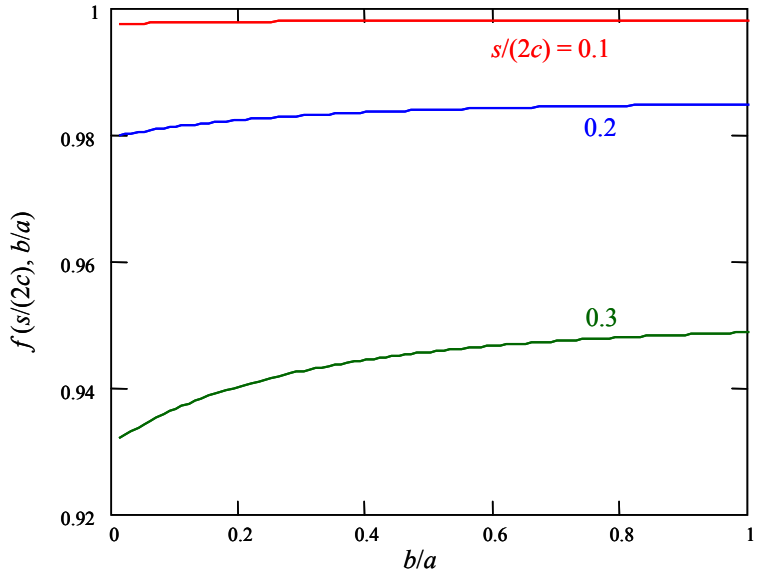

Figure 3.22. Function f in (3.10) versus b/a for $s/(2c) = 0.1$, 0.2 and 0.3.

3.5.2 Circular Segmented Fracture

The mechanical principles considered in the previous section using 2-D model can now be applied to 3-D fractures observed in our experiments. Specifically, given that the spacing between the segments and the parent fracture is still small, their mechanical interaction can be taken into account by considering the pressurized "effective" single circular fracture (Figure 3.23) of the same size. For small injection rates implemented in the discussed laboratory setup (Table 3.1), we can ignore the fluid lag zone near the fracture tip (front) and consider the pressure distribution inside the fracture as uniform.

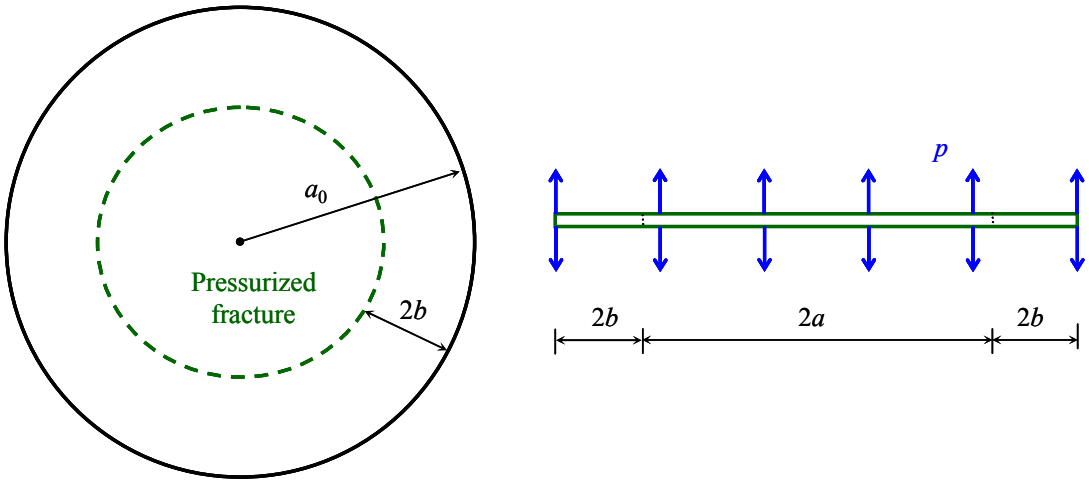

(a) (b)

Figure 3.23. (a) Pressurized "effective" circular fracture, and (b) cross section perpendicular to the fracture plane.

Then, the stress intensity factor, K_I, can be estimated by that for a uniformly pressurized, circular fracture perpendicular to the axis of an infinite elastic cylinder:

$$K_I = \frac{2}{\pi} p\sqrt{\pi a_0} F(a_0/R) \tag{3.14}$$

where p is the pressure inside the fracture, $a_0 = a + 2b$ is the effective fracture radius, R is the radius of the cylinder, and function

$$F(a_0/R) = \frac{1 - 0.5(a_0/R) + 0.148(a_0/R)^3}{\sqrt{1 - a_0/R}} \tag{3.15}$$

is given by *Tada et al.* [1985].

We adopt the same fracture growth criterion (3.12) and substitute (3.14) into $K_I = K_{Ic}$. Then, the fluid pressure in the fracture can be expressed as

$$p(a_0) = \frac{\sqrt{\pi} K_{Ic}}{2\sqrt{R} F(a_0/R)} \sqrt{\frac{R}{a_0}} \tag{3.16}$$

The corresponding volume of the pressurized fracture is

$$V(a_0) = \frac{16(1-\nu^2)}{3E} p a_0^3 G(a_0/R) \tag{3.17}$$

where function $G(a_0/R)$ is also given by *Tada et al.* [1985]. Comparing $G(a_0/R)$ and $F(a_0/R)$, it appears that for $a_0/R < 0.9$ (i.e., for fractures that do not approach the sample boundary), the difference between $G(a_0/R)$ and $F(a_0/R)$ is less than 5%. Therefore, with an accuracy sufficient for our purposes, $G(a_0/R) = F(a_0/R)$. Then, combining expressions (3.16) and (3.17) results in

$$V(a_0) = \frac{8\sqrt{\pi}(1-\nu^2) K_{Ic} a_0^{5/2}}{3E} \tag{3.18}$$

Ignoring the compressibility of the injection fluid, the crack volume can also be written as

$$V(t) = V_i + qt \tag{3.19}$$

where V_i is the volume of initial fracture (just before the segmentation), q is the injection rate, and t is the injection time starting from the mixed mode fracture propagation (segmentation). Then, combining (3.16) through (3.19), we obtain

$$a_0(t) = a\left[1 + \frac{qt}{V_i}\right]^{2/5} \tag{3.20}$$

where V_i is found by substituting $a_0 = a$ into (3.18):

$$V_i = V(a) = \frac{8\sqrt{\pi}(1-\nu^2)K_{Ic}}{3E} a^{5/2} \tag{3.21}$$

The dependence of the injection pressure, p, on time, t, is obtained by substituting (3.20) into (3.16). As can be seen from (3.20), (3.21), and (3.16), $p(t)$ depends upon two material parameters, K_{Ic} and $E' = E/(1- \nu^2)$. We can find the values of these parameters by fitting the theoretical dependence $p(t)$ to the experimental curve by the least square method.

The fitting results for the type *A* fractures in samples 4-10 (Figure 3.15) and 4-7 (Figure 3.12) are shown in Figure 3.24 and Figure 3.25, respectively. Another type *A* (sample 4-13) as well as the corresponding injection pressure curve and the fitting result are shown in Figure 3.26. An example for type *B* fracture (sample 4-11) is given in Figure 3.27. The fitting parameters for these cases are listed in Table 3.4. While these values differ, they are of the same order and agree with those reported in the literature.

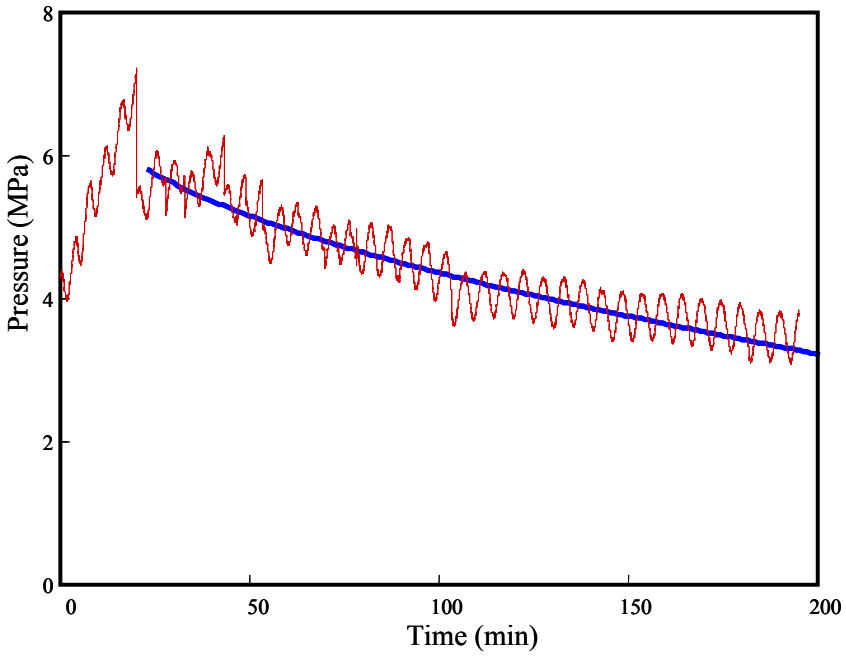

Figure 3.24. Measured and fitting injection pressure curves for sample 4-10.

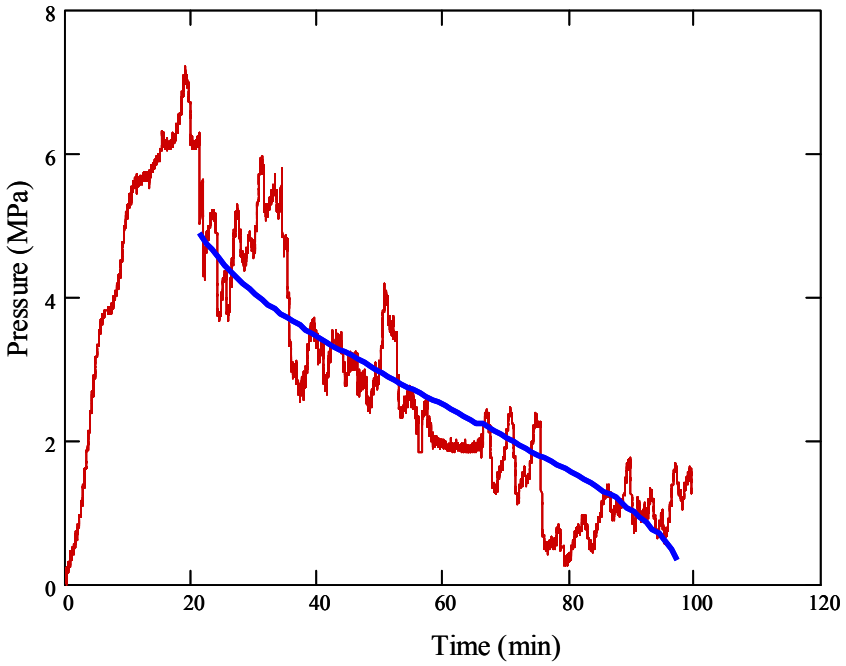

Figure 3.25. Measured and fitting injection pressure curves for sample 4-7.

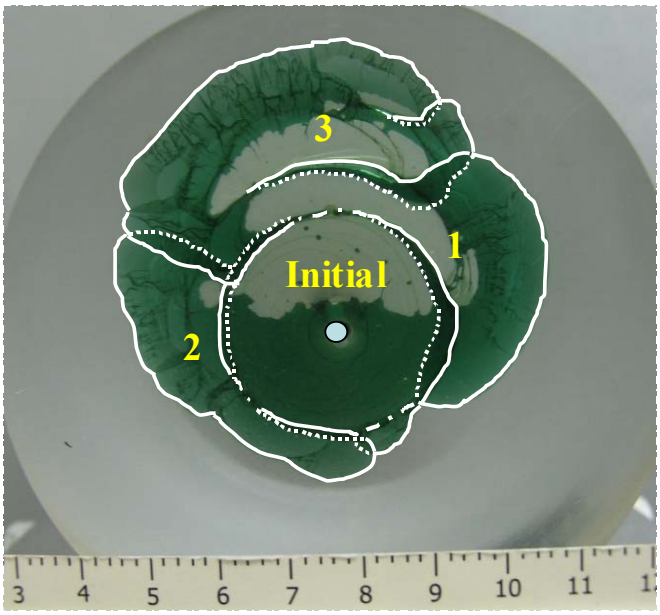

(a)

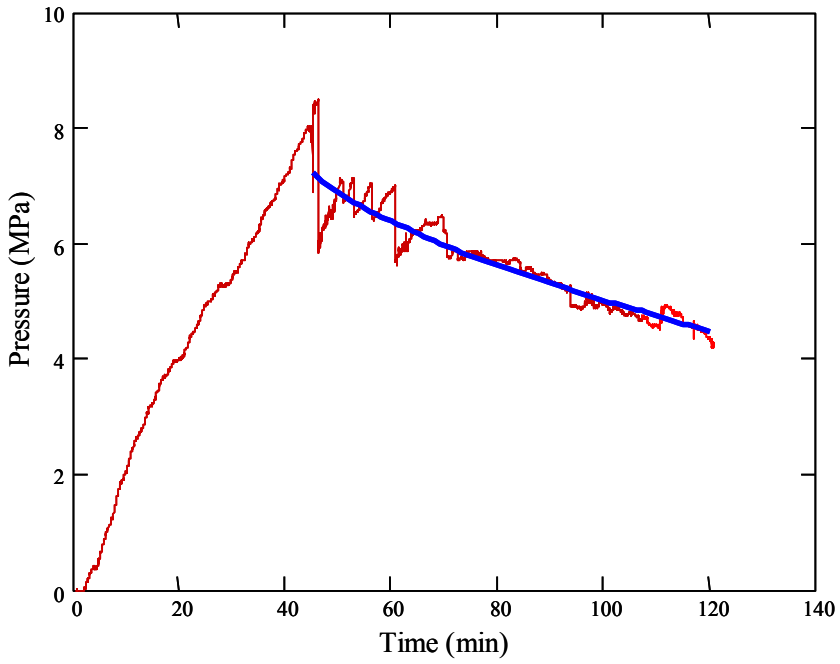

(b)

Figure 3.26. Type *A* fracture in sample 4-13: (a) segmented fracture geometry; (b) measured and fitting injection pressure curves.

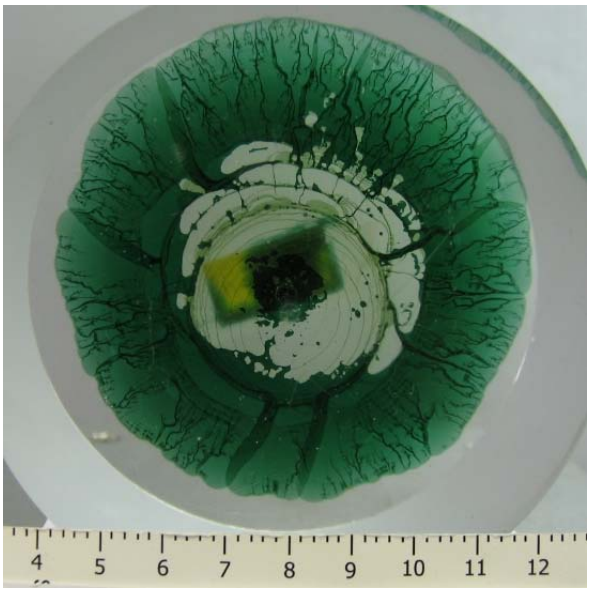

(a)

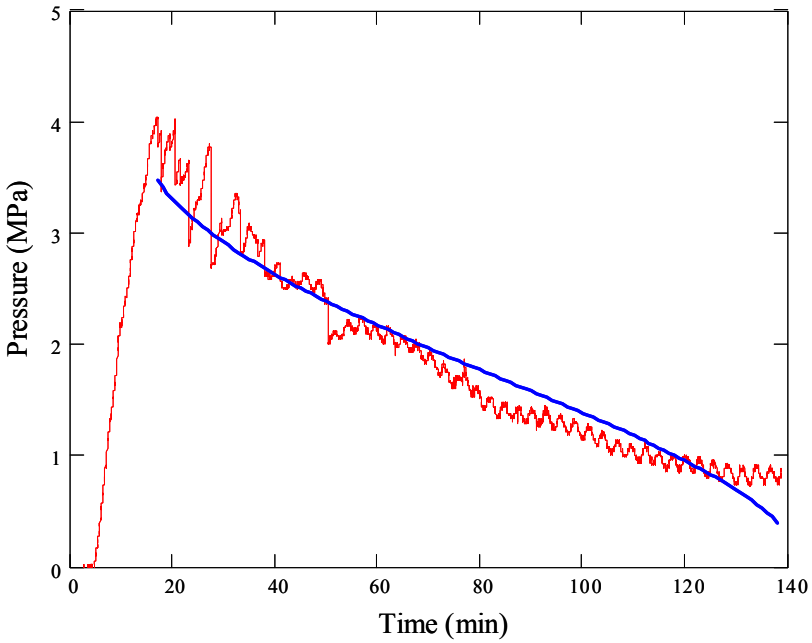

(b)

Figure 3.27. Type *B* fracture in sample 4-11: (a) segmented fracture geometry; (b) measured and fitting injection pressure curves.

Table 3.4. Summary on the fitting parameters

Sample	E' (GPa)	K_{Ic} (MPa·m$^{1/2}$)
Type A fractures		
4-7	8.89	0.84
4-10	2.04	1.02
4-13	4.68	1.24
Type B fractures		
4-11	3.88	0.60
4-14	2.87	1.10

The considered model is simplified, but seems to be rather robust. For example, the fracture in Sample 4-13 (Figure 3.26a) is highly asymmetric. Yet the model shows a good agreement (Figure 3.26b) with experimental results.

After we obtain the value of K_{Ic}, by substituting it and the injection pressure, p_f, at the final stage into (3.16), we can also estimate the radius of the effective fracture, a_0. For example, for sample 4-10, p_f = 3.84 MPa, and expression (3.16) yields a value of a_0 = 3.5 cm. The measured average radius of the final "effective" circular fracture is approximately 3.7 cm. The difference between the theoretical and experimental values is about 5%, which is similar to other experiments. This indicates that when the injection rate is low, the segmented fracture may behave like a simple mode I fracture and it can be simulated by uniformly pressurized effective circular fracture.

3.6 Discussion

In general, during the fracture segmentation process, the injection pressure declined. However, in some experiments, the pressure remained more or less constant or even increased. Examples for type *A* (sample 4-2, Figure 3.10) and *B* (sample 4-5, Figure 3.12) fractures are shown in Figures 3.28a and 3.28b, respectively. The quasi-constant value of the propagation pressure is not consistent with the expectation based on conventional linear elastic fracture mechanics. Indeed, if one choses to ignore the fracture segmentation, then for mode I fracture, $K_I = K_{Ic}$, where, in the case of quasi-circular fracture (Figure 3.12b), K_I is given by (3.1) or (3.15). Accordingly, the increasing radius, a, of the fracture should correspond to a decreasing pressure, p, which is hardly the case in Figure 3.28. One major reason for this discrepancy might be the small connections between the segments and the parent fracture, mentioned in section 3.3.2. These narrow connections significantly restrict the fluid flow, which may raise the entry pressure in the drill hole. In our interpretation, this is why occasionally the injection pressure curve observed in the mixed-mode I+III loading was relatively constant during fracture propagation in some tests.

One of the many industrial applications of hydraulic fracturing is in oil and gas recovery. In the field, decisions during hydraulic fracturing treatment are often made in real time. Since the hydraulic fracture develops at the depth of up to several kilometers beneath the ground, in the majority of practical cases, the response of the injection pressure versus the injection time is the only measurable data that can be used to infer the fracture geometry and, consequently, the effectiveness of hydraulic fracturing treatment.

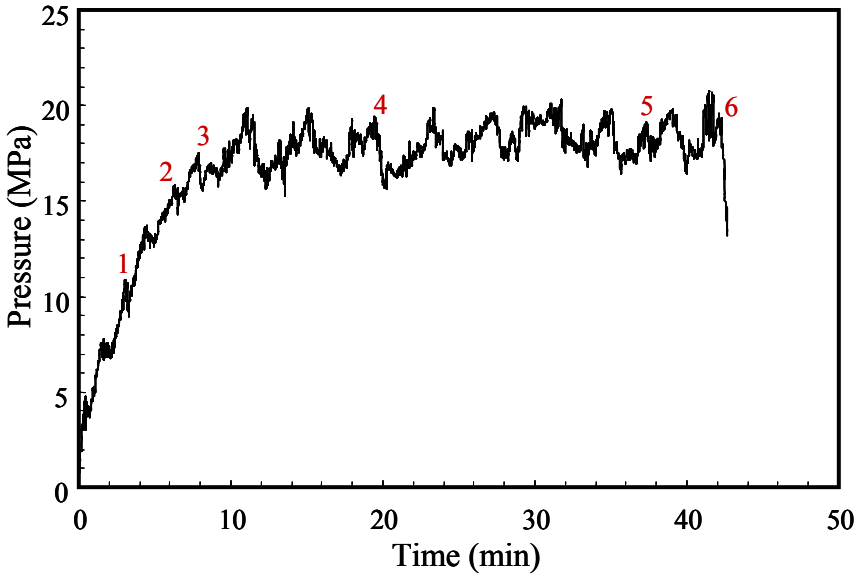

(a)

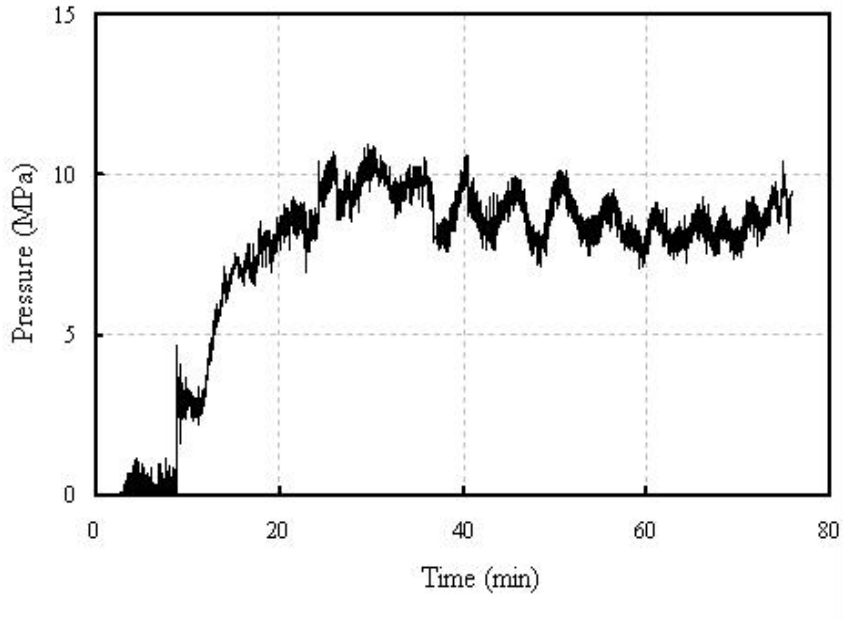

(b)

Figure 3.28. Injection pressure curves during fracture propagation in (a) sample 4-2 shown in Figure 3.10 and (b) sample 4-5 shown in Figure 3.12.

An example of the pressure curve and the associated hydraulic fracture geometry for a field case is given in Figure 3.29a [*Economides and Nolte*, 2000]. Figure 3.29a shows the recorded injection pressure. The fracture geometry was inferred using the following arguments. According to the conventional hydraulic fracture theory, the injection pressure curve features three stages as fluid is injected into the borehole (Figure 3.29b). During Stage 1, a radial fracture is created and the injection pressure decreases. During Stage 2, the propagated hydraulic fracture is confined within the pay zone. Hence, its geometry becomes elongated. This is frequently modeled by the Perkins-Kern-Nordgren (PKN) fracture and the injection pressure increases. Finally, during Stage 3, as the size of the hydraulic fracture keeps on increasing, its height grows beyond the pay zone. At this time, the injection pressure remains quasi-constant. This stage is also referred to as "height growth".

According to this theory, for a field observed pressure curve (Figure 3.29a), if the possibility of segmentation was ignored, one would conclude that the geometry of the hydraulic fracture is first radial, then PKN, and finally PKN with height growth. This is, in fact, how this geometry was interpreted in the real case shown in Figure 3.29a [*Economides and Nolte*, 2000]. However, based on the experimental results reported herein, the hydraulic fracturing may also be a radial fracture with segmentation. Since generally the size of the radial fracture is significantly smaller than that of the PKN geometry, by ignoring segmentation, not only can the fracture geometry be incorrectly inferred, but the area of the hydraulic fracture treatment region is also likely to be considerably overestimated. Alternatively, if proppant is injected, fracture segmentation may result in the early screen-out of the hydrofrac job.

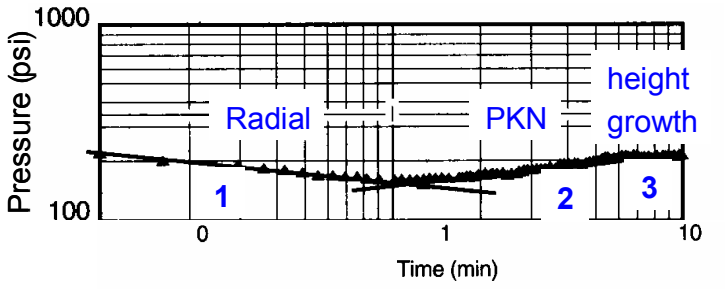

(a)

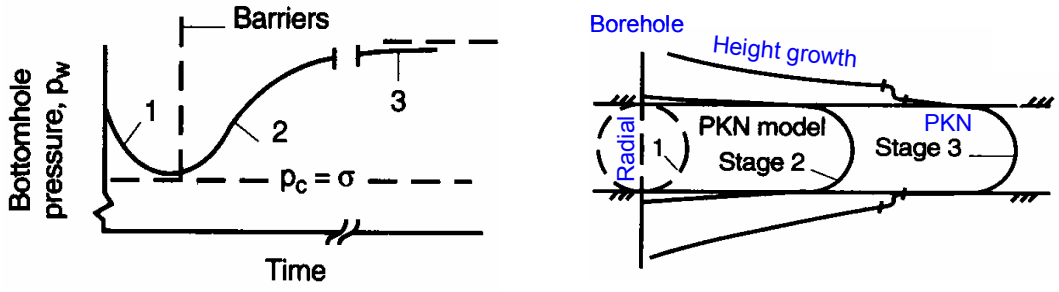

(b)

Figure 3.29. (a) Field observed fracture injection pressure curve and inferred fracture geometry, and (b) typical hydraulic fracture injection pressure curve and interpretations of this curve based on the conventional theory [*Economides and Nolte*, 2000].

3.7 Conclusions

In this work, we experimentally studied not only the effect of mode III loading on the onset of fracture segmentation but also the effect of segmentation on the subsequent fracture growth when the K_{III}/K_I ratio was rather small (1-10%). We used transparent, cylindrical PMMA samples with circular internal fractures perpendicular to the sample axis. Fracture orientation was controlled by thermoelastic stresses induced in each sample by preheating it before creating a fracture. In order to apply mode III loading to the initial fracture, a constant torque was applied to the specimen while fluid was injected into the fracture at a constant rate to pressurize it and to induce mode I loading. In spite of a small magnitude of the mode III component, we observed segmented fracture fronts in all the

tested samples. The segments had similar dimensions and an elongated shape. When the fractures were further pressurized by injecting additional fluid into the sample, second-order segments developed along the fronts of the first-order segments.

We also developed a simple asymptotic model of a multi-segmented mode I+III fracture propagating in conditions of a low level mode III loading, which takes into account mechanical interaction between the segments and the parent fracture. The model shows good agreement with the experimental observations.

The obtained results indicate that a K_{III}/K_I ratio as small as a few percent is sufficient for fracture front segmentation even in materials as homogeneous and fracture resistant as PMMA. In reality, a small component of mode III is always expected, for example, due to slight deviations of a three-dimensional fracture from a planar shape or interaction with boundaries or other fractures. As a result, front segmentation (at an appropriate scale) is likely to accompany the growth of most (if not all) real fractures, at least in quasi-brittle materials.

Nomenclature

Latin Symbols

a	radius of initial fracture
a_0	radius of effective fracture
b	half-width of segment along the propagation direction
c	overlap length
d	half-length of segment along the fracture front

E	Young's modulus
E'	plane strain elastic modulus, $E/(1- \nu^2)$
f	function in (3.11) defining the SIF (3.10) for the 2-D fracture (Figure 3.25)
$F(a_0/R)$	function in (3.15) defining the SIF (3.14) for a circular fracture in the infinite cylinder
F_n	resistance force from the ligament
I	area moment of inertia
K_I, K_{II}, K_{III}	mode I, II and III stress intensity factors
K_{Ic}	fracture toughness
K_I^0	stress intensity factor for an unsegmented circular crack, $2p(a/\pi)^{1/2}$
L	cylinder length
p	injection pressure
p_f	injection pressure at the final stage
q	injection rate
R	cylinder radius
s	spacing between the fractures
t	injection time
u	displacement
v	crack side displacement
V	fracture volume
V_i	volume of initial fracture
w_1, w_2	deflections at the ends of the beam (ligament)
x, y, z	cartesian coordinate set

Greek Symbols

ν	Poisson's ratio

σ	normal stress
τ	shear stress

References

Abass, H.H., S. Hedayati, and D.L. Meadows (1996), Nonplanar fracture propagation from a horizontal wellbore: Experimental study, *SPE Prod. Facil.*, *11*, 133-137.

Abelson, M., and A. Agnon (1997), Mechanics of oblique spreading and ridge segmentation, *Earth Planet. Sc. Lett.*, *148*, 405-421.

Alfaiate, J., G.N. Wells, and L.J. Sluys (2002), On the use of embedded discontinuity elements with crack path continuity for mode-I and mixed-mode fracture, *Eng. Fract. Mech.*, *69*, 661-686.

Bakala, M. (1997), Fracture propagation in sediment-like materials, M.S. thesis, 83 pp., Univ. of Oklahoma, OK.

Broberg, K.B. (1999), *Cracks and Fractures*, Academic Press, San Diego, USA, 752 pp.

Carter, B.J., P.A. Wawrzynek, and A.R. Ingraffea (2000), Automated 3D crack growth simulaiton, *Int. J. Num. Meth. Eng.*, *47*, 229-253.

Chang, S.-H., C.-I. Lee, and S. Jeon (2002), Measurement of rock fracture toughness under modes I and II and mixed-mode conditions by using disc-type specimens, *Eng. Geol*, *66*, 79-97.

Cooke, M.L., and D.D. Pollard (1996), Fracture propagation paths under mixed mode loading within rectangular blocks of polymethyl methacrylate, *J. Geophys. Res.*, *101*, 3387-3400.

Cox, S.J.D., and C.H. Scholtz (1988), On the formation and growth of faults: an Experimental Study, *J. Struct. Geol.*, *10*, 413-430.

Crouch, S.L., and A.M. Starfield (1983), *Boundary Element Methods in Solid Mechanics: with Applications in Rock Mechanics and Geological Engineering*, George Allen and Unwin, London, 322 pp.

Davenport, J.C.W., and D.J. Smith (1993), A study of superimposed fracture modes I, II and III on PMMA, *Fatigue Fract. Eng. Mater. Struct.*, *16*, 1125-1133.

Delaney, P.T. (1996), Personal communication.

Delaney, P.T., and D.D. Pollard (1981), Deformation of host rocks and flow of magma during growth of Minette Dikes and Breccia-bearing Intrusions near Ship Rock, New Mexico, *Geological Survey Professional Paper 1202, U.S. Government Printing Office, WA*.

Economides, M.J., and K.G. Nolte (2000), *Reservoir Stimulation*, 3rd Edition, John

Wiley & Sons, LTD.

Erdogan, F., and G.C. Sih (1963), On the crack extension in plates under plane loading and transverse shear, *J. Basic Eng.*, *85*, 519-527.

Germanovich, L.N., D.K. Astakhov, M.J. Mayerhofer, J. Shlyapobersky, and L.M. Ring (1997), Hydraulic fracture with multiple segments - I: Observations and model formulation, *Int. J. Rock Mech. Min. Sci.*, *34*, 471.

Germanovich, L.N., D.K. Astakhov, J. Shlyapobersky, M.J. Mayerhofer, C. Dupont, and L.M. Ring (1998), Modeling multisegmented hydraulic fracture in two extreme cases: No leakoff and dominating leakoff, *Int. J. Rock Mech. Min. Sci.*, *35*.

Germanovich, L.N., B.J. Carter, A.R. Ingraffea, A.V. Dyskin, and K.K. Lee (1996), Mechanics of 3D crack growth in compression, *Rock Mechanics Tools and Techniques*, *2nd North American Rock Mechanics Symposium*, Montreal, Canada, 1151-1160.

Gerstle, W.H., and A.R. Ingraffea (1986), Boundary element modeling of crack propagation in three dimensions, *Proc. of the 2nd Boundary Element Technology Conference*, June 17-19, Cambridge, MA, 651-662.

Hallam, S.D., and N.C. Last (1991), Geometry of hydraulic fractures from modestly deviated wellbores, *J. Petrol. Techol.*, *43*, 742-748.

Hoek, H. (1994), Mafic dykes of the Vestfold Hills, East Antarctica, Ph.D. thesis, University of Utreht.

Hubbert, M.K., and D.G. Willis (1957), Mechanics of hydraulic fracturing, *J. Petrol. Techol.*, *9*, 153-166.

Hussain, M.A., S.L. Pu, and J.H. Underwood (1974), Strain energy release rate for a crack under combined mode I and mode II, *Fract. Analysis*, *ASTM STP*, *560*, 2-28.

Ingraffea, A.R., and F.E. Heuze (1980), Finite element models for rock fracture mechanics, *Int. J. Numer. Analyt. Meth. Geomech.*, *4*, 25-43.

Kamat. S.V., and J.P. Hirth (1996), Effect of aging on mixed-mode I/III fracture toughness of 2034 aluminum alloys, *Acta Mater.*, *44*, 1047-1054.

Kanninen, M.F., and C.H. Popelar (1985), *Advanced Fracture Mechanics*, Oxford University Press, New Yok, 563 pp.

Knauss, W.G. (1970), An observation of crack propagation in anti-plane shear, *Int. J. Fract. Mech.*, *6*, 183-187.

Li, H, R.J. Kurtz, and R.H. Jones (1998), Effect of thickness and loading mode on the fracture properties of V-4Cr-4Ti at room temperature, *J. Nucl. Mater.*, *258-263*,

1386-1391.

Mahajan, R.V., and K. Ravi-Chandar (1989), An experimental investigation of mixed-mode fracture*, Int. J. Fract.*, *41*, 235-252.

Mahrer, K.D. (1999), A review and perspective on far-field hydraulic fracture geometry studies, *J. Petrol. Sci. Eng.*, *24*, 13-28.

Maji, A.K., M.A. Tasdemir, and S.P. Shah (1991), Mixed mode crack propagation in quasi-brittle materials, *Eng. Fract. Mech.*, *38*, 129-145.

Murdoch, L.C. (1993), Hydraulic fracturing of soil during laboratory experiments, Part I Methods and observations, *Geotechnique*, *43*, 255-265.

Petrovic, J. J. (1985), Mixed-mode fracture of hot-pressed Si3N4, *J. Am. Ceram. Soc.*, *68*, 348-355.

Pollard, D.D., and A. Aydin (1988), Progress in understanding jointing over the past century, *Geol. Soc. Am. Bull.*, *100*, 1181-1204.

Pollard, D.D., and R.C. Fletcher (2005), *Fundamentals of Structural Geology*, Cambridge University Press, Cambridge, 500 pp.

Pollard, D.D., P. Segall, and P.T. Delaney (1982), Formation and interpretation of dilatant echelon cracks, *Geol. Soc. Am. Bull.*, *93*, 1291-1303.

Pook, L.P. (1985), The fatigue crack direction and threshold behavior of mild steel under mixed mode I and III loading, *Int. J. Fatigue*, *7*, 21-30.

Qian, J., and A. Fatemi (1996), Mixed mode fatigue crack growth: a literature survey, *Eng. Fract. Mech.*, *55*, 969-990.

Richard, H.A., and M. Kuna (1990), Theoretical and experimental study of superimposed fracture modes I, II and III, *Eng. Fract. Mech.*, *35*, 949-960.

Roering, C. (1968), The geometrical significance of natural en-echelon crack-arrays, *Tectonophysics*, *5*, 107-123.

Roy, A., Y.R. Narasimhan, and P.R. Arora (1999), An experimental investigation of constraint effects on mixed mode fracture initiation in a ductile aluminum alloy, *Acta Mater.*, *47*, 1587-1596.

Rubin, A.M. (1995), Propagation of magma-filled cracks, *Annu. Rev. Earth Pl. Sci.*, *23*, 287-336.

Shi, H.-J., L.-S. Niu, G. Mesmacque, and Z.-G. Wang (2000), Branched crack growth behavior of mixed-mode fatigue for an austenitic 304L steel, *Int. J. Fatigue*, *22*, 457-465.

Shimamoto, A., M. Kosai, and A.S. Kobayashi (1994), Crack arrest at a tear strap under mixed mode loading, *Eng. Fract. Mech.*, *47*, 59-74.

Sih, G.C. (1974), Strain energy density factor applied to mixed-mode crack problems, *Int. J. Fract.*, *10*, 305-321.

Sim, Y. (2004), Mechanics of complex hydraulic fractures in the Earth's crust, Ph.D. thesis, 325 pp., Georgia Institute of Technology, GA.

Sommer, E. (1969), Formation of fracture lances in glass, *Eng. Fract. Mech.*, *1*, 539-546.

Song, L., S.M. Huang, and S.C. Yang (2004), Experimental investigation on criterion of three-dimensional mixed-mode fracture for concrete, *Cement Concrete Aggr.*, *34*, 913-916.

Srinivas, M., S.V. Kamat, and P. Rama Rao (2004), Influence of mixed mode I/III loading on fracture toughness of mild steel at various strain rates, *Mater. Sci. Tech.*, *20*, 235-242.

Tada, H., P.C. Paris, and G.R. Irwin (1985), *The stress analysis of cracks handbook*, 2nd ed., Paris Productions Incorporated, St. Louis, MO.

Thomas, A.L., and D.D. Pollard (1993), The geometry of echelon fractures in rock: implications from laboratory and numerical experiments, *J. Struct. Geol.*, *15*, 323-334.

Ueda, Y., K. Ikeda, T. Yao, and M. Aoki (1983), Characteristics of brittle fracture under general combined modes including those under bi-axial tensile loads, *Eng. Fract. Mech.*, *18*, 1131-1158.

Yates, J.R., and K.J. Miller (1989), Mixed mode (I-III) fatigue threshholds in a forging steel, *Fatigue Fract. Eng. Mater. Struct.*, *12*, 259-270.

Yates, J.R., and R.A. Mohammed (1996), Crack propagation under mixed mode (I + III) loading, *Fatigue Fract. Eng. Mater. Struct.*, *19*, 1285-1290.

Wu, R., L.N. Germanovich, P. van Dyke, and R.P. Lowell (2006), A laboratory technique for controlling hydraulic fractures, *J. Geophys. Res.*, accepted.

Zhao, Y. (1989), Experimental study on mixed mode crack propagation, *Eng. Fract. Mech.*, *34*, 891-899.

CHAPTER 4
EFFFECTS OF CRACK TIP PLASTICITY ON HYDRAULIC FRACTURING IN COHESIONLESS MATERIALS

Abstract. In this chapter, we consider two models of hydraulic fracturing in uncemented sediments. We first introduce a model of a simple localized plastic band to describe the process zone at the tip of a fracture in cohesionless particulate material in the Dugdale-Barenblatt manner. Even though the physical nature of the localized plastic zone appearing in compression and the mechanism of localized fluid flow into cohesionless materials are unclear, the model still results in a stress state that is compressive everywhere, including the fracture tip zone. Since cohesionless materials cannot bear tensile stress, this model is appealing and yields a simple and convenient approach for modeling fracture propagation. The other model utilizes the physical mechanism of shear banding, which is characteristic for particulate materials with strain-softening behaviour. It explicitly describes the fracture front and the fluid flow mechanism. The model is consistent with experimental observations and is based on modeling the shear bands by properly oriented and positioned dislocations. To test the shear band hypothesis, we also conducted numerical simulations of the localized plastic deformation at the tip of a fracture in the particulate material with strain softening.

4.1 Introduction

4.1.1 Hydraulic Fracturing in Particulate Material

Hydraulic fracturing has been used in petroleum engineering for more than fifty years to create deep-penetrating fractures in hydrocarbon reservoirs for the purpose of stimulation of oil and gas production [*Howard and Fast*, 1970; *Sasaki*, 1998; *Berumen et al.*, 2000; *Economides and Nolte*, 2000]. During the last decade, it has also been used as an alternative sand control method in soft rock reservoirs, especially in unconsolidated or poorly consolidated formations [*Abass et al.*, 2003; *Abou-Sayed et al.*, 2004]. In addition, as a novel technique, hydraulic fracturing has been employed to construct subsurface permeable reactive barriers for groundwater remediation [*Murdoch and Slack*, 2002].

On the other hand, hydraulic fracturing may sometimes be harmful, causing soil foundation rupture and loss of grouting fluid during pressure grouting [e.g., *Warner*, 1997], and dam failure (such as the failure of Hyttejuvet Dam in Norway and Teton Dam in Idaho, USA [e.g., *Jaworski et al.*, 1981]). Another significant example is the shallow-water flow (SWF) during borehole drilling [e.g., *Ostermeier et al.*, 2000]. Shallow water flow (SWF) may occur if during drilling, shallow over-pressure forms at deepwater sites. Figure 4.1 schematically shows an example of the over-pressure effect on the decrease of the fracturing pressure at a SWF site in the Gulf of Mexico. The mechanism of SWF is often attributed to hydraulic fracturing of the host sediments by the drilling mud. As a result, large uncontrollable flows may erupt, and large craters and trenches may form on the seafloor [*Ostermeier et al.*, 2000]. Figure 4.2 shows a trench formed on the sea floor by SWF in the Gulf of Mexico [*Ostermeier et al.*, 2000]. These consequences of SWF

lead to the loss of drilled wells and cause significant environmental pollution.

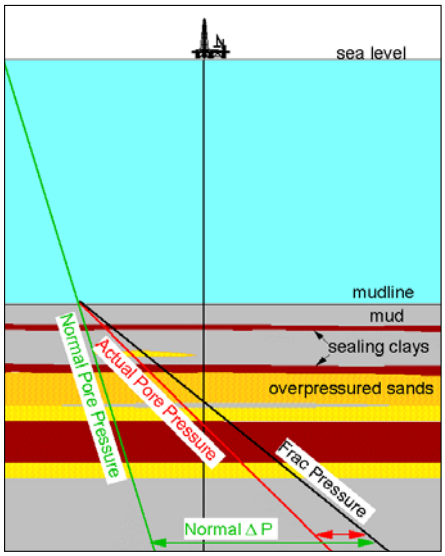

Figure 4.1. Effect of over-pressured zones on the decrease of the pressure margin at a SWF site in the Gulf of Mexico [*Ostermeier et al.*, 2000].

Figure 4.2. Trench formed by SWF [*Ostermeier et al.*, 2000].

To better prevent undesirable hydraulic fracturing and to optimize its useful applications, in-depth knowledge of hydraulic fracturing in particulate materials is needed, because this type of hydraulic fracturing is significantly different from that in solid materials [*Chang*, 2004; *Hurt et al.*, 2005]. Based on the different material properties, hydraulic fracturing in particulate materials can be divided into hydraulic

fracturing in cohesive materials and that in cohesionless materials. A brief discussion of the two different cases is given in the next section.

4.1.2 Cohesive and Cohesionless Particulate Materials

In general, the hydraulic fracturing in *cohesive* particulate materials is pictured to be somewhat similar to that in solid materials [e.g., *Murdoch*, 1993a, 1993b, and 1993c; *Murdoch and Slack*, 2002]. That is, the fracturing is assumed to occur when the tensile stress at the fracture tip is sufficient to break the material bonds (i.e., it exceeds the material tensile strength).

The conventional model of hydraulic fracturing in a solid material is schematically presented in Figure 4.3. Material representative volume elements are shown as small squares. The material is in ambient compression (i.e., $0 \leq \sigma_3 \leq \sigma_1$) at the location away from the crack (the remote element 1) while it is in tension in the fracture process zone (element 3). The latter tensile stress is required to separate the two fracture surfaces and to overcome the tensile strength of the material. These assumptions are commonly used (explicitly or implicitly) when modeling hydraulic fracturing in cohesive particulate materials.

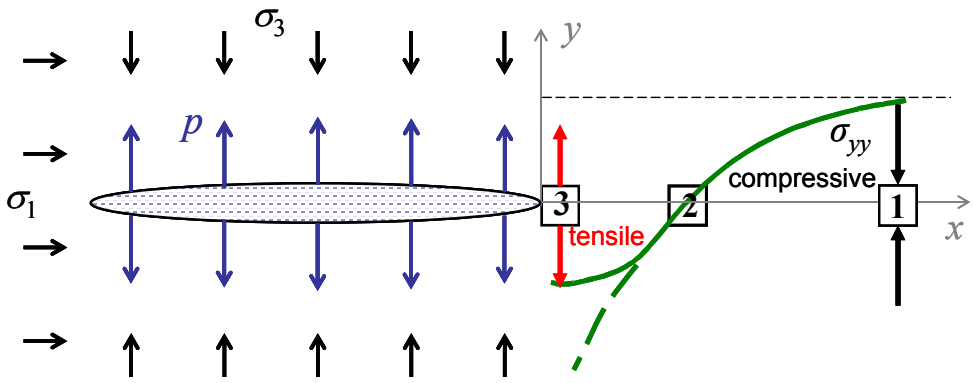

Figure 4.3. Stress distribution near the fracture tip in cohesive material with a non-zero tensile strength, σ_t. The dashed line indicates the singular stress distribution for a discontinuity in an ideally elastic material.

Linear elastic fracture mechanics (LEFM) specifies the above postulates, and further assumes that [e.g., *Broberg*, 1999]:

- Material is elastic everywhere except in the process zone near the fracture tip.
- The process zone is small compared to the fracture size.
- Fracture is infinitesimally thin and can be modeled by a discontinuity.
- Tensile stresses near the tip of this discontinuity (but outside the fracture process zone) can be described as an elastic singular stress distribution (shown as a dashed line in Figure 4.3; compression is positive in section 4.1 and 4.2):

$$\sigma_{yy} = -\frac{K_I}{\sqrt{2\pi r}} \quad (x > 0,\ y = 0) \tag{4.1}$$

- In plane strain, the fracture aperture in the vicinity of the fracture tip is given by

$$w = \frac{4(1-\nu^2)}{\sqrt{2\pi}E} K_I \sqrt{r} \quad (x < 0,\ y = 0) \tag{4.2}$$

- The fracture growth criterion is

$$K_I = K_{Ic} \tag{4.3}$$

Here K_I is the elastic stress intensity factor (SIF) and K_{Ic} is the material fracture toughness; r is a small distance from the origin along the x-axis (i.e., $r = |x|$ in the coordinate set shown in Figure 4.3); and E and ν are Young's modulus and Poisson's ratio, respectively.

As opposed to cohesive solids, *cohesionless* particulate materials are already "fractured." Hence, no material bonds exist between particles and no new surfaces are created at the grain/particle (i.e., micro) scale (unless the particles are being crushed, which is not the case considered in this work). Furthermore, all material parts are in compression (since the material cannot bear any tension) and no fracturing process breaking material bonds is involved under hydraulic pressure. Rather, hydraulic pressure causes liquid to flow in self-localized, thin, propagating, crack-like conduits [*Chang*, 2004; *Hurt et al.*, 2005; examples are given in the next section]. By analogy, we call this phenomenon "hydraulic fracturing," and the corresponding features (conduits) "cracks" or "hydraulic fractures." While these "fractures" resemble displacement discontinuities typical for cracks in solids (and this is why the terms "crack" or "fracture" seem to be appropriate), the conventional fracture mechanics principles are hardly applicable without modification.

One conceptual model, which is helpful for understanding some issues associated with hydraulic fracturing in cohesionless materials, is schematically presented in Figure 4.4. Similar to the case of cohesive materials (Figure 4.3), the remote part of the material is in ambient compression. The material adjacent to the fracture sides is elastic (e.g., the corresponding plastic layer is thin compared to the fracture size). In addition, since the fluid pressure tends to open the fracture, stresses $\sigma_{yy}(x, 0)$ and $\sigma_{xx}(x, 0)$ reduce towards the fracture tip (i.e., when $x > 0$ decreases). Distribution of $\sigma_{yy}(x, 0)$ along x is schematically shown by the solid curve in Figure 4.4. On the other hand, being different from the singular tensile stress corresponding to a crack in elastic material (dashed curve in Figure 4.4), the cohesionless material is still in compression everywhere, even including the fracture process zone (shown in grey between elements 1 and 2). Thus, the material is unloaded at the fracture tip (i.e., σ_{yy} and σ_{xx} are reduced from remote stresses σ_3 and σ_1), where it reaches the Mohr-Coulomb failure criterion (Figure 4.4). Note that the shape of the process zone in Figure 4.4 should not be taken literally. It has to be defined as a result of modeling (section 4.3.1).

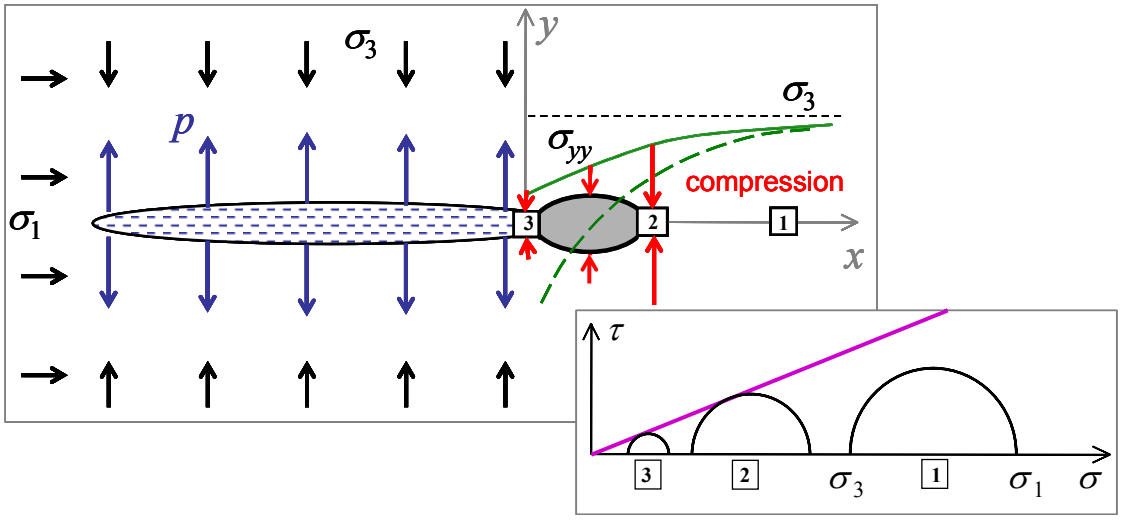

Figure 4.4. Schematic of stress distribution at fracture tip in a cohesionless material. The stress near the fracture tip is less than the ambient value. The Mohr-Coulomb diagram illustrates that yielding near the fracture front occurs as a result of decreasing stresses compared to the remote in-situ stresses.

4.1.3 *Chang*'s [2004] Laboratory Experiments

To understand the hydraulic fracturing in low-cohesive or cohesionless particulate material, a series of laboratory experiments have recently been conducted by *Chang* [2004]. In her tests, the hydraulic fracturing in particulate material was visualized by injecting solidifying fracturing fluid into dry specimens. After the injected fluid settled and the host particulate materials removed, it was possible to directly observe the obtained "hydraulic fractures" (fracture impressions). Several controlling parameters, including the properties of particulate materials and fracturing fluids, the boundary conditions, the initial stress states, and the injection volumes and rates, were varied in the tests to investigate their effects on hydraulic fracturing. The test results showed that hydraulic fracturing in cohesionless particulate materials is possible if the fluid leak-off is minimized. In addition, the analyses of *Chang*'s [2004] tests showed that in particulate

materials with low or no cohesion, all parts of the particulate material are indeed likely to be in compression during hydraulic fracturing.

Chang's [2004] tests also showed that the fracturing behavior (including the shape and thickness of the front) in particulate materials is sensitive to the properties of the particulate materials (in terms of the particle gradation and mean particle size), the viscosity and the injection volume of the fracturing fluid, and the external stress condition (i.e., stress ratio and magnitude). The hydraulic fracture fronts created in cohesionless particulate materials have different characteristics compared to those in brittle solid materials. Three types of fracture front have been observed: beveled (Figure 4.5a), fingered (Figure 4.5b) and round (Figure 4.5c). In all cases, the observed fronts had thichnesses many times larger then the particle size.

(a) (b) (c)

Figure 4.5. Three typical fracture fronts of hydraulic fractures observed in particulate material [*Chang*, 2004]: (a) beveled front (in silica flour); (b) fingered front (in Georgia Red Clay); (c) round front (in silica flour).

Although some conceptual models attempting to explain experimental observations have been offered [*Chang*, 2004; *Hurt et al.*, 2005], our literature review

shows that by now, no fundamental and systematic research has been conducted to provide physically sound models for the hydraulic fracturing mechanisms in cohesionless particulate materials. To the best of our knowledge, almost all the previous works were devoted to cohesive particulate materials [e.g., *Bjerrum et al.*, 1972; *Lo and Kaniaru*, 1990; *Andersen et al.*, 1993; *Murdoch*, 1993a, 1993b, 1993c, and 2002; *Soga et al.*, 2004]. Currently, there are no fracture initiation and propagation criteria specifically developed for hydraulic fracturing in unconsolidated, cohesionless particulate materials. Existing criteria used for modeling fractures in cohesive particulate materials are based on conventional fracture mechanics that assumes non-zero material tensile strength in the fracture tip zone [*Murdoch*, 1993a, 1993b, 1993c]. While in some cases these criteria have been successfully applied to cohesive particulate materials [*Murdoch*, 1993a, 1993b, 1993c, and 2002], as discussed in the previous section, utilizing them for describing hydraulic fracturing in cohesionless particulate materials does not have yet a solid, fundamental justification. Therefore, a quantitative model applicable to cohesionless particulate materials needs to be developed. Our work is a step forward in this direction.

4.1.4 Theoretical Models for Crack Tip Plasticity

Particulate materials often exhibit pronounced non-linear behavior and yielding even at relatively small strains. Therefore, in order to adequately describe hydraulic fracturing in particulate materials with low or no cohesion, the plasticity at the crack tip needs to be explicitly considered. *Papanastasiou and Thiercelin* [1993] and *Papanastasiou* [1997] investigated the influence of plastic deformation in hydraulic fracturing (in cohesive material) by using a coupled elasto-plastic model based on finite element analysis. Their analyses showed that the plastic yielding near the tip of a

propagating fracture provides an effective shielding, resulting in an increase of the effective fracture toughness by more than an order of magnitude [*Papanastasiou and Thiercelin*, 1993]. Hence, propagating an elasto-plastic fracture requires a higher pressure than that for an elastic fracture. In addition, the elasto-plastic hydraulic fracture is likely to be shorter and wider than the elastic fracture of the same volume [*Papanastasiou*, 1997].

Apart from hydraulic fracturing, numerous theoretical models have been proposed to describe plasticity at the crack tip. Below we briefly describe only a few of them that are most relevant to our work.

In his pioneering work, *Dugdale* [1960] detected a thin, plastic band on the continuation of a crack in the tensile tests of thin low-carbon steel plates. He used thin strip collinear with the crack to represent the plastic zone. He further assumed that the strip had a constant normal stress Y (the yield limit of the material) and solved the corresponding elastic boundary value problem. The infinitesimally thin inelastic band near the fracture tip was also described in the models of *Barenblatt* [1962] and *Leonov et al.* [1963]. Dugdale – Barenblatt model laid the foundation for many works in fracture mechanics, and a thin plastic band often represents the first attempt in modeling fracture process zone.

Bilby et al. [1963] used a distribution of edge or screw dislocations collinear with the crack to represent the plastic field at the tip of a crack. By assuming that the dislocations were subject to a constant friction stress, σ_i, which is associated with the yield stress of the material, and by assuming that the crack was loaded by a constant

shear stress applied at infinity, they calculated the plastic zone length required to relax the singularity at the crack tip.

Cherepanov [1979] considered displacement discontinuity distributed in two narrow slip shear bands to analyze the plastic zone near the tip of a crack. He stated [p. 118] that "the plastic strains which arise near the tip of a crack long before it begins to move … are concentrated along two narrow slip bands, departing symmetrically from the tip of a crack at a certain angle to the continuation of the crack. This form of plastic zone under plane strain conditions can be considered a certain approximation of the "blurred" plastic zone; for certain materials, possibly, it is closer to the true state of affairs." By using Tresca – St. Venant yielding criterion and maximizing the extend of the plastic zone, *Cherepanov* [1979] calculated the angle between the shear bands and the crack to be 72°. He also used this model to analyze the influence of the lateral loading (along the crack) on the plastic zone. His results showed that the crack tip opening displacement (CTOD) depends substantially upon the loads parallel to the crack surface.

Atkinson and Kay [1971] proposed a model whereby the plastic flow at a crack tip is represented by a single dislocation of unknown Burgers vector emitting from the crack tip along each slip direction. In their model, *Atkinson and Kay* [1971] reduced the problem to two algebraic equations with two unknowns: the magnitude of the Burgers vector and the distance of each dislocation from the crack tip. They solved this problem by using two conditions: (1) no stress singularity at the crack tip, and (2) zero total force on the dislocation in its slip plane (assuming it has resistance to motion equal to the friction stress). They also compared the obtained results with other models [e.g., *Bilby et*

al., 1963] for the case when the dislocations are collinear with the crack. A good agreement was found for the predicted displacement at the crack tip. A virtue of *Atkinson and Kay*'s [1971] model is that it can be extended relatively simply to situations where the relaxation is not collinear with the crack tip.

Atkinson and Kanninen [1977] applied this approach to a crack in a Von Mises material. In their calculation, they chose a particular angle, $\theta = 70.53°$, to maximize the extent of yielding. *Atkinson and Kanninen* [1977] pointed out that "the superdislocation cannot be expected to give precise information about the size and shape of the plastic zone. However, this will be unimportant if it does reflect with reasonable accuracy the effect of the plastic deformation at the crack tip" under small scale yielding conditions. Although this simple representation has its limitations, e.g., in predicting the plastic zone size [*Atkinson and Kanninen*, 1977], its mathematical simplicity and the possibility to directly and rather accurately evaluate the crack tip opening displacement [e.g., *Hills et al.*, 1996] are very appealing features. Hence, the super-dislocation model has been widely used to simulate the plastic zones at crack tips in Von Mises materials [e.g., *Kanninen et al.*, 1977; *Kanninen and Atkinson*, 1980; *Jagannadhan and Marcinkowski*, 1982; *Shiue and Lee*, 1992; *Gerberich et al.*, 1994; *Sadananda and Ramaswamy*, 2001].

Motivated by the potential applications of the super-dislocation model to the design of hydraulic fracturing in weak rock reservoirs, *Papanastasiou and Atkinson* [2000] extended the super-dislocation model to represent the crack tip plastic zone in Mohr-Coulomb pressure sensitive geomaterials. Based on parametric studies, *Papanastasiou and Atkinson* [2000] concluded that the super-dislocation model can

capture the essentials of the crack tip plasticity in Mohr-Coulomb materials. However, the recent study of *Germanovich and Wu* [2006] (Chapter 5 of this dissertation) showed that this is not always the case and great care needs to be taken when applying the super-dislocation model to Mohr-Coulomb materials.

The main goal of this work is to study the relevant physical mechanisms of hydraulic fracturing in cohesionless materials by explicitly considering the plasticity at the fracture tip. For this purpose, we investigate the feasibility of two mathematical models: a localized process zone model and a super-dislocation model. The localized process zone model is the simplest and describes plastic yielding at the fracture tip in the Dugdale-Barenblatt manner. The super-dislocation model accounts for the shear bands that often appear in particulate materials with strain-softening behaviour.

In essence, these two models represent an attempt to test if the two corresponding classic fracture mechanics approaches can be used in new conditions, that is, when the fracture propagates in the stress field, which is compressive everywhere, including the fracture process zone. For example, for crak growth in a crystal, the first approach is based on the Barenblatt's cohesive forces and the clivage of the crystal between the lattice planes while the second approach describes the dislocation emission from the fracture tip. It is tempting to follow historical developments in Fracture Mechanics and to try similar models in the case of fractures in particulate materials. Although from the physical standpoint, fracture phenomena in solid crystals and particulate materials are rather different (and even not quite clear in the case of particulate materials), the mathematical similarity and simplicity of the corresponding models are appealing and

warrant further analysis.

4.2 A Model of the Localized Process Zone

4.2.1 Problem Descriptions and Main Assumptions

In conventional fracture mechanics, a process zone is assumed to exist at the fracture tip. The existence of this process zone removes the elastic stress singularity and provides a finite displacement opening at the end of the fracture. In the case of hydraulic fracturing, this is important for the fluid transport into the fracture since viscous fluid cannot generally flow into an infinitesimally thin aperture [*Detournay*, 2004]. The Dugdale-Barenblatt model is well suited to describe this process zone in solid or cohesive materials. It treats the process zone as a localized linear cohesive zone with a *tensile* stress distribution, $\sigma(x)$ [e.g., *Broberg*, 1999]. This model provides the conditions for fracture propagation in terms of either critical crack tip opening displacement, δ_c, or fracture toughness, K_{Ic}. In the following section, we will explore the possibility of extending this model to cohesionless Mohr-Coulomb material.

As in the Dugdale-Barenblatt model, a localized rectilinear process zone (depicted as the gray zone in Figure 4.6) is assumed to exist near the fracture tip. In addition, we make the following assumptions when describing the fracture process in cohesionless material:

- The state of stress is *compressive* everywhere in the material, including in the vicinity of the fracture tip.
- Material is in elastic state (does not yield) prior to fracture propagation. The layer

of yielded material adjacent to the fracture sides is thin relative to the fracture size, and does not have to be considered in the fracturing process. Material yielding occurs only in the process zone (as a result of the stress change near the fracture tip).

- Material yielding can be described by the simplest Mohr-Coulomb criterion, $|\tau| = \sigma_n \tan\phi$ ($\sigma_n > 0$), i.e., at failure,

$$\sigma_{\min} = k\sigma_{\max}, \quad k = \frac{1-\sin\phi}{1+\sin\phi} < 1 \tag{4.4}$$

where τ and σ_n are the shear and normal stresses, respectively, ϕ is the angle of internal friction, and σ_{max} and σ_{min} are the maximum and minimum principal stresses, respectively.

- The fracture opening (i.e., thickness) in the process zone is significantly greater than the internal, micro-mechanical scales that are characteristic of yielding processes (e.g., grain scale, arching scale, or small-scale shear band spacing).
- The process zone length, d, is considerably greater than its thickness (Figure 4.6a). As in cohesive material, there is no stress singularity at the tip of the process zone:

$$K_I = 0 \tag{4.5}$$

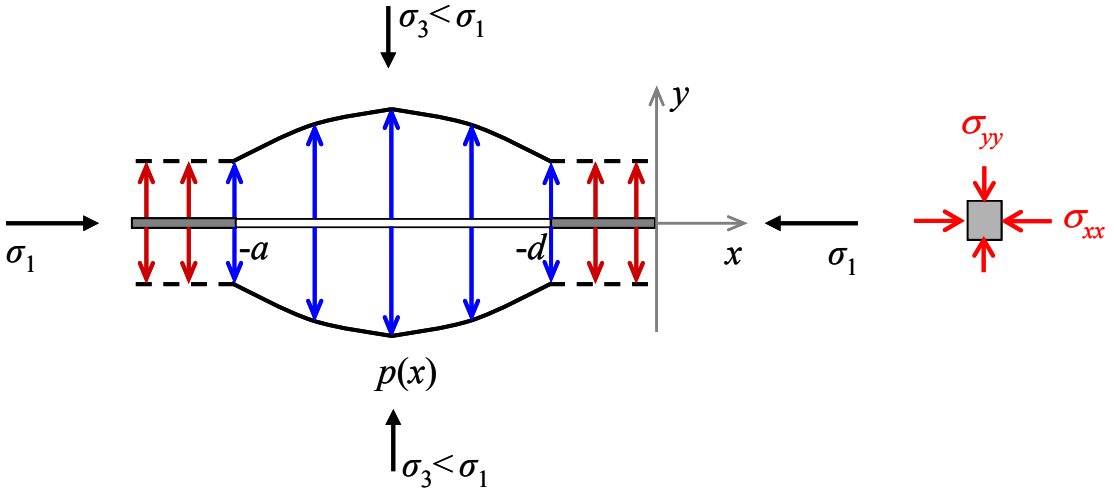

Figure 4.6. A model of the localized process zone: (a) Dugdale-Barenblatt model applied to cohesionless material, and (b) a representative element in the process zone in a state of compression. Grey areas indicate the process zones at the crack tips.

Consider a crack $\{-a-d < x < 0,\ y = 0\}$ with a length $a+d$, an internal pressure distribution $p(x)$ inside the crack, and a process zone of a length d at the fracture tip (Figure 4.6a). The boundary conditions on the two fracture surfaces can be written as

$$\sigma_{yy}(x,\ \pm 0) = p(x) \quad (-a < x < -d) \tag{4.6}$$

In the remote stress field, σ_{xx} and σ_{yy} are equal to σ_1 and σ_3, respectively, and $\sigma_1 \geq \sigma_3 > 0$. Recall that in this section 4.2, compressive stresses are positive. Note that the difference between the classic Dugdale-Barenblatt model and that considered here (Figure 4.6a) is not only in Mohr-Coulomb boundary condition (4.4) but also in compressive stress state in the process zone (Figure 4.6b).

4.2.2 Stresses inside the Process Zone

Near the crack tip, the stresses are given by [e.g., *Broberg*, 1999]

$$\begin{Bmatrix}\sigma_{yy}\\ \sigma_{xx}\end{Bmatrix}=\frac{K_I}{\sqrt{2\pi x}}+f(0)+\begin{Bmatrix}0\\ \sigma_1-\sigma_3\end{Bmatrix}+O(x^{1/2})\quad (x>0,\ y=0) \tag{4.7}$$

where $f(x) = \sigma_{yy}\ (x, \pm 0)\ (-a\text{-}d < x < 0)$ (actually, $f(x) = p(x)$ for $-a < x < -d$). Substituting (4.5) into (4.7) results in

$$\sigma_{xx}=\sigma_{yy}+\sigma_1-\sigma_3\quad (y=0) \tag{4.8}$$

which is valid not only for $x = 0$, but for any point on the x-axis.

Since all stresses are compressive (positive), and $\sigma_1 \geq \sigma_3$, (4.8) yields $\sigma_{xx} \geq \sigma_{yy}$ ($y = 0$). On the other hand, in the process zone, σ_{xx} and σ_{yy} should satisfy the Mohr-Coulomb failure criterion (4.4). Therefore, $\sigma_{min} = \sigma_{yy}$, $\sigma_{max} = \sigma_{xx}$, so that (4.4) can be rewritten as

$$\sigma_{yy}=k\sigma_{xx}\qquad (y=0,\ -d<x<0) \tag{4.9}$$

Substituting (4.9) into (4.8), we obtain the stresses inside the process zone

$$\begin{Bmatrix}\sigma_{xx}^0(x)\\ \sigma_{yy}^0(x)\end{Bmatrix}=\begin{Bmatrix}1/(1-k)\\ k/(1-k)\end{Bmatrix}(\sigma_1-\sigma_3)\quad (-d<x<0,\ y=0) \tag{4.10}$$

Expression (4.10) shows that the stresses inside the process zone are not only uniform but also independent of the fluid pressure, $p(x)$. They are determined only by the remote stresses and material properties (friction angle). Therefore, the stresses inside the process zone are fully defined.

In the far field (Figure 4.6), where the material is intact (in elastic state), according to the Mohr-Coulomb criterion (4.4), $\sigma_3 > k\sigma_1$. In this case, (4.10) results in

$$\sigma_{xx}^{0} < \sigma_1, \quad \sigma_{yy}^{0} < \sigma_3 \tag{4.11}$$

which shows that the stresses ahead of the fracture tip are indeed *reduced* compared to those at infinity.

4.2.3 Stresses outside the Process Zone

Now consider the stresses outside the process zone. In order to obtain these stress values, the problem shown in Figure 4.7 is decomposed into two auxiliary problems: (*i*) remote stress problem, and (*ii*) crack loaded by $\sigma_0 = \sigma_{yy}^{\ 0} - \sigma_3$ in the process zone ($0 < x_1 < d$) and by $\sigma(x_1) = p(x_1) - \sigma_3$ inside the crack ($x_1 < 0$), as shown in Figure 4.8 (translated coordinate set (x_1, y_1) is used for this auxiliary problem).

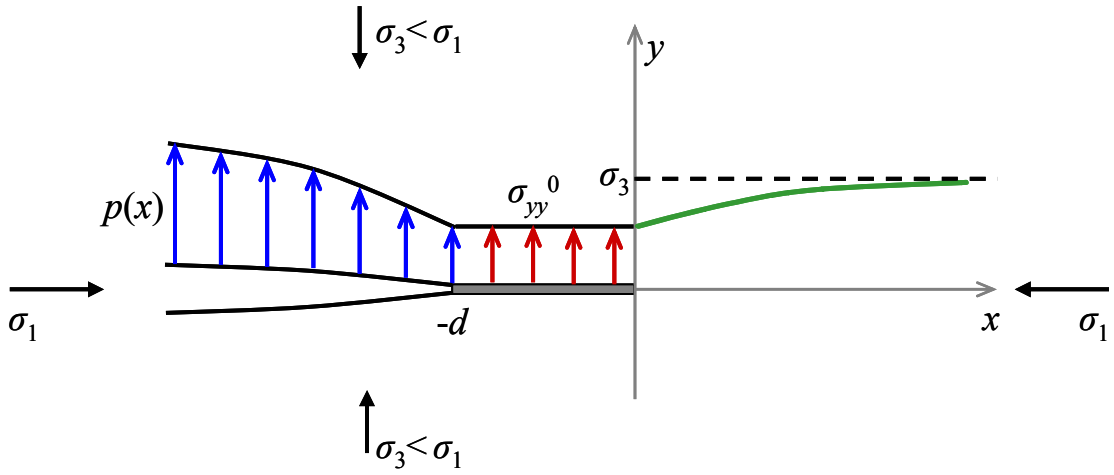

Figure 4.7. Localized process zone model: fracture loaded by $\sigma_{yy}^{\ 0}$ in the process zone and $p(x)$ inside the crack in addition to the remote load, σ_1 and σ_3.

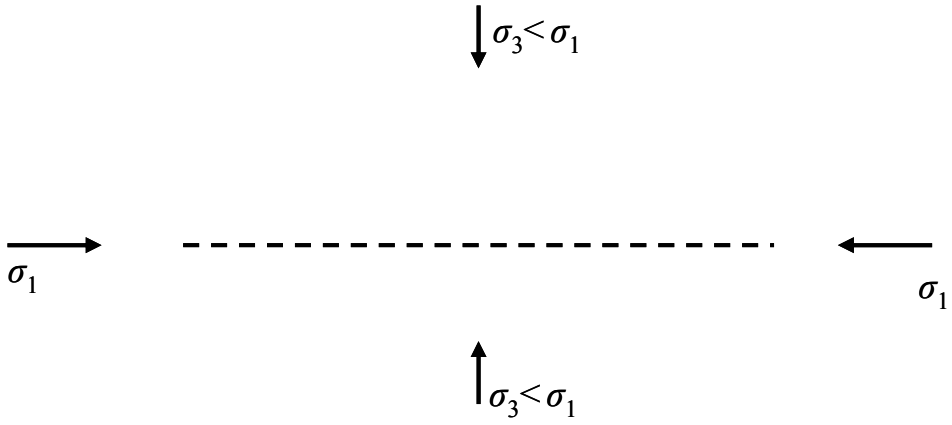

(a)

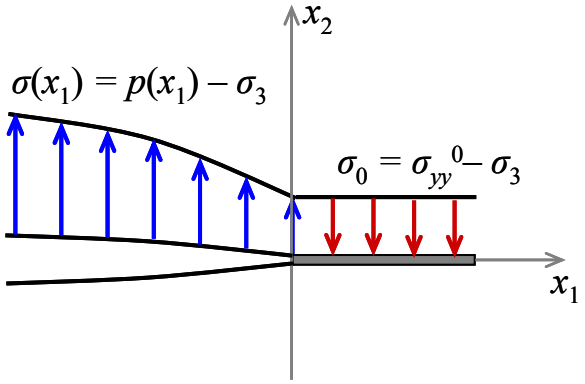

(b)

Figure 4.8. Auxiliary problems for the localized process zone model: (a) remote stress problem, and (b) crack loaded by σ_0 in the process zone and $\sigma(x)$ inside the crack. Note different (translated) coordinate set (compared to that in Figure 4.7). Also note that stress $\sigma_0 < 0$ closes the crack at the process zone.

The solution to the second problem (Figure 4.8b) is given by [*Rice*, 1968]

$$\begin{cases} \sigma_{22} - i\tau_{12} = \varphi'(z) + \overline{\Omega'(z)} + (z - \bar{z})\overline{\varphi''(z)} \\ \sigma_{11} + \sigma_{22} = 4\,\mathrm{Re}(\varphi'(z)) \end{cases} \tag{4.12}$$

where $z = x_1 + ix_2$ (Figure 4.8a) and the potentials are

$$\varphi'(z) = \Omega'(z) = \frac{\sigma_0}{\pi} \arctan \sqrt{\frac{d}{z-d}} \tag{4.13}$$

Then for the second problem, the stresses at a small distance, δ, from the crack near the process zone are obtained by substituting $z = x_1 \pm i\delta$ ($\delta > 0$) into (4.12), (4.13) and keeping two leading terms:

$$\begin{cases} \sigma_{11}(x_1 \pm i\delta) = \sigma_{22}(x_1 \pm i\delta) = \sigma_0 \left[1 - \dfrac{\delta}{\pi x_1} \sqrt{\dfrac{d}{d-x_1}} \right] + O(\delta^2) \\ \tau_{12}(x_1 \pm i\delta) = O(\delta^2) \end{cases} \quad (0 < x_1 < d,\ \delta \to 0) \tag{4.14}$$

Adding the stresses $\sigma_{xx} = \sigma_1$, $\sigma_{yy} = \sigma_3$, $\tau_{xy} = 0$ from the first problem (Figure 4.8a), the total stresses outside the process zone are given by

$$\begin{cases} \sigma_{xx} = \sigma_{11} + \sigma_1 = \sigma_{xx}^0 - (\sigma_3 - \sigma_{yy}^0) \dfrac{\delta}{\pi x_1} \sqrt{\dfrac{d}{d-x_1}} \\ \sigma_{yy} = \sigma_{22} + \sigma_3 = \sigma_{yy}^0 + (\sigma_3 - \sigma_{yy}^0) \dfrac{\delta}{\pi x_1} \sqrt{\dfrac{d}{d-x_1}} \quad (0 < x_1 < d,\ \delta \to 0) \\ \tau_{xy} = 0 \end{cases} \tag{4.15}$$

where we ignored the higher order terms.

Taking into account (4.11), we obtain from (4.15) that

$$k\sigma_{xx} < \sigma_{yy} < \sigma_{xx} \qquad (k < 1) \tag{4.16}$$

which means that the material adjacent to the process zone is in elastic state. Using (4.12),

(4.13) again, but considering now $d/|z|$ as a small parameter, the same conclusion can be obtained for the material far away. Based on (4.12), (4.13), it represents no difficulty to check numerically that Mohr-Coulomb criterion (4.4) is not satisfied in the intermediate zone. Hence, only the material inside the process zone yields, which suggests that the model is self-consistent with respect to the assumptions made on the plastic behaviour of the host material.

4.2.4 Size of the Process Zone

Since stress σ_0 in the process zone is constant and, according to (4.11), negative, that is, closing the crack (Figure 4.8b), further consideration is exactly the same as in the Dugdale model. As in the elastic case, the size of the process zone is determined by the condition (4.5) of no singularity at the end of the process zone. We have

$$K_I^{\,0} + K_I^{\,el} = 0 \tag{4.17}$$

where $K_I^{\,el}$ is the "elastic" stress intensity factor obtained by taking into account only the load $\sigma(x_1)$ inside the fracture (i.e., $\sigma_{yy} = 0$ in the process zone), and K_I^0 is the stress intensity factor obtained by considering only the stress, σ_0, inside the process zone. In the case of small scale yielding, $d << a$ and based on the solution given by Tada [*Tada et al.*, 1985], we have

$$K_I^{\,0} = -\frac{8}{\pi}\sigma_0\sqrt{d} \tag{4.18}$$

where

$$\sigma_0 = \sigma_{yy}^0 - \sigma_3 = -\frac{\sigma_3 - k\sigma_1}{1-k} \quad (\sigma_3 > k\sigma_1) \tag{4.19}$$

The length of the process zone is found by substituting (4.19) into (4.17):

$$d = \left[\frac{\pi}{8}\frac{K_I^{elastic}}{\sigma_0}\right]^2 \quad (d << a) \tag{4.20}$$

which in this form coincides with common formulation of Dugdale's model [e.g., *Rice*, 1968]. Here d is a function of the remote stresses, material properties (i.e., friction angle), fracture size (through K_I^{el}), and the fluid pressure (also through K_I^{el}).

4.2.5 Discussion

In the coordinate set shown in Figure 4.7, the condition for fluid pressure at the end of the process zone can now be expressed as

$$p(-d) = \sigma_{yy}(-d, 0) = \frac{k}{1-k}(\sigma_1 - \sigma_3) > 0 \tag{4.21}$$

and, similar to the case of cohesive materials, the fluid pressure distribution $p(x)$ can be calculated from the fluid flow equations inside the fracture and the elastic theory for material outside [*Detournay*, 2004, and references herein]. In cohesionless material, the fluid lag is not allowed, and the fluid fills the entire fracture, up to the process zone. In plane strain, the fracture width at the beginning of the process zone ($x_1 = 0$ in Figure 4.8b) is given by [*Rice*, 1968]:

$$\delta(-d) = \frac{(K_I^{elastic})^2(1-\nu^2)}{E\,|\,\sigma_0\,|} \quad (d << a) \tag{4.22}$$

where $x = -d$ corresponds to $x_1 = 0$.

The finite width and condition (4.22) are likely to be consistent, so that negative pressure at the crack tip [*Detournay*, 2004] is not expected. We do not analyze this further because a more important issue in the considered model is the criterion of fracture propagation. As well known [*Barenblatt*, 1962; *Entov*, 1999], any local criterion of crack growth requires a parameter of dimension of length. For example, this could be a critical crack opening displacement, δ_c, so that at the onset of propagation, similar to cohesive materials, $\delta(-d) = \delta_c$. A possible approach to obtain the value of δ_c could be to use controlled experimental results from hydraulic fracturing [e.g., *Chang*, 2004]. Then (4.23) could be used to compute δ_c using the known value of $K_I^{el} = K_{Ic}$ reached in the experiments. In other words, the idea would be to employ K_{Ic} as a criterion of fracture growth. Obviously this approach is fully equivalent to LEFM. In particular, in plane strain, the "apparent" fracture energy $\gamma = K_{Ic}^2(1-\nu^2)/(2E)$, and this energy is spent on the work against σ_0.

It is important to emphasize that the described localized process zone model is the simplest way to take into account that all parts of cohesionless material, including the fracture process zone, are in compression. Accordingly, this simple model yields a convenient approach for modeling fracture propagation in particulate materials. However, the physical nature of the thin, localized process zone appearing in compression is not clear. Therefore, while the fracture characteristics (e.g., δ and d) can be computed, at present, the actual propagation criterion is not constrained. Also, this model does not address the mechanism of localized fluid in-flow in cohesionless materials. In other

words, it remains unclear how the fluid is forced into the particulate material that is under compressive stresses everywhere. This is why further detailization of the model of the localized process zone does not appear warranted. Instead, these issues are considered in the next section using the shear band model.

4.3 Shear Band Model

The beveled fracture front (e.g., Figure 4.5*a*) observed in *Chang*'s [2004] tests consists of a distinct flat plane that is inclined to the direction of fracture propagation. This geometry seems to be consistent with the shear bands emanating from the fracture tip (Figure 4.9). In strain-softening materials (such as used in *Chang*'s [2004] experiments), yield of the host material adjacent to the fracture front may result in localized shear bands that are inclined with respect to the fracture direction (Figure 4.9). The discontinuity of the shear displacements between the opposing sides of a shear band can also generate a fracture aperture (i.e., an opening normal to the fracture plane) that provides the necessary volume for the fluid inflow (Figure 4.9). Therefore, this scenario [*Chang*, 2004; *Hurt et al.*, 2005] shows how the fracture propagation may occur in the state of stress, which is compressive everywhere, including near the fracture tip.

Since in physical experiments, it is quite difficult to observe the shear bands near the tip of a propagating hydraulic fracture, in this work, we conducted numerical simulation of a fracture in cohesionless material. While our conclusions appear to be rather general, in setting up the numerical model, we attempted to be as close as possible to the conditions in *Chang*'s [2004] experiments.

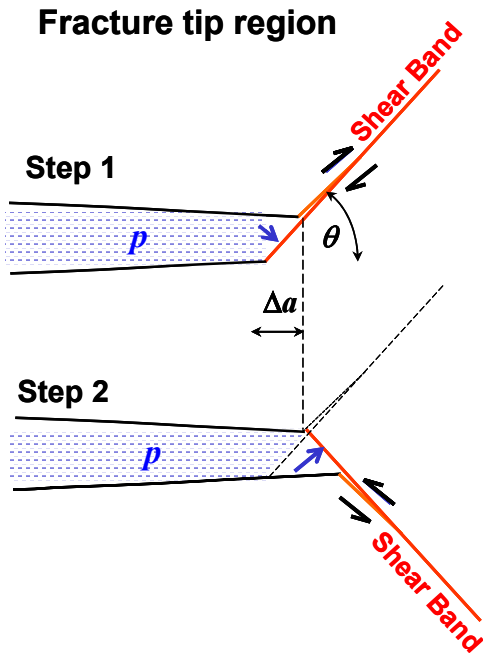

Figure 4.9. Shear band model. Here, p is the injection pressure inside the fracture, θ is the angle of the shear band with respect to the fracturing direction, and Δa is the incremental advance of the fracture in the fracturing direction.

4.3.1 Numerical Modeling

A numerical simulation using *FLAC2D* code (Fast Lagrangian Analysis of Continua) [e.g., *Detournay and Hart*, 1999; *Billaux et al.*, 2001; *Andrieux, et al.*, 2003] was conducted to gain insight into the shear band hypothesis. We used a two-dimensional numerical model of a thin fracture inside a rectangular body that is pressurized by the internal fluid pressure. In this model, we chose non-associative Mohr-Coulomb material with strain softening behaviour and ignored gravitation (since we considered stresses that are much greater than the gravitational loads).

An overall view and a magnification of the grid fragment in the vicinity of the fracture tip are shown in Figures 4.10a and 4.10b, respectively. The fracture is modeled

by a thin crack-like slot. Because of the symmetry about the *y*-axis, only one half of the domain is simulated. The dimensions of the rectangular body that contains the half-fracture are 70 cm by 60 cm. The half-fracture has a length of 4.8 cm and a width of 0.48 cm. Therefore, fracture aspect ratio (i.e., aperture / length) is 0.05. The grid used for this simulation was 160 units wide by 141 units high. The mesh in the vicinity of the fracture front is denser than that of the surrounding area. The fracture thickness is 3 elements, which sets up the characteristic scale of stress-strain concentration at the fracture tip. To avoid high stress-strain gradients within the model domain with elongated grid elements (Figure 4.10a), the simulation is stopped when the plastic strain starts developing outside the high-density grid zone with square elements.

In general, it is expected that the results of this type of modeling will be mesh dependent (although the mesh cells can sometimes be interpreted as material structural elements). Yet for establishing qualitative effects (e.g., the existence of the shear bands, not their exact physical characteristics), *FLAC* modeling appears to be quite suitable.

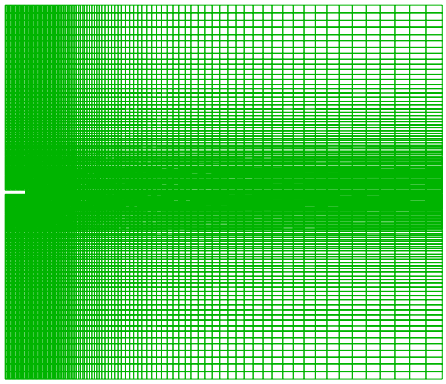

(a)

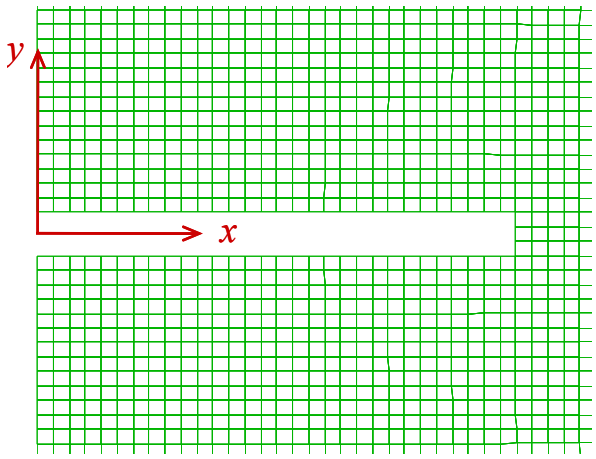

(b)

Figure 4.10. (a) Overview of the grid fragment, and (b) magnified view of the grid fragment in the vicinity of the fracture front.

The material properties used in the *FLAC* analysis are as follows: the shear modulus G = 10 MPa, Poisson's ratio $\nu = 0.3$, the peak friction angle ϕ linearly decreases from 40° to 35° in softening, the peak dilation angle ψ also linearly decreases from 5° to 0° as a result of softening. We use a bi-linear model without an ascent portion but with the residual values attained at the plastic strain of 1%. Similar to the model and fracture dimensions, these parameters are close to the properties of the materials used in the experiments of *Chang* [2004], and so are the applied remote stresses $\sigma_1 = \sigma_{xx} = 0.552$

MPa and $\sigma_3 = \sigma_{yy} = 0.276$ MPa. The internal fracture pressure has a uniform distribution along the fracture length (perimeter), which has an initial value of $p_0 = 0.276$ MPa, and increases with an increment of $\Delta p = p_0/20 = 0.0138$ MPa for each loading step. After each pressure increase (σ_1 and σ_3 are kept constant throughout the simulations), the system is equilibrated mechanically and the plastic deformation (if any) is registered.

The developed plastic zone has two localized bands that are inclined with respect to the fracture plane, which is in agreement with the shear band model hypothesized in Figure 4.6. Because the fracture is not ideally thin, plastic deformation at the tip begins not immediately, but after two to four steps of loading (depending upon the stress level in the boundary conditions). For the parameters described above, the plastic zone and the contour of the maximum shear strain increment corresponding to the internal fracture pressure $p = 0.593$ MPa are given in Figures 4.11a and 4.11b, respectively.

Therefore, while at present shear bands are rather difficult to detect in physical experiments, they manifested themselves quite noticeably in our numerical experiments. In fact, we have observed the development of similar shear bands in all numerical experiments with strain-softening materials, except when the in-situ stress was hydrostatic.

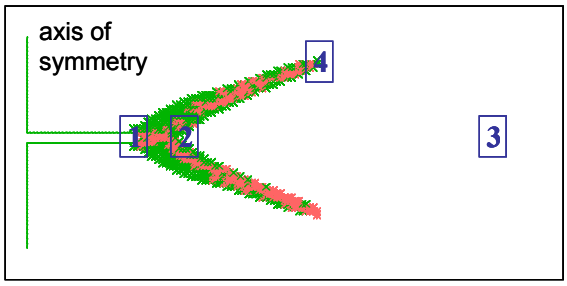

(a)

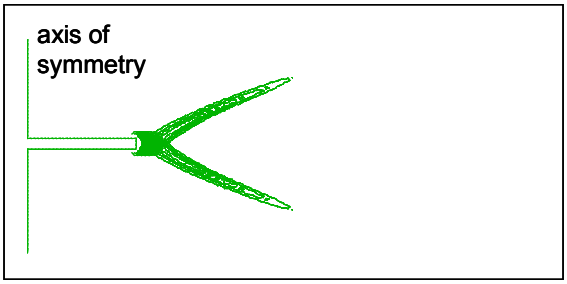

(b)

Figure 4.11. (a) Plastic zone (red color; green color shows elements that are currently elastic, but were plastic in the past), and (b) contour of maximum shear strain increment. Elements 1, 2, 3, and 4 are also shown in Figure 4.12 and described in the text.

The distributions of the stresses σ_{xx} and σ_{yy} ahead of the fracture tip at the stage of loading, which is shown in Figure 4.11, are plotted in Figure 4.12a. As expected, far from the fracture (towards the right boundary), σ_{xx} and σ_{yy} are equal to the applied in-situ stresses, σ_1 and σ_3, respectively. Closer to the fracture, both σ_{xx} and σ_{yy} first decrease (compressive stress is positive in this section), and then increase near the fracture tip (in the process zone). This stress state is consistent with that hypothesized and shown in Figure 4.4. The decrease of the stresses from element 3 to element 2 can be attributed to the material unloading (tensile strain) near the tip of the fracture due to its mode I opening. At the fracture tip (i.e., at the end of the process zone), σ_{xx} is equal to the applied pressure (as specified by the corresponding boundary condition and because the fracture

tip has the finite thickness). The stress state is compressive everywhere in the material (i.e., in all elements).

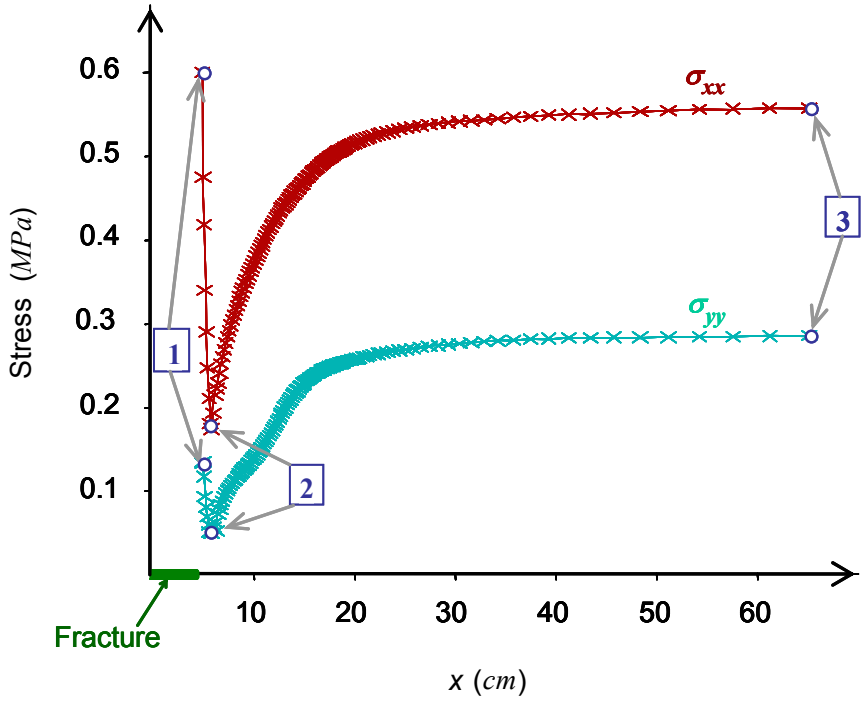

(a)

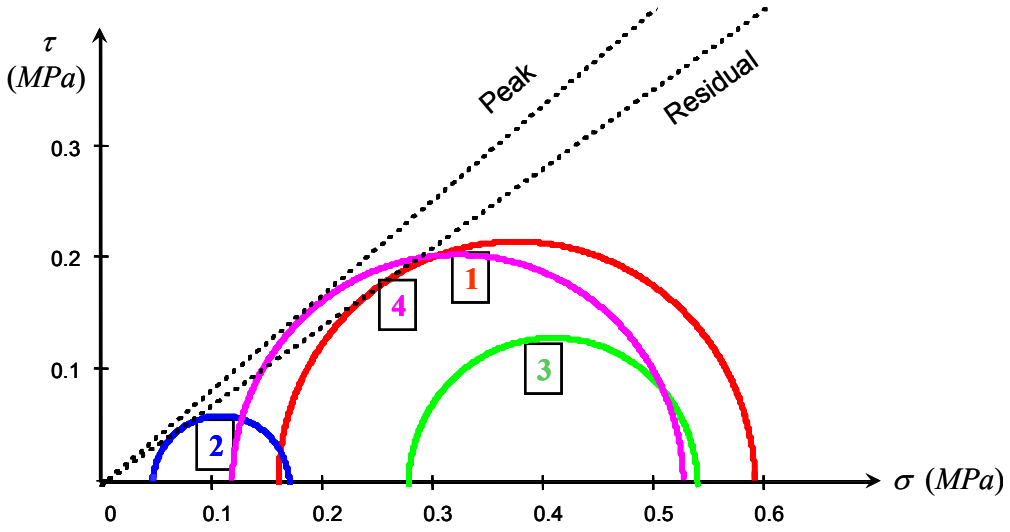

(b)

Figure 4.12. (a) Stress distribution of σ_{xx} and σ_{yy} ahead of the fracture tip, and (b) Mohr circles for elements 1, 2, 3, and 4 shown in Figure 4.11a.

The Mohr circles for all three elements as well as for element 4 (Figure 4.11a) are plotted in a σ-τ space in Figure 4.12b. The schematic locations of elements 1, 2, and 3 along the x-axis can also be seen in Figure 4.12a. For elements 1 and 2 in the plastic zone, the material yielding corresponds to the *residual* friction angle (i.e., in Figure 4.12b the Mohr circles touch the failure envelopes for $\phi = 35°$). The stresses at the very end (tip) of the upper localized plastic zone in Figure 4.10a (i.e., at the last upper right, red element 4) are σ_{xx} = 0.5113 MPa, σ_{yy} = 0.1357 MPa, and τ_{xy} = 0.08143 MPa (stresses for elements 1 through 3 can be inferred from Figure 4.11a). Note that element 4 is at *peak* load (friction) (Figure 4.12a) while element 2 at the base of the localized plastic zone is at the *residual* friction state (Figure 4.12b), which is consistent with *Palmer and Rices's* [1973] shear band model (see also *Puzrin and Germanovich* [2005]).

Therefore, the localized plastic zones in Figure 4.11 (and in similar simulations we conducted) can be interpreted as shear bands. First, the shear strain and shear displacements experience high gradients (changes) across these zones. Second, the stress state in these plastic zones does correspond to a growing shear band in the Mohr-Coulomb material with strain softening. Note, however, that our results only suggest that the shear bands should appear for the studied history of loading. Since, strictly speaking, in the real hydraulic fracturing, the history of loading is different; our numerical results do not necessarily suggest that the shear bands *always* occur. Similarly, the absence of the shear bands in the hydrostatic in-situ stress field, observed in our numerical experiments, does not mean yet that they would not appear for a history of loading different from that considered in this work.

4.3.2 Super-dislocation Model

In the model discussed by *Cherepanov* [1979], every point on the shear band is required to satisfy the Mohr-Coulomb criterion. Using Mellin transforms and the Wiener-Hopf method, he found the distribution of displacement discontinuity (i.e., the dislocation density) along the two inclined shear bands emanating symmetrically from the crack tip in Tresca material. Unfortunately, this problem becomes far less tractable analytically in the case of Mohr-Coulomb material. In this case, *Cherepanov*'s [1979] approach results in much more difficult factorization in the Wiener-Hopf method than that in the case of Tresca material. This is why we represent the shear band at the crack tip by employing the super-dislocation model [*Hills et al.*, 1996] that has its origin in the works of *Atkinson* [1966] and *Atkinson and Kay* [1971]. In the spirit of the super-dislocation model [e.g., *Atkinson and Kanninen* 1977; *Hills et al.*, 1996; *Papanastasiou and Atkinson*, 2000; *Germanovich and Wu*, 2006; Chapter 5], the shear band is modeled by a single dislocation (called "super-dislocation"). Accordingly, the *varying* displacement discontinuity along the shear band is represented by some *constant* displacement discontinuity, equal to the dislocation strength or the magnitude of the Burgers vector. The beveled fracture front observed in the laboratory experiments (Figure 4.9) is consistent with this model.

Let the dislocation (simulating the shear band) be located at the point of $z_1 = le^{i\theta}$, where l is the dislocation "length," θ is the dislocation angle, and $i^2 = -1$. When the stresses at the conjugated position, $z_2 = le^{-i\theta}$, satisfy the Mohr-Coulomb criterion, the second dislocation is assumed to appear (similar to Figure 4.9), so that the fracture propagates one step. We further assume that at this moment, the stresses at both $z_1 = le^{i\theta}$

and $z_2 = le^{-i\theta}$ satisfy the Mohr-Coulomb criterion, but with different friction angles. For the new super-dislocation to appear at z_2, the *peak* friction angle, ϕ_2, should be used. On the other hand, the dislocation at z_1 is at the residual state, and we use the *residual* friction angle, ϕ_1. This assumption of a strain-softening constitutive model is consistent with other shear band models [e.g., *Palmer and Rice*, 1973; *Puzrin and Germanovich*, 2005] and numerical simulation described in section 4.3.1. That we introduced two frictional angles and, therefore, seemingly increased the number of parameters, should not be disturbing since in material with no strain softening (i.e., characterized by a single friction angle) shear bands near the fracture tip do not propagate at all [e.g., *Papanastasiou and Thiercelin*, 1993; P*apanastasiou*, 1997].

As shown in Figure 4.12b, the stresses at the very end of the upper localized plastic zone (element 4 in Figure 4.11a) are at peak load, and element 2 at the base of the localized plastic zone is at the residual friction state. Here, by analogy, z_1 corresponds to element 4 while the stress state at z_2, where the new super-dislocation is to appear, is similar to the state at element 2 in Figure 4.12. Note, that we do not consider the growth and equilibrium of the second dislocation, but only the onset of its generation. Accordingly, our model involves a fracture with a single dislocation near its tip.

The corresponding plane strain problem is shown in Figure 4.13. Let a finite crack with the length of $2a$ be loaded by the biaxial remote stress field, σ_1 and σ_3, and internal fluid pressure, $p(x)$. As characteristic in hydraulic fracturing problems [e.g., *Hubbert and Willis*, 1957], the minimum principal in-situ stress, σ_3, is assumed to be perpendicular to the crack plane while the maximum principal in-situ stress, σ_1, acts along the crack axis.

Hereafter, the compressive stresses are negative, so that at infinity,

$$\sigma_{xx} = -\sigma_1, \quad \sigma_{yy} = -\sigma_3 \quad (\sigma_1 \geq \sigma_3 > 0) \tag{4.23}$$

As discussed above, the crack tip plastic deformation is represented by a single super-dislocation at the position $z_1 = le^{i\theta}$. The force equilibrium at the dislocation is specified by the Mohr-Coulomb failure criterion (4.4), which we write here in the usual form of

$$|\tau| + \sigma_n \tan\phi = c \quad (\sigma_n < 0) \tag{4.24}$$

where τ and σ_n are the shear and normal stresses at the dislocation position (not including the self stresses of the dislocation), and ϕ and c are the material friction angle and cohesion, respectively. We need to determine the angle, θ, strength, b, and length, l, of the dislocation.

Following *Papanastasiou and Atkinson* [2000], we have two conditions: (*i*) the mode I stress intensity factor at the fracture tip is zero, i.e., $K_I = 0$; (*ii*) the total stresses at the dislocation satisfy the Mohr-Coulomb criterion (4.24). Here, we also require condition (*iii*): the mode II stress intensity factor equals zero as well, i.e., $K_{II} = 0$. *Papanastasiou and Atkinson* [2000] followed by *Germanovich and Wu* [2006] (Chapter 5) considered two symmetrical dislocations, so that condition (*iii*) was automatically satisfied. In our case, conditions (*i*) and (*iii*) together guarantee the absence of the singularity and that the stresses are finite everywhere.

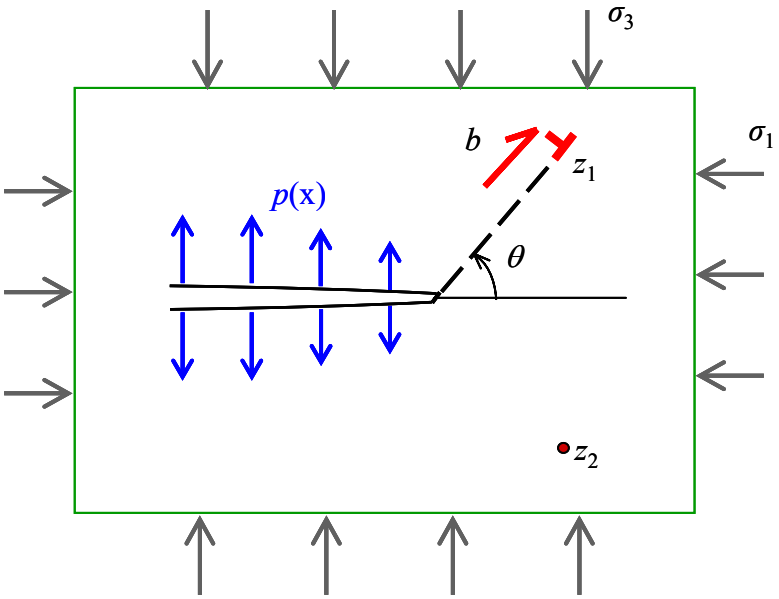

Figure 4.13. Single superdislocation model.

The solution of the problem under consideration (Figure 4.13) is well known [e.g., *Rice and Thomson*, 1974; *Weertman*, 1996]. Substituting this solution into criteria (*i*) through (*iii*), in the case of small scale yielding, $l << a$, where a is the fracture half-size (not shown in Figure 4.13), we represent the considered quantities in the following form [e.g., *Germanovich and Wu*, 2006; Chapter 5]:

$$\theta = 70.5° \tag{4.25}$$

$$\sqrt{\frac{l}{a}} = \frac{1}{\sqrt{2}} \frac{f_1(\theta) + f_2(\theta)\tan\phi}{f_0} \tag{4.26}$$

$$\frac{D}{\Delta p}\frac{|b|}{a} = \sqrt{\frac{l}{2a}} \frac{1}{3\sin\theta\cos(\theta/2)} \tag{4.27}$$

where

$$f_0 = \frac{c}{\Delta p} - \frac{\sigma_1 - \sigma_3}{2\Delta p}\sin(2\theta) + \tan\phi\left[\frac{p(0)}{\Delta p} + \frac{\sigma_1 - \sigma_3}{2\Delta p}(1 - \cos(2\theta))\right] \tag{4.28}$$

$$f_1(\theta) = \frac{3\sin^2\theta\cos^2(\theta/2) - 2}{6\sin\theta\cos(\theta/2)} \tag{4.29}$$

$$f_2(\theta) = \frac{\cos(2\theta) - 4\cos\theta + 3}{24\sin^2\theta\cos(\theta/2)} + \cos^3(\theta/2) \tag{4.30}$$

$$\Delta p = \frac{K_I}{\sqrt{\pi a}} \tag{4.31}$$

and $p(0)$ is the fluid pressure at the crack tip. The case of small scale yielding is discussed in detail in Chapter 5.

Note that (4.25) results from condition (*iii*), $K_{II} = 0$. The determined dislocation angle of 70.5º is independent of other parameters and conditions, and is the same as the angle obtained by *Atkinson and Kanninen* [1977] for *two* dislocations in Von Mises material by maximizing the extent of plasticity, l.

After the position and the strength of the dislocation are determined by (4.26) and (4.27), respectively, the stresses at the position, $z_2 = le^{-i\theta}$, can be computed. If the stresses at z_2 satisfy the Mohr-Coulomb failure criterion, the fracture propagates one step. Similar to *Atkinson and Kanninen* [1977] and *Papanastasiou and Atkinson* [2000], the increment of fracture propagation (Figure 4.12) is defind here by

$$\Delta a = b\cos\theta \tag{4.32}$$

and a new dislocation would appear at $\Delta a + le^{-i\theta}$. Therefore, we shall now check whether the stresses at $\Delta a + le^{-i\theta}$ satisfy the Mohr-Coulomb criterion. However, since $l >> b$, the

difference between $\Delta a + le^{-i\theta}$ and $le^{-i\theta}$ can be neglected (similar to *Kanninen et al.* [1977]). Therefore, we check the Mohr-Coulomb criterion at $z_2 = \overline{z_1} = le^{-i\theta}$.

As discussed above, different friction angles should be used at z_1 and z_2, i.e., the residual, ϕ_1, and the peak, ϕ_2, friction angles, respectively. Hence, the conditions at these points read

$$\begin{cases} \tau\big|_{z_1} + \sigma_n\big|_{z_1} \tan\phi_1 = c & (\tau > 0,\ \sigma_n < 0) \\ \tau\big|_{z_2} - \sigma_n\big|_{z_2} \tan\phi_2 \geq -c & (\tau < 0,\ \sigma_n < 0) \end{cases} \tag{4.33}$$

where the " > " means the absence of yielding at z_2. Note that the shear stress is positive at $z_1 = le^{i\theta}$ and negative at $z_2 = le^{-i\theta}$.

Substituting the stresses

$$\begin{cases} \sigma_n\big|_{z_1} = \dfrac{Db}{l}\left[\dfrac{\cos 2\theta - 4\cos\theta + 3}{8\sin\theta} + 3\sin\theta\cos^4\dfrac{\theta}{2}\right] - p(0) - \dfrac{\sigma_1 - \sigma_3}{2}(1 - \cos 2\theta) \\ \tau\big|_{z_1} = \dfrac{Db}{l}\left[\dfrac{3\sin^2\theta\cos^2(\theta/2)}{2} - 1\right] + \dfrac{\sigma_1 - \sigma_3}{2}\sin 2\theta \end{cases} \tag{4.34}$$

at the position $z_1 = le^{i\theta}$ and the stresses

$$\begin{cases} \sigma_n\big|_{z_2} = \dfrac{Db}{l}\left[\dfrac{3}{8}\sin(2\theta)+\dfrac{\cos\theta(\cos(2\theta)+\cos\theta)}{2\sin\theta}+3\sin\theta\cos^4(\theta/2)\right] \\ \qquad\qquad -p(0)-\dfrac{\sigma_1-\sigma_3}{2}[1-\cos(2\theta)] \\ \tau\big|_{z_2} = -\dfrac{3}{2}\dfrac{Db}{l}\sin^2\theta\cos^2(\theta/2)-\dfrac{\sigma_1-\sigma_3}{2}\sin(2\theta) \end{cases} \tag{4.35}$$

at the position $z_2 = le^{-i\theta}$ into (4.33) yields

$$p(0)\left(\tan\phi_2-\tan\phi_1\frac{h_1(\theta)+h_2(\theta)\tan\phi_2}{g_1(\theta)+g_2(\theta)\tan\phi_1}\right)\geq\frac{h_1(\theta)+h_2(\theta)\tan\phi_2}{g_1(\theta)+g_2(\theta)\tan\phi_1}g_0-h_0 \tag{4.36}$$

where

$$g_0\left(\frac{\sigma_1-\sigma_3}{2},c,\phi_1,\theta\right)=c-\frac{\sigma_1-\sigma_3}{2}\sin(2\theta)+\tan\phi_1\frac{\sigma_1-\sigma_3}{2}(1-\cos(2\theta)) \tag{4.37}$$

$$g_1(\theta)=\frac{3\sin^2\theta\cos^2(\theta/2)}{2}-1 \tag{4.38}$$

$$g_2(\theta)=\frac{\cos(2\theta)-4\cos\theta+3}{8\sin\theta}+3\sin\theta\cos^4(\theta/2) \tag{4.39}$$

$$h_0\left(\frac{\sigma_1-\sigma_3}{2},c,\phi_2,\theta\right)=c-\frac{\sigma_1-\sigma_3}{2}\sin(2\theta)+\tan\phi_2\frac{\sigma_1-\sigma_3}{2}(1-\cos(2\theta)) \tag{4.40}$$

$$h_1(\theta)=\frac{3\sin^2\theta\cos^2(\theta/2)}{2} \tag{4.41}$$

$$h_2(\theta)=\frac{3}{8}\sin(2\theta)+\frac{\cos\theta(\cos(2\theta)+\cos\theta)}{2\sin\theta}+3\sin\theta\cos^4(\theta/2) \tag{4.42}$$

Expressions (4.34) and (4.35) can be obtained based on the *Muskhelishvili* [1953] potentials described by *Germanovich and Wu* [2006] (Chapter 5). In a different form, they are also available elsewhere [*Hills et al.*, 1996; *Weertman*, 1996].

Rewriting (4.36), we find the condition for fluid pressure at the crack tip before the ejection of the next dislocation:

$$p(0) \le \frac{g_0\left[h_1(\theta)+h_2(\theta)\tan\phi_2\right]-h_0\left[g_1(\theta)+g_2(\theta)\tan\phi_1\right]}{\tan\phi_2\left[g_1(\theta)+g_2(\theta)\tan\phi_1\right]-\tan\phi_1\left[h_1(\theta)+h_2(\theta)\tan\phi_2\right]} \tag{4.43}$$

where the equal sign gives the critical fluid pressure at the crack tip corresponding to the fracture propagation. Inequality (4.43) is applicable if

$$\tan\phi_2 - \tan\phi_1 \frac{h_1(\theta)+h_2(\theta)\tan\phi_2}{g_1(\theta)+g_2(\theta)\tan\phi_1} < 0 \tag{4.44}$$

Expression (4.43) shows that the critical fluid pressure at the crack tip depends on the dislocation angle, θ (here, θ = 70.5º is constant), the remote stress field, and the material properties, i.e., cohesion, c, and peak, ϕ_2, and residual, ϕ_1, friction angles. However, the critical fluid pressure is independent of either K_I or the crack dimension, $2a$. Expression (4.43) also shows that the critical fluid pressure at the tip depends only on the differential in-situ stress, $\sigma_1 - \sigma_3$, rather than on σ_1 and σ_3 separately.

One typical result for the dependence of the critical pressure, $p(0)$, at the fracture tip on ϕ_2 is shown in (4.43) in the case of cohesionless material (ϕ_1 = 10º, 20º, 30º, c = 0). The pressure is normalized by the maximum in-situ shear stress, $\tau_{max} = (\sigma_1 - \sigma_3)/2 > 0$. Values of $p(0)$ below the plotted curve correspond to "*no yielding*" range of parameters, while values of $p(0)$ on the curve indicate that the Mohr-Coulomb criterion has been reached and the fracture now propagates. As can be seen from (4.43), values of $p(0)$ above the plotted curves are not possible for a stable fracture (propagating or not). We

observe that $p(0)$ increases with the peak friction angle, ϕ_2, which is indeed expected. As mentioned above, in perfectly plastic materials without strain softening (i.e., $\phi_1 = \phi_2$), the shear band is unlikely to appear, so that the model is applicable for $\phi_2 > \phi_1$ rather than $\phi_2 \geq \phi_1$. Note that the results presented in Figure 4.14 are valid only if condition $\sigma_n \leq 0$ of compressive stresses (otherwise the Mohr-Coulomb criterion is not applicable) and the small scale yielding condition, $(l/a)^{1/2} << 1$ (rather than $l/a << 1$ as discussed by *Germanovich and Wu* [2006] and in Chapter 5), are satisfied. In addition, the angle of $\theta = 70.5^\circ$ is always in the dislocation stability range defined by *Germanovich and Wu* [2006] (Chapter 5).

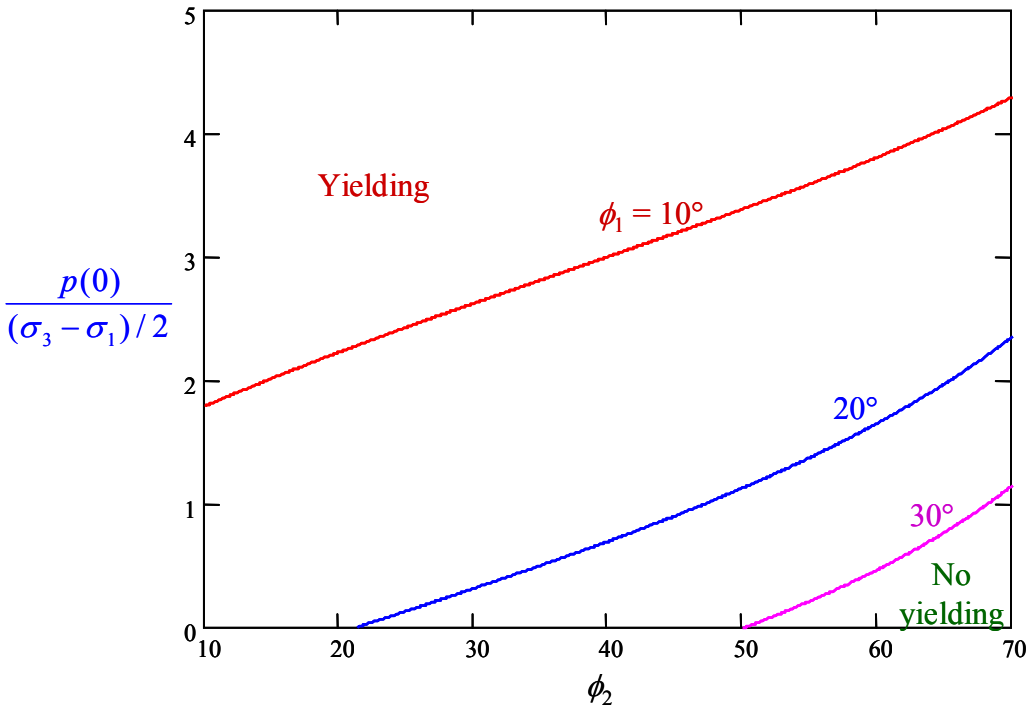

Figure 4.14. Dependence of the normalized fluid pressure at the crack tip on ϕ_2 for $\phi_1 = 10^\circ$, 20°, 30°, and $c = 0$.

While this model is simplistic, it appears to capture the main physical mechanisms associated with the shear band at the fracture tip. The model explains how

hydraulic fracture propagation is possible in the state of compressive stresses everywhere in the material, including the near tip region. Also, the advantage of (4.43) is that it actually does give a criterion of fracture growth. That is, the fracture propagates if the pressure at the tip reaches the critical value, determined by the equal sign in (4.43). Since the fracture has finite aperture at the tip, the absence of the fluid lag does not necessarily result in the singular tensile pressure at the fracture tip as it may be the case otherwise [e.g., *Detournay*, 2004].

4.4 Conclusions

Most, if not all, particulate mateials exhibit pronounced non-linear behaviour and yielding even at relatively small strains. Therefore, in order to adequately describe hydraulic fracturing in particulate materials with low or no cohesion, plasticity at the crack tip needs to be explicitly taken into account. In this work, we attempted to understand mechanism of hydraulic fracturing in uncemented sediments by considering the feasibility of two mathematical models: a localized process zone model and a super-dislocation model. The localized zone model describes yielding at the fracture tip in the Dugdale-Barenblatt manner, which is the simplest way to take into account that all parts of cohesinles particulate material are in compression, including the tip zone itself. The super-dislocation model is based on the mechanism of shear band strain localization in strain-softening materials. This mechanism also takes into account the fact that cohesionless material can not bear tension, and is in compression everywhere, including near the fracture front. In addition, this model explains the localized fluid flow into cohesionless materials. Since at present it is quite difficult to observe the shear bands

near the tip of a propagating fracture in physical experiments, to test the shear band hypothesis, we also conducted numerical simulations of the plastic deformation near the tip of a fracture in particulate material with strain softening.

Nomenclature

Latin Symbols

a	crack half-length
b	dislocation strength
c	cohesion
d	process zone size
E	Young's modulus
f_0	Function (4.28) of in-situ stresses and material properties defining dislocation length
$f_1(\theta), f_2(\theta)$	functions (4.29), (4.30) of θ defining dislocation length
G	shear modulus
$g_1(\theta), g_2(\theta)$	functions (4.38), (4.39) of θ defining stresses on the dislocation
g_0, h_0	functions (4.37), (4.40) of in-situ stresses and material properties defining stresses on the dislocation
$h_1(\theta), h_2(\theta)$	functions (4.41), (4.42) of θ defining critical pressure at the fracture tip
k	Mohr-Coulomb parameter, $(1-\sin\phi)/(1+\sin\phi)$
K_I, K_{II}	elastic mode I and II stress intensity factors
K_I^{el}	"elastic" SIF due to the "pressure" $\sigma(x) = p(x) - \sigma_3$ inside the fracture
K_I^0	SIF due to the stress, σ_0, inside the process zone (closing the fracture)
K_{Ic}	material fracture toughness
l	dislocation length

$p(x)$	pressure distribution inside the fracture
p_0	initial value of internal fracture pressure in *FLAC* simulation
$p(0)$	fluid pressure at the fracture tip
r	a small distance from the fracture tip
w	fracture aperture
x, y	rectangular coordinates
x_1, x_2	local (translated) rectangular coordinates
z	complex variable
z_1, z_2	dislocation positions

Greek Symbols

δ	a small distance from the crack sides in y direction
$\delta, \delta(-d)$	crack opening displacement at the beginng of the process zone
δ_c	critical crack opening displacement
Δa	increment of fracture propagation
Δp	internal pressure increment in *FLAC* simulation
Δp	net pressure in (4.31)
ϕ	friction angle
ϕ_1, ϕ_2	peak and residual friction angles
φ, Ω	complex potentials
θ	dislocation angle
ν	Poisson's ratio
σ_0	stress inside the process zone (closing the fracture)
σ_1, σ_3	in-situ (remote) stresses
$\sigma_{11}, \sigma_{22}, \tau_{12}$	normal and shear stresses

σ_{max}, σ_{min}	maximum and minimum principal stresses
σ_n, τ	normal and shear stresses at the dislocation position
σ_{xx}, σ_{yy}, τ_{xy}	rectangular stress components
σ_{xx}^{0}, σ_{yy}^{0}	stresses inside the process zone
σ_t	material tensile strength
τ_{max}	maximum in-situ shear stress, $(\sigma_1 - \sigma_3)/2$
ψ	peak dilation angle used in *FLAC* simulation

References

Abass, H.H., A.H. Habbtar, A. Shebatalhamd, and S. Aramco (2003), Sand control during drilling, perforation, completion and production, SPE 81492, paper presented at *the SPE 13th Middle East Oil Show & Conference*, Bahrain, 9-12 June.

Abou-Sayed, A., K. Zaki, G. Wang, F. Meng, and M. Sarfare (2004), Fracture propagation and formation disturbance during injection and frac-pack operations in soft compacting rocks, SPE 90656, paper presented at *the SPE Annual Technical Conference and Exhibition*, Houston, TX, USA, 26-29 September.

Andersen, K.H., T.A. Lunne, C.G. Rawlings, and T.H. By (1993), Hydraulic fracture as a criterion for conductor setting depth in silt-clay, *Proceedings of the 4th Canadian Conference in Marine Geotechnical Engineering, St. Johns*, *7*, 4-26.

Andrieux, P., R. Brummer, C. Detournay, and R. Hart (2003), *FLAC and Numerical Modeling in Geomechanics – 2003*, *Proceedings of the Third International FLAC Symposium*, Sudbury, Ontario, 21-24 October, Taylor & Francis, 356 pp.

Atkinson, C. (1966), The interaction between a dislocation and a crack, *Int. J. Frac. Mech.*, *2*, 567-575.

Atkinson, C., and T.R. Kay (1971), A simple model of relaxation at a crack tip, *Acta Metall. Mater.*, *19*, 679-683.

Atkinson, C., and M.F. Kanninen (1977), A simple representation of crack tip plasticity: the inclined strip yield superdislocation model, *Int. J. Fracture*, *13*, 151-163.

Barenblatt, G.I. (1962), The mathematical theory of equilibrium cracks in brittle fracture, *Adv. Appl. Mech.*, *7*, 55-129.

Berumen, S., D. Tiab, and F. Rodriguez (2000), Constant rate solutions for a fractured well with an asymmetric fracture, *J. Petrol. Sci. Eng.*, *25*, 49-58.

Bilby, B.A., A.H. Cottrell, and K.H. Swinden (1963), Spread of plastic yield from notch, *P. Roy. Soc. Lon. SER. –A*, *272*, 304-314.

Billaux, D., C. Detournay, R. Hart, and X. Rachez (2001), *FLAC and Numerical Modeling in Geomechanics – 2001*, *Proceedings of the Second International FLAC Symposium*, Lyon, France, 29-31 October, Taylor & Francis, 432 pp.

Bjerrum, L., J.K.T.L. Nash, R.M. Kennard, and R.E. Gibson (1972), Hydraulic fracturing in field permeability testing, *Geotechnique*, *22*, 319-332.

Broberg, K.B. (1999), *Cracks and Fractures*, Academic Press, San Diego, USA, 752 pp.

Broek, D. (1978), *Elementary engineering fracture mechanics*, 2nd edition, Alphen aan

den Rijn : Sijthoff & Noordhoff, 437pp.

Chang, H. (2004), Hydraulic fracturing in particulate materials, Ph.D. thesis, 267 pp., Georgia Institute of Technology, GA.

Cherepanov, G.P. (1979), *Mechanics of Brittle Fracture*, translated from the Russian by A.L. Peabody, translation edited by R. de Wit and W. C. Cooley, McGraw-Hill Inc., New York, 939 pp.

Detournay, C., and R. Hart (1999), *FLAC and Numerical Modeling in Geomechanics*, *Proceedings of the International FLAC Symposium*, Minneapolis, MN, 1-3 September, Taylor & Francis, 528 pp.

Detournay, E. (2004), Propagation regimes of fluid-driven fractures in impermeable rocks, *Int. J. Geomech.*, *4*, 35-45.

Dugdale, D. S. (1960), Yielding of steel sheets containing slits, *J. Mech. Phys. Solids*, *8*, 100-104.

Economides, M.J., and K.G. Nolte (2000), *Reservoir Stimulation*, 3rd Edition, John Wiley & Sons, LTD.

Entov, V. (1999), Microstructural aspect of fracture mechanics, *Int. J. Fracture*, *99*, 13-23.

Gerberich, W.W., P.G. Marsh, and J.W. Hoehn (1994), Hydrogen induced cracking mechanisms – Are there critical experiments? *Hydrogen Effects in Materials*, *Proceedings for the Fifth International Conference on the Effect of Hydrogen on the Behavior of Materials*, Moran, WY, 11-14 Sep, 539-551.

Germanovich, L.N., and R. Wu (2006), On representation of crack-tip plasticity in Mohr-Coulomb materials, *Int. J. Fracture*, in preparation.

Hills, D.A., P.A. Kelly, D.N. Dai, and A.M. Korsunsky (1996), *Solutions of Crack Problems: The Distributed Dislocation Technique*, Kluwer Academic Publishers, the Netherlands.

Howard, G.C., and C.R. Fast (1970), *Hydraulic Fracturing*, American Institute of Mining, Metallurgical, and Petroleum Engineers, Inc., Monograph, *2*, Henry L. Doherty Series.

Hubbert, M.K., and D.G. Willis (1957), Mechanics of hydraulic fracturing, *J. Petrol. Techol.*, *9*, 153-166.

Hurt, R.S., R. Wu, L.N. Germanovich, H. Chang, and P. van Dyke (2005), On mechanisms of hydraulic fracturing in cohesionless materials, *EOS Trans. AGU*, *86*(*52*), *Fall Meet. Suppl.*, *Abstract H41B-0416*.

Jagannadhan, K., and M.J. Marcinkowski (1982), *Unified Theory of Fracture*, Aedermonnsdorf: Trans Tech, Materials science survey, No.1.

Jaworski, G.W., J.M. Duncan, and H.B. Seed (1981), Laboratory study of hydraulic fracturing, *J. Geotech. Eng. – ASCE*, *107*, 713-733.

Kanninen, M.F., C. Atkinson, and C.E. Feddersen (1977), A fatigue crack-growth analysis method based on a simple representation of crack-tip plasticity, in *Cyclic Stress-Strain and Plastic Defromation Aspects of Fatigue Crack Growth, ASTM-STP*, *637*, 122-140.

Kanninen, M.F., and C. Atkinson (1980), Application of an inclined-strip-yield crack tip plasticity model to predict constant amplitude fatigue crack growth, *Int. J. Fracture.*, *16*, 53-69.

Leonov, M.Y., D.M. Vitvitskiy, and S. Y. Yarema (1963), Plasticity bands in extension of plates with crack concentrators, *DAN SSSR*, *148*.

Lo, K.Y., and K. Kaniaru (1990), Hydraulic fracture in earth and rock-fill dams, *Can. Geotech. J.*, *27*, 496-506.

Murdoch, L.C. (1993a), Hydraulic fracturing of soil during laboratory experiments, Part I Methods and observations, *Geotechnique*, *43*, 255-265.

Murdoch, L.C. (1993b), Hydraulic fracturing of soil during laboratory experiments, Part II Propagations, *Geotechnique*, *43*, 267-276.

Murdoch, L.C. (1993c), Hydraulic fracturing of soil during laboratory experiments, Part III Theoretical analysis, *Geotechnique*, *43*, 277-287.

Murdoch, L.C. (2002), Mechanical Analysis of Idealized Shallow Hydraulic Fracture, *J. Geotech. Geoenviron.*, *128*, 488-495.

Murdoch, L.C., and W.W. Slack (2002), Forms of hydraulic fractures in shallow fine-grained formations, *J. Geotech. Geoenviron.*, *128*, 479-487.

Muskhelishvili, N.I. (1953), *Some Basic Problems of the Mathematical Theory of Elasticity*, P. Noordhoff Ltd., Groningen.

Ostermeier, R.M., J.H. Pelletier, C.D. Winker, J.W. Nicholson, F.H. Rambow, and K.M. Cowan (2000), Dealing with shallow-water flow in the deepwater Gulf of Mexico, *Proceedings of the Annual Offshore Technology Conference*, *1,* 75-86.

Palmer, A.C., and J.R. Rice (1973), The growth of slip surfaces in the progressive failure of over-consolidated clay. *P. Roy. Soc. Lon. SER. –A*, *332*, 527-548.

Papanastasiou, P. (1997), The influence of plasticity in hydraulic fracturing, *Int. J. Fracture*, *84*, 61-79.

Papanastasiou, P., and M. Thiercelin (1993), Influence of inelastic rock behaviour in hydraulic fracturing, *Int. J. Rock Mech. Min. Sci.*, *30*, 1241-1247.

Papanastasiou, P., and C. Atkinson (2000), Representation of crack-tip plasticity in pressure sensitive geomaterials, *Int. J. Fracture.*, *102*, 271-286.

Puzrin, A.M., and L.N. Germanovich (2005), The mechanism of tsunamigenic landslides, *Geotechnical Special Publication*, n 143, *Geomechanics: Testing, Modeling, and Simulation – Proceedings of the First Japan-U.S. Workshop on Testing, Modeling, and Simulation*, 421-428.

Rice, J.R. (1968), Mathematical analysis in the mechanics of fracture, *Fracture*, *An Advanced Treatise*, H. Liebowitz, ed., Academic, New York, II, 3, 191-311.

Rice, J.R., and R. Thomson (1974), Ductile versus brittle behavior of crystals, *Philos. Mag.*, *29*, 73-97.

Sadananda, K., and D.-N. V. Ramaswamy (2001), Role of crack tip plasticity in fatigue crack growth, *Philos. Mag.*, *81*, 1283-1303.

Sasaki, S. (1998), Characteristics of microseismic events induced during hydraulic fracturing experiments at the Hijiori hot dry rock geothermal energy site, Yamagata, Japan, *Tectonophysics*, *289*, 171-188.

Shiue, S.-T., and S. Lee (1992), The effect of superdislocation on fracture: Dislocation-free zone in the front of a semi-infinite crack tip, *J. Appl. Phys.*, *72*, 2209-2214.

Soga, K., S.K.A. Au, M.R. Jafari, and M.D. Bolton (2004), Laboratory investigation of multiple grout injections into clay, *Géotechnique*, *54*, 81-90.

Tada, H., P.C. Paris, and G.R. Irwin (1985), *The Stress Analysis of Cracks Handbook*, 2nd ed., Paris Productions Incorporated, St. Louis, MO.

Warner, J. (1997), Compaction grouting mechanism – What do we know? *Grouting: Compaction/Remediation/Testing*, Geotechnical Special Publication, *66*, ASCE, New York, 1-17.

Weertman, J. (1996), *Dislocation Based Fracture Mechanics*, World Scientific, River Edge, NJ, 524 pp.

CHAPTER 5
A SUPER-DISLOCATION MODEL OF CRACK-TIP PLASTICITY IN MOHR-COULOMB MATERIALS

Abstract. The super-dislocation model is an important tool to model crack-tip plasticity in different settings. In this chapter, we reassess the super-dislocation model recently developed by *Papanastasiou and Atkinson* [2000] for simple representation of plastic deformation at the tip of hydraulic fractures in such pressure sensitive materials as soft sediments in hydrocarbon reservoirs. We show that in the case of the small scale yielding, the conventional approach of determining the dislocation angle by maximizing the crack opening displacement, dislocation strength, or dislocation length is only effective for frictionless materials as originally suggested by *Atkinson and Kanninen* [1977]. As an alternative, we propose a criterion based on the maximum shear stress at the dislocation position. We show that maximizing the shear stress on the dislocation makes the super-dislocation model consistent for a wide range of pressure sensitive cohesive-frictional materials.

5.1 Introduction

Formation of the macroscopic plastic zone at the crack tip is a complex phenomenon observed in many engineering and natural materials. Following *Atkinson* [1966] and *Atkinson and Kay* [1971], *Atkinson and Kanninen* [1977] introduced a model based on the dislocation theory for simple representation of plastic deformation at the crack tip. In this model, which is now known as the *super-dislocation* model [*Hills et al.*,

1996], the plasticity associated with the crack tip is simulated by a pair of appropriately positioned dislocations (Figure 5.1) with cumulative Burgers vectors and a yield condition enforced on their places. These dislocations are called "super-dislocations" meaning that they are equivalent or effective dislocations defined at the scale of the fracture process zone. Their effect on the fracture tip is approximately the same as that of numerous dislocations distributed at the microscale and characterizing plastic behaviour of the material hosting the fracture [*Weertman*, 1996]. Although this simple representation has its limitations (e.g., in predicting the plastic zone size [*Atkinson and Kanninen*, 1977]), its mathematical simplicity and the ability to directly and accurately evaluate the crack tip opening displacement [*Hills et al.*, 1996] are appealing. Hence, the super-dislocation model has been widely used to simulate the plastic zones at crack tips in Von Mises materials [*Kanninen et al.*, 1977; *Kanninen and Atkinson*, 1980; *Jagannadhan and Marcinkowski*, 1982; *Shiue and Lee*, 1992; *Gerberich et al.*, 1994; *Sadananda and Ramaswamy*, 2001].

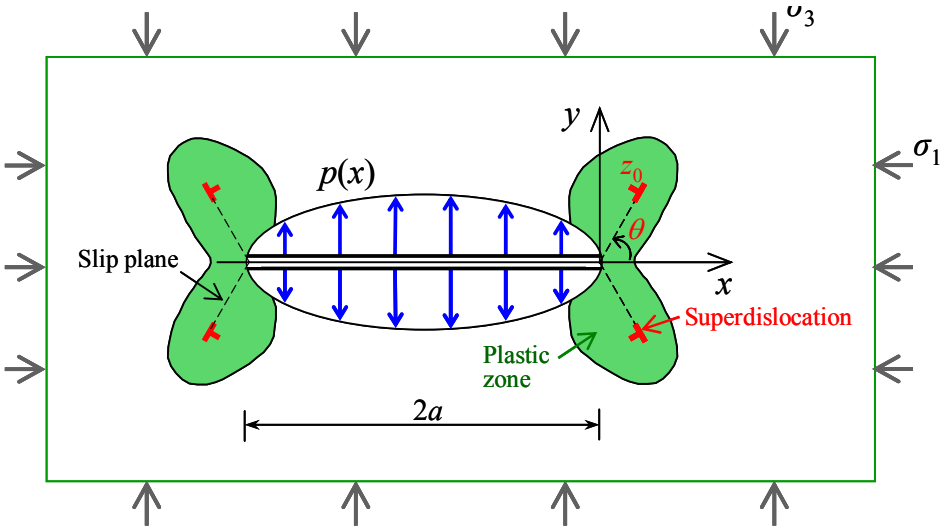

Figure 5.1. Schematic representation of the super-dislocation model (modified after *PA*).

Motivated by the potential applications of the super-dislocation model to the design of hydraulic fracturing in weak rock reservoirs, *Papanastasiou and Atkinson* [2000] extended the super-dislocation model to represent the crack tip plastic zone in Mohr-Coulomb pressure sensitive materials. The hydraulic fracturing technique is critically important for production of hydrocarbons from unconsolidated or weakly consolidated petroleum formations [e.g., *Ayoub et al.*, 1992; *Hannah et al.*, 1994; *Roodhart et al.*, 1994; *Smith and Hannah*, 1996] while the corresponding "soft" rocks are typically modeled by the macroscopic Mohr-Coulomb continua [*Charlez*, 1991, 1997]. In addition, hydraulic fracturing in Mohr-Coulomb materials is important for such applications as the stimulation of geothermal reservoirs [*Sasaki*, 1998; *Berumen et al.*, 2000], remediation of soil and groundwater aquifers [*Murdoch and Slack*, 2002; *Bradner and Murdoch*, 2005], injection of wastes [*Hunt et al.*, 1994; *Hainey et al.*, 1999; *Guo et al.*, 2004], and measurement of in-situ stresses [*Hayashi et al.*, 1997; *Raaen et al.*, 2001]. Finally, if the material exhibits postpeak softening behaviours, under certain conditions [*Chang*, 2004; *Hurt et al.*, 2005], the plastic zones at the tips of hydraulic fractures tend to localize in thin shear bands. Then, representing these bands by single dislocations become even more appealing from the physical standpoint since in this case we simply model the distributed displacement discontinuity by a slip of a constant magnitude.

Based on parametric studies, *Papanastasiou and Atkinson* [2000] (hereafter referred to as *PA*) concluded that the super-dislocation model can capture the essentials of the crack tip plasticity in Mohr-Coulomb materials. Due to the practical importance of this conclusion, in this work we reassess the super-dislocation model proposed by *PA*. We correct an algebraic mistake in their derivations and reexamine their numerical results,

which in turn, changes their conclusion. Nevertheless, we show that *PA*'s formulation of the super-dislocation model can be adjusted and become applicable to a wide range of Mohr-Coulomb materials. Also, we obtain a more general, closed-form solution for the case of arbitrary internal pressure inside the fracture (*PA* considered constant pressure distribution). While straightforward, this generalization may be important for modeling hydraulic fractures in such pressure sensitive cohesive-frictional materials, as weakly-cemented sediments, which are characteristic for many hydrocarbon reservoirs [e.g., *Ayoub et al.*, 1992; *Hannah et al.*, 1994; *Roodhart et al.*, 1994; *Smith and Hannah*, 1996; *Charlez*, 1997].

5.2 The Super-dislocation Model

5.2.1 Mathematical Background

Consider the same plane strain problem as that addressed by *PA* (Figure 5.1). Let a finite crack with the length 2*a* be loaded by the biaxial remote (in-situ) stress field and internal fluid pressure. As characteristic in hydraulic fracturing problems [*Hubbert and Willis*, 1957], the minimum principal in-situ stress, σ_3, is assumed to be perpendicular to the crack plane while the maximum principal in-situ stress, σ_1, acts along the crack axis. Hereafter, the compressive stresses are negative, so that at infinity,

$$\sigma_{xx} = -\sigma_1, \quad \sigma_{yy} = -\sigma_3 \quad (\sigma_1 \geq \sigma_3 > 0) \tag{5.1}$$

The crack tip plastic deformation is represented by two pairs of dislocations. Following *PA*'s paper, the force equilibrium at the dislocation will be specified by the Mohr-Coulomb failure criterion

$$|\tau| + \sigma_n \tan\phi = c \quad (\sigma_n < 0) \tag{5.2}$$

where τ and σ_n are the shear and normal stresses at the dislocation position (not including the self stresses of the dislocation), and ϕ and c are the material friction angle and cohesion, respectively. Due to the symmetry, we further apply criterion (5.2) only to the upper right dislocation shown in Figure 5.1 at the position $z_0 = le^{i\theta}$, where l is the dislocation "length," θ is the dislocation angle, and $i^2 = -1$. At this position, the physically meaningful dislocation strength is positive (we adopt the usual sign convention; e.g., *Hills et al.* [1996]), so that the resulting slip plane relaxes the singularity at the crack tip [e.g., *Cherepanov et al.*, 1995]. Then, the complex Burgers vector of the dislocation can be represented as $b = b_1 + ib_2 = |b|e^{i\theta}$ where $b_2 > 0$ for $0 < \theta < \pi$ while $b_1 \geq 0$ for $0 < \theta \leq \pi/2$ and $b_1 < 0$ for $\pi/2 < \theta < \pi$.

According to the *PA*'s super-dislocation model, the position, angle and strength of the dislocations are determined by the following governing conditions:

(*i*) The total stress intensity factor at the crack tip is zero.

(*ii*) The total stresses at the dislocations satisfy the Mohr-Coulomb criterion (5.2).

(*iii*) The total crack opening displacement is maximized.

As it will be discussed in detail below, the displacement criterion (*iii*) cannot be satisfied in most cases.

Since the crack and dislocations are in an elastic material in which plastic zones are replaced by the dislocations, we follow *PA* and evaluate the stress field by

superimposing the well-known solutions of the following auxiliary problems:

1. Problem *A*: remote stress field (no crack present; Figure 5.2a).
2. Problem *B*: crack loaded by the internal net pressure, $\sigma(x) = p(x) - \sigma_3$ (no dislocations present; Figure 5.2b).
3. Problem *C*: unloaded crack in the field of the dislocations (Figure 5.2c).

The *exact* solutions to problems *B* and *C* can be expressed in the form of complex potentials of the elastic theory [*Muskhelishvili*, 1953]. However, in most publications on the super-dislocation model, the case of *small scale yielding* attracted the main interest [*Atkinson and Kanninen*, 1977; *Kanninen et al.*, 1977; *Kanninen and Atkinson*, 1980; *Shiue and Lee*, 1992; *Cherepanov et al.*, 1995; *Papanastasiou and Atkinson* 2000; *Sadananda and Ramaswamy*, 2001]. In this case, the plastic zone is assumed to be much smaller than the crack size and, accordingly, $l << a$. The most straightforward and mathematically appropriate way to arrive at this case is *first* to obtain the exact solution, and *then* to extract an asymptotic expression for $l/a \rightarrow 0$ [e.g., *Atkinson and Kanninen*, 1977]. Yet, this procedure may be rather cumbersome and, more importantly, requires the exact knowledge of the entire fracture geometry. This is why it is rather tempting to make the limit transition, $l/a \rightarrow 0$, *before* solving the problem and to consider a *semi-infinite* crack with (super) dislocations near its tip [e.g., *Lin and Thomson*, 1986; *Cherepanov et al.*, 1995; *Sadananda and Ramaswamy*, 2001]. In this case, the fracture load could be conveniently characterized by a parameter such as stress intensity factor (SIF). To a great degree, the super-dislocation model loses its appeal if the full fracture geometry has to be accounted for to represent crack tip plasticity. Also, it seems unlikely that such a simple

representation “works” when the plastic zone is comparable to the fracture size.

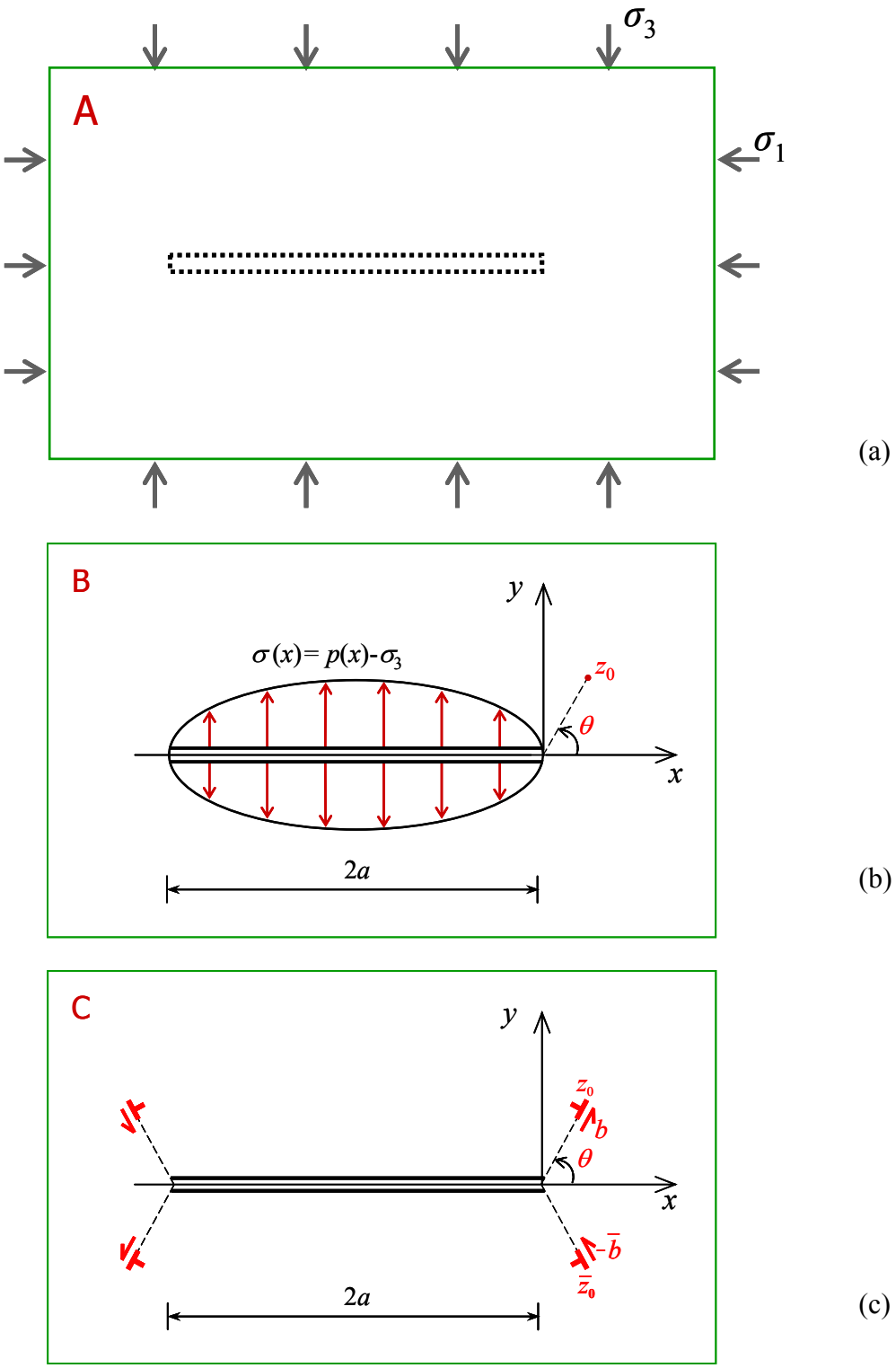

Figure 5.2. Auxiliary problems: (a) remote stress problem, (b) crack with internal pressure, and (c) crack interacting with dislocations.

Similar to *PA* and others, hereafter, we consider small scale yielding $l << a$. Accordingly, below we keep the first *two* leading terms in the corresponding asymptotic expansions. These terms are of the order of $(l/a)^{1/2}$ and $O(1)$, respectively, and, in general, the second term should be kept since the right hand side in (5.2) (i.e., c) has the same order. In addition, in the case of Mohr-Coulomb material, to ensure the normal stress, σ_n, in (5.2) to be negative, keeping only the first, $O((l/a)^{1/2})$, term is insufficient and, as will be shown below, the *second* term is required. *PA* kept both terms in Problem *B*, while they only kept the first term in Problem *C*. This is why after briefly addressing Problem *B*, we consider Problem *C* in more detail. Keeping all second-order terms allows evaluating the asymptotic consistency of the super-dislocation model proposed by *PA*.

We start with Problem *B* for a crack loaded by the non-uniform surface tractions $\sigma(x) = p(x) - \sigma_3$ (Figure 5.2b). Near the crack tip, the *Muskhelishvili* [1953] potential can be expressed as

$$\Phi_{el}(z) = \frac{K_I^{el}}{2\sqrt{2\pi z}} - \frac{\sigma(0)}{2} + O\left(\sqrt{\frac{z}{a}}\right)\sigma_* \qquad (|z| << a) \tag{5.3}$$

where

$$K_I^{el} = (p_* - \sigma_3)\sqrt{\pi a} \tag{5.4}$$

is the mode I SIF,

$$p_* = \sigma_3 + \frac{1}{\pi a}\int_{-2a}^{0} \sigma(x)\sqrt{\frac{2a+x}{-x}}dx \qquad (5.5)$$

is a certain characteristic (scaling) pressure driving hydraulic fracture, and

$$\sigma_* = \frac{1}{4a}\int_{-2a}^{0} \frac{\sigma(x)(x-2a)}{\sqrt{-x(2a+x)}}dx - 2a\int_{-2a}^{0} \frac{\sigma(x)-\sigma(0)}{x\sqrt{-x(2a+x)}}dx \qquad (5.6)$$

is another characteristic crack load in Problem *B*. Note that if $\sigma(x)$ satisfies Hölder's condition, $|\sigma(x_1) - \sigma(x_2)| = O(|x_1 - x_2|^{\gamma})$, where $0 < \gamma \le 1$ is a constant, in a vicinity of $x = 0$, the second integral in (5.6) converges in a regular sense [e.g., *Muskhelishvili*, 1953]. Since all differentiable functions satisfy Hölder's condition [*Muskhelishvili*, 1953], this is not a serious limitation in realistic hydraulic fracturing problems where pressure is a differentiable function in the majority of cases. To simplify notation, we further omit such dimensional factors as σ_*. Then, in Problem *B*, stresses on the place of the dislocation located at z_0 in Problem *C* (Figure 5.2b) are given by

$$\begin{cases} \sigma_n^B = \dfrac{K_I^{el}}{(2\pi l)^{1/2}}\cos^3\dfrac{\theta}{2} - [p(0)-\sigma_3] + O\left(\sqrt{\dfrac{l}{a}}\right) \\ \tau^B = \dfrac{K_I^{el}}{(2\pi l)^{1/2}}\dfrac{1}{2}\sin\theta\cos\dfrac{\theta}{2} + O\left(\sqrt{\dfrac{l}{a}}\right) \end{cases} \quad (l << a) \qquad (5.7)$$

Here we employed the *Muskhelishvili* [1953] expressions for normal, $\sigma_n = \sigma_{rr}$, and shear, $\tau = \tau_{r\theta}$, stresses at $z = x + iy = re^{i\theta}$:

$$\sigma_n + i\tau = \Phi_c(z) + \overline{\Phi_c(z)} + \left[\overline{\Phi}_c(z) - \Phi_c(z) - (z-\bar{z})\Phi_c'(z) + \Gamma'\right] e^{2i\theta} \qquad (5.8)$$

where $\Gamma' = 0$ in the case of zero stresses at infinity. Expressions (5.7) represent the first two asymptotic terms for a stress state near the tip of a mode I crack [*Broberg*, 1999].

Noting that K_I^{el} is independent of l, we formally have from (5.4) – (5.6) that

$$\frac{K_I^{el}}{\sqrt{\pi a}} = O(1), \qquad \frac{K_I^{el}}{\sqrt{\pi l}} = O\left(\sqrt{\frac{a}{l}}\right) \qquad (l << a) \qquad (5.9)$$

Hereafter, we assume that a is constant when $l \to 0$ and that the pressure distribution, $p(x)$, in (5.5) and (5.6) [$\sigma(x) = p(x) - \sigma_3$] is either independent of a or this dependence is such that relations (5.9) hold when l is fixed and $a \to \infty$ (i.e., in the limit of the semi-infinit crack). Problem *C* includes two parts: stresses due to the dislocations alone and stresses due to the interaction between the dislocations and the crack. First, consider an elastic problem for the unloaded crack interacting with a single dislocation located at $z_0 = le^{i\theta}$ (Figure 5.3). The *Muskhelishvili* [1953] potential produced by the crack loaded by the non-uniform surface tractions canceling the corresponding stresses generated by this dislocation on the crack plane is readily available [e.g., *Atkinson and Kanninen*, 1977; *Cherepanov et al.*, 1995]. Here we write it in the convenient form that does not contain singularities at z_0 and $\bar{z}_0$:

$$\Phi_c(z)=\frac{Db}{2i\sqrt{z(z+2a)}}\left[2-\frac{z+z_0+2a}{\sqrt{z(z+2a)}+\sqrt{z_0(z_0+2a)}}-\frac{z+\bar{z}_0+2a}{\sqrt{z(z+2a)}+\sqrt{\bar{z}_0(\bar{z}_0+2a)}}\right]$$
$$-\frac{D\bar{b}(z_0-\bar{z}_0)a^2}{2i\sqrt{z\bar{z}_0(z+2a)(\bar{z}_0+2a)}\left[\sqrt{z\bar{z}_0(z+2a)(\bar{z}_0+2a)}+z\bar{z}_0+a(z+\bar{z}_0)\right]} \qquad (5.10)$$

where $D = E[8\pi(1-\nu^2)]^{-1}$, E is the Young's Modulus, and ν is the Poisson's ratio.

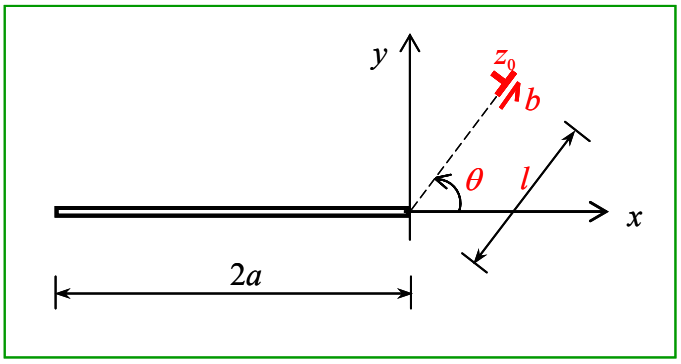

Figure 5.3. An elastic problem of an unloaded crack interacting with a single dislocation of a given strength, b.

Since in the Mohr-Coulomb condition (5.2) (i.e., condition (*ii*)), we are only interested in the stresses at $z = z_0$ (or $z = \bar{z}_0$), we first find an asymptotic expression for potential (5.10) in the case of z that is of the order of z_0 ($z \sim z_0$). Keeping two leading terms in (5.10), we write for such z and small scale yielding:

$$\Phi_c(z) = -\frac{Db}{2i}\frac{1}{z}\left[\frac{\sqrt{z}}{\sqrt{z}+\sqrt{z_0}} + \frac{\sqrt{z}}{\sqrt{z}+\sqrt{\bar{z}_0}} + \frac{\bar{b}}{b}\frac{(z_0-\bar{z}_0)\sqrt{z}}{2\sqrt{\bar{z}_0}\left(\sqrt{z}+\sqrt{\bar{z}_0}\right)^2} - \sqrt{\frac{2z}{a}} + O\left(\frac{l}{a}\right)\right] \quad (l/a \ll 1, \quad r/a \ll 1, \quad l/r \sim 1) \tag{5.11}$$

Note that $(2z/a)^{1/2}$ term in (5.11) gives the *second* order correction to the semi-infinite crack (given by other terms in (5.11)) in the problem of the crack-dislocation interaction.

Since $l/a \ll 1$, the two dislocations near the left crack tip (Figure 5.2c) have a negligible effect on the stresses in the vicinity of the right crack tip (i.e., they contribute only to the higher order terms $O(l/a)$). The complex potentials of the dislocation located at $\bar{z}_0 = le^{-i\theta}$ with the Burgers vector of $-\bar{b} = -b_1 + ib_2$ (Figure 5.2c) are given by (5.10) and (5.11) with the corresponding substitutions. Inserting (5.11) and the potential corresponding to the dislocation at $\bar{z}_0$ into (5.8) gives the stresses due to the interaction between the dislocations and the crack. Adding stresses

$$\sigma_n = \frac{D|b|}{l}\left[\cot\theta + \sin(2\theta)\right], \qquad \tau = -\frac{D|b|}{l}\cos(2\theta) \tag{5.12}$$

induced by the dislocation at $\bar{z}_0$ directly at z_0 [*Hills et al.*, 1996], we arrive at the total stresses on the plane of the dislocation at z_0 in Problem *C*:

$$\begin{cases} \sigma_n^C = \dfrac{D|b|}{l}\left[\cot\theta + \sin(2\theta) - \dfrac{\sin(\theta/2)(9\cos^2\theta + 12\cos\theta - 1)}{4\cos(\theta/2)}\right. \\ \qquad\qquad \left. + 2\sin\theta\cos^3(\theta/2)\sqrt{\dfrac{2l}{a}} + O\left(\dfrac{l}{a}\right)\right] \qquad (l << a) \\ \tau^C = \dfrac{D|b|}{l}\left[-1 + \sin^2\theta\cos(\theta/2)\sqrt{\dfrac{2l}{a}} + O\left(\dfrac{l}{a}\right)\right] \end{cases} \tag{5.13}$$

Since per condition (*i*), the total SIF at the crack tip is zero, the SIF, K_I^d, caused by the two dislocations at the right crack tip in Problem *C* should cancel the SIF, K_I^{el}, in Problem B ($K_{II} = 0$ in both problems due to symmetry):

$$K_I^{el} + K_I^d = 0 \tag{5.14}$$

where the dislocation induced SIFs can be obtained from the general formula [e.g., *Broberg*, 1999]

$$K_I - iK_{II} = \lim_{z\to 0}[2\sqrt{2\pi z}\Phi(z)] \tag{5.15}$$

and due to symmetry, the mode I SIFs caused by the dislocations located at z_0 and $\bar{z}_0$ are equal. While the exact value of K_I for a crack-dislocation configuration shown in Figure 5.3 is well known [e.g., *Atkinson and Kanninen*, 1977; *Weertman*, 1996], it is more convenient to obtain an asymptotic expression for K_I^d by directly substituting (5.10) into (5.15), setting z to zero, and considering that $l << a$. This immediately results in

$$\frac{1}{2}K_I^d = -\frac{2\pi D|b|\sin\theta}{(2\pi l)^{1/2}}\left[3\cos(\theta/2) - \sqrt{\frac{2l}{a}} + O\left(\frac{l}{a}\right)\right] \quad (l << a) \tag{5.16}$$

For a given θ ($0 < \theta < \pi$) and sufficiently small l, $K_I^d < 0$ in (5.16). Therefore, a positive K_I^{el} can indeed be cancelled by a negative K_I^d. Inserting (5.16) into (5.14), we obtain

$$\frac{D|b|}{l} = \frac{K_I^{el}}{(2\pi l)^{1/2}} \frac{1}{6\sin\theta\cos(\theta/2)} \left[1 + \boxed{\frac{1}{3\cos(\theta/2)}\sqrt{\frac{2l}{a}}} + O\left(\frac{l}{a}\right) \right] \quad (l << a) \qquad (5.17)$$

In (5.17), the first term agrees with the result of *PA* (equation (3) in their paper), which in turn, coincides with that obtained by *Atkinson and Kanninen* [1977]. Hereafter, the additional second order terms are shown in a box.

Expression (5.17) gives the relationship between $|b|$ and l, which depends not only upon K_I^{el}, but also on the crack dimension, a (in the second order). Substituting (5.17) into (5.13), we arrive at the two-term asymptotic expansions for stresses:

$$\begin{aligned} \sigma_n^C = & \left[\frac{K_I^{el}}{(2\pi l)^{1/2}} + \boxed{\frac{K_I^{el}}{(\pi a)^{1/2}} \frac{1}{3\cos(\theta/2)}} \right] \\ & \times \left[\frac{\cot\theta + \sin(2\theta)}{6\sin\theta\cos(\theta/2)} - \frac{9\cos^2\theta + 12\cos\theta - 1}{48\cos^2(\theta/2)} + O\left(\frac{l}{a}\right) \right] \quad (l << a) \\ & + \boxed{\frac{K_I^{el}}{3(\pi a)^{1/2}} \cos^2\frac{\theta}{2}} \end{aligned} \qquad (5.18)$$

$$\begin{aligned} \tau^C = & -\left[\frac{K_I^{el}}{(2\pi l)^{1/2}} + \boxed{\frac{K_I^{el}}{(\pi a)^{1/2}} \frac{1}{3\cos(\theta/2)}} \right] \left[\frac{1}{6\sin\theta\cos(\theta/2)} + O\left(\frac{l}{a}\right) \right] \\ & + \boxed{\frac{K_I^{el}}{(\pi a)^{1/2}} \frac{\sin\theta}{6}} \quad (l << a) \end{aligned} \qquad (5.19)$$

where the first and second "boxed" terms in each expression are due to the $(l/a)^{1/2}$ and

$(z/a)^{1/2}$ terms in (5.17) and (5.11), respectively.

In Problem A, the remote stress field is given by (5.1), so that on the plane of the dislocation at z_0,

$$\sigma_n^A = -\frac{\sigma_1+\sigma_3}{2} + \frac{\sigma_1-\sigma_3}{2}\cos(2\theta), \quad \tau^A = \frac{\sigma_1-\sigma_3}{2}\sin(2\theta) \quad (\sigma_1 \geq \sigma_3 > 0) \tag{5.20}$$

Taking into account (5.9), the superposition of problems A, B, and C (expressions (5.7), (5.18), and (5.20)) gives the normal

$$\sigma_n = \frac{K_I^{el}}{\sqrt{2\pi a}}\left[\sqrt{\frac{a}{l}} + \frac{\sqrt{2}}{3\cos(\theta/2)}\right] f_2(\theta) - p(0) - \frac{\sigma_1-\sigma_3}{2}[1-\cos(2\theta)] + O\left(\sqrt{\frac{l}{a}}\right) \quad (l << a) \tag{5.21}$$

and shear

$$\tau = \frac{K_I^{el}}{\sqrt{2\pi a}}\left[\sqrt{\frac{a}{l}} + \frac{\sqrt{2}}{3\cos(\theta/2)}\right] f_1(\theta) + \frac{\sigma_1-\sigma_3}{2}\sin(2\theta) + O\left(\sqrt{\frac{l}{a}}\right) \quad (l << a) \tag{5.22}$$

stresses at the dislocation located at $z_0 = le^{i\theta}$. Here

$$f_1(\theta) = \frac{3\sin^2\theta\cos^2(\theta/2)-1}{6\sin\theta\cos(\theta/2)} \tag{5.23}$$

$$f_2(\theta) = \frac{\cot\theta + \sin(2\theta)}{6\sin\theta\cos(\theta/2)} - \frac{9\cos^2\theta + 12\cos\theta - 1}{48\cos^3(\theta/2)} + \cos^3(\theta/2) \tag{5.24}$$

and we corrected an algebraic error in equation (20) of PA's paper for $f_2(\theta)$. When

obtaining (5.21) and (5.22), we used (5.9) in (5.18).

Since $f_2(\theta)$ is always positive (i.e., for all θ between 0 and π; Figure 5.4), the leading term of the order of $K_I^{el}/l^{1/2} = O((a/l)^{1/2})$ in (5.21) results in a positive σ_n. Stress σ_n can become negative only due to the last two negative $O(1)$ terms in (5.21). While these terms are formally of the higher order than the leading $O((a/l)^{1/2})$ term, they are "allowed" to exceed the leading term numerically since they come from Problems *A* and *B*, which are independent of Problem *C*, the origin of the leading term. The boxed, $O(1)$, term in (5.21) also comes from Problem *C*, and should, therefore, be directly compared to the leading term.

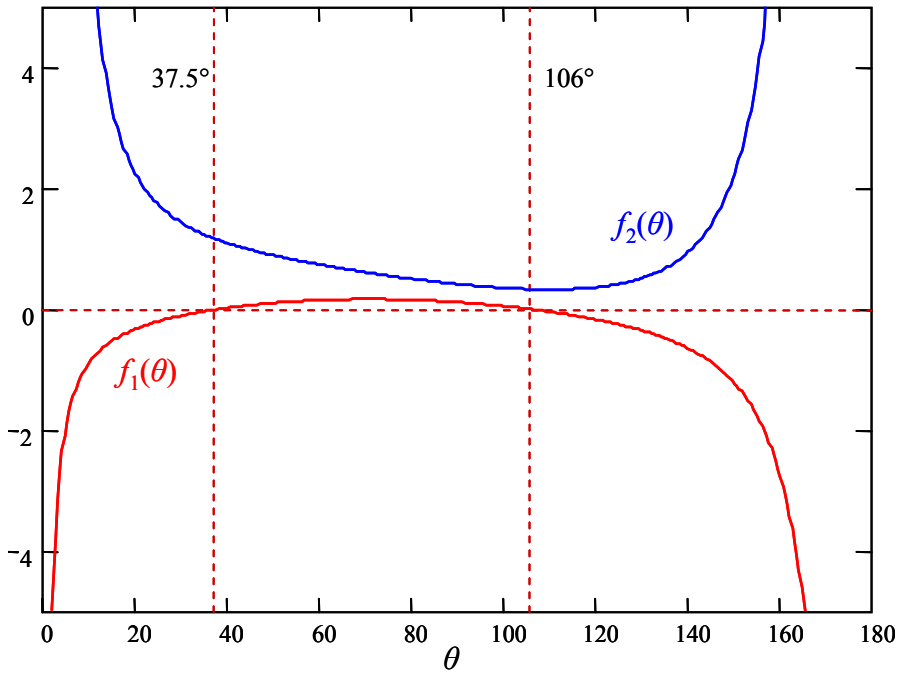

Figure 5.4. The dependence of $f_1(\theta)$ and $f_2(\theta)$ on θ.

Since τ and σ_n appear linearly in the Mohr-Coulomb criterion (5.2), the expression for τ should include the terms of the same order as that for σ_n. Expression (5.22) indeed

includes two complete first asymptotic terms, that is, $K_I^{el}/l^{1/2} = O((a/l)^{1/2})$ and $O(1)$ terms. The latter consists of the boxed, $O(1)$, term and the last, also $O(1)$, term, which is due to the remote stresses. Similar to (5.21), the boxed term in (5.22) comes from Problem *C* and should also be directly compared to the leading term $(a/l)^{1/2}$.

We now recall that the boxed terms in (5.21) and (5.22) represent the second order correction to the solution for the semi-infinite crack given by the first terms in brakets in (5.21) and (5.22). Hence, it turns out that if

$$\sqrt{\frac{l}{a}} << \frac{3}{\sqrt{2}}\cos\frac{\theta}{2} \tag{5.25}$$

the boxed terms in (5.21) and (5.22) are small compared to $(a/l)^{1/2}$ and can be omitted. As discussed above, other $O(1)$ terms in (5.21) and (5.22) should be kept. While, in general, keeping some terms of a given asymptotic order and discarding others may not be a good idea, in the case under consideration this is permissible and will be done in all subsequent expressions. Futhermore, it is this "mixed-order" approximation we call, hereafter, *small scale yielding*.

Our analysis, therefore, shows that while *PA* implicitly kept two leading terms in Problem *B* and only one leading term in Problem *C*, this did not create a problem. Note that for a given K_I^{el}, only the omitted (boxed) terms "know" about the fracture geometry (i.e., fracture size in our case). In this work, we have the advantage of knowing these terms explicitly, which allowed finding condition (5.25). Even though $O((l/a)^{1/2})$ terms in (5.21) and (5.22) are not possible to evaluate unless the pressure distribution $p(x)$ in Problem *B* is known (more discussion follows in the next section), condition (5.25) is

quite specific and is necessary for the boxed terms in (5.21) and (5.22) to be negelible. In other words, while not sufficient, condition (5.25) is necessary for the small scale yielding approximation to be applicable to the super-dislocation model. Therefore, we further require condition (5.25) to be satisfied and call it small scale yielding condition.

5.2.2 Dislocation Stability and Main Equations

Substituting expressions (5.21) and (5.22) into Mohr-Coulomb criterion (5.2) and considering condition (5.25), we obtain the corrected (*PA*'s equation (11)) relationship between the length, l, and angle, θ, of the dislocation located at point $z_0 = le^{i\theta}$:

$$\begin{aligned} &\frac{K_I^{el}}{(2\pi l)^{1/2}}\left[\pm f_1(\theta) + \tan\phi f_2(\theta)\right] \\ &\pm\frac{\sigma_1-\sigma_3}{2}\sin(2\theta) - \tan\phi\left\{p(0) + \frac{\sigma_1-\sigma_3}{2}[1-\cos(2\theta)]\right\} = c \end{aligned} \tag{5.26}$$

where the signs of plus and minus correspond to $\tau > 0$ and $\tau < 0$, respectively (due to the modulus sign in (5.2)). The sign of τ, which is defined by (5.22), is not obvious *a priori* because $f_1(\theta)$ in (5.23) can be both negative and positive (Figure 5.4).

It is well known [e.g., *Rice and Thomson*, 1974; *Cherepanov et al.*, 1995] that the force of interaction between the dislocation and the external field or, simpler, the fracture force, $\tau^B|b|$, acting on the dislocation at z_0, is positive (as also seen directly from (5.7)). Hence, it tends to drive the dislocation away from the crack tip. So does the positive (per (5.20)) "in-situ" force, $\tau^A|b|$. As observed from (5.13), which includes the direct effect (5.12) of the dislocation positioned at $\bar{z}_0$, the image (self-induction) force, $\tau^C|b|$, is negative and tends to run the dislocation towards the crack tip [e.g., *Rice and Thomson*,

1974; *Cherepanov et al.*, 1995]. The interplay between these forces results in the uncertainty in the sign of the total shear force, $\tau|b|$, defined by (5.22), although the force, $F_r = 2|b|(-\sigma_n \tan\phi + c)$ ($\sigma_n \le 0$), resisting the dislocation movement, is always directed against the driving force, $\tau|b|$. Since the direction of forces may affect the dislocation stability [e.g., *Rice and Thomson*, 1974], we first test (5.26) by considering an infinitesimal deviation of the dislocation from the equilibrium position, z_0, and analyzing condition (5.26).

Denote the left hand side in (5.26) by $F(l, \theta)$. For a given θ and a small change of the dislocation length from l to $l+\Delta l$,

$$\Delta F = \frac{\partial F}{\partial l}\Delta l = -\frac{K_I^{el}}{2\sqrt{2\pi}l^{3/2}}\left[\pm f_1(\theta) + \tan\phi f_2(\theta)\right]\Delta l \qquad (5.27)$$

where again "+" and "–" correspond to $\tau > 0$ or $\tau < 0$, respectively. In the case of $\tau > 0$ and $\Delta l < 0$, the dislocation is stable for either $\Delta F > 0$ or $\Delta F < 0$. Indeed, $\Delta F > 0$ corresponds to $|\tau| + \sigma_n \tan\phi > c$ or, in other words, to $\tau|b| > F_r$, and the dislocation will be returning back to the equilibrium position, z_0 (i.e., from $l + \Delta l = l - |\Delta l|$ to l). For $\Delta F < 0$, $|\tau| + \sigma_n \tan\phi < c$ and the dislocation is stable because it cannot leave the equilibrium position at all. If $\tau > 0$ and $\Delta l > 0$, the dislocation can be stable only when $\Delta F < 0$ (since otherwise $\tau|b| > F_r$ and $l + \Delta l > l$, so that the dislocation would be driven away from z_0). Then, as follows from (5.27), the equilibrium of the dislocations is stable for $\Delta l > 0$ when $\partial F/\partial l < 0$ and for $\Delta l < 0$ when $\partial F/\partial l < 0$ or $\partial F/\partial l > 0$. Because the stability condition has to be satisfied *simultaneously* for both $\Delta l > 0$ and $\Delta l < 0$, we conclude that in the case of $\tau > 0$ the dislocation is stable if and only if $\partial F/\partial l < 0$, which (per (5.27)) is equivalent to

$f_1(\theta) + \tan\phi f_2(\theta) > 0$.

Exactly the same arguments suggest that in the case of $\tau < 0$, the dislocation can be stable only when $[-f_1(\theta) + \tan\phi f_2(\theta)] < 0$. However, this implies that $f_1(\theta) > 0$ (since $f_2(\theta) > 0$ for $0 < \theta < \pi$; Figure 5.4) and according to (5.22), τ must be positive (since $\sigma_1 \geq \sigma_3$ and $K_I^{el} > 0$). This mathematical contradiction indicates that $\tau < 0$ corresponds to the *unstable* equilibrium of the dislocation. Since the super-dislocation model aims to simulate *stable* plastic zones, the case of $\tau < 0$ shall be excluded from further consideration. Accordingly, in what follows, only the plus sign will be kept in expression (5.26).

Therefore, the necessary and sufficient condition for the stable equilibrium of the dislocation located at z_0 (and the conjugate dislocation at $\bar{z}_0$) can be expressed as two inequalities

$$\tau(l,\theta) > 0, \qquad f_1(\theta) + \tan\phi f_2(\theta) > 0 \tag{5.28}$$

that should be satisfied simultaneously. In (5.28), $\tau(l, \theta)$ is given by (5.22) while the equilibrium value of l is defined by (5.26). *PA* implicitly chose plus sign in (5.26), which corresponds to the first condition in (5.28). Our analysis shows that the second condition is also important.

Figure 5.5 shows the dependence of $f(\theta) = f_1(\theta) + \tan\phi f_2(\theta)$ on θ for several values of ϕ representative for Mohr-Coulomb materials [e.g., *Charlez*, 1991, 1997]. While not sufficient, the condition of $f(\theta) > 0$ (i.e., the second condition in (5.28)) is

necessary for determining the physically meaningful range of θ. As can be seen from Figure 5.5, for large friction angles, $\phi > 35.4^\circ$, $f(\theta) > 0$ for all dislocation angles, $0 < \theta < \pi$. However, for smaller friction angles, $\phi < 35.4^\circ$, the condition of $f(\theta) > 0$ results in a narrower range of θ. For $8.9^\circ < \phi < 35.4^\circ$, this range consists of *two* intervals that are subsets of $(0^\circ, 180^\circ)$. For example, if $\phi = 30^\circ$ (Figure 5.5), *two* intervals, $0 < \theta < 124^\circ$ and $148.5^\circ < \theta < 180^\circ$, satisfy the $f(\theta) > 0$ condition. Friction angles $0^\circ < \phi < 8.9^\circ$ correspond to the range of θ, which consists of *three* intervals. In particular, if $\phi = 8^\circ$, these are $0^\circ < \theta < 10.4^\circ$, $21.2^\circ < \theta < 110.5^\circ$, and $172^\circ < \theta < 180^\circ$ (Figure 5.5). In the case of a frictionless material, $\phi = 0$, the dislocation angle should be in the *narrowest*, *single* interval of $37.5^\circ < \theta < 106^\circ$ to satisfy the condition of $f(\theta) > 0$.

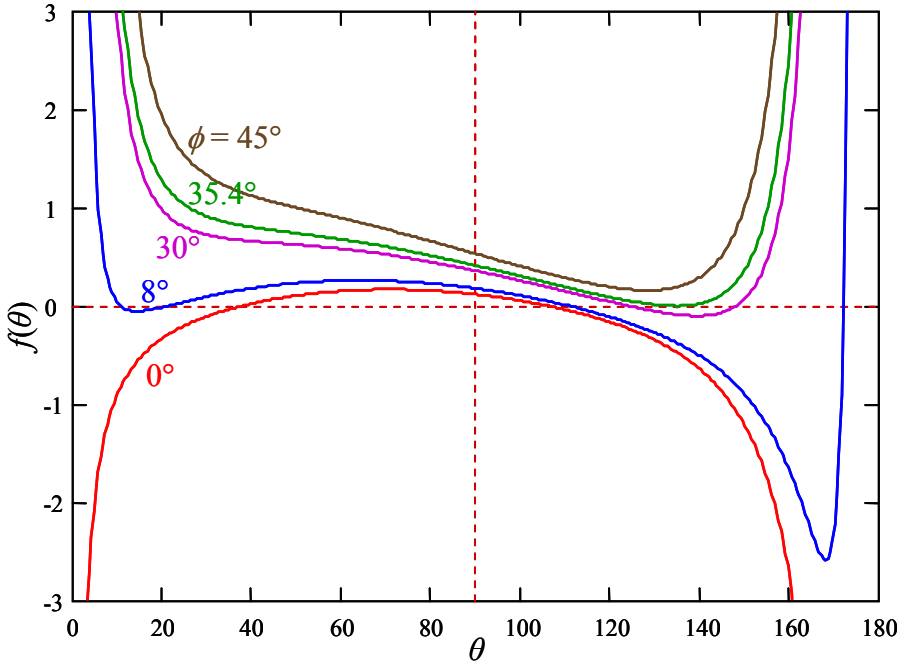

Figure 5.5. The dependence of $f(\theta) = f_1(\theta) + \tan\phi f_2(\theta)$ on θ for several values of ϕ.

It is important to note that in addition to the stability conditions (5.28), the super-

dislocation model, revised in this work, is based on the original condition adopted by *PA*

$$\sigma_n \le 0 \tag{5.29}$$

and on the condition

$$(l/a)^{1/2} << 1 \tag{5.30}$$

of small scale yielding, which corresponds to (5.25) and to omitting the $O(1)$ boxed terms in (5.21) and (5.22) in the actual computations of σ_n and τ. Condition (5.30) is more restrictive than that adopted by *PA* (i.e., $l/a << 1$). For simplicity, below we use condition (5.30) rather than (5.25) unless the relevant value of θ significantly decreases the allowable range of $(l/a)^{1/2}$. In the majority of cases, this does not happen since θ is typically between 0º and 90º.

If condition (5.29) is not satisfied, the model results cannot be considered physically meaningful since the Mohr-Coulomb criterion (5.2) is generally not applicable in the case of tensile normal stresses ($\sigma_n > 0$). This is why we checked the condition $\sigma_n \le 0$ as well as conditions (5.28) in all of our calculations. When these conditions were not satisfied, we excluded such cases by indicating that the considered super-dislocation model could not be used for the corresponding combinations of parameters.

The situation is somewhat different for the condition (5.30) of small scale yielding since this condition is necessary but not sufficient. Although in this extreme case, the mathematical problem is simplified, strictly speaking, for actual calculations, one needs to estimate the errors resulting from the truncations of asymptotic expressions or, at

least, evaluate the first neglected terms of the order of $(l/a)^{1/2}$. Otherwise, the accuracy of the obtained expressions is not really known and the condition $(l/a)^{1/2} << 1$ only means that $l/a \to 0$.

In our case, although cumbersome, it is still straightforward to obtain the first ignored $O(l/a)^{1/2}$ terms in (5.11) and (5.13) from potential (5.10) or even to employ the corresponding exact solutions for the crack-dislocation interaction (Problem *C*) [*Atkinson*, 1966; *Weertman*, 1996]. However, the $O((l/a)^{1/2})$ terms in (5.7), ignored in the elastic problem for the pressurized fracture (Problem *B*), can only be evaluated if the complete pressure distribution $p(x)$ inside the fracture is fully known (as can be seen from (5.3) and (5.6)). Since we characterize the elastic fracture load only by two quantities, K_I^{el} and $p(0)$, this uncertainty in the ignored higher order terms is the "price" for reducing the number of parameters (especially those affecting $p(x)$ since they are generally difficult to define).

Given that in Problem B we do not know $O(l/a)^{1/2}$ terms, we also do not need to solve Problem *C* more accurately. Furthermore, if condition (5.30) is satisfied, we do not need to keep even $O(1)$ terms in Problem *C*. In other words, as discussed in the previous section, the boxed terms in (5.21) and (5.22) can be omitted in the small scale yielding approximation. Contrary to keeping all second order terms in (5.21) and (5.22), this corresponds to reducing the problem to the model of a semi-infinite crack since for a specified K_I^{el}, the crack half-size, a, disappears from expressions (5.21), (5.22), and (5.26). Nevertheless, having condition (5.30) of small scale yielding in mind, we further use a as a normalizing parameter for l. Then, the dimensionless dislocation length, $L = l/a$, can be obtained directly from (5.26) (with plus sign per (5.28)):

$$\sqrt{\frac{l}{a}} = \frac{1}{\sqrt{2}} \frac{f_1(\theta) + f_2(\theta)\tan\phi}{h_0} \tag{5.31}$$

where

$$h_0 = \frac{c}{\Delta p} - \frac{\sigma_1 - \sigma_3}{2\Delta p}\sin(2\theta) + \tan\phi\left[\frac{p(0)}{\Delta p} + \frac{\sigma_1 - \sigma_3}{2\Delta p}(1 - \cos(2\theta))\right] \tag{5.32}$$

and

$$\Delta p = p_* - \sigma_3 = \frac{K_I^{el}}{\sqrt{\pi a}} \tag{5.33}$$

which is equivalent to (5.4). It is convenient to use Δp for normalizing stress parameters since in hydraulic fracturing problems with $K_I^{el} > 0$, this quantity is strictly positive (i.e., not zero).

Note that because $(l/a)^{1/2}$ in (5.31) has been obtained by formally substituting stresses (5.21) and (5.22) into the independent Mohr-Coulomb condition (5.2), the resulting expression (5.31) does not guarantee that $(l/a)^{1/2}$ is positive. Therefore, substituting (5.31) into $(l/a)^{1/2} > 0$ and taking into account the second stability condition in (5.28), we find that the dislocation angle, θ, should be within the range defined by inequality

$$h_0 > 0 \tag{5.34}$$

However, it is often easier to compute $(l/a)^{1/2}$ directly by using (5.31) and simply omit those values that happen to be negative. We do this in most of the following cases since

in these instances the super-dislocation model does not result in physically meaningful values and can not be used.

The dimensionless dislocation strength, $B = (D/\Delta p)(|b|/a)$, can be found by rewriting (5.17) as

$$\frac{D}{\Delta p}\frac{|b|}{a} = \sqrt{\frac{l}{2a}}\frac{1}{6\sin\theta\cos(\theta/2)} \tag{5.35}$$

where, per condition (5.30), we again ignored the boxed (second) term. Apart from the different normalization, (5.35) agrees with the corresponding expression for the dislocation strength in *PA*'s paper, provided that expression (5.31), which is used for the dislocation length, is based on the corrected formula (5.24) for $f_2(\theta)$.

Since $\delta = 2|b|\sin\theta$ is the dimensional crack aperture at the crack tip, $x = 0$ (Figure 5.1), the dimensionless crack tip opening displacement (CTOD), $\Delta = (D/\Delta p)(\delta/a)$, will be defined by

$$\frac{D}{\Delta p}\frac{\delta}{a} = \frac{D}{\Delta p}\frac{|b|}{a}2\sin\theta \tag{5.36}$$

Finally, the dimensionless normal

$$\frac{\sigma_n}{\Delta p} = \sqrt{\frac{a}{2l}}f_2(\theta) - \frac{p(0)}{\Delta p} - \frac{\sigma_1 - \sigma_3}{2\Delta p}[1 - \cos(2\theta)] \tag{5.37}$$

and shear

$$\frac{\tau}{\Delta p} = \sqrt{\frac{a}{2l}} f_1(\theta) + \frac{\sigma_1 - \sigma_3}{2\Delta p} \sin(2\theta) \tag{5.38}$$

stresses are obtained by substituting (5.33) into (5.21) and (5.22), respectively, and ignoring the boxed, $O(1)$, and the higher order, $O((l/a)^{1/2})$, terms.

5.3 Parametric Study

To compare our results with those given in *PA*'s paper, we calculated L, B, Δ, and θ for various loading conditions and the same material parameters as *PA*, i.e., a = 1 m, E = 10^{10} Pa, ν = 0.25, c = 1 or 10 MPa, and K_I^{el} = 5 MPa×m$^{1/2}$. We also used other parameter values when required. As *PA* did, we kept the in-situ stresses, σ_1 and σ_3, in the range of

$$0 \le \lambda < \cos\phi, \qquad \lambda = \frac{\sigma_1 - \sigma_3}{2c + (\sigma_1 + \sigma_3)\tan\phi} \tag{5.39}$$

where the upper limit guarantees that the host material does not yield in the remote region, before the crack propagates, while the lower limit corresponds to the adopted stress order convention (i.e., $\sigma_1 \ge \sigma_2 \ge \sigma_3 \ge 0$).

5.3.1 Frictionless Material

Frictionless material, ϕ = 0, represents an important extreme case idealizing material with a low friction angle. Petroleum reservoirs that require hydraulic fracturing stimulation often consist of shale-bearing sediments with a friction angle as low as a few degrees [e.g., *Byerlee*, 1978; *Rice*, 1983; *Lockner*, 1995]. When ϕ = 0, the Mohr-

Coulomb criterion (5.2) reduces to $\tau = c$, which is equivalent to the Von Mises criterion if $c = Y/\sqrt{3}$ where Y is the material yielding strength. In general, the normal stress, σ_n, is not necessarily negative in the Von Mises material. Nevertheless, because we consider frictionless material as an extreme case of *geomaterial* with low friction, unless stated otherwise, we still require the condition $\sigma_n \leq 0$ in (5.29) to be satisfied. We describe this case in detail since it yields a closed-form solution, which will be helpful for analyzing the more complex case of $\phi \neq 0$ in the subsequent sections.

For $\phi = 0$, expression (5.31) is simplified to

$$\sqrt{\frac{l}{a}} = \frac{1}{\sqrt{2}} \frac{\Delta p}{c} \frac{3\sin^2\theta\cos^2(\theta/2) - 1}{6\sin\theta\cos(\theta/2)\left[1 - \lambda\sin(2\theta)\right]} \tag{5.40}$$

where the loading parameter, λ, defined by (5.39), is reduced to $\lambda = (\sigma_1 - \sigma_3)/(2c)$.

PA suggested maximizing the CTOD, δ, to determine the dislocation angle, θ. Following this suggestion, we substitute (5.40) and (5.35) into (5.36) to obtain an expression for CTOD:

$$\frac{D}{\Delta p}\frac{\delta}{a} = \frac{\Delta p}{c} \frac{3\sin^2\theta\cos^2(\theta/2) - 1}{36\sin^2\theta\cos^2(\theta/2)\left[1 - \lambda\sin(2\theta)\right]} \tag{5.41}$$

Therefore, for $\phi = 0$, the value of θ, which maximizes δ, depends only on λ. Differentiating (5.41) with respect to θ, we arrive at the relationship

$$\lambda = \frac{\cos\theta\cos\frac{\theta}{2}\left(3\sin^2\theta\cos^2\frac{\theta}{2}+1\right)-\sin\theta\sin\frac{\theta}{2}}{\sin\theta\left[6\cos^3\frac{\theta}{2}\sin^4\theta+2\cos\frac{\theta}{2}(3\cos^2\theta-1)-\sin\frac{\theta}{2}\sin 2\theta\right]} \tag{5.42}$$

between θ and λ, which is plotted in Figure 5.6 for $0 \le \lambda < \cos\phi = 1$.

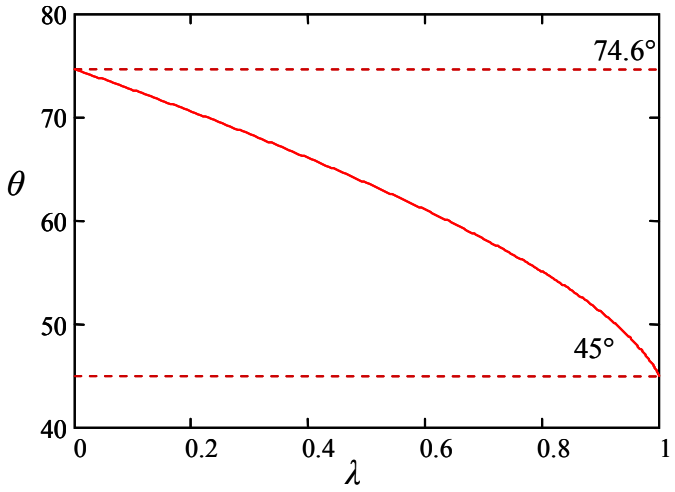

Figure 5.6. Frictionless material, $\phi = 0$: the dependence of the value of θ, which maximizes δ, on the loading parameter, $\lambda = (\sigma_1 - \sigma_3)/(2c)$.

Figure 5.6 shows that as λ increases from 0 to 1, the dislocation angle, maximizing δ, decreases from 74.5° to 45°. However, these values of θ are only physically meaningful when they satisfy conditions (5.28), (5.29), (5.30), and (5.34).

As expected, for frictionless material, substituting (5.40) into (5.38) results in $\tau = c > 0$ and the first stability condition in (5.28) is automatically satisfied. Then, according to the second stability condition in (5.28), the dislocation angle should be in the range of $37.5^\circ < \theta < 106^\circ$ (which corresponds to the curve of $\phi = 0$ in Figure 5.5). As we see from Figure 5.6, the whole range of dislocation angles maximizing δ happens to be within the

dislocation stability range.

As can be seen from (5.35) through (5.38), (5.40) and (5.42), in the case of frictionless material, the super-dislocation model depends upon three parameters, $c/\Delta p$, λ, and $p(0)/\Delta p$ (since $(\sigma_1 - \sigma_3)/(2\Delta p) = \lambda(c/\Delta p)$). However, $p(0)$ affects only σ_n and according to (5.21), affects it linearly. Substituting (5.40) into (5.37) and taking into account (5.23) and (5.24), we obtain that $\sigma_n \le 0$ if

$$\frac{p(0)}{c} = \frac{p(0)}{\Delta p}\left(\frac{c}{\Delta p}\right)^{-1} \ge \left[1 - \lambda \sin(2\theta)\right]\frac{f_2(\theta)}{f_1(\theta)} - \lambda\left[1 - \cos(2\theta)\right] \tag{5.43}$$

The right hand side of (5.43) is plotted in Figure 5.7 considering θ as a function of λ given by (5.42), that is, maximizing δ in (5.41). Values of $p(0)$ above the plotted curve correspond to $\sigma_n < 0$ and condition $\sigma_n \le 0$ in (5.29) is satisfied. For $p(0)$ below the curve, $\sigma_n > 0$ and the Mohr-Coulomb criterion is not applicable. Parameter $p(0)$ is "external" with respect to the super-dislocation model and should be determined based on a model of hydraulic fracture propagation. Yet, this may not be a trivial task, since in general the super-dislocation model itself is intended to provide an input to hydraulic fracture simulation. Accordingly, $p(0)$ becomes coupled with inherently non-linear, non-local, multi-scale processes characteristic of hydraulic fracturing [e.g., *Economides and Nolte*, 2000; *Murdoch*, 2002; *Detournay*, 2004].

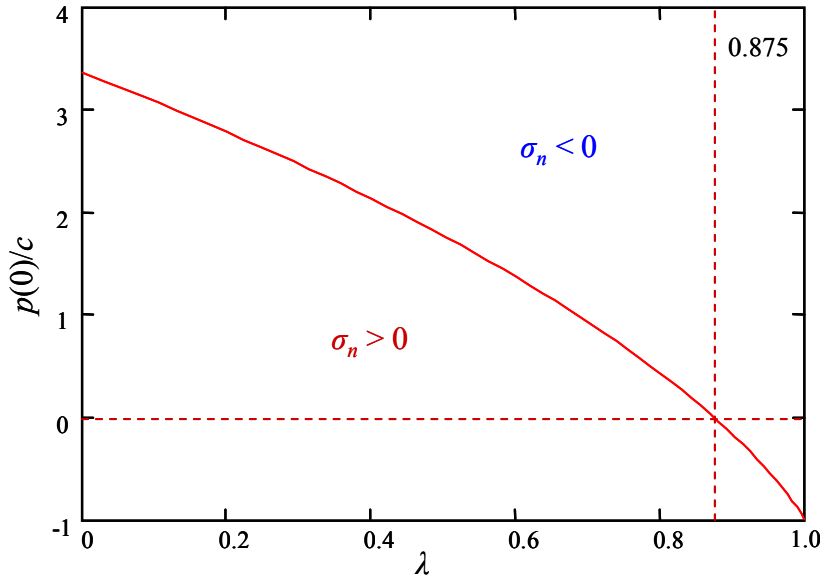

Figure 5.7. Frictionless material, $\phi = 0$: the dependence of the critical fluid pressure at the fracture tip on the loading parameter, λ.

However, in a propagating hydraulic fracture, the fluid pressure, $p(x)$, decreases towards the fracture tip. For the sake of example, $p(0)$ can be constrained by two extreme values, $p(0) = 0$ and $p(0) = p(x) = K_I^{el}/(\pi a)^{1/2} + \sigma_3$. The former corresponds to a fast pressure drop at the fracture tip, which is rather characteristic for typical rates of hydraulic fracturing [e.g., *Economides and Nolte*, 2000]. The latter represents a slow or quasi-stationary fracture with nearly constant pressure distribution (this is the case considered by *PA*). As one can see from Figure 5.7, in the end-member case of $p(0) = 0$, the negative value of σ_n is achieved only for a narrow range of $0.875 < \lambda < 1$. In contrast, in another end-member case of constant $p(x) = p(0) = K_I^{el}/(\pi a)^{1/2} + \sigma_3$, for given K_I^{el} and a, the tip pressure, $p(0)$, becomes sufficiently large for σ_n to be negative with increasing σ_3 (e.g., with increasing depth) for any $0 \le \lambda < 1$.

For further analysis, we need to specify a value of $c/\Delta p$, compute $(l/a)^{1/2}$ based on

(5.40) for different loading parameters, λ, and to make sure that $(l/a)^{1/2} << 1$ per (5.30). If $\phi = 0$, condition (5.34) of non-negative $(l/a)^{1/2}$ can be written as $\sin(2\theta) < 2c/(\sigma_1 - \sigma_3) = 1/\lambda$, which is satisfied for any $0 < \theta < \pi$ since per (5.39) $\lambda < 1$. This can also be seen from Figure 5.8a, which shows dimensionless dependence of $(l/a)^{1/2}$ on θ for different values of the loading parameter, λ. Condition (5.34) is satisfied because for all plots in Figure 5.8a, $(l/a)^{1/2}$ is positive.

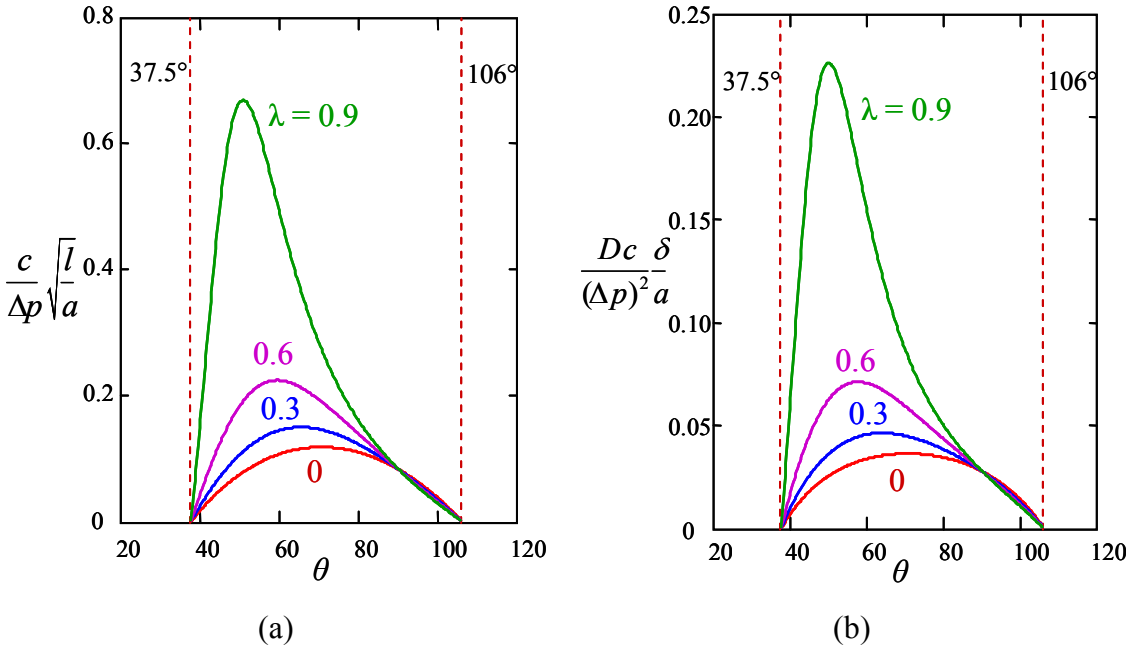

Figure 5.8. Frictionless material, $\phi = 0$: (a) normalized dislocation length versus dislocation angle, and (b) normalized CTOD versus dislocation angle for different loading parameters, $\lambda = 0$, 0.3, 0.6, and 0.9.

Examples of $\delta(\theta)$ are shown in Figure 5.8b, from which one can see that the dislocation angles, θ, given by (5.42) and shown in Figure 5.6, indeed provide the global maximum for δ within the dislocation stability range, $37.5^\circ < \theta < 106^\circ$. The corresponding plots of $(l/a)^{1/2}$ and δ/a as functions of λ are shown in Figure 5.9. The dependence of θ on λ is given in Figure 5.6 and does not depend upon the value of $c/\Delta p$ (though this value

does determine the range of λ through condition $(l/a)^{1/2} << 1$).

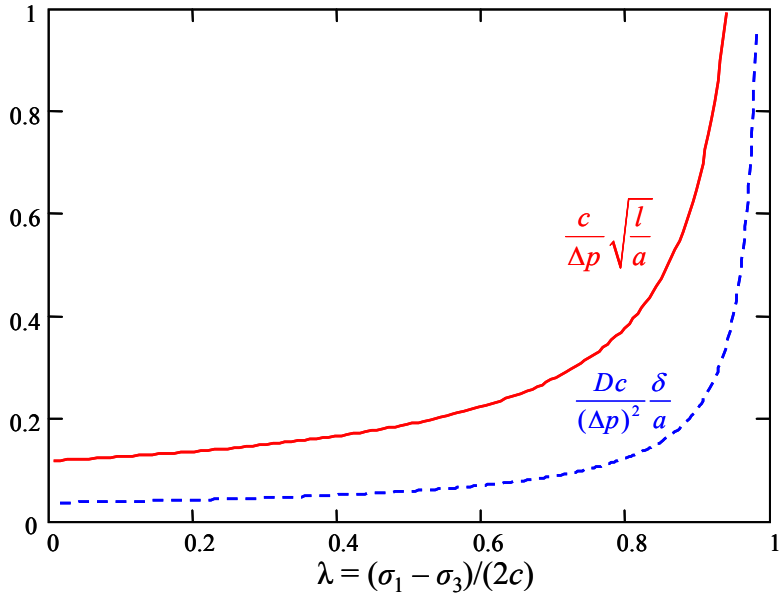

Figure 5.9. Frictionless material, $\phi = 0$: dependence of normalized dislocation length and CTOD on loading parameter, λ.

The numerical result of *PA* agrees with solution (5.42). However, contrary to their conclusion, the super-dislocation model developed for Mohr-Coulomb material does not exactly recapture the *Atkinson and Kanninen* [1977] model in the case of Von Mises material ($\phi = 0$) for $\sigma_1 = 0$. Actually, it only recaptures their model if material cohesion, c, is sufficiently large, that is, if $c >> \sigma_1 - \sigma_3$. According to (5.39), the condition $c >> \sigma_1 - \sigma_3$ suggests that $\lambda << 1$ (since $\phi = 0$), so that the dislocation angle maximizing δ in (5.41) becomes independent of λ and equals $\theta = 74.5°$ (i.e., the same as for $\lambda = 0$ in Figure 5.6). In this case, expressions (5.40) and (5.41) indeed become identical to those originally obtained by *Atkinson and Kanninen* [1977] for small scale yielding in Von Mises material with large yield strength. Note that these authors used a different condition for the dislocation angle. Specifically, they maximized the extent of plasticity, l, rather than

the crack opening, δ, which resulted in a slightly different value of θ, that is, θ = arccos(1/3) = 70.53º. Nevertheless, $\lambda = 0$ still makes (5.40) and (5.41) identical with *Atkinson and Kanninen* [1977]. If, however, λ is not small (i.e., condition $c >> \sigma_1 - \sigma_3$ is not satisfied), θ differs significally from 70.53º (or 74.5º in Figure 5.6).

If λ is not too close to 1 (i.e., c is not too close to $(\sigma_1 - \sigma_3)/2$), exression (5.40) suggests that condition $(l/a)^{1/2} << 1$ of small scale yielding requires that $c/\Delta p >> 1$. Hence, in either case, whether one maximizes δ or l, keeping the small scale yielding approximation only the first order terms is indeed possible in the super-dislocation model for the frictionless material *provided that* the material cohesion, c, is much higher than the fracture driving (net) pressure, Δp.

However, in many conditions typical for hydraulic fracturing in petroleum formations (e.g., soft rocks, weakly-cemented sediments, unconsolidated particulate materials, cohesionless soils, etc.), c is likely to be of the same order as Δp (as well as $\sigma_1 - \sigma_3$, though this is less important). For example, substituting *PA*'s parameters, $K_I^{el} = 5$ MPa×m$^{1/2}$ and $a = 1$ m, into (5.33), we have $\Delta p = 2.82$ MPa, so that $c/\Delta p = 0.35$ for *PA*'s value of cohesion, $c = 1$ MPa. Then, for $\lambda = 0$ in Figure 5.8, the maximum value of $(l/a)^{1/2}$ is 0.34. Therefore, the small scale yielding condition (5.30), $(l/a)^{1/2} << 1$, is hardly satisfied even for $\lambda = 0$, while for greater values of λ, $(l/a)^{1/2}$ increases (Figures 5.8 and 5.9). Since for $\phi = 0$, the complete range of λ is $0 \le \lambda < 1$ (Figure 5.6), in general, *the super-dislocation model is not likely to be applicable to all loading conditions*.

For $c = 0.1$ MPa, which is more realistic for soft sediments, $c/\Delta p = 0.035$ and the

maximum value of $(l/a)^{1/2} = 3.4$ for $\lambda = 0$ and grows with increasing λ. Therefore, in this case, the assumption of small scale yielding is not valid for any λ, and for these material properties, the super-dislocation model is probably inapplicable for any loading conditions.

In summary, even in the case of frictionless materials, a fairly restrictive condition is necessary for the super-dislocation model to be applicable. That is, $c/\Delta p$ should be sufficiently large. While this condition may be relatively easy to satisfy for conventional Von Mises materials (e.g., metals), this does not appear to be the case for reservoir sediments undergoing hydraulic fracturing treatment and the super-dislocation model should be used with care.

5.3.2 Cohesionless Material

Cohesionless material ($c = 0$) represents another important extreme case of material with a low cohesion. During the last decades, hydraulic fracturing has been used in many soft rock reservoirs, unconsolidated or poorly consolidated sediments, and soils with low cohesion [e.g., *Ayoub et al.*, 1992; *Hannah et al.*, 1994; *Roodhart et al.*, 1994; *Smith and Hannah*, 1996]. When $c = 0$, the Mohr-Coulomb criterion (5.2) reduces to $\tau + \sigma_n \tan\phi = 0$. Therefore, if the condition $\sigma_n < 0$ in (5.29) is satisfied, the condition $\tau > 0$ in (5.28) will be automatically satisfied as well. As a result, we only need to check one of these two conditions. Below we will check the condition $\tau > 0$.

For $c = 0$, (5.39) is simplified to

$$0 \le \lambda < \cos\phi, \quad \lambda = \frac{\sigma_1 - \sigma_3}{(\sigma_1 + \sigma_3)\tan\phi} \tag{5.44}$$

so that, σ_1 can be expressed as

$$\sigma_1 = \sigma_3 \frac{1 + \lambda \tan\phi}{1 - \lambda \tan\phi} \tag{5.45}$$

Substituting (5.45) into (5.32) for c = 0, and considering an extreme case of slowly propagating fracture with a nearly constant pressure distribution $p(x) \approx p(0)$ (to reduce the number of parameters), that is, $\sigma_3 = p(0) - \Delta p$, we obtain

$$h_0 = \tan\phi \frac{p(0)}{\Delta p} + \left(\frac{p(0)}{\Delta p} - 1 \right) \frac{\lambda \tan\phi}{1 - \lambda \tan\phi} \left[\tan\phi(1 - \cos(2\theta)) - \sin(2\theta) \right] \tag{5.46}$$

According to (5.31), (5.35), (5.36), and (5.46), in contrast to the case of frictionless material, the value of the dislocation angle, θ, which maximizes δ, depends not only on λ (expression (5.41)), but also on other parameters, i.e., $p(0)/\Delta p$ and ϕ. As a result, no closed-form solution could be found, although numerically this represents no difficulty.

First, consider cohesionless material (c = 0) that has a relatively low friction angle of ϕ = 10°. The range of the dislocation angles, θ, satisfying the second condition in (5.28), has two intervals, i.e, 0º < θ < 112º and 170º < θ < 180º (similar to the ϕ = 30° curve in Figure 5.5). For further analysis, we need to specify values of Δp and $p(0)$. Substituting *PA*'s parameters, K_I^{el} = 5 MPa×m$^{1/2}$ and a = 1 m, into (5.33), we have Δp = 2.82 MPa. Let $p(x) = p(0)$ = 15 MPa. In this case, $\sigma_3 = p(x) - \Delta p$ = 12.2 MPa, which

corresponds to a depth of a few hundred meters.

To check condition (5.34), we compute $(l/a)^{1/2}$ based on (5.31) for different loading parameters, λ. Then, by excluding $(l/a)^{1/2} < 0$, we further narrow down the range of the dislocation angle to $0 < \theta < 112^{\circ}$ for $0 \le \lambda < \cos\phi = \cos(10^{\circ}) = 0.98$ (Figure 5.10). To check the first condition in (5.28), $\tau > 0$, we plot $\tau(\theta)$ per (5.22) in Figure 5.11. This yields an even narrower range of θ. Finally, $\delta(\theta)$ in (5.36) is plotted in Figure 5.12 for different parameters, λ. The dislocation angle, θ, is determined by maximizing δ in the defined range (Figure 5.12). The dependence of $\theta(\lambda)$ is plotted in Figure 5.13.

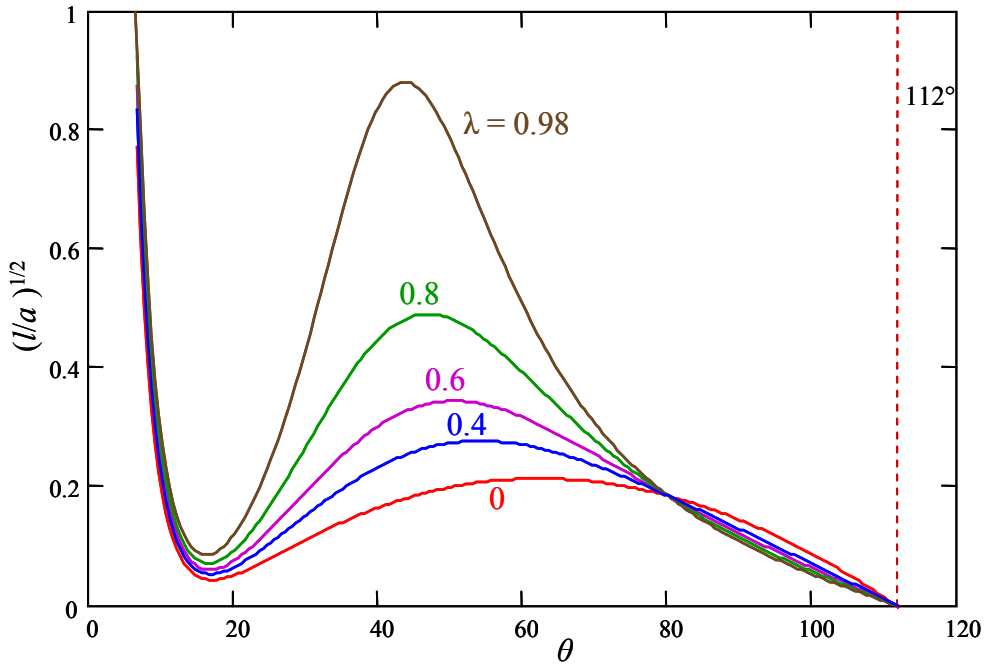

Figure 5.10. Cohesionless material, $c = 0$, $\phi = 10°$: normalized dislocation length versus dislocation angle for different loading parameters, λ, $\Delta p = 2.82$ MPa, and $p(0) = p(x) = 15$ MPa.

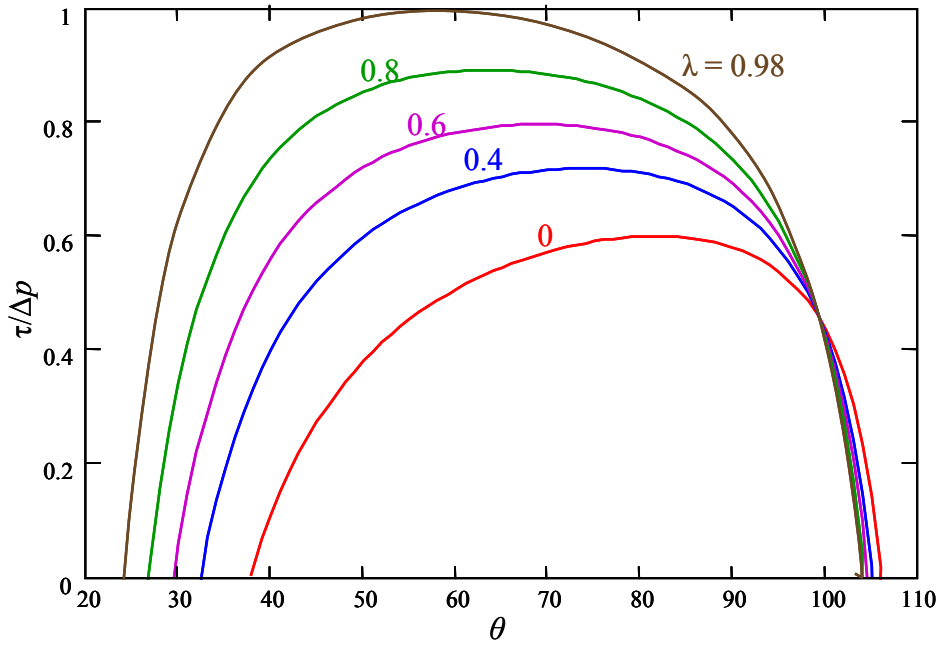

Figure 5.11. Cohesionless material, $c = 0$, $\phi = 10°$: normalized shear stress on the dislocation versus dislocation angle for different loading parameters, λ, $\Delta p = 2.82$ MPa, and $p(0) = p(x) = 15$ MPa.

Figure 5.12. Cohesionless material, $c = 0$, $\phi = 10°$: normalized CTOD versus dislocation angle (in the range satisfying conditions (5.28), (5.29), and (5.34)) for different loading parameters, λ, $\Delta p = 2.82$ MPa, and $p(0) = p(x) = 15$ MPa.

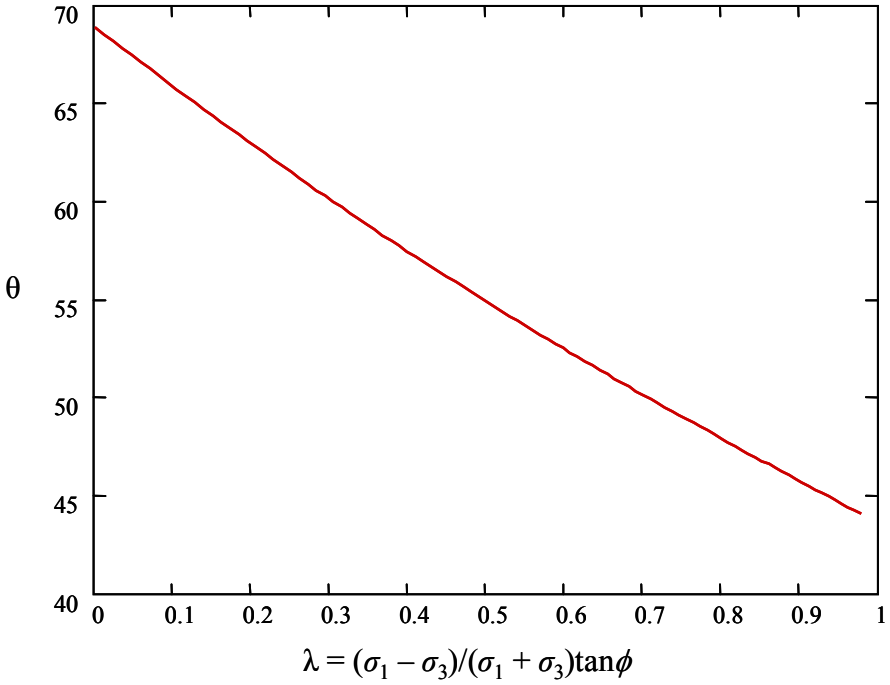

Figure 5.13. Cohesionless material, $c = 0$, $\phi = 10°$: dependence of dislocation angle on the loading parameter, λ, for $\Delta p = 2.82$ MPa and $p(0) = p(x) = 15$ MPa.

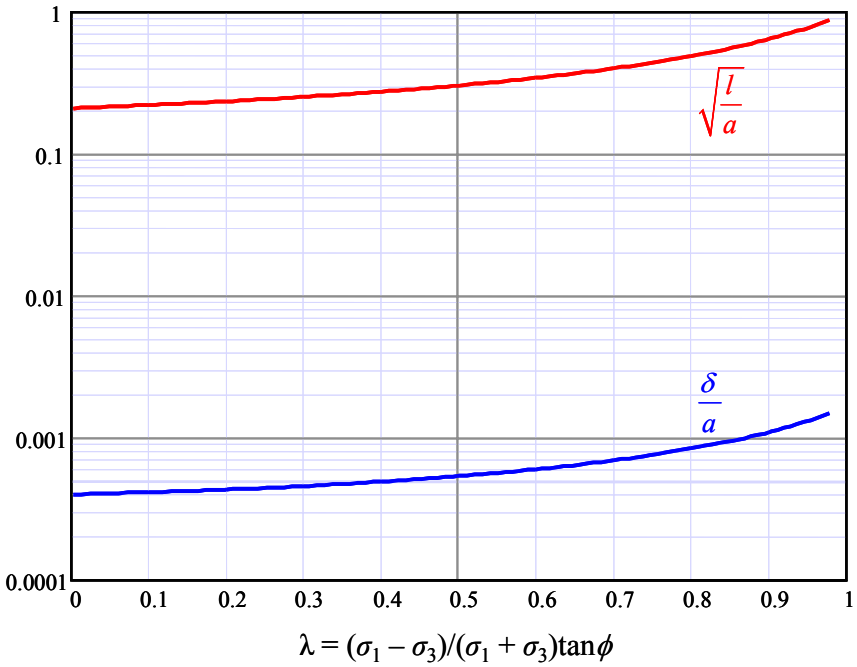

Figure 5.14. Cohesionless material, $c = 0$, $\phi = 10°$: dependence of the normalized dislocation length and CTOD on the loading parameter, λ, for $\Delta p = 2.82$ MPa and $p(0) = p(x) = 15$ MPa.

To check condition (5.30), $(l/a)^{1/2}$ versus λ is plotted in Figure 5.14, which also shows the dependence of δ/a on λ. As can be seen, for the chosen parameters, the small scale yielding condition, $(l/a)^{1/2} << 1$, is satisfied sufficiently well only for $\lambda << 1$. As $\lambda > 0.5$, $(l/a)^{1/2} > 0.3$ and the super-dislocation model can hardly be used.

Note that when $\phi = 10°$, a maximum value of δ could be found in the defined range of dislocation angles, at least for $\lambda << 1$. However, this maximum might not exist when the friction angle, ϕ, increases. Consider an example of cohesionless material ($c = 0$) that has a relatively high (but still quite realistic; e.g., *Chang* [2004]) friction angle of $\phi = 40°$ whereas the other parameters are the same. Following the same procedure as described for $\phi = 10°$, we note that since $\phi > 35.4°$, the dislocation angle, θ, satisfying the second stability condition in (5.28) is in the range of $0º < \theta < 180º$ (Figure 5.5). To narrow down this range, the dependence of $(l/a)^{1/2}$ and τ on θ is plotted for different λ in Figures 5.15 and 5.16. Finally, δ versus θ is plotted in Figure 5.17, where we cut off those values of θ for which $l/a > 1$ (Figure 5.15) or $\tau < 0$ (Figure 5.16). We see that, unlike the cases of frictionless material and cohesionless material with relatively low friction angle (e.g., $\phi = 10°$), δ decreases monotonically in the defined range of dislocation angles (even in the extended range of $(l/a)^{1/2} < 1$). Hence, for cohesionless material with relatively high friction angle (e.g., $\phi = 40°$), the dislocation angle cannot be determined by maximizing the CTOD, δ.

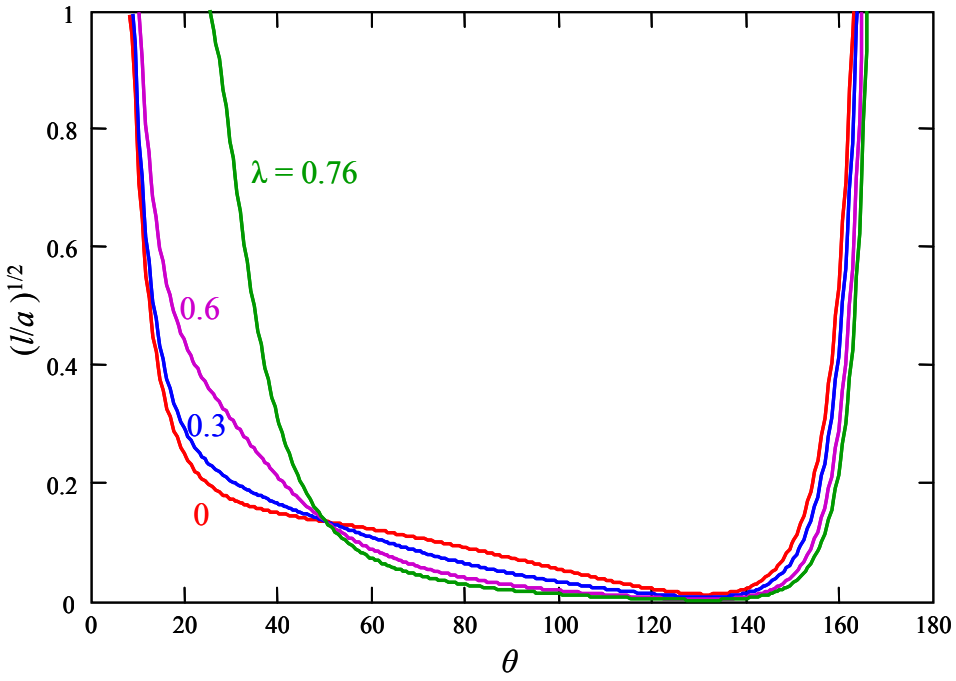

Figure 5.15. Cohesionless material, $c = 0$, $\phi = 40°$: normalized dislocation length versus dislocation angle for loading parameters, λ, for $\Delta p = 2.82$ MPa and $p(0) = p(x) = 15$ MPa.

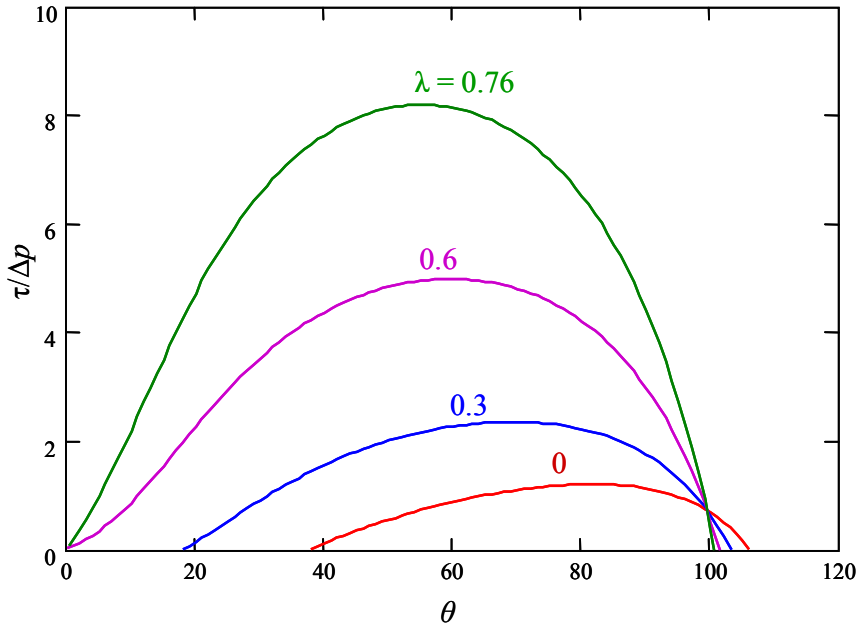

Figure 5.16. Cohesionless material, $c = 0$, $\phi = 40°$: normalized shear stress on the dislocation versus dislocation angle for loading parameters, λ, for $\Delta p = 2.82$ MPa and $p(0) = p(x) = 15$ MPa.

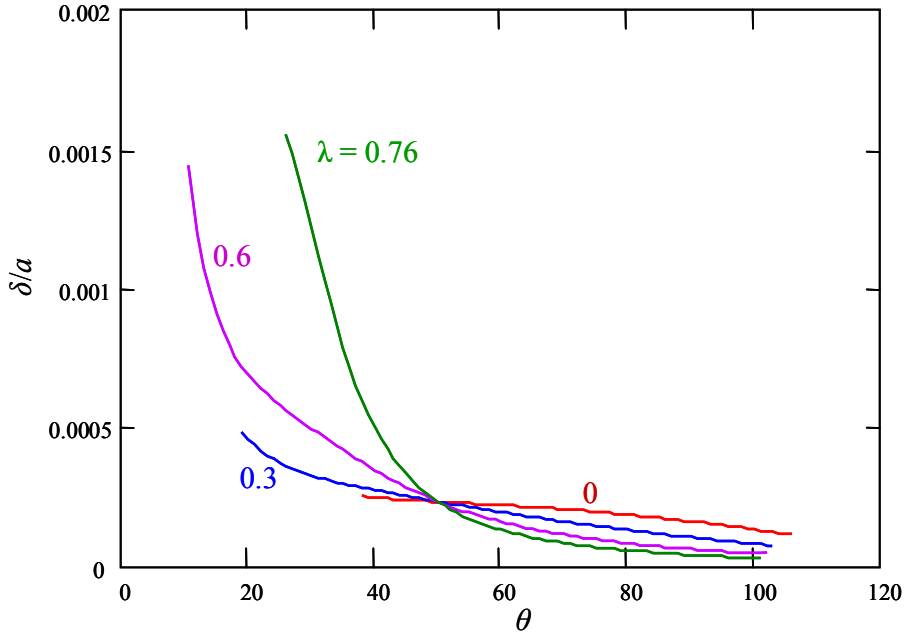

Figure 5.17. Cohesionless material, $c = 0$, $\phi = 40°$: normalized CTOD versus dislocation angle (in the range satisfying the conditions (5.28), (5.29), and (5.34)) for different loading parameters, λ, $\Delta p = 2.82$ MPa, and $p(0) = p(x) = 15$ MPa.

Similar analyses show that for the chosen set of parameters, the values of $|b|$ and l are also monotonically dependent upon θ for any λ in the range of θ determined accordingly (e.g., Figure 5.15). Thus, in the case of $\phi = 40°$, $p(0) = 15$ MPa, and $\Delta p = 2.82$ MPa, the criteria of maximizing dislocation strength, $|b|$, or dislocation length, l, are not applicable either. Therefore, similar to the case of frictionless materials, *the super-dislocation model is unlikely to be applicable to cohesionless materials for all loading conditions*.

5.3.3 Cohesive-Frictional Material

For a cohesive-frictional material, we have to use the full expressions (5.31) through (5.36). Since the "plus" sign is taken in (5.26), the Mohr-Coulomb criterion (5.2)

becomes $\tau + \sigma_n \tan\phi = c$. Furthermore, cohesion $c \geq 0$; therefore, if the condition $\sigma_n \leq 0$ in (5.29) is satisfied, the condition $\tau > 0$ in (5.28) will be automatically satisfied as well. As a result, we only need to check the condition $\sigma_n \leq 0$.

From (5.44), we can express σ_1 as

$$\sigma_1 = \sigma_3 \frac{1+\lambda\tan\phi}{1-\lambda\tan\phi} + 2c\frac{\lambda}{1-\lambda\tan\phi} \tag{5.47}$$

For simplification and to reduce the number of parameters, consider again the case of constant $p(x) = p(0)$. Then, $\sigma_3 = p(0) - \Delta p$ and substituting (5.45) into (5.32) yields

$$h_0 = \frac{c}{\Delta p} + \tan\phi\frac{p(0)}{\Delta p} + \frac{\lambda\left[\tan\phi(1-\cos(2\theta)) - \sin(2\theta)\right]}{1-\lambda\tan\phi}\left[\left(\frac{p(0)}{\Delta p} - 1\right)\tan\phi + \frac{c}{\Delta p}\right] \tag{5.48}$$

Therefore, for cohesive-frictional material, the value of the dislocation angle, θ, which maximizes δ, depends on four parameters: λ, ϕ, $p(0)/\Delta p$, and $c/\Delta p$. No closed-form solution could be found, but the numerical parametric analysis shows that the main conclusion of the previous two sections remains the same. That is, *the super-dislocation model cannot be used for arbitrary values of material properties and loading parameters*.

For the sake of example, here, we only consider the hydrostatic in-situ stress field, i.e., $\sigma_1 = \sigma_3$. Then, from (5.39) and (5.32),

$$\lambda = 0, \quad h_0 = \frac{c}{\Delta p} + \tan\phi \frac{p(0)}{\Delta p} \tag{5.49}$$

which does not require $p(x)$ to be constant. Inserting (5.31) into (5.35) and the result into (5.36), we have

$$\frac{D}{\Delta p}\frac{\delta}{a} = \frac{f_1(\theta) + \tan\phi f_2(\theta)}{6h_0 \cos(\theta/2)} \tag{5.50}$$

Since h_0 is independent of θ, the maximum of $\delta(\theta)$ (if any) is reached at the same θ as that of $F(\theta) = [f_1(\theta) + \tan\phi f_2(\theta)]/\cos(\theta/2)$. Function $F(\theta)$ is plotted in Figure 5.18 for several values of θ. As can be seen, for sufficiently large friction angles, $F(\theta)$ and, hence, $\delta(\theta)$, does not have a maximum.

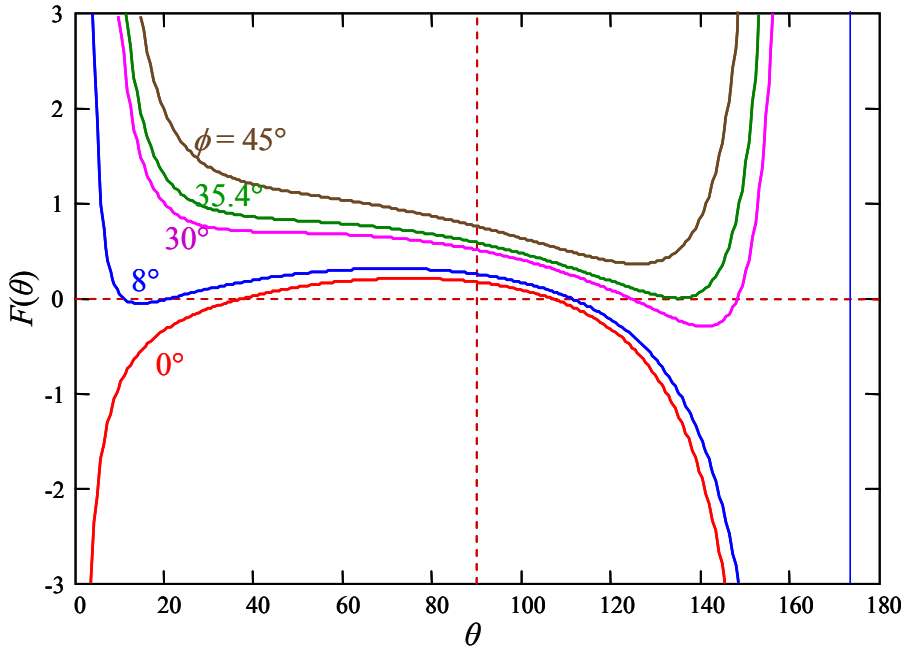

Figure 5.18. The dependence of $F(\theta) = [f_1(\theta) + \tan\phi f_2(\theta)]/\cos(\theta/2)$ on θ for several values of ϕ.

For example, in the case of $\phi = 30°$ considered by *PA*, $\delta(\theta)$ cannot be maximized and, accordingly, the super-dislocation model is not applicable if $\lambda = 0$, $\phi = 30°$ (other parameters are arbitrary). This conclusion differs from that of *PA* who obtained the value $\theta \approx 72°$ (Figure 5 in *PA*'s paper). Moreover, the analysis of *PA*'s computations suggests that their expression (20) for $f_2(\theta)$ also does not result in a maximum for $\delta(\theta)$.

Hence, while the simplicity of the considered super-dislocation model is appealing, in most cases it is too constrained and not self-consistent, that is, the modeling results may not satisfy the physical assumption on which the model is based. In this sense, our results do not support *PA*'s conclusions. Yet, as shown in the next section, the model can be modified and adjusted for a wide range of Mohr-Coulomb materials.

5.4 Maximum Shear Stress Criterion

We have shown that it is not always possible to determine the dislocation angle by maximizing the crack opening displacement, dislocation strength, or dislocation length. These conditions are only effective for frictionless materials with sufficiently high cohesion as originally suggested by *Atkinson and Kanninen* [1977] or frictional materials with sufficiently small friction angle. Here we suggest an alternative criterion, that is, to determine the dislocation angle by maximizing the shear stress, τ, at the dislocation position.

Following the procedure described in section 4.4, we first determine the range of the dislocation angles that satisfy all the required conditions (5.28), (5.29), (5.30), and (5.34). Then, we calculate the dislocation angle that maximizes the shear stress at the

dislocation position. In the following section, we will apply this criterion to the examples discussed in section 5.3.2.

For cohesionless material ($c = 0$) with a friction angle $\phi = 10°$, the dependence of τ on θ is plotted in Figure 5.11 for different loading parameters. In this case, the dislocation angle maximizing the shear stress (Figure 5.11) is indeed in the range of the dislocation angles satisfying all the required conditions. The dependence of the dislocation angle on the loading parameter, λ, is plotted in Figure 5.19 (solid line). The dislocation angles determined by maximizing δ are also plotted in Figure 5.19 (dashed line). In general, both criteria show that the dislocation angle decreases with an increasing λ. The dislocation angle determined by maximizing τ is greater than that found by maximizing δ, but the difference is relatively insignificant ($\approx 13°$).

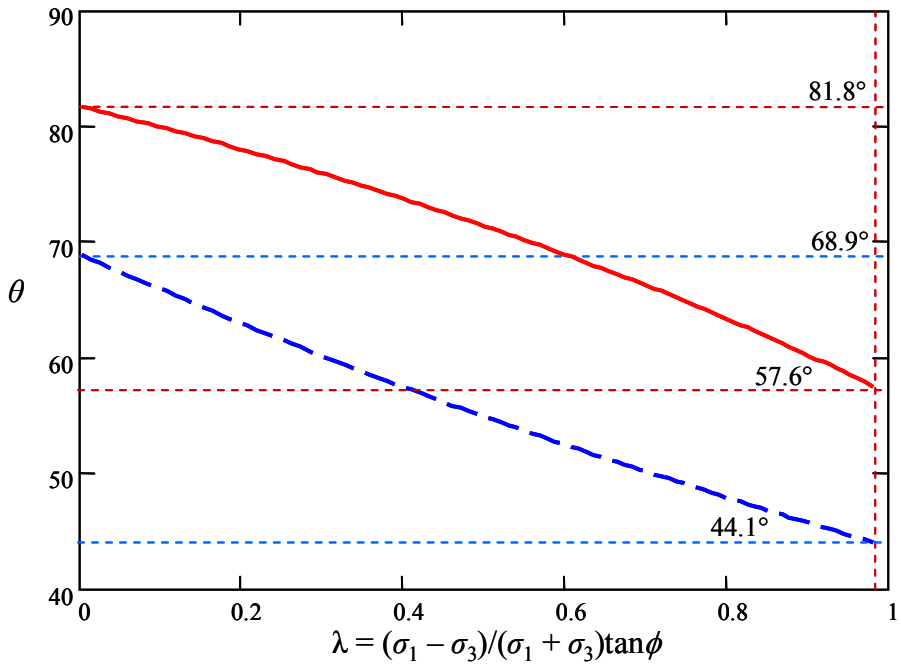

Figure 5.19. Cohesionless material, $c = 0$, $\phi = 10°$: dependence of θ on the loading parameter, λ ($0 \le \lambda < \cos\phi = 0.98$), for $\Delta p = 2.82$ MPa and $p(0) = p(x) = 15$ MPa. Solid and dashed lines are obtained by maximizing τ and δ, respectively.

For cohesionless material ($c = 0$) with a frictional angle $\phi = 40°$, while the crack opening displacement, δ, decreases monotonically in the defined range of dislocation angles, the peak value of shear stress, τ, does exist. The dependence of τ on θ is plotted in Figure 5.16 for different loading parameters. In this case, the dislocation angle corresponding to the maximum shear stress is still in the range of the dislocation angles satisfying all the required conditions. The dependence of the dislocation angle on the loading parameter for $\phi = 40°$ is plotted in Figure 5.20.

To show the effects of material properties, we also conducted the parametric analysis with various values of ϕ and $c/\Delta p$. For brevity, we omit the intermediate steps and only give the final results in Figures 5.20 and 5.21. Other parameters are the same as used by *PA* and in the previous section: $K_I^{el} = 5$ MPa×m$^{1/2}$ and $a = 1$ m (or $\Delta p = 2.82$ MPa), $p(0) = p(x) = 15$ MPa.

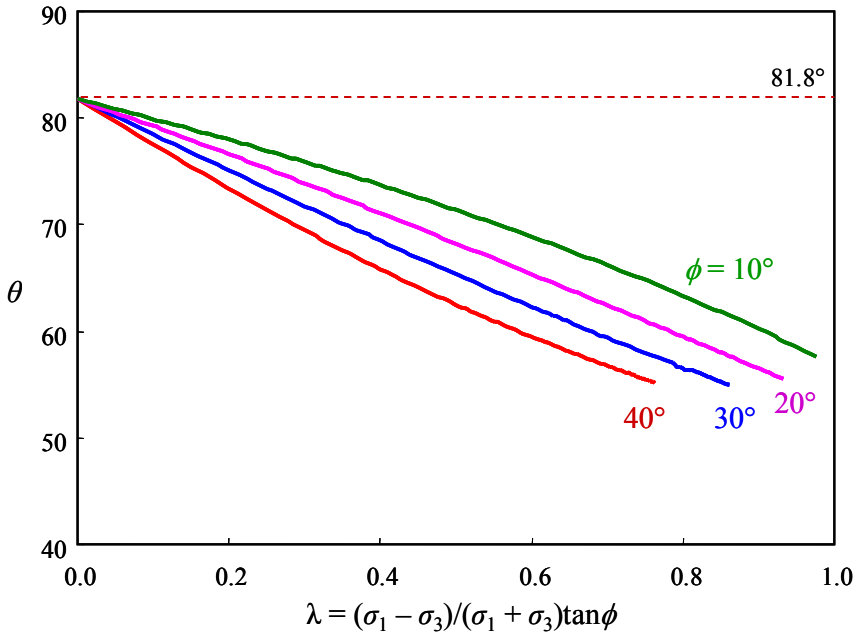

Figure 5.20. Cohesionless material, $c = 0$: dependence of θ on the loading parameter, λ ($0 \le \lambda < \cos\phi$) for different values of ϕ, $\Delta p = 2.82$ MPa, and $p(0) = p(x) = 15$ MPa.

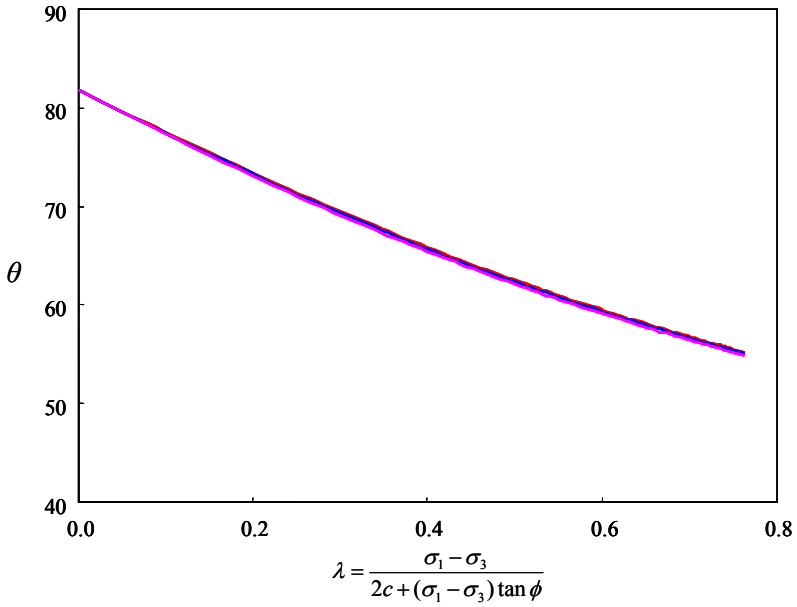

Figure 5.21. Cohesive-frictional material, ϕ = 40°: dependence of θ on the loading parameter, λ ($0 \le \lambda < \cos\phi$). Curves plotted for $c/\Delta p$ = 0, 0.35, and 1.06 are hardly distinguishable.

Figures 5.20 and 5.21 show that while the dislocation angle is insensitive to the variation of the $c/\Delta p$ ratio, it increases with the increasing frictional angle for $\lambda > 0$. When $\lambda = 0$ (the hydrostatic loading condition, $\sigma_1 = \sigma_3$), the dislocation angle, $\theta = 81.8°$, is constant and independent of ϕ or $c/\Delta p$. This can also be seen directly from (5.38).

Substituting (5.31) and (5.32) into (5.38), and considering $\lambda = 0$, we find

$$\frac{\tau}{\Delta p} = \left(\frac{c}{\Delta p} + \tan\phi \frac{p(0)}{\Delta p} \right) \frac{f_1(\theta)}{f_1(\theta) + f_2(\theta)\tan\phi} \tag{5.51}$$

Differentiating (5.51) with respect to θ and setting it equal to zero, we obtain the equation, $f_1'(\theta)\, f_2(\theta) - f_1(\theta)\, f_2'(\theta) = 0$, for the value of θ that maximizes τ. This equation is independent of ϕ and $c/\Delta p$. Hence, for the hydrostatic loading condition, the dislocation

angle is indeed a constant, i.e., $\theta = 81.8°$.

For ideal frictionless material, the maximum shear stress criterion might not be applicable since $\tau = c$ = constant. On the other hand, our parametric study shows that this criterion indeed "works" for cohesive-frictional materials with small friction angle. The dependence of the dislocation angle on the loading parameters corresponding to different values of ϕ (i.e., $\phi = 3°$, 1°, 0.1°, and 0.01°) are plotted in Figure 5.22. Other parameters are the same as those used both by *PA* and in the previous section: c = 1 MPa, K_I^{el} = 5 MPa×m$^{1/2}$ and a = 1 m (or Δp = 2.82 MPa), and $p(0) = p(x)$ =15 MPa. Figure 5.22 shows that for $\lambda \to 0$ (hydrostatic loading condition), the dislocation angle determined by the maximum shear stress criterion indeed converges to constant (i.e., $\theta = 81.8°$). Curves $\phi =$ 0.1° and 0.01° are not distinguishable, which indicates the convergence at $\phi \to 0$.

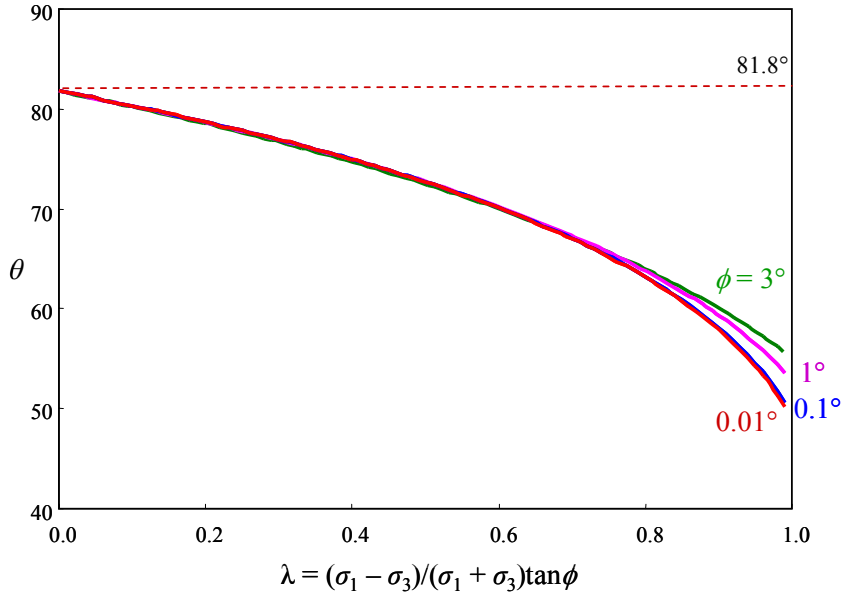

Figure 5.22. Cohesive-frictional material, c = 1 MPa: dependence of θ on the loading parameter, λ ($0 \le \lambda < \cos\phi$) for different values of ϕ, Δp = 2.82 MPa, and $p(0) = p(x)$ =15 MPa. Curves ϕ = 0.1° and 0.01° are not distinguishable, which indicates the convergence at $\phi \to 0$.

5.5 Conclusions

The super-dislocation model is an important tool to model crack-tip plasticity in different settings. In this chapter, we reassess the super-dislocation model recently developed by *Papanastasiou and Atkinson* [2000] for simple representation of plastic deformation at the tip of hydraulic fractures in such pressure sensitive materials as soft sediments in hydrocarbon reservoirs. We show that in the case of the small scale yielding, the conventional approach of determining the dislocation angle by maximizing the crack opening displacement, dislocation strength, or dislocation length is only effective for frictionless materials as originally suggested by *Atkinson and Kanninen* [1977]. As an alternative, we propose a criterion based on the maximum shear stress at the dislocation position. We show that maximizing the shear stress on the dislocation makes the super-dislocation model consistent for a wide range of pressure sensitive cohesive-frictional materials.

Nomenclature

Latin Symbols

a	crack half length
B	dimensionless dislocation strength, $B = (D/\Delta p)(\|b\|/a)$
b	complex Burgers vector, $b = b_1 + ib_2$
b_1, b_2	real and imagine parts of Burgers vector
c	cohesion
D	elastic constant, $E[8\pi(1-\nu^2)]^{-1}$
E	Young's Modulus

$f(\theta)$	$f_1(\theta) + \tan\phi f_2(\theta)$
$f_1(\theta), f_2(\theta)$	functions of θ in (5.23) and (5.24), respectively
$F(\theta)$	$[f_1(\theta) + \tan\phi f_2(\theta)] / \cos(\theta/2)$
F_r	force resisting to the dislocation mobement, $F_r = 2\|b\|(-\sigma_n \tan\phi + c)$
h_0	function of loading stresses and material parameters
K_I^d	the SIF caused by the interaction of the dislocations with the crack
K_I^{el}	mode I SIF caused by external loads
K_{II}	mode II SIF
l	dislocation length
L	dimensionless dislocation length, $L = l/a$
p	internal fluid pressure
p_*	characteristic (scaling) fluid pressure
$p(0)$	fluid pressure at the fracture tip
x, y	cartesian coordinate
Y	material yielding strength
z	complex variable, $z = x + iy$
z_0	the position of the upper right dislocation

Greek Symbols

δ	crack aperture at the crack tip (CTOD)
Δ	dimensionless crack tip opening displacement (CTOD), $\Delta = (D/\Delta p)(\delta/a)$
Δp	$p_* - \sigma_3$
θ	dislocation angle
λ	loading parameter in (5.39)
ν	Poisson's ratio

σ	net (driving) pressure, $\sigma(x) = p(x) - \sigma_3$
σ_1, σ_3	principal in-situ stresses
σ_n	normal stresses at the dislocation position
σ_{xx}, σ_{yy}	rectangular stress components
σ_*	characteristic (scaling) crack load
τ	shear stresses at the dislocation position
ϕ	friction angle
$\Phi(z)$	*Muskhelishvili* potential

References

Atkinson, C. (1966), The interaction between a dislocation and a crack, *Int. J. Frac. Mech.*, *2*, 567-575.

Atkinson, C., and T.R. Kay (1971), A simple model of relaxation at a crack tip, *Acta Metall. Mater.*, *19*, 679-683.

Atkinson, C., and M.F. Kanninen (1977), A simple representation of crack tip plasticity: The inclined strip-yield superdislocation model, *Int. J. Fracture*, *13*, 151-163.

Ayoub, J.A., J.M. Kirksey, B.P. Malone, and W.D. Norman (1992), Hydraulic fracturing of soft formations in the Gulf Coast, *SPE 23805*, paper presented at *SPE Formation Damage Control Symposium*, Lafayette, LO, 26-27 February.

Berumen, S., D. Tiab, and F. Rodriguez (2000), Constant rate solutions for a fractured well with an asymmetric fracture, *J. Petrol. Sci. Eng.*, *25*, 49-58.

Bradner, G.C., and L.C. Murdoch (2005), Effects of skin and hydraulic fractures on SVE wells, *J. Contam. Hydrol.*, *77*, 271-297.

Broberg, K.B. (1999), *Cracks and Fractures*, Academic Press, San Diego, USA, 752 pp.

Byerlee, J.D. (1978), Friction of rocks, *Pure Appl. Geophy.*, *116*, 615-626.

Chang, H. (2004), Hydraulic fracturing in particulate materials, Ph.D. thesis, 267 pp., Georgia Institute of Technology, GA.

Charlez, Ph.A. (1991), *Rock Mechanics*: Vol. 1 – Theoretical Fundamentals, Editions Technip, Paris, 333 pp.

Charlez, Ph.A. (1997), *Rock Mechanics*: Vol. 2 – Petroleum Applications, Editions Technip, Paris, 661 pp.

Cherepanov, G.P. (1979), *Mechanics of Brittle Fracture*, translated from the Russian by A.L. Peabody, translation edited by R. de Wit and W.C. Cooley, McGraw-Hill Inc., New York, NY.

Cherepanov, G.P., A. Richter, V.E. Verijenko, S. Adali, and V. Sutyrin (1995), Dislocation generation and crack growth under monotonic loading, *J. Appl. Phys.*, *78*, 6249-6264.

Detournay, E. (2004), Propagation regimes of fluid-driven fractures in impermeable rocks, *Int. J. Geomech.*, *4*, 35-45.

Economides, M.J., and K.G. Nolte (2000), *Reservoir Stimulation*, 3rd Edition, John Wiley & Sons, LTD.

Gerberich, W.W., P.G. Marsh, and J.W. Hoehn (1994), Hydrogen induced cracking mechanisms – Are there critical experiments? *Hydrogen Effects in Materials*, *Proceedings for the Fifth International Conference on the Effect of Hydrogen on the Behavior of Materials*, Moran, WY, 11-14 Sep, 539-551.

Guo, Q., T. Geehan, and A. Ovalle (2004), Increases assurance of drill cuttings re-injection – Challenges, recent advances and case studies, *Proceedings of the IADC/SPE Asia Pacific Drilling Technology Conference and Exhibition*: *Sharing for drilling excellence*, Kualur Lumpar, Malaysia, 13-15 Sep, 115-122.

Hainey, B.W., R.G. Keck, M.B. Smith, K.W. Lynch, and J.W. Barth (1999), On-site fracturing disposal of oilfield-waste solids in Wilmington field, California, *SPE Prod. Facil.*, *14*, 88-93.

Hannah, R.R., E.I. Park, R.E. Walsh, D.A. Porter, J.W. Black, and F. Waters (1994), A field study of a combination fracturing/gravel packing completion technique on the Amberjack, Mississippi Canyon 109 field, *SPEPE*, *262*.

Hayashi, K., A. Sato, and T. Ito (1997), In situ stress measurements by hydraulic fracturing for a rock mass with many planes of weakness, *Int. J. Rock Mech. Min. Sci.*, *34*, 45-58.

Hills, D.A., P.A. Kelly, D.N. Dai, and A.M. Korsunsky (1996), *Solutions of Crack Problems: The Distributed Dislocation Technique*, Kluwer Academic Publishers, the Netherlands.

Howard, G.C., and C.R. Fast (1970), *Hydraulic Fracturing*, American Institute of Mining, Metallurgical, and Petroleum Engineers, Inc., Monograph, *2*, Henry L. Doherty Series.

Hubbert, M.K., and D.G. Willis (1957), Mechanics of hydraulic fracturing, *J. Petrol. Techol.*, *9*, 153-166.

Hunt, J.L., K. Frazier, B.P. Pendergraft, and M.Y. Soliman (1994), Evaluation and completion procedure for produced brine and waste-water disposal wells, *J. Petrol. Sci. Eng.*, *11*, 51-60.

Hurt, R.S., R. Wu, L.N. Germanovich, H. Chang, and P. van Dyke (2005), On mechanisms of hydraulic fracturing in cohesionless materials, *EOS Trans. AGU*, *86*(*52*), *Fall Meet. Suppl.*, *Abstract H41B-0416*.

Jagannadhan, K., and M.J. Marcinkowski (1982), *Unified Theory of Fracture*, Aedermonnsdorf: Trans Tech, Materials science survey, No.1.

Kanninen, M.F., C. Atkinson, and C.E. Feddersen (1977), A fatigue crack growth analysis method based on a simple representation of crack-tip plasticity, *Cyclic Stress-Strain and Plastic Deformation Aspects of Fatigue Crack Growth*, *ASTM*

STP, *637*, 122-140.

Kanninen, M.F., and C. Atkinson (1980), Application of an inclined-strip-yield crack tip plasticity model to predict constant amplitude fatigue crack growth, *Int. J. Fracture*, *16*, 53-69.

Lin, I.-H., and R. Thomson (1986), Cleavage, dislocation emission, and shielding for cracks under general loading, *Acta Merall. Mater*, *34*, 187-206.

Lockner, D. A., and J. D. Byerlee (1995), An earthquake instability model based on faults containing high fluid-pressure compartments, *Pure Appl. Geophy.*, *145* (*2*/*3*), 717-745.

Murdoch, L.C. (2002), Mechanical analysis of idealized shallow hydraulic fracture, *J. Geotech. Geoenviron.*, *128*, 488-495.

Murdoch, L.C., and W.W. Slack (2002), Forms of hydraulic fractures in shallow fine-grained formations, *J. Geotech. Geoenviron.*, *128*, 479-487.

Muskhelishvili, N.I. (1953), *Singular Integral Equations; Boundary Problems of Funciton Theory and their Application to Mathematical Physics*, translated from the Russian edited by J.R.M. Radok, P. Noordhoff Ltd., Groningen, 447 pp.

Muskhelishvili, N.I. (1953), *Some Basic Problems of the Mathematical Theory of Elasticity*: *Fundamental Equations, Plane Theory of Elasticity, Torsion, and Bending*, translated from the Russian edited by J.R.M. Radok, P. Noordhoff Ltd., Groningen, 704 pp.

Papanastasiou, P., and C. Atkinson (2000), Representation of crack-tip plasticity in pressure sensitive geomaterials, *Int. J. Fracture*, *102*, 271-286.

Raaen, A.M., E. Skomedal, H. Kjorholt, P. Markestad, and D. Okland (2001), Stress determination from hydraulic fracturing tests: The system stiffness approach, *Int. J. Rock Mech. Min. Sci.*, *38*, 529-541.

Rice, J. (1983), Constitutive relations for fault slip and earthquake instabilities, *Pure Appl. Geophy.*, *121*, 443-475.

Rice, J.R., and R. Thomson (1974), Ductile versus brittle behavior of crystals, *Philos. Mag.*, *29*, 73-97.

Roodhart, L.P., P.A. Fokker, D.R. Davies, J. Shlyapobersky, and G.K. Wong (1994), Frac-and-pack stimulation: application, design, and field experience, *JPT*, *46*, 230-238.

Sadananda, K., and D.-N. V. Ramaswamy (2001), Role of crack tip plasticity in fatigue crack growth, *Philos. Mag.*, *81*, 1283-1303.

Sasaki, S. (1998), Characteristics of microseismic events induced during hydraulic fracturing experiments at the Hijiori hot dry rock geothermal energy site, Yamagata, Japan, *Tectonophysics*, *289*, 171-188.

Shiue, S.-T., and S. Lee (1992), The effect of superdislocation on fracture: Dislocation-free zone in the front of a semi-infinite crack tip, *J. Appl. Phys.*, *72*, 2209-2214.

Smith, M.B., and R.R. Hannah (1996), High-permeability fracturing: the evolution of a technology, *JPT*, *48*, 628-633.

Weertman, J. (1996), *Dislocation Based Fracture Mechanics*, World Scientific, River Edge, NJ, 524 pp.

CHAPTER 6
DISCRETE ELEMENT SIMULATION OF FLUID INJECTION INTO PARTICULATE MATERIALS

Abstract. To investigate the fracture initiation mechanism in water flooding conditions, we conducted a numerical simulation of fluid injection into particulate material using the discrete element method. We observed three distinct stages in the cavity evolution as the injection velocity increases: (1) cavity initiation in the vicinity of the injection point when the velocity of fluid reaches a certain critical value; (2) stable cavity development when the cavity propagates incrementally in response to each increment of velocity increase; and (3) unstable cavity propagation after the injection velocity reaches a second critical value (usually much higher than the critical velocity of cavity initiation).

These stages can be explained by considering the drag forces applied to the particles by the fluid continuously seeping through the particle assembly. Due to the drag forces, particles tend to move away from the injection point. As a result, the particulate material is unloaded near the injection point, which causes a positive volumetric strain in its vicinity. Once the strain reaches a critical value corresponding to the loss of contact between the particles in all directions, a cavity forms. This critical strain value corresponds to the "fluidization" of the particle-fluid mixture. When the injection velocity increases, the cavity begins propagating until it reaches the stable state. Once the resultant magnitude of the drag forces exceeds the reaction on the boundary of the entire particle assembly (at the second critical velocity), the body equilibrium is not possible any more and the cavity begins developing in an unstable manner, that is, without further

increase in the injection velocity.

We considered a poroelastic model of cavity initiation based on the fluidization mechanism. This model suggests that the critical fluid velocity is *proportional* to the fluid viscosity if the latter is not too high. However, if the fluid viscosity is sufficiently large, the critical velocity is *inversely proportional* to the fluid viscosity. From the physical standpoint, such dependence of the injection velocity on the fluid viscosity corresponds to two different flow regimes: inertial governing regime and viscosity governing regime. The inertial governing regime occurs with low fluid viscosity when the energy dissipation is mainly due to the second term in the nonlinear Darcy law. When fluid viscosity increases, the first linear term gradually becomes dominant, and the energy dissipates mainly through the fluid viscosity. Even though the developed model is oversimplified and does not result in the correct state of stress near the injection point, the critical velocity, estimated based on this model, fits remarkably well the values obtained from numerical simulations with PFC^{2D}.

6.1 Introduction

An important practical application related to hydraulic fracturing in particulate materials is *water flooding*. Water flooding is one of the most common methods used worldwide for improving oil recovery [*Mayerhofer et al.*, 1997; *Azeemuddin*, 2002; *Sommerauer and Petersen*, 2003; *Souza et al.*, 2005]. Hydraulic fracturing during some water flooding operations is undesirable because it creates permeable channels that limit the pressure in the formation undergoing water flooding treatment. On the other hand, the waterfrac method of hydraulic fracturing (that is, essentially using water as a fracturing

fluid), also often referred to as water flooding, is becoming increasingly popular [*Mayerhofer et al.*, 1997; *Sommerauer and Petersen*, 2003; *Zhao et al.*, 2005]. Its advantages, such as relatively low cost, increased near-borehole permeability, fracture extension, and easy cleanup, are very attractive. Numerous production results show that waterfrac with a dramatically lower treatment cost (perhaps 50% lower than conventional hydraulic fracturing treatment [*Mayerhofer et al.*, 1997]) are unexpectedly successful, even in particulate materials [*Mayerhofer et al.*, 1997].

As an extreme case of industrial hydraulic fracturing, water flooding fracturing exhibits several important differences from the conventional hydraulic fracturing. First, the injected water has a low viscosity (of 1 cp) compared to the high viscosity (up to ~10^4 cp) of typical polymer-based fracturing liquids. Second, the injection time of water flooding (i.e., ranging from weeks to months) is significantly longer than that of the conventional hydraulic fracturing treatment (i.e., from minutes to hours). The extremely high level of leak-off is also characteristic for water flooding fracturing. In fact, the leak-off zone around the fracture is most likely to be much larger than the size of the fracture itself.

Although several models have been proposed for the hydraulic fracturing in particulate materials [e.g., *Panah and Yanagisawa*, 1989; *Lo and Kaniaru*, 1990; *Murdoch*, 1993a, 1993b, 1993c, and 2002; *Chang*, 2004; *Hurt et al.*, 2005], these models were not designed to describe fluid injection with extremely high leak-off and cannot be directly employed for water flooding conditions. As a result, the mechanisms of water flooding are poorly understood by currently available theoretical models.

Due to the aforementioned unique features of water flooding, at present, it is difficult, if not impossible, to simulate this process in the laboratory. The existing techniques [*Chang*, 2004; *Hurt et al.*, 2005] are not feasible due to the difficulties associated with recording and preserving the developed fracture, as well as with the large volume of fluid that needs to be pumped through the samples of particulate materials.

Based on this circumstance, we conducted a series of numerical experiments to model fluid injection into a particulate material by using the discrete element code *PFC*^{2D} [*Itasca*, 2005]. We considered a "fluidization" criterion for the critical fluid velocity corresponding to fracture initiation.

6.2 Numerical Model

6.2.1 *PFC* Background

PFC has been widely applied to solid mechanics and granular flow problems [e.g., *Potyondy et al.*, 1996; *Huang et al.*, 1999; *Hart and Fairhurst*, 2000]. It discretizes a solid medium into circular or spherical particles, and uses the distinct elements method [e.g., *Cundall and Strack*, 1979] to model the mechanical response of the particles. The particles are assumed to be rigid (incompressible), but can overlap at the contacts. The mechanical behavior of the particles is simulated in a dynamic manner. The particle movement obeys Newton's laws of motion and particles interact with each other through contacts. Different contact models are provided in *PFC*^{2D}. The elastic response of the contact is described either by a linear stiffness model (employed in this work) or by a Hertz-Mindlin contact model. The inelastic response of the contact is described through

slip or bonding models.

The linear stiffness model describes the linear relationship between the contact force, F, and the relative displacement, U, via:

$$F_n = K_n U_n, \quad \Delta F_s = -K_s \Delta U_s \tag{6.1}$$

where K_n and K_s are the normal and tangential stiffnesses, respectively. Note that the normal stiffness is a *secant* stiffness since it relates the total normal force, F_n, to the total normal displacement, U_n, while the shear stiffness is a *tangent* stiffness since it relates the shear force increment, ΔF_s, to the increment of shear displacement, ΔU_s. The values assigned to these stiffnesses influence the macroscopic material properties [e.g., *Oger et al.*, 1998; *Huang*, 2000; *Potyondy and Cundall*, 2004].

The slip model enforces the strength condition, so that the shear force on a contact remains less than or equal to the friction coefficient times the normal force. When the equality condition is reached, the two contacting entities may slip relative to each other.

The bonding model serves to reproduce the cohesive materials or solids by enforcing the bond strength limits. Two basic bonding models are supported in PFC^{2D}: the contact-bond model and the parallel-bond model. The contact bond can only transmit force (therefore the contact bond strengths have units of force), while the parallel bond can transmit both force and moment. In our simulations, a linear stiffness model with slip as shown in Figure 6.1 is employed. No bonding is added between the particles since we are interested in cohesionless materials.

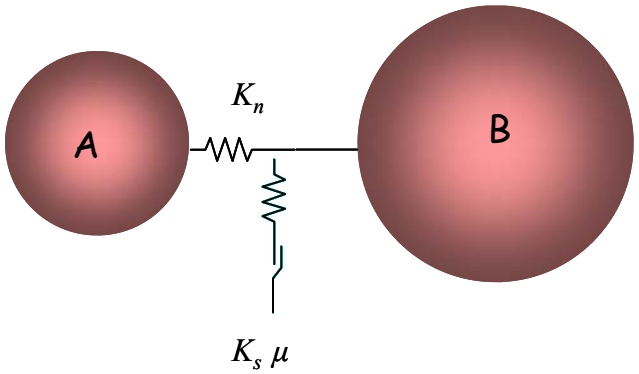

Figure 6.1. *PFC*^{2D}: the assembly is discretized by circular or spherical particles interacting through contacts.

PFC^{2D} describes an assembly, even a quasi-static system, with a dynamic scheme. Therefore, in order to obtain a stable solution, the adapted numerical mechanical time step needs to be small enough. In other words, during a single time step, disturbances cannot propagate from any particle further than its immediate neighbors [e.g., *Cundall and Strack*, 1979]. In *PFC*^{2D}, the mechanical time step is related to the mass of the particle, m, and the stiffness of the springs connecting it to the neighbors, K. The time step for a multiple mass-spring system can be expressed as

$$t \propto \sqrt{m/K} \tag{6.2}$$

Although *PFC* treats the solid phase as discrete particles, it models the fluid as a continuum in a fixed-coarse grid scheme [*Shimizu,* 2004]. Fluid flow is calculated using the Navier-Stokes equations based on locally averaged quantities, i.e., averaged over each cell. In general, for a stable simulation, the fluid time step needs to be much larger than the mechanical time step.

The interaction between the fluid and the particles is modeled including a drag

force, F_j, in the Navier-Stokes equation:

$$\frac{\partial(nv_j)}{\partial t} = -\nabla_i(nv_j v_i) - \frac{F_j}{\rho_f} - \frac{1}{\rho_f}\nabla_i \tau_{ij} + ng_j \tag{6.3}$$

where j is the spatial direction, n is the porosity, v_j is the fluid velocity, ρ_f is the fluid density, and τ_{ij} is the viscous shear stress tensor. The interaction (drag) force between the fluid and the particles is related to the pressure gradient, $\nabla_j p$ and the porosity, n by

$$F_j = n\nabla_j p \quad (j = 1,\ 2,\ 3) \tag{6.4}$$

The interaction force (6.4) is a part of the total driving force generated by the fluid flow. This force is applied to a particle as the body force

$$f_j = -\left(\frac{F_j}{1-n} + \nabla_j p\right)\frac{\pi}{6}D_p^3 \quad (j = 1,\ 2,\ 3) \tag{6.5}$$

where D_p is the particle diameter. The second term in (6.5) represents the force applied to the particles due to the pressure gradient [*Shimizu*, 2004].

The numerical scheme solves the continuity equation

$$\frac{\partial n}{\partial t} = -\nabla_i(nv_i) \tag{6.6}$$

and the Navier-Stokes equation (6.3) numerically in Euler Cartesian coordinates [*Shimizu*, 2004], and then derives the pressure and the velocity vector for each cell in the fluid grid at the current time step.

6.2.2 Model Set-up

A rectangular domain (Figure 6.2) is chosen for our simulations due to the limited flexibility of PFC^{2D} in providing versatile geometry for fluid flow. Only a half of the targeted physical problem is simulated because of the geometrical symmetry about the y-axis. Fluid was injected into the assembly in the x-direction from the inlet located at the center of the left side boundary ($x = 0$ and $y = 0$). The domain had zero pressure ($p = 0$) on the right boundary. All the other boundaries were impermeable for fluid ($q_n = 0$) everywhere except at the place of injection. The simulated rectangular domain had the dimensions of $H = 120$ mm and $L = 90$ mm ($H/D_p = 120$ and $L/D_p = 90$, where D_p is the average particle diameter). The applied effective confining stresses were $\sigma_1' = 0.2$ MPa on the right boundary, and $\sigma_3' = 0.1$ MPa on the top and bottom boundaries. The condition of zero displacement in x-direction and zero shear stress were imposed on the left boundary.

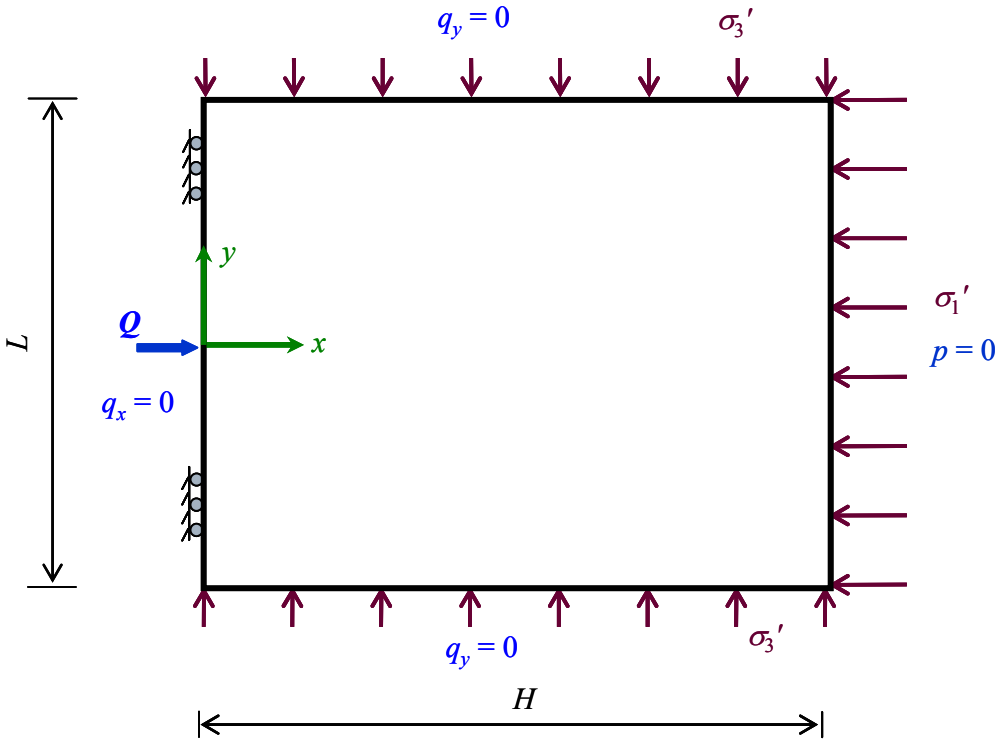

Figure 6.2. Boundary conditions in PFC^{2D} simulations.

The particle diameters had a uniform distribution between 0.5 mm and 1.5 mm. They were chosen to be much greater than those of the real particles (~ 20 to 100 μm) in order to improve numerical efficiency. In total, 11,000 particles were generated. The initial 2D porosity of the assembly was specified as 0.16. In most of the cases we studied, no bond was applied between particles in order to simulate cohesionless materials. However, cohesive materials can also be simulated by specifying normal, T_n, and shear, T_s, bond strengths between the particles. Figure 6.3 shows the assembly employed in our simulation together with the fluid cells. Each fluid cell contains about 10 particles. The colors of the particles in the figure were used only to visualize the migration of particles, i.e., particles had the same material properties regardless of their colors.

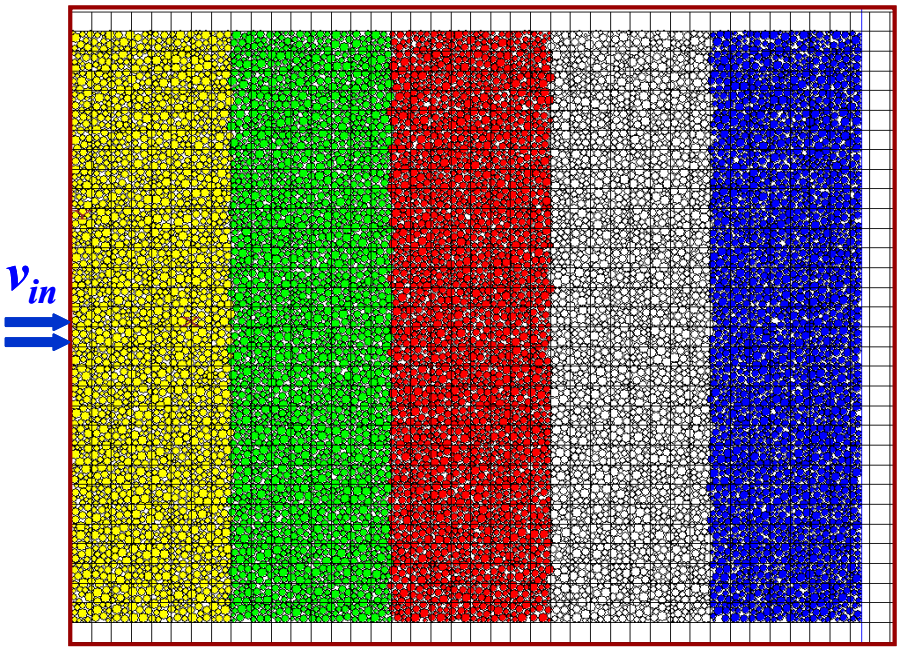

Figure 6.3. Fluid cells (solid lines) and the assembly of particles (circles) employed in the PFC^{2D} simulation.

The matrix material properties (particle density, ρ_p, and normal and shear stiffnesses, K_n and K_s) and fluid properties (fluid density, ρ_f, and viscosity, μ_f) used in the *base* simulation case were as follows: ρ_p = 2650 kg/m^3, μ = 0.839 (interparticle friction angle of $\phi = 40°$), ρ_f = 1000 kg/m^3, μ_f = 100 cp, and $K_n = K_s$ = 50 MN/m. The normal, K_n, and shear, K_s, stiffnesses are micro-scale material properties and related to macroscopic material elastic parameters, i.e., E and v [e.g., *Huang*, 1999]. The chosen stiffnesses corresponded to the macroscopic material elastic properties, E = 14.2 MPa and v = 0.494, determined by the simulation of a confined compression test on the assembly.

The effect of fluid cell size was investigated to obtain a proper resolution for the fluid flow. Nearly identical results were achieved with the coarse (6 mm) and fine (3 mm) meshes, as shown in Figures 6.4 and 6.5. The fine mesh was used in the simulations

afterwards.

It is important to note that the fluid velocities shown in Figure 6.4 and in the following sections are unrealistically high due to the numerical difficulties in creating a dense packing as well as due to the timestep restriction with small particle sizes in *PFC*^{2D}. In fact, our numerical simulations are modeling a loose assembly with high permeability. Using empirical equations such as that of Kozeny-Carmen [e.g., *Bear*, 1988], the permeability of the assembly can be estimated by

$$k = c_k \frac{D_p^2 n^3}{(1-n)^2} \tag{6.7}$$

Using the default value of c_k employed in *PFC*^{2D}, i.e., $c_k = 1/150$, (6.7) results in the permeability, $k \approx 220$ Darcy, of the assembly used in our simulation, which is much higher than that of the particulate material tested in the laboratory (typically only a few darcy). Note that in (6.7) 3D porosity should be used.

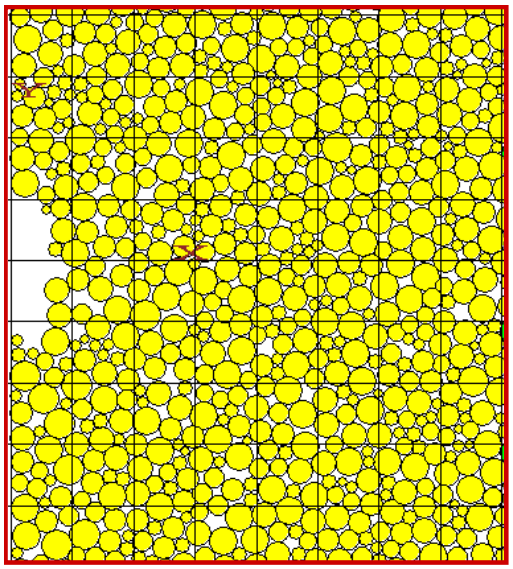

(a)

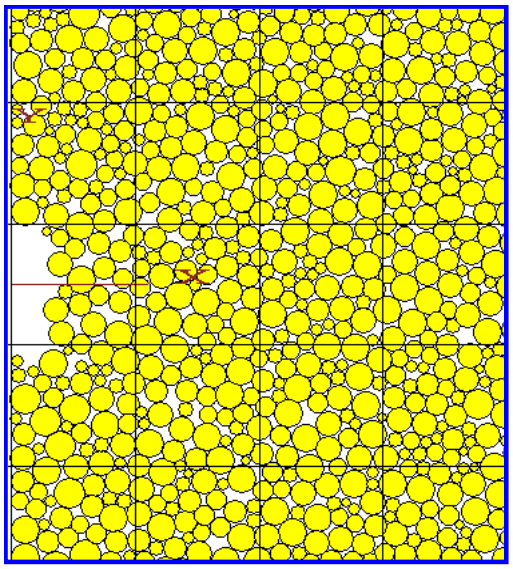

(b)

Figure 6.4. Cavity formation at the injection velocity v_{in} = 123 m/s in the (a) fine mesh (c = 3 mm) and (b) coarse mesh (c = 6 mm).

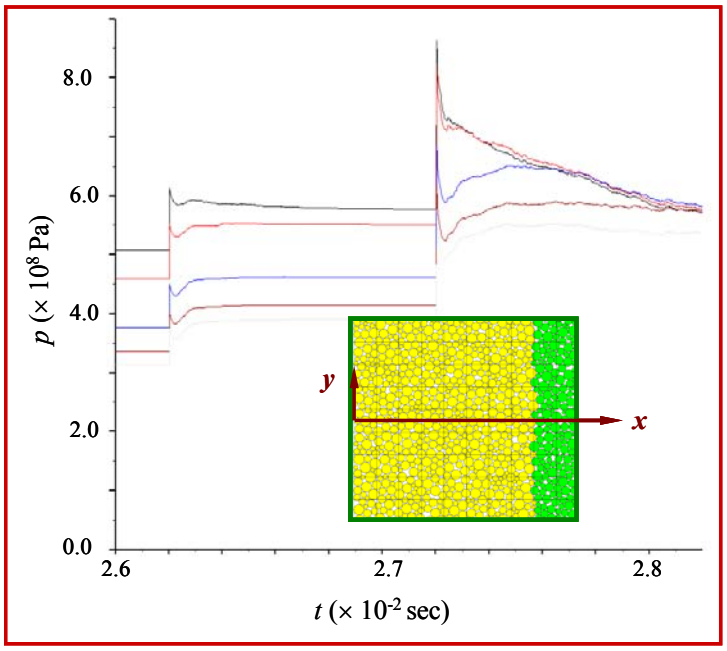

(a)

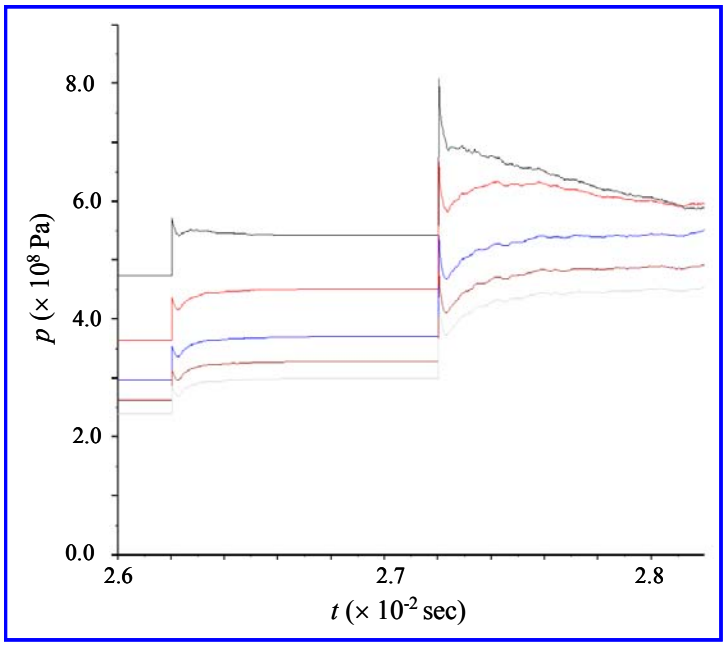

(b)

Figure 6.5. Pressure history at the first five fluid cell along the x-axis in the (a) fine mesh (c = 3 mm) and (b) coarse mesh (c = 6 mm).

6.3 Results of Numerical Simulation

Fluid was injected into the assembly from the left side boundary at a velocity increased stepwisely. Due to the drag forces applied by the fluid flow, particles tend to move away from the injection point. When the fluid velocity reaches a critical value, a cavity forms in the vicinity of the injection point. For all considered cases, we observed three stages of cavity propagation (Figure 6.6) with increasing injection fluid velocity. These three stages are cavity initiation, stable cavity growth, and unstable cavity propagation. The pressure history curve corresponding to the loading process is shown in Figure 6.7 for the base combination of parameters.

When the injection velocity is low, the drag force is not sufficient to overcome the confinement and particles do not move (i.e., only small elastic deformation occurs). Thus, no cavity forms at this time, and the pore pressure inside the assembly quickly reaches a stable state, which is called “fixed bed flow” (Figure 6.6a). As the injection velocity increases, the drag force exerted on the particles increases as well. At the critical injection velocity, the drag force becomes sufficiently large to overcome the resistance due to the boundaries confinement. Particles start to move and a cavity begins to form, which ends the cavity initiation stage.

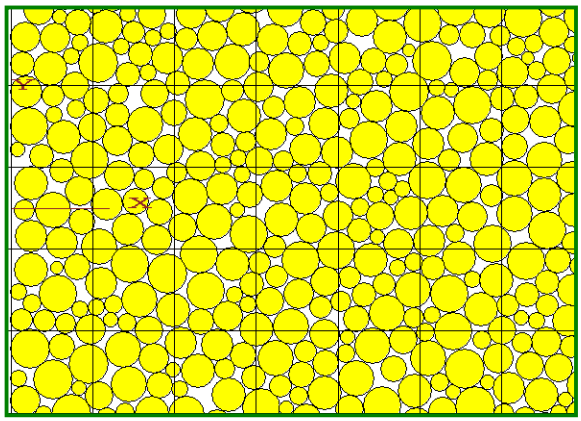

(a)

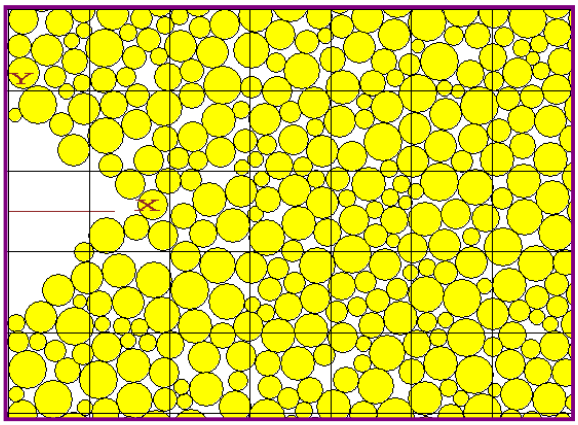

(b)

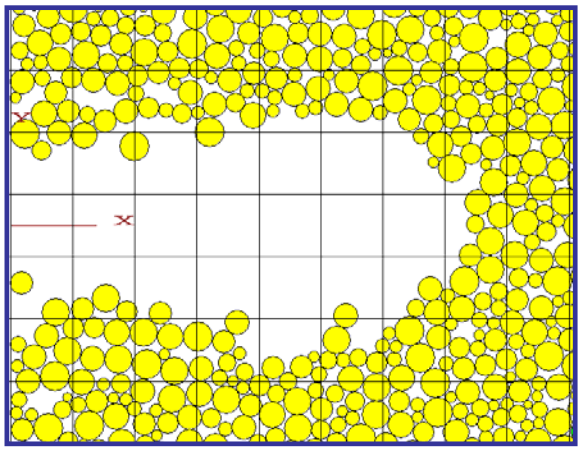

(c)

Figure 6.6. Observed stages of cavity propagation: (a) “fixed bed flow” during the cavity initiation stage, (b) stable cavity development, and (c) unstable cavity propagation.

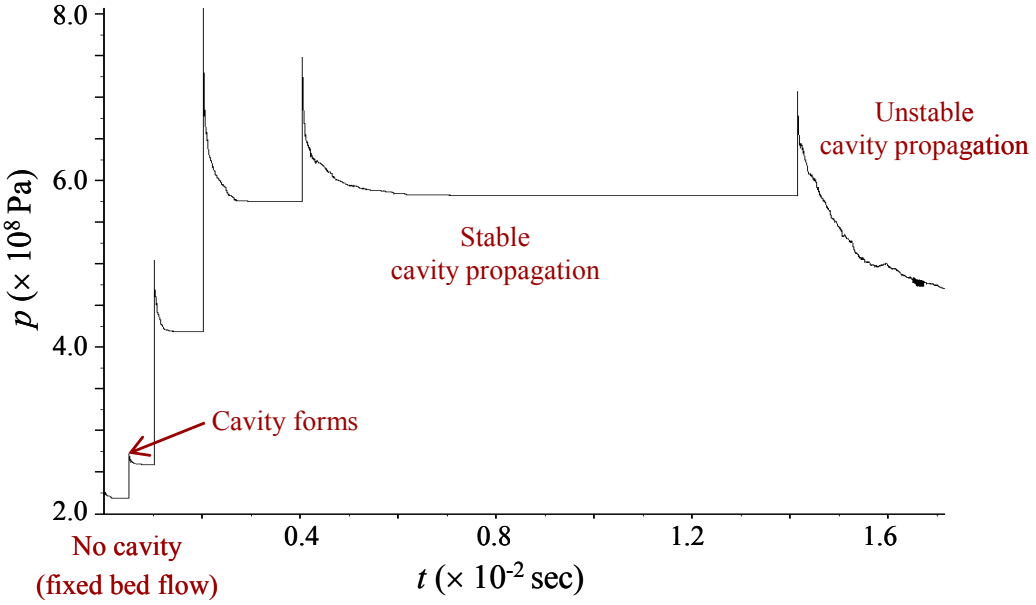

Figure 6.7. Pressure history curve for the base combination of parameters and the injection velocities, v_{in} = 135 m/s, 154m/s, 230 m/s, 338m/s, 395 m/s, and 445 m/s.

The occurrence of cavity initiation is identified with respect to two subsequent stages, i.e., no cavity stage and stable cavity propagation stage. In our simulation, the second injection stage is identified as the stage of cavity initiation with the maximum ratio of particle displacement in x-direction to the particle diameter exceeding 0.1 (Figure 6.8).

When the injection velocity increases, the cavity starts propagating, and after a certain period of time, pressure stabilizes and the cavity growth stops. This is the stage of stable cavity development (Figure 6.6b).

The stage of unstable cavity propagation (Figure 6.6c) occurs when the fluid velocity reaches a second critical value (usually much higher than the critical velocity of cavity initiation). At this moment, the cavity growth becomes unstable. In this work, we

are more interested in the mechanism of cavity initiation, and in the dependence of the critical injection velocity on the fluid and matrix material properties, as well as on the boundary loading parameters (confinement).

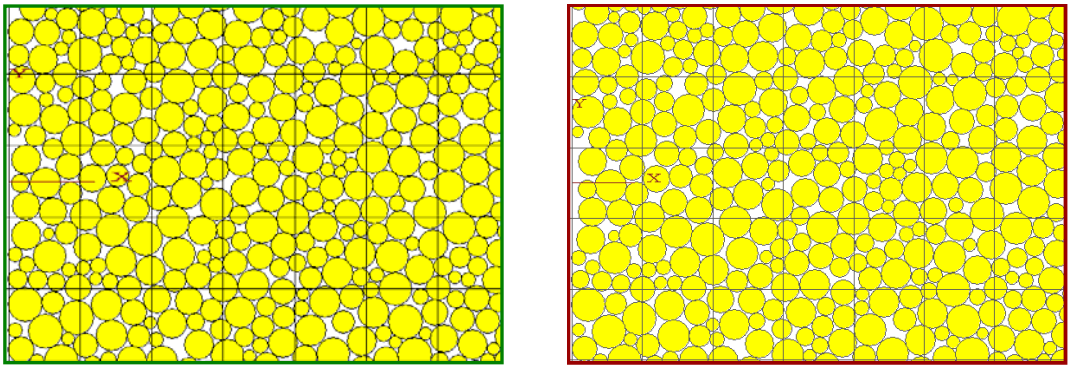

(a) (b)

Figure 6.8. Stabilized particle positions near the injection point just (a) before and (b) after the cavity initiation. The fluid velocities at these moments are 135 m/s and 154 m/s, respectively, and correspond to the first two steps in Figure 6.7.

To investigate the effect of fluid viscosity on the cavity initiation velocity, we conducted numerical experiments with five different viscosity values, i.e., μ_f = 1 cp, 10 cp, 100 cp, 10^3 cp, and 10^4 cp. The dependence of the critical injection velocity, v_{cr}, corresponding to cavity initiation, on the fluid viscosity is shown in Figure 6.9. The figure shows that while in the low viscosity region the fluid viscosity has little or no effect on the critical velocity, the critical velocity decreases considerably with increasing fluid viscosity when the fluid viscosity is greater than 100 cp.

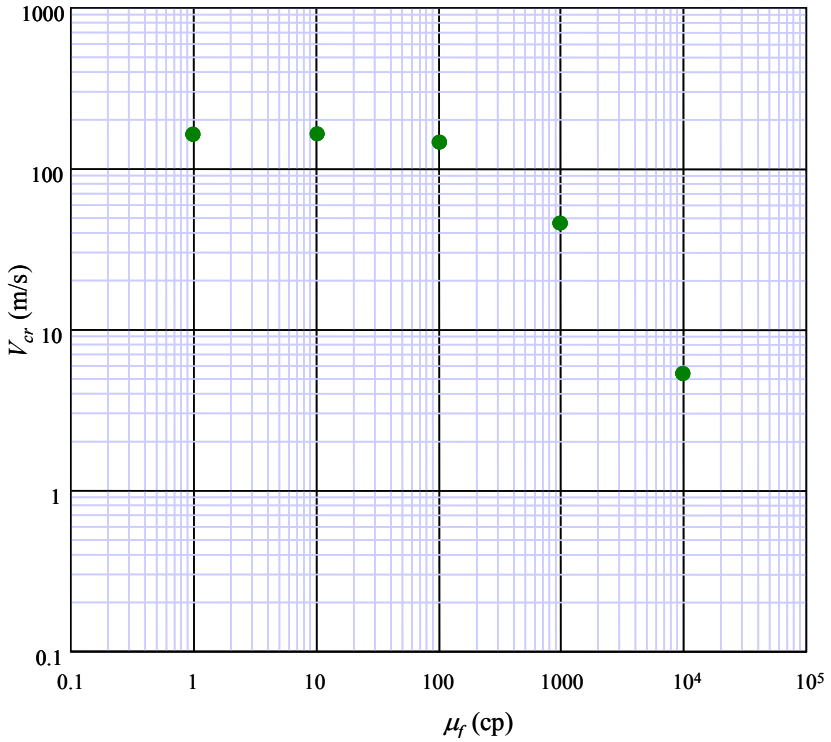

Figure 6.9. Dependence of the critical initiation velocity on fluid viscosity for the base combination of material parameters.

To conduct further parametric analysis, it is highly desirable to have at least a simplified theoretical model as a guideline. Indeed, the large number of relevant parameters (i.e., ρ_p, ρ_f, K_n, K_s, σ_1', σ_3', μ, μ_f, D_p, n) makes it hardly practical to vary them all. One such model, which also helps to understand principal mechanisms more clearly, is described below.

6.4 Fluidization Mechanism of Cavity Initiation

The contact forces between the particles at both low fluid velocity and critical fluid velocity (before the cavity initiates) in the *PFC*^{2D} simulation are shown in Figure 6.10. As can be seen, the contact forces between the particles located near the injection

inlet decrease with increasing injection velocity. At critical velocity, these forces are close to zero. This suggests that, although the overall particle assembly is loaded by confining stresses, due to the drag forces induced by the fluid flow, particles in the vicinity of the injection point become loose, which indicates that particles are effectively fluidized at the stage of cavity initiation.

In fluid dynamics, fluidization represents a typical example of vertical liquid-solid flow. In the fluidized bed system, solid particles start to fluidize when the velocity of the liquid is so large that gravity and buoyancy forces acting on the particles could be counterbalanced by the drag force induced by liquid. One common method to predict the minimum fluidization velocity is to utilize a dynamic pressure drop-velocity relationship from a fixed bed, e.g., Ergun's equation [*Ergun*, 1952], and to let it be equal to the apparent weight of the solid particles of a unit cross-sectional bed area [*Jean and Fan*, 1998]. The process of fluidization is equivalent to liquefaction in soil mechanics terms, in which case the total stress is balanced by the pore pressure and the effective stress becomes zero.

Since for our problem gravitation is ignored while the particle is loaded by confining stress, by simple analogy, if one could replace the gravitational gradient with a certain stress gradient, it would be possible to find a simple criterion for predicting the critical cavity initiation velocity. However, the appropriate physical mechanism of this stress gradient is difficult to obtain. Instead, we will hypothesize the cavity initiation mechanism as follows.

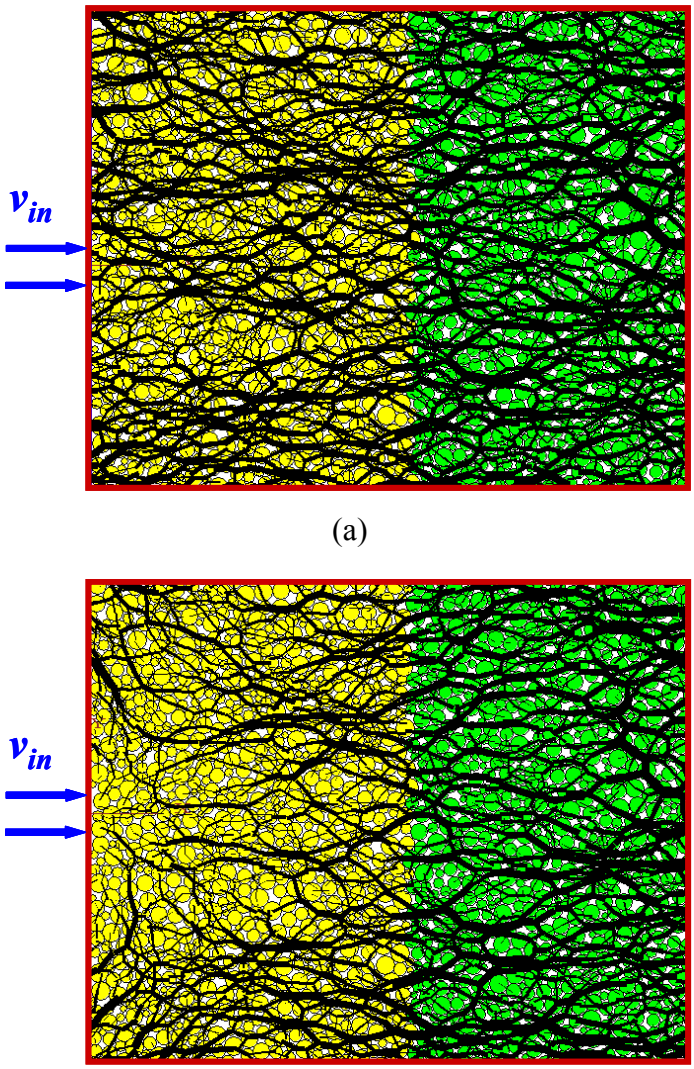

Figure 6.10. Distribution of contact forces between the particles for (a) low fluid velocity (v_{in} = 1 m/s) and (b) critical fluid velocity (v_{in} = 5 m/s). In this PFC^{2D} simulation, the fluid viscosity is 10^4 cp. The thickness of the black lines indicates the relative scale of contact force magnitude.

In the zone adjacent to the injection source, particles are unloaded due to the drag forces generated by the fluid flow. These forces tend to move the particles away from the source. When both principal components of the effective stresses between the particles become zero, the contact between the particles is lost in all direction. At this moment, the

process of liquefaction begins in the particle assembly, and a "liquefied" zone forms near the injection source (Figure 6.11a). This is similar to the liquefaction hypothesis for hydraulic fracture initiation in particulate materials [*Chang*, 2004; *Hurt et al.*, 2005] and for simulating slurry flow in soft rocks [*Chin and Montgomery*, 2004].

However, immediately after liquefaction, the strain is still small, meaning that the particles only lost contact but have not moved any noticeable distance. When the fluid injection velocity increases, so do the drag forces, and the liquefaction front propagates into the particulate material enveloping the injection source (Figure 6.11a). On the liquefaction boundary, the principal effective stresses are equal to zero. Assuming for simplicity that the liquefied zone behind the liquefaction front has a quasi-radial shape (since the fluid flow is approximately radial near the source), we can write the condition on the liquefaction boundary as

$$\sigma_{rr}' = \sigma_{\theta\theta}' = 0 \qquad (r = r_1) \tag{6.8}$$

The actual fluidization of the material inside the "liquefied" zone may occur only when the packing of the particles becomes sufficiently loose for them to start moving distances comparable to their sizes. Therefore, the fluidization occurs when the volumetric strain, ε_v, in the liquefied zone reaches a critical value, ε_{cr}. Therefore, we hypothesize that the cavity initiation begins when

$$\varepsilon_v = \varepsilon_{cr} \tag{6.9}$$

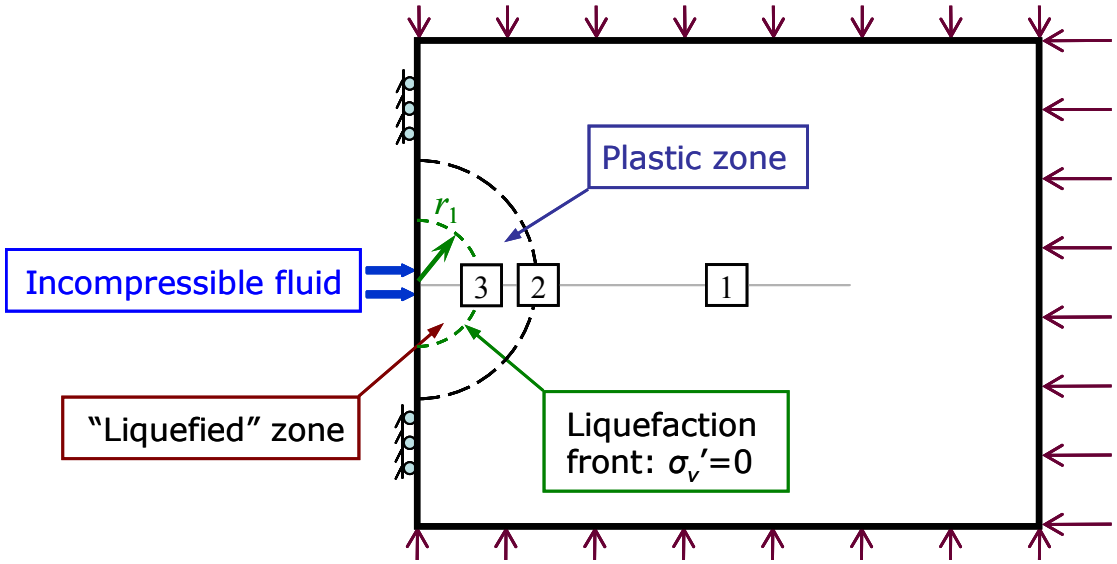

(a)

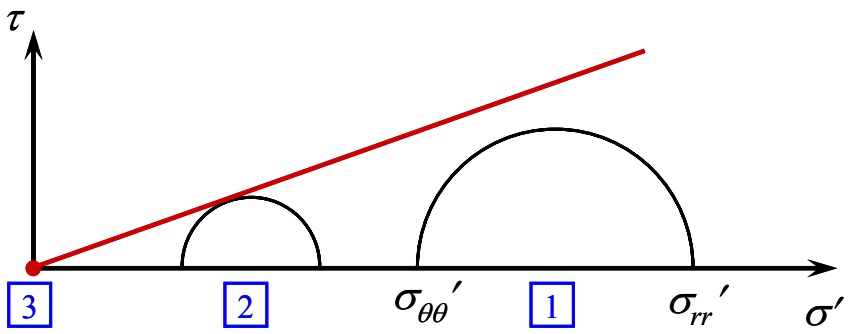

(b)

Figure 6.11. Cavity initiation mechanism: (a) the "liquefied" and plastic zones, and (b) Mohr-Coulomb diagram showing the state of three representative volume elements located in the elastic zone (element 1), plastic zone (element 2) and liquefied zone (element 3), respectively.

Consider now three representative volume elements as shown in Figure 6.11a. For a Mohr-Coulomb material, the stress states in these elements are shown in Figure 6.11b. Element 3 (expression (6.8)) represents the material on the liquefaction boundary (Figure 6.11b), while element 1 represents the material in the ambient compression at a location away from the source. Note that since the cohesionless particulate material cannot bear tensile stress, all material parts are in compression and at some point, the material yields due to the stress decrease.

The Mohr-Coulomb diagram in Figure 6.11b shows that with stress decreasing from the remote location to the liquefaction boundary, the plastic zone (element 2) must appear outside the "liquefied" zone. Nevertheless, in order to obtain a closed-form solution and clarify the scaling relationships, we further ignore the existence of this plastic zone and give an approximate poroelastic solution for the problem under consideration.

6.5 Closed-Form Solution for Pressure Distribution

6.5.1 Exact Solution for Darcy Flow

The pressure distribution of the point source located at the center of the rectangular plate $\{-H < x < H, -L/2 < y < L/2\}$ (Figure 6.12) satisfies the Poisson equation [e.g., *Bear*, 1988]

$$\frac{\partial^2 p}{\partial x^2} + \frac{\partial^2 p}{\partial y^2} = -\frac{\mu_f}{k} Q\delta(x)\delta(y) \tag{6.10}$$

and boundary conditions

$$p(x,y) = p_1 \qquad (x = \pm H, \quad -L/2 < y < L/2) \tag{6.11}$$

$$\frac{\partial p}{\partial y}(x,y) = 0 \qquad (y = \pm L/2, \quad -H < x < H) \tag{6.12}$$

Here, we consider a slightly more general case than in *PFC* simulations (Figure 6.2), that is, the pressure at the left and right boundaries of the rectangular domain is not necessarily zero (Figure 6.12).

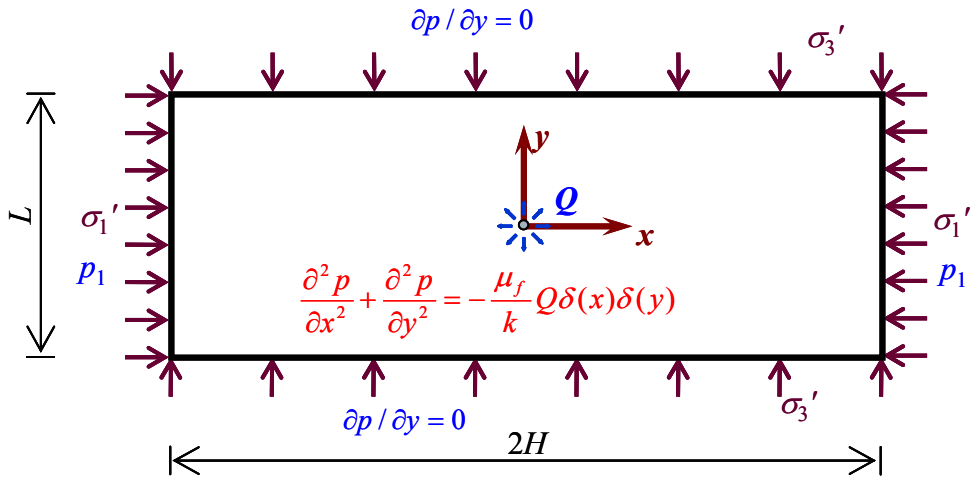

Figure 6.12. Simplified model: a point source in a finite rectangular plate.

The exact solution to this boundary value problem can be written in the form of Fourier series:

$$p(x,y) = p_1 + \frac{\mu_f}{k}\frac{4Q}{\pi^2 HL}\sum_{n=1}^{\infty}(-1)^{n+1}\sin\frac{\pi(2n-1)(x+H)}{2H}\left[\frac{H^2}{(2n-1)^2} + \sum_{k=1}^{\infty}\frac{(-1)^k}{\frac{(2n-1)^2}{4H^2}+\frac{4k^2}{L^2}}\cos\frac{\pi k(2y+L)}{L}\right] \tag{6.13}$$

The contour plot of pressure distribution (6.13) is shown in Figure 6.13 for $p_1 = 0$.

Expression (6.13) can further be used to find the corresponding stress and strain distributions, which is possible based on the fundamental solutions of the biharmonic equation for a rectangular domain. This process, however, is quite laborious, and, more importantly, (6.13) only describes the linear Darcy flow. Since we further need a solution for non-Darcy fluid flow, we obtain below an approximate simplified solution that can be employed for non-Darcy flow as well.

Figure 6.13 suggests that the pressure distribution can be approximated by the radial flow near the injection source and by the 1-D flow in the remote zone. This indicates that it may be possible to find an approximate solution by matching (interpolating) the radial (source) and 1-D flow solutions at a certain point, r_0.

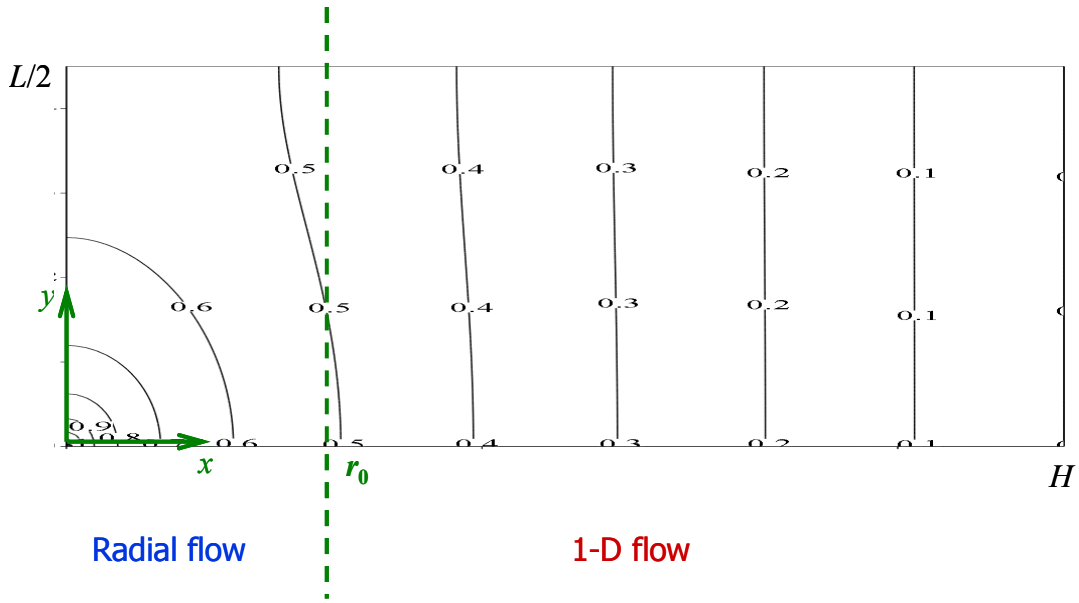

Figure 6.13. Contour plot of pressure distributions (6.13) in a finite, rectangular plate.

6.5.2 Approximate Solution for Darcy flow

For the radial Darcy flow, the pressure gradient is given by

$$\frac{\partial p}{\partial r} = -\frac{\mu_f}{k}\frac{Q}{2\pi}\frac{1}{r} \tag{6.14}$$

where μ_f is the dynamic viscosity of the injection fluid, k is the permeability, and Q is the injection rate. Hence, the pressure distribution is

$$p = -\frac{\mu_f}{k}\frac{Q}{2\pi}\ln\frac{r}{r_0} + p_0 \tag{6.15}$$

Here r_0 is the matching point where pressure $p = p_0$.

The 1-D Darcy flow is described by

$$\frac{\partial p}{\partial x} = -\frac{\mu_f}{k}q \tag{6.16}$$

where

$$q = \frac{Q}{2L} \tag{6.17}$$

is the apparent fluid velocity independent of x, y. Therefore, the pressure distribution that corresponds to (6.16) and the boundary condition $p(H) = p_1$ is

$$p(x) = \frac{\mu_f}{k}\frac{Q}{2L}(H - x) + p_1 \tag{6.18}$$

To use the combination of the radial and 1-D flows, we further require that both the pressure and the pressure gradient are continuous at $r = x = r_0$

$$\left.\frac{\partial p(r)}{\partial r}\right|_{r=r_0} = \left.\frac{\partial p(x)}{\partial x}\right|_{x=r_0} \tag{6.19}$$

$$\left.p(r)\right|_{r=r_0} = \left.p(x)\right|_{x=r_0} \tag{6.20}$$

Substituting (6.15), (6.16), and (6.17) into (6.19), we find

$$r_0 = \frac{L}{\pi} \tag{6.21}$$

while substituting (6.14) and (6.18) into (6.20), we obtain the corresponding pressure at $r = x = r_0$:

$$p_0 = \frac{\mu_f}{k}\frac{Q}{2L}(H - r_0) + p_1 \tag{6.22}$$

Hence, the pressure distribution along the x-axis can be expressed by combining (6.14) and (6.18):

$$p = \begin{cases} -\dfrac{\mu_f}{k}\dfrac{Q}{2\pi}\ln\dfrac{\pi x}{L} + p_0 & (0 < x < r_0 = L/\pi,\ y = 0) \\ -\dfrac{\mu_f}{k}\dfrac{Q}{2}\left(\dfrac{x}{L} - \dfrac{H}{L}\right) + p_1 & (x \geq r_0 = L/\pi,\ y = 0) \end{cases} \tag{6.23}$$

The normalized pressure distribution

$$P = p\left(\frac{\mu_f}{k}Q\right)^{-1} \tag{6.24}$$

along the x-axis calculated using both the approximate (6.23) and exact (6.13) solutions for the value of $H/L = 4/3$ (employed in our PFC^{2D} simulations) is plotted in Figure 6.14.

The plot shows that the approximate solution (6.23) fits well the exact solution (6.13).

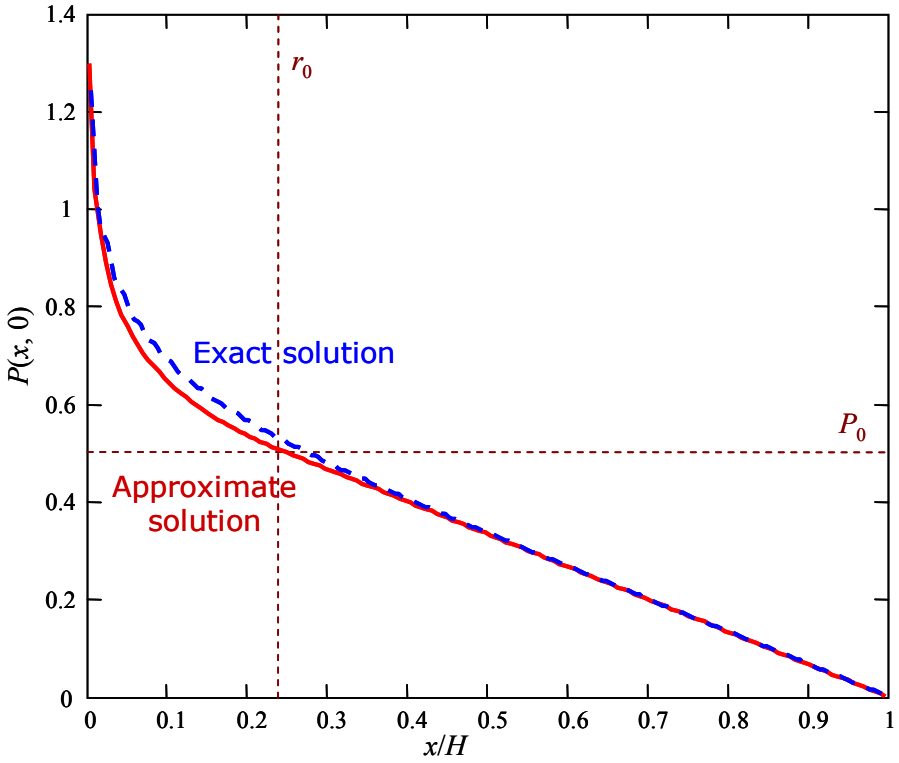

Figure 6.14. Source in a rectangular plate: normalized pressure distribution along the x-axis. The solid and dash lines represent the approximate (6.23) and exact (6.13) solutions, respectively.

6.5.3 Approximate Solution for non-Darcy flow

In order to match the numerical simulation results, it is desirable to consider non-Darcy flow and include the nonlinear fluid effect ($\sim q^2$) in the pressure gradient. However, in the case of non-Darcy flow, no exact solution is available. A similar approximate solution as that for Darcy flow is adopted here for the nonlinear flow problem.

For non-Darcy flow, the pressure gradient is typically written in the quadratic form [e.g., *Bear*, 1988]:

$$\nabla p = -\frac{\mu_f}{k} q - \beta \rho_f q^2 \tag{6.25}$$

where the first term represents the viscous resistance to the fluid flow while the second term, describing the deviation from the Darcy law, is often attributed to the inertial forces [e.g., *Bear*, 1988]. Since the inertial forces are proportional to the square of velocity and independent of viscosity, the non-Darcy flow rate coefficient, β, is a parameter related to material structure. For example, in *PFC*^{2D}, β is estimated by *Ergun's* [1952] empirical expression

$$\beta = 1.75 \frac{1-n}{D_p n^3} \tag{6.26}$$

For the radial flow, expression

$$q = \frac{Q}{2\pi r} \tag{6.27}$$

is valid for both Darcy and non-Darcy flows. Substituting (6.27) into (6.25) yields

$$\frac{\partial p}{\partial r} = -\frac{\mu_f}{k} \frac{Q}{2\pi} \frac{1}{r} - \beta \rho_f \frac{Q^2}{4\pi^2} \frac{1}{r^2} \tag{6.28}$$

which, after integrating, results in the expression

$$p(r) = -\frac{\mu_f}{k} \frac{Q}{2\pi} \ln \frac{r}{r_0} + \beta \rho_f \frac{Q^2}{4\pi^2} \left(\frac{1}{r} - \frac{1}{r_0} \right) + p_0 \tag{6.29}$$

for the pressure distribution in the case of non-Darcy radial flow.

For 1-D flow, according to (6.25) and (6.17),

$$\frac{\partial p}{\partial x} = -\frac{\mu_f}{k}\frac{Q}{2L} - \beta\rho_f \frac{Q^2}{4L^2} \tag{6.30}$$

Integrating (6.30) and considering that $p(H) = p_1$, we obtain the pressure distribution in the case of 1-D non-Darcy flow:

$$p(x) = \left(\frac{\mu_f}{k}\frac{Q}{2L} + \beta\rho_f \frac{Q^2}{4L^2}\right)(H - x) + p_1 \tag{6.31}$$

As in the case of the linear Darcy flow, we require that both the pressure and the pressure gradient are continuous at $r = x = r_0$ (conditions (6.19) and (6.20)). Substituting (6.28) and (6.30) into (6.19) and solving the obtained quadratic equation we find

$$r_0 = \frac{\mu_f}{k}\frac{Q}{4\pi}\left(\frac{\mu_f}{k}\frac{Q}{2L} + \beta\rho_f \frac{Q^2}{4L^2}\right)^{-1}\left[1 + \sqrt{1 + 4\beta\rho_f \frac{k^2}{\mu_f^2}\left(\frac{\mu_f}{k}\frac{Q}{2L} + \beta\rho_f \frac{Q^2}{4L^2}\right)}\right] \tag{6.32}$$

As expected, substituting $\beta = 0$ into (6.32) reduces it to expression (6.21) for Darcy flow.

Substituting (6.29) and (6.31) into (6.20), we have the corresponding pressure at $x = r_0$:

$$p_0 = \left(\frac{\mu_f}{k}\frac{Q}{2L} + \beta\rho_f \frac{Q^2}{4L^2}\right)(H - r_0) + p_1 \tag{6.33}$$

Combining (6.29) and (6.31), we express the pressure distribution along the x-axis by

$$p(x)=\begin{cases}-\dfrac{\mu_f}{k}\dfrac{Q}{2\pi}\ln\dfrac{r}{r_0}+\beta\rho_f\dfrac{Q^2}{4\pi^2}\left(\dfrac{1}{r}-\dfrac{1}{r_0}\right)+p_0 & (0<r<r_0,\ \ y=0)\\ -\left(\dfrac{\mu_f}{k}\dfrac{Q}{2L}+\beta\rho_f\dfrac{Q^2}{4\pi^2}\right)(x-H) & (x\ge r_0,\ \ y=0)\end{cases} \tag{6.34}$$

which also reduces to the Darcy case (6.23) when $\beta = 0$.

6.6 Stress and Strain Distributions

The notation applied in this chapter is that compressive stresses are negative and fluid pressure is positive. The Terzagi effective stresses are defined as

$$\sigma_{rr}{}' = \sigma_{rr} + p, \qquad \sigma_{\theta\theta}{}' = \sigma_{\theta\theta} + p \tag{6.35}$$

6.6.1 Radial flow

We first review the plane-strain poroelastic problem with radial symmetry in the case when the pressure distribution, $p(r)$, is assumed to be known [e.g., *Wang*, 2000]. In a polar coordinate system, the equilibrium equation can be written in displacements as

$$\frac{d}{dr}\left[\frac{1}{r}\frac{d(ru)}{dr}\right]=c_m\frac{dp}{dr} \tag{6.36}$$

where u is the radial displacement and

$$c_m=\frac{\alpha(1+\nu)(1-2\nu)}{E(1-\nu)} \tag{6.37}$$

is the material parameter.

The general solution to (6.36) is

$$u = \frac{c_m}{r}\int_a^r p(r) r dr + \frac{1}{2} C_1 r + \frac{C_2}{r} \tag{6.38}$$

where a is the radius of the injection hole (which is of the order of the cell size in the *PFC* modeling), C_1 and C_2 are the arbitrary constants yet to be determined. Substituting (6.38) into

$$\varepsilon_{rr} = \frac{du}{dr}, \quad \varepsilon_{\theta\theta} = \frac{u}{r} \tag{6.39}$$

results in

$$\varepsilon_{rr} = c_m \left[p(r) - \frac{1}{r^2}\int_a^r p(r) r dr \right] + \frac{C_1}{2} - \frac{C_2}{r^2} \tag{6.40}$$

$$\varepsilon_{\theta\theta} = \frac{c_m}{r^2}\int_a^r p(r) r dr + \frac{C_1}{2} + \frac{C_2}{r^2} \tag{6.41}$$

Therefore, the corresponding volumetric strain

$$\varepsilon_v = \varepsilon_{rr} + \varepsilon_{\theta\theta} = c_m p(r) + C_1 \tag{6.42}$$

is independent of constant C_2.

Substituting (6.40) and (6.41) into the plane-strain constitutive equations [e.g., *Wang*, 2000]

$$\sigma_{rr} = \frac{E(1-\nu)}{(1+\nu)(1-2\nu)}\left[\varepsilon_{rr} + \frac{\nu}{1-\nu}\varepsilon_{\theta\theta}\right] - \alpha p \tag{6.43}$$

$$\sigma_{\theta\theta} = \frac{E(1-\nu)}{(1+\nu)(1-2\nu)}\left[\varepsilon_{\theta\theta} + \frac{\nu}{1-\nu}\varepsilon_{rr}\right] - \alpha p \tag{6.44}$$

gives the total radial and tangential stresses

$$\sigma_{rr} = -\alpha\frac{1-2\nu}{1-\nu}\frac{1}{r^2}\int_a^r p(r)rdr + \frac{\alpha C_1}{2c_m(1-\nu)} - \frac{1-2\nu}{1-\nu}\frac{C_2}{c_m r^2} \tag{6.45}$$

$$\sigma_{\theta\theta} = -\alpha\frac{1-2\nu}{1-\nu}p(r) + \alpha\frac{1-2\nu}{1-\nu}\frac{1}{r^2}\int_a^r p(r)rdr + \frac{\alpha C_1}{2c_m(1-\nu)} + \frac{1-2\nu}{1-\nu}\frac{C_2}{c_m r^2} \tag{6.46}$$

where α is the Biot poroelastic coefficient. In the case of incompressible solid grains, which is of interest here since it corresponds to the *PFC*^{2D} formulation (section 7.2.1),

$$\alpha = 1 \tag{6.47}$$

Expressions (6.38), (6.43), (6.44), (6.45), and (6.46) represent the general solution of the plane-strain poroelastic problem with radial symmetry. The corresponding effective stresses are defined by (6.35), so that

$$\sigma_{rr}' = -\frac{1-2\nu}{1-\nu}\frac{1}{r^2}\int_{r_1}^r p(r)rdr + p(r) + \frac{C_1}{2c_m(1-\nu)} - \frac{1-2\nu}{1-\nu}\frac{C_2}{c_m r^2} \tag{6.48}$$

$$\sigma_{\theta\theta}' = \frac{\nu}{1-\nu}p(r) + \frac{1-2\nu}{1-\nu}\frac{1}{r^2}\int_{r_1}^r p(r)rdr + \frac{C_1}{2c_m(1-\nu)} + \frac{1-2\nu}{1-\nu}\frac{C_2}{c_m r^2} \tag{6.49}$$

and

$$\sigma_v' = \sigma_{rr}' + \sigma_{\theta\theta}' = \frac{c_m p(r) + C_1}{c_m(1-\nu)} \qquad (r < r_0) \tag{6.50}$$

6.6.2 1-D flow

As in section 6.5, this is the flow in the region $x > r_0$ (Figure 6.13). In the Cartesian coordinate set (x, y), the corresponding plane-strain poroelastic problem can be written [e.g., *Wang*, 2000] in terms of stresses using the equilibrium conditions

$$\frac{\partial \sigma_{xx}}{\partial x} + \frac{\partial \tau_{xy}}{\partial y} = 0, \quad \frac{\partial \tau_{xy}}{\partial x} + \frac{\partial \sigma_{yy}}{\partial y} = 0 \tag{6.51}$$

the compatibility condition

$$\left(\frac{\partial^2}{\partial x^2} + \frac{\partial^2}{\partial y^2} \right)(\sigma_{xx} + \sigma_{yy} + 2\eta_0 p) = 0, \quad \eta_0 = \frac{1-2\nu}{2(1-\nu)}\alpha \tag{6.52}$$

and the fluid diffusion equation

$$\left(\frac{\partial^2}{\partial x^2} + \frac{\partial^2}{\partial y^2} \right)\left[\sigma_{xx} + \sigma_{yy} + \frac{3}{B(1+\nu)} p \right] = 0 \tag{6.53}$$

where B is the Skempton pore pressure coefficient.

The solution of (6.51) – (6.53) that satisfies the boundary conditions

$$\sigma_{xx}'(x,y)=\sigma_1', \quad p(x,y)=p_1 \qquad (x=\pm H, \quad -L/2<y<L/2) \tag{6.54}$$

$$\sigma_{yy}'(x,y)=\sigma_3', \quad \frac{\partial p(x,y)}{\partial y}=0 \qquad (y=\pm L/2, \quad -H<x<H) \tag{6.55}$$

is given by equation (6.34) for pressure and expressions

$$\sigma_{xx}(x,y)=\sigma_1'-p_1, \quad \sigma_{yy}(x,y)=\sigma_3'-p(x), \quad \tau(x,y)=0 \tag{6.56}$$

for total stresses. This can be checked by the direct substitution of (6.34) and (6.56) into (6.51) – (6.53).

As can be concluded from (6.35) and (6.56), the effective stresses

$$\sigma_{xx}'(x,y)=\sigma_1'+[p(x)-p_1], \quad \sigma_{yy}'(x,y)=\sigma_3' \tag{6.57}$$

are negative (compressive) everywhere in the region of 1-D flow. Strains in this region can be written as

$$\varepsilon_{xx}=\varepsilon_{xx}^0+\Delta\varepsilon_{xx}, \quad \varepsilon_{yy}=\varepsilon_{yy}^0+\Delta\varepsilon_{yy} \tag{6.58}$$

where

$$\varepsilon_{xx}^0=\frac{1-\nu^2}{E}\left[\sigma_1'-\frac{\nu}{1-\nu}\sigma_3'\right], \quad \varepsilon_{yy}^0=\frac{1-\nu^2}{E}\left[\sigma_3'-\frac{\nu}{1-\nu}\sigma_1'\right] \tag{6.59}$$

are the strains due to the confining stresses, σ_1' and σ_3', and

$$\Delta\varepsilon_{xx} = -\frac{1-\nu^2}{E}[p_1 - p(x)], \quad \Delta\varepsilon_{yy} = \frac{\nu(1+\nu)}{E}[p_1 - p(x)] \tag{6.60}$$

are the strains due to the seepage (drag) forces caused by the fluid flow. Therefore, the corresponding volumetric strains are given by $\varepsilon_v{}^0 = \varepsilon_{xx}{}^0 + \varepsilon_{yy}{}^0 = c_m(1-\nu)(\sigma_1' + \sigma_3')$, and $\Delta\varepsilon_v = \Delta\varepsilon_{xx} + \Delta\varepsilon_{yy} = c_m(1-\nu)p(x)$, so that the total volumetric strain is

$$\varepsilon_v = \varepsilon_v^0 + \Delta\varepsilon_v = c_m\left[(1-\nu)p(x) + \sigma_1^{'} + \sigma_3^{'}\right] \tag{6.61}$$

6.6.3 Matched solution

The integration constants, C_1 and C_2, can be determined by matching displacements and strains at $r = x = r_0$, that is,

$$u(r)\Big|_{r=r_0} = u(x)\Big|_{x=r_0} \tag{6.62}$$

$$\frac{\partial u}{\partial r}\Big|_{r=r_0} = \frac{\partial u}{\partial x}\Big|_{x=r_0} \tag{6.63}$$

One of these conditions, say (6.63), can be replaced by their linear combination. Therefore, the continuity of volumetric strain can be used instead of (6.63):

$$\varepsilon_v(r)\Big|_{r=r_0} = \varepsilon_v(x)\Big|_{x=r_0} \tag{6.64}$$

Substituting (6.39) and (6.40) into (6.64), we obtain

$$C_1 = c_m[-\nu p_0 + (1-\nu)(\sigma_1' + \sigma_3' - p_1)] \tag{6.65}$$

We do not give here an expression for C_2 since we do not need it for further

purposes. Also note that (6.42), (6.43), and (6.19) ensure that all stress components are also matched at $r = x = r_0$, which is expected in continuous material.

6.6.4 Fluidization Criterion

In this section, we estimate the volumetric strain near the injection source, i.e., on the boundary, $r = a$, of a circular area with a diameter equal to the size, a, of the injection place in the *PFC* model.

Substituting $r = a$ into (6.61) and considering (6.42), we obtain the expression for the total volumetric strain:

$$\varepsilon_v = \frac{(1+\nu)(1-2\nu)}{E}\left[\sigma_1' + \sigma_3' + \frac{\nu}{1-\nu}p_1 + \left(\frac{\mu_f}{k}\frac{Q}{2L} + \beta\rho_f\frac{Q^2}{4L^2}\right)(H-r_0) + \right.$$
$$\left. - \frac{1}{1-\nu}\frac{\mu_f}{k}\frac{Q}{2\pi}\ln\frac{a}{r_0} + \frac{\beta\rho_f}{1-\nu}\frac{Q^2}{4\pi^2}\left(\frac{1}{a}-\frac{1}{r_0}\right)\right] \tag{6.66}$$

Combining (6.9) and (6.66), we arrive at the equation for the critical flow rate of fluidization:

$$(1-\nu)\left(\frac{\mu_f}{k}\frac{Q_{cr}}{2L} + \beta\rho_f\frac{Q_{cr}^2}{4L^2}\right)(H-r_0) - \frac{\mu_f}{k}\frac{Q_{cr}}{2\pi}\ln\frac{a}{r_0} + \beta\rho_f\frac{Q_{cr}^2}{4\pi^2}\left(\frac{1}{a}-\frac{1}{r_0}\right) =$$
$$= \frac{E(1-\nu)}{(1+\nu)(1-2\nu)}\varepsilon_{cr} - (1-\nu)(\sigma_1' + \sigma_3') - \nu p_1 \tag{6.67}$$

where r_0 is given by (6.32).

The critical injection velocity for the problem shown in Figure 6.2 is defined as

$$v_{cr} = \frac{Q_{cr}/2}{2a} = \frac{Q_{cr}}{4a} \tag{6.68}$$

We introduce the characteristic velocity

$$v_0 = \sqrt{\frac{D}{\beta \rho_f A_2}} \tag{6.69}$$

and define the dimensionless velocity

$$v_{cr}^* = \frac{2a}{L}\frac{v_{cr}}{v_0} \tag{6.70}$$

and the dimensionless viscosity

$$\mu_f^* = \frac{\mu_f}{k\beta\rho_f v_0}\frac{A_1}{A_2} \tag{6.71}$$

where

$$D = \frac{E(1-\nu)}{(1+\nu)(1-2\nu)}\varepsilon_{cr} - (1-\nu)(\sigma_1' + \sigma_3') \tag{6.72}$$

$$A_1 = (1-\nu)\left(H - \frac{L}{\pi}\right) + \frac{L^2}{\pi^2}\left(\frac{1}{a} - \frac{\pi}{L}\right) \tag{6.73}$$

$$A_2 = (1-\nu)\left(H - \frac{L}{\pi}\right) - \frac{L}{\pi}\ln\frac{\pi a}{L} \tag{6.74}$$

Based on expression (6.67), the dependence of the dimensionless injection velocity v_{cr}^* on the dimensionless fluid viscosity μ_f^* is plotted in Figure 6.15. For the two end-member cases, $\mu_f^* << 1$ and $\mu_f^* >> 1$, the critical velocity shows different dependence

on the viscosity:

$$v_{cr}^{*}=\begin{cases}1-\dfrac{1}{2}\mu_f^{*}+O(\mu_f^{*2}) & (\mu_f^{*}\to 0)\\ \dfrac{1}{\mu_f^{*}}+O(1/\mu_f^{*2}) & (\mu_f^{*}\to\infty)\end{cases} \tag{6.75}$$

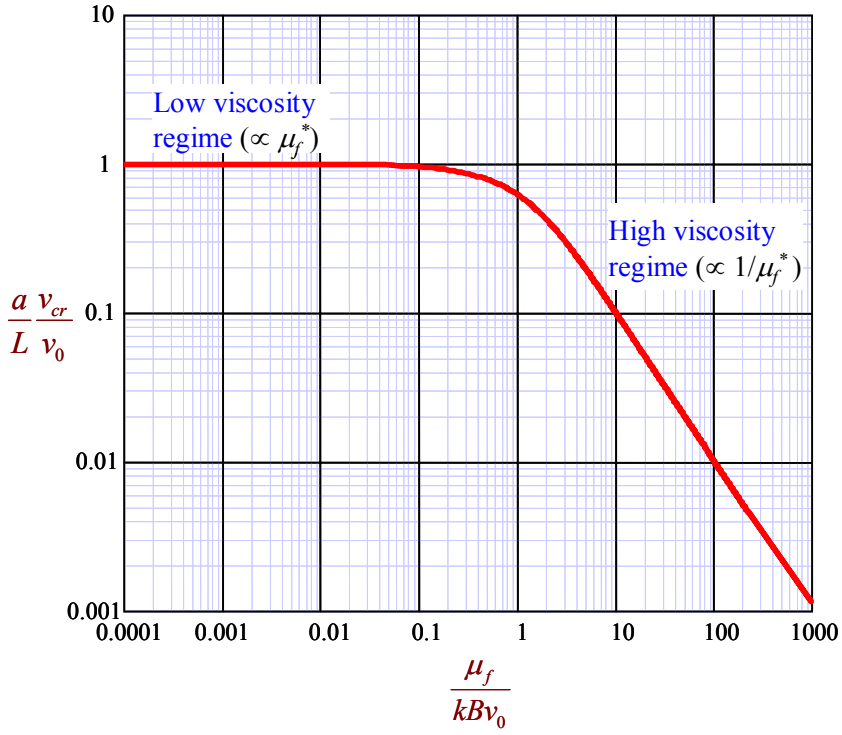

Figure 6.15. The dependence of dimensionless injection velocity v_{cr}^{*} on the dimensionless fluid viscosity μ_f^{*}.

In this dimensionless form, there are no matching parameters. As a result, theoretical and possible experimental results would be completely independent. The comparisons between the theoretical prediction and numerical experiments are given in the next section.

As shown in Figure 6.15, the dependence of the injection velocity on the fluid

viscosity can be distinguished by two regimes: inertial governing regime and viscosity governing regime. The inertial governing regime occurs with low fluid viscosity when the energy dissipation is mainly due to the second term, Bq^2. In this regime, cavity growth direction is controlled by the confining stress state and becomes an elongated conduit (Figure 6.16a). When fluid viscosity increases, the first term, $(\mu_f/k)q$, gradually becomes dominant, and the energy dissipates mainly through the fluid viscosity. As a result, the cavity propagates along the slipping boundary (Figure 6.16b).

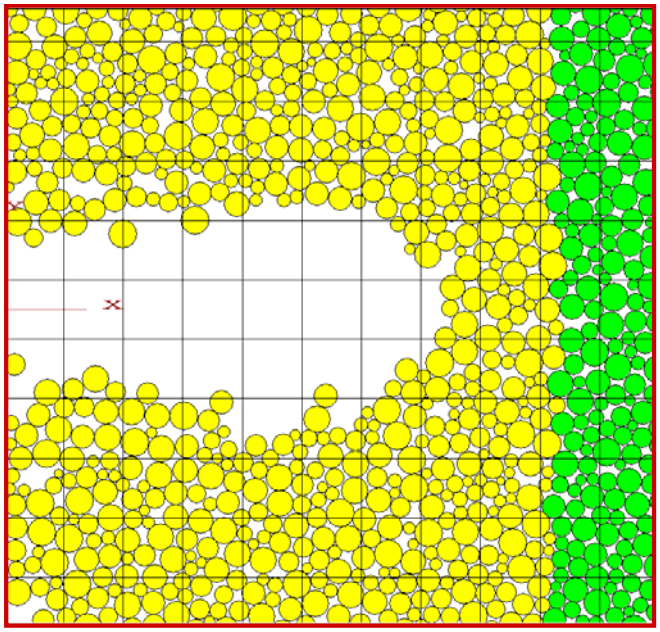

(a)

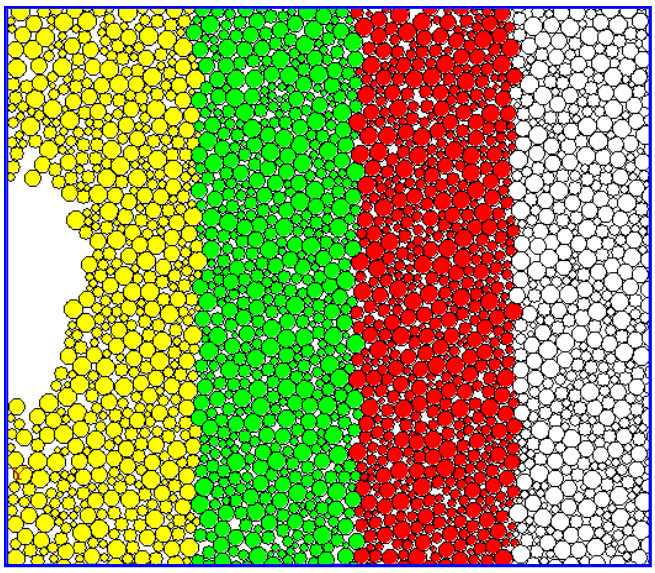

(b)

Figure 6.16. Cavity shape for different fluid viscosities: (a) μ_f = 100 cp, and (b) μ_f = 10,000 cp.

6.6.5 Comparison with Numerical Experiments

The dependence of the dimensional critical injection velocity, v_{cr}, given by expressions (6.67) and (6.68), on the dimensional fluid viscosity, μ_f, for the base combination of parameters used in PFC^{2D} simulations is plotted in Figure 6.17 (solid curve). The dots represent the critical fluid viscosities given by PFC^{2D} simulations (Figure 6.8). We used the same elastic parameters, E = 14.2 MPa and ν = 0.494, as these obtained by the numerical simulation with PFC^{2D} (section 6.3). We employed ε_{cr} as the fitting parameter. The least square method resulted in a value of ε_{cr} = 0.61.

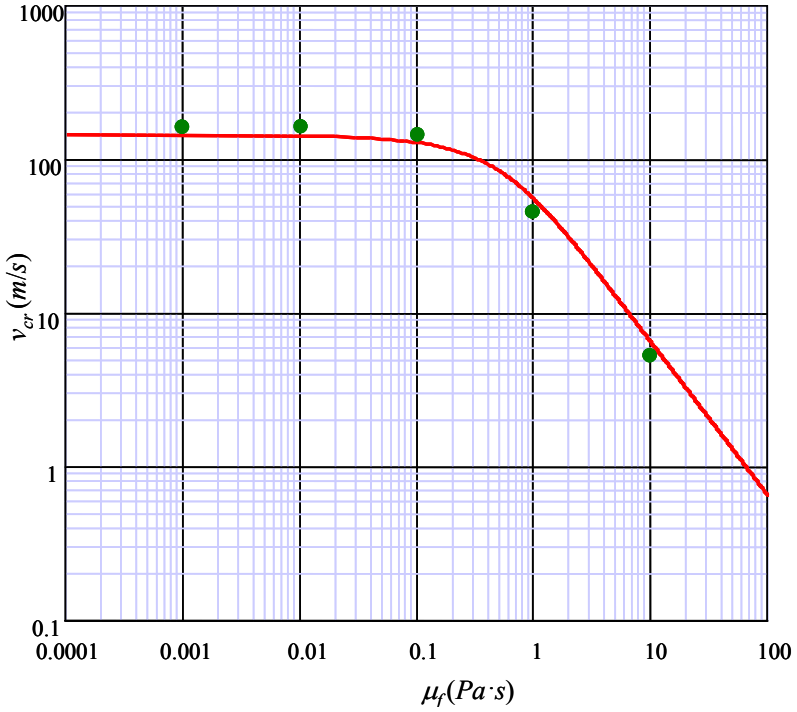

Figure 6.17. The dependence of dimensional injection velocity v_{cr} on the dimensional fluid viscosity, μ_f. The dots show the critical injection velocity obtained from PFC^{2D} simulations (Figure 6.8).

Figure 6.17 shows that the given approximate solution fits well the results of numerical experiments even though the obtained high value of the critical volumetric

strain, ε_{cr}, suggests that the assumption of the small strains is not satisfied near the injection place.

We also compared the pressure distribution given by the approximate solution (6.34) with PFC^{2D} simulation results. In PFC^{2D}, the parameter β is estimated by (6.26) while the permeability is calculated using the Kozeny-Carman equation (6.7). One typical example of the pressure distribution along x-axis is given in Figure 6.18 for the case where μ_f = 10 cp and Q = 0.96 m^2/s. This figure shows that the approximation solution fits well the PFC^{2D} results.

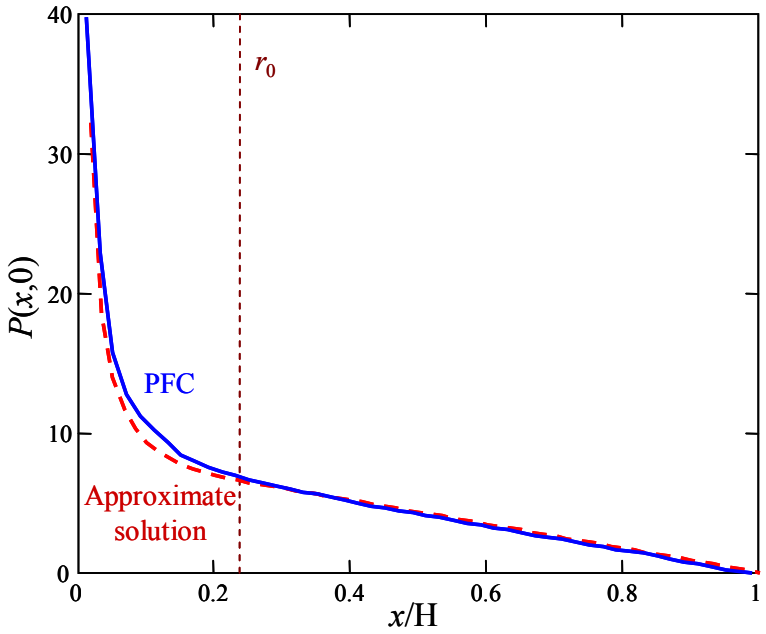

Figure 6.18. The pressure distribution along x-axis: comparison between the approximate solution (6.34) and PFC^{2D} simulation results for the case of μ_f = 10 cp and Q = 0.96 m^2/s.

Finally, the relationship

$$\sigma_v' = c_m(1-\nu)\varepsilon_v \tag{6.76}$$

between the volumetric stress and strain follows from (6.42) and (6.50) and implies that ε_v and σ_v' have the same sign. Since the fluidization criterion (6.9) requires a tensile volumetric strain, according to (6.76), the volumetric stress is also tensile, which is inconsistent with the assumption that the material is in compression everywhere in the cohesionless materials. This contradiction results from neglecting the plastic deformation near the injection point (Figure 6.11). In fact, since (6.76) is essentially a constitutive relationship independent of the boundary conditions, this suggests that in the problem under consideration, *tensile* strain and *compressive* stress can coexist *only* if the plastic deformation develops near the appearing cavity.

Nevertheless, the fact that the approximate solution fits the results of numerical experiments remarkably well indicates that the approximate model probably still captures the main features of the cavity initiation process, in particular, the dependence of the critical injection velocity on the fluid viscosity. This is why we used the obtained approximate solution to simplify the parametric analysis conducted with PFC^{2D} and to derive the relevant scaling relationships.

6.7 Parametric Analysis

In addition to the geometrical parameters (H, L, a, c, D_p, n), the model includes the following relevant material properties (ρ_p, ρ_f, K_n, K_s, μ, μ_f), and loading parameters,

(σ_1', σ_3'). According to expressions (6.26), (6.69), (6.71), (6.72), and (6.7),

$$v_{cr} = \frac{L}{a} v_{cr}^{*} \Phi \left(\frac{K_n D_p}{\rho_f L}, \frac{(\sigma_1' + \sigma_3') D_p}{\rho_f L}, \frac{\mu_f}{D_p \rho_f v_0}, \mu, \frac{H}{L}, \frac{c}{a}, n \right), \tag{6.77}$$

where we took into account that $K_s = K_n \sim E$ [*Huang*, 1999].

When the values of the geometrical parameters and μ are kept constant, (6.77) shows that the injection velocity depends only on three numbers: $K_n D_p/(\rho_f L)$, $(\sigma_1'+\sigma_3')D_p/(\rho_f L)$, and $\mu_f/(D_p \rho_f v_0)$. Accordingly, we varied the following values in the base case proportionally and simultaneously in order to fix the following values: K_n, σ_1', σ_3', ρ_f, and μ_f. Typical results of the cavity shape and the pressure history for the case where K_n = K_s = 100 MN/m, σ_1' = 0.4 MPa, σ_3' = 0.2 MPa, ρ_p = 5300 kg/m^3, ρ_f = 2000 kg/m^3, μ_f = 200 cp, and v_{in} = 242 m/s are shown in Figure 6.19b. The results for the base case are also shown in Figure 6.19a for the sake of comparison. As expected, Figures 6.19a and 6.19b show that the size and the shape of the cavities for both cases are almost identical.

Under the assumption of fluid flow in porous medium, since the gravity force is ignored in the simulation and the particle density only appears in the Newton Law governing the particle motion, particle density is not included in (6.77) and should not affect the stabilized pressure. However, since the fluid velocity is extremely high in the simulation, it is necessary to check whether the inertial effect due to particle flow is important. For example, considering the case of slurry flow, the pressure gradient of non-Darcy flow (i.e., (6.25) and (6.26)) should be expressed as

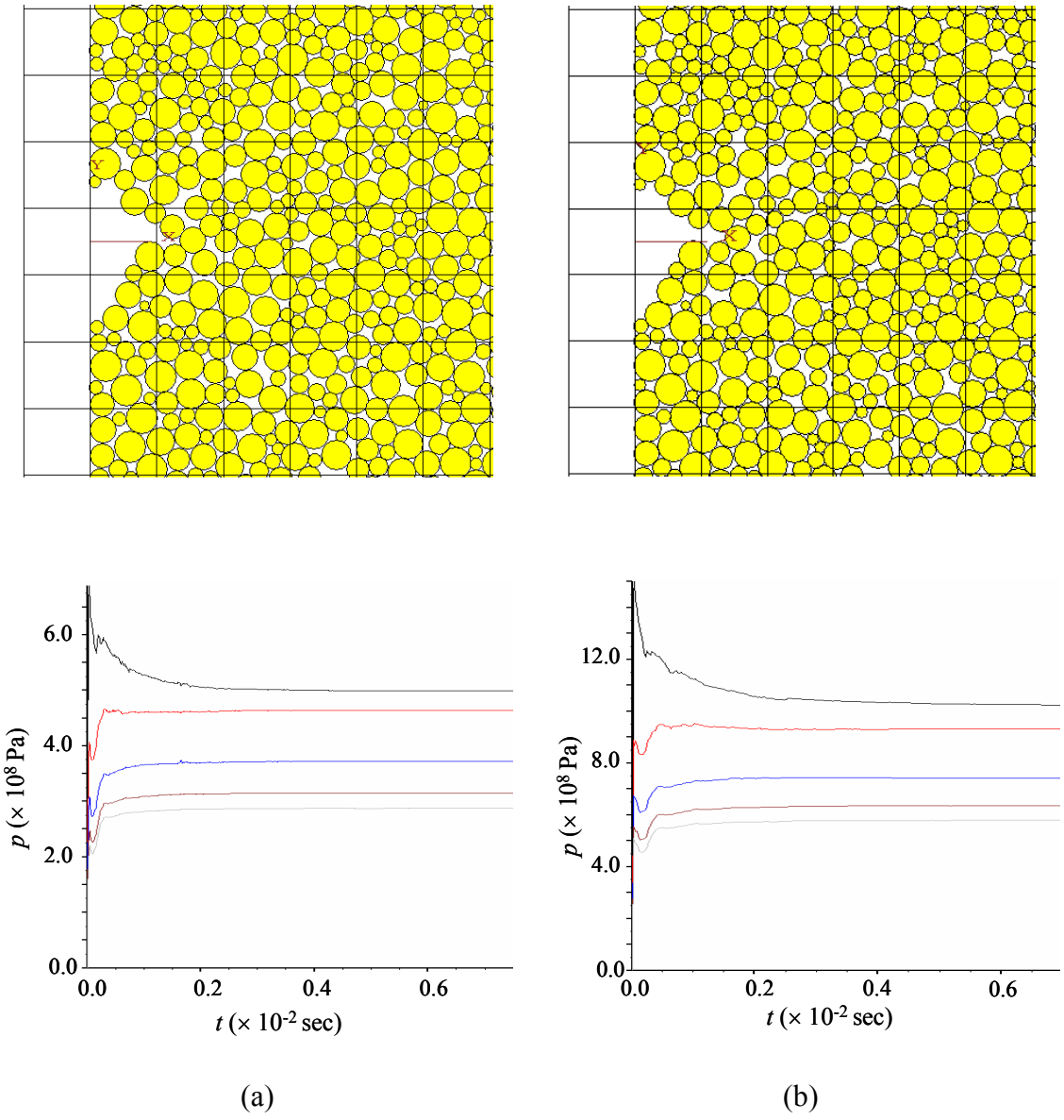

(a) (b)

Figure 6.19. Cavity shape and pressure history for different group parameters: (a) ρ_p = 2650 kg/m^3, ρ_p = 1000 kg/m^3, μ_f = 100 cp, $K_n = K_s$ = 50 MN/m σ_1' = 0.2 MPa, σ_3' = 0.1 MPa; (b) all parameters are doubled compared to case (a), that is, ρ_p = 5300 kg/m^3, ρ_p = 2000 kg/m^3, μ_f = 200 cp, $K_n = K_s$ = 100 MN/m, σ_1' = 0.4 MPa, σ_3' = 0.2 MPa. In both cases, v_{in} = 242 m/s.

$$\nabla p = -\frac{\mu_f}{k} q - \beta \rho_* q^2 \tag{6.78}$$

where

$$\rho_* = (1-n)\rho_f + n\rho_p \tag{6.79}$$

The simulation results for ρ_p = 2650 kg/m^3 and 5300 kg/m^3 are given in Figure 6.20. These results show that the cavity shape and the stabilized pressure do not vary with the particle densities, which indicates in turn that the inertial effect due to particle flow is not important.

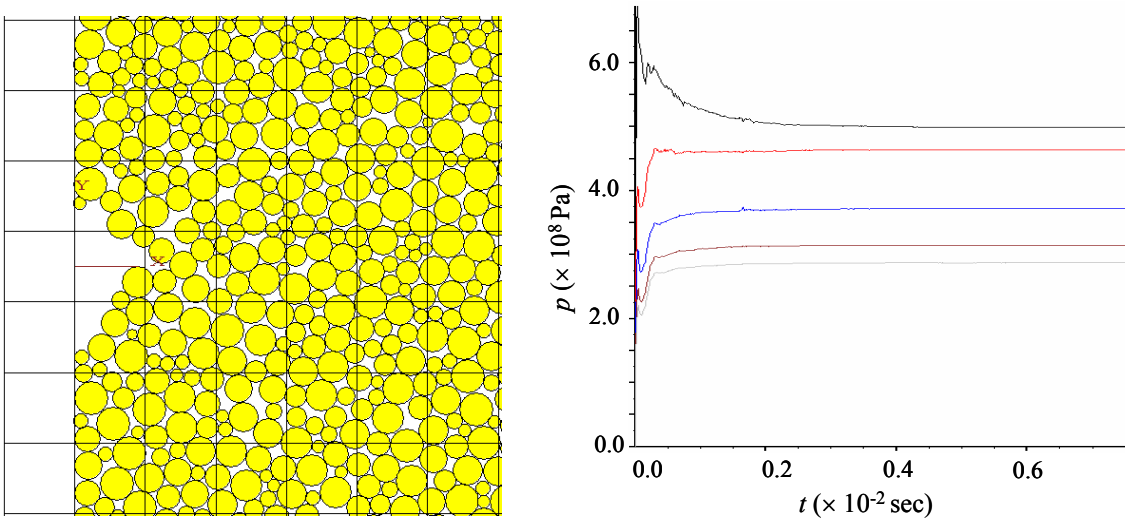

(a)

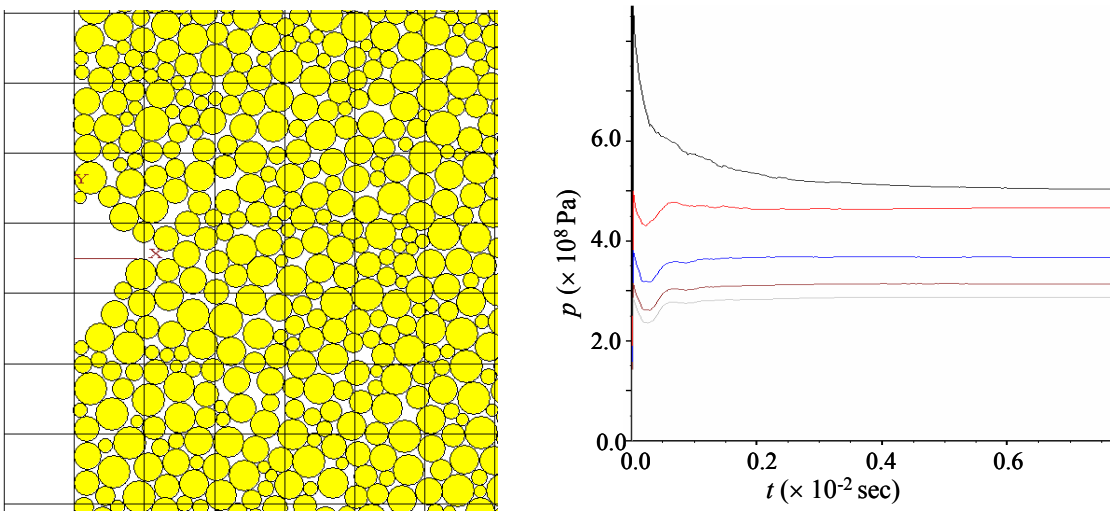

(b)

Figure 6.20. Cavity shape and pressure history for different particle densities, (a) ρ_p = 2650 kg/m^3 and (b) ρ_p = 5300 kg/m^3, in the case of μ_f = 100 cp and the injection velocity v_{in} = 242 m/s. In the pressure history figures, the curves from top to bottom are in the first five cells close to the injection point along the x-axis.

6.8 Conclusions

To investigate the fracture initiation mechanism in water flooding conditions, we conducted a numerical simulation of fluid injection into particulate material using the discrete element method. We observed three distinct stages in the cavity evolution as the injection velocity increases: (1) cavity initiation in the vicinity of the injection point when the velocity of fluid reaches a certain critical value; (2) stable cavity development when the cavity propagates incrementally in response to each increment of velocity increase; and (3) unstable cavity propagation after the injection velocity reaches a second critical value (usually much higher than the critical velocity of cavity initiation).

These stages can be explained by considering the drag forces applied to the particles by the fluid continuously seeping through the particle assembly. Due to the drag forces, particles tend to move away from the injection point. As a result, the particulate material is unloaded near the injection point, which causes a positive volumetric strain in its vicinity. Once the strain reaches a critical value corresponding to the loss of contact between the particles in all directions, a cavity forms. This critical strain value corresponds to the "fluidization" of the particle-fluid mixture. When the injection velocity increases, the cavity begins propagating until it reaches the stable state. Once the resultant magnitude of the drag forces exceeds the reaction on the boundary of the entire particle assembly (at the second critical velocity), the body equilibrium is not possible any more and the cavity begins developing in an unstable manner, that is, without further increase in the injection velocity.

We considered a poroelastic model of cavity initiation based on the fluidization

mechanism. This model suggests that the critical fluid velocity is *proportional* to the fluid viscosity if the latter is not too high. However, if the fluid viscosity is sufficiently large, the critical velocity is *inversely proportional* to the fluid viscosity. From the physical standpoint, such dependence of the injection velocity on the fluid viscosity corresponds to two different flow regimes: inertial governing regime and viscosity governing regime. The inertial governing regime occurs with low fluid viscosity when the energy dissipation is mainly due to the second term in the nonlinear Darcy law. When fluid viscosity increases, the first linear term gradually becomes dominant, and the energy dissipates mainly through the fluid viscosity. Even though the developed model is oversimplified and does not result in the correct state of stress near the injection point, the critical velocity, estimated based on this model, fits remarkably well the values obtained from numerical simulations with PFC^{2D}.

Acknowledgement

The PFC^{2D} simulation presented in this chapter is based on the work conducted by R. Wu during the 2005 summer internship at Schlumberger, Sugar Land. She is grateful to Dr. H. Huang for her leadership in this work and to Drs J. Ayoub, J. Adachi and E Siebrits for their valuable comments and suggestions.

Nomenclature

Latin Symbols

a	radius of the injection hole
A_1	$(1-v)(H-L/\pi)+L^2/\pi^2(1/a-\pi/L)$

A_2	$(1\text{-}v)(H\text{-}L/\pi)\text{-}\ln(\pi a/L)L/\pi$
B	Skempton pore pressure coefficient
c	fluid cell size
c_k	Kozeny-Carman constant
c_m	material parameter
C_1, C_2	integral constants
D	$\varepsilon_{cr}E(1\text{-}v)/[(1+v)(1\text{-}2v)]\text{-}(1\text{-}v)(\sigma_1'+\sigma_3')$
D_p	particle diameter
E	Young's modulus
f_j	body force
F	contact force
F_j	drag force
F_n	total normal force
H	half length of the rectangular domain
j	spatial direction
k	permeability
K_n, K_s	normal and shear stiffnesses
L	height of the simulated rectangular domain
m	particle mass
n	porosity
p	pressure
P	normalized pressure
p_0	pressure at the matching point
p_1	pressure at the boundaries
q	apparent fluid velocity

Q	injection rate
r_0	matching point
t	time step
T_n, T_s	normal and shear bond strengthes
u	radial displacement
U	relative displacement
U_n	total normal displacement
v	fluid velocity
v_{cr}	critical injection velocity
v_{cr}^*	dimensionless critical injection velocity
v_{in}	injection fluid velocity
v_0	characteristic velocity
x, y	cartesian coordinate set

Greek Symbols

α	Biot poroelastic coefficient
β	non-Darcy flow rate coefficient
ε_{cr}	critical volumetric strain
ε_v	volumetric strain
ΔF_s	shear force increment
ΔU_s	increment of shear displacement
η_0	$\alpha(1\text{-}2\nu)/[2(1\text{-}\nu)]$
μ	interparticle frictional coefficient
μ_f	fluid dynamic viscosity
μ_f^*	dimensionless fluid viscosity

ν	Poisson's ratio
ρ_f	fluid density
ρ_p	particle density
ρ_*	equivalent density
σ_1', σ_3'	effective confining stresses
σ_{rr}, $\sigma_{\theta\theta}$	total stresses
σ_{rr}', $\sigma_{\theta\theta}'$	Terzagi effective stresses
σ_v'	effective volumetric stress
τ	viscous shear stress
ϕ	interparticle friction angle

References

Azeemuddin, M., S.G. Ghori, S. Saner, and M.N. Khan (2002), Injection-induced hydraulic fracturing in a naturally fractured carbonate reservoir: A case study from Saudi Arabia, SPE 73784, paper presented at *the 2002 SPE International Symposium and Exhibition on Formation Damage Control*, Lafayette, LA, USA, 20-21 Feb, p 789-799

Bear, J. (1988), Dynamics of Fluids in Porous Media, 764 pp., Dover Publications, Inc., N.Y.

Chang, H. (2004), Hydraulic fracturing in particulate materials, Ph.D. thesis, 267 pp., Georgia Institute of Technology, GA.

Chin, L.Y., and C.T. Montgomery (2004), A numerical model for simulating solid waste injection in soft rock reservoirs, SPE 90507, presented at *the SPE Annual Technical Conference and Exhibition*, Houston, TX, USA, 26-29 Sep.

Cundall, P.A., and O.D. Strack (1979), Discrete numerical model for granular assemblies, *Geotechnique*, *29*, 47-65.

Ergun, S. (1952), Fluid flow through packed columns, *Chemical Engineering Progress*, *48*, 89-94.

Hart, R., and C. Fairhurst (2000), Application of discontinuum modeling in geotechnical studies for nuclear waste isolation, in Geoecology and Computers (*Proceedings of the 3rd International Conference on Advances of Computer Methods in Geotechnical and Geoenvironmental Engineering*, *Moscow*, *Russia*, *February*), S. A. Yufin, Ed. Rotterdam: A. A. Balkerma, 15-28.

Huang, H. (1999), Discrete element modeling of tool-rock interaction, Ph.D. thesis, 131 pp., University of Minnesota, MN.

Hurt, R.S., R. Wu, L.N. Germanovich, H. Chang, and P. van Dyke (2005), On mechanisms of hydraulic fracturing in cohesionless materials, *EOS Trans. AGU*, *86*(*52*), *Fall Meet. Suppl.*, *Abstract H41B-0416*.

Itasca Consulting Group Inc. (2005), *PFC2D User Manual*, Minneapolis, MN.

Jean, R.-H., and L.-S. Fan (1998), Multiphase flow: liquid/solid fluidized bed system, in *The Handbook of Fluid Dynamics*, edited by R.W. Johnson, CRC Press LLC.

Lo, K.Y., and K. Kaniaru (1990), Hydraulic fracture in earth and rock-fill dams, *Can. Geotech. J.*, *27*, 496-506.

Mayerhofer, M.J., M.F. Richardson, R.N. Walker Jr., D.N. Meehan, M.W. Oehler, and R.R. Browning Jr. (1997), Proppants? We don't need no proppants, SPE 38611,

Proceedings of the 1997 SPE Annual Technical Conference and Exhibition, *part Delta*, *Drilling and Completion*, San Antonio, TX, USA, 5-8 Oct, 457-464.

Murdoch, L.C. (1993a), Hydraulic fracturing of soil during laboratory experiments, Part I Methods and observations, *Geotechnique*, *43*, 255-265.

Murdoch, L.C. (1993b), Hydraulic fracturing of soil during laboratory experiments, Part II Propagations, *Geotechnique*, *43*, 267-276.

Murdoch, L.C. (1993c), Hydraulic fracturing of soil during laboratory experiments, Part III Theoretical analysis, *Geotechnique*, *43*, 277-287.

Murdoch, L.C. (2002), Mechanical Analysis of Idealized Shallow Hydraulic Fracture, *J. Geotech. Geoenviron.*, *128*, 488-495.

Oger, L., S.B. Savage, D. Corriveau, and M. Sayed (1998), Yield and deformation of an assembly of disks subjected to a deviatoric stress loading, *Mech. Mater.*, *27*, 189-210.

Panah K, A, and E. Yanagisawa (1989), Laboratory studies on hydraulic fracturing criteria in soil, *Soils and Foundations*, *29*, 14-22.

Potyondy, D.O., P.A. Cundall, and C. Lee (1996), Modeling rock using bonded assemblies of circular particles, in Rock Mechanics Tools and techniques (*Proceedings of the Second North America Rock Mechanics Symposium*, *Montréal*, *June*), edited by M. Aubertin et al. Rotterdam: A. A. Balkerma, 1937-1944.

Potyondy, O.O., and P.A. Cundall (2004), A bonded-particle model for rock, *Int. J. Rock Mech. Mining Sci.*, *41*,1329-1364.

Shimizu, Y. (2004), Fixed coarse-grid fluid scheme in *PFC*^{2D}, Itasca Consulting Group, Inc., Minnesota.

Sommerauer, G., and R. Petersen (2003), Implementation of pressure maintenance in Seria Field using limited entry fractured water injection, SPE 84884, paper presented at *the SPE International Improved Oil Recovery Conference in Asia Pacific*, Kuala Lumpur, Malaysia, 20-21 Oct.

Souza, A.L.S., P.D. Fernandes, R.A. Mendes, A.J. Rosa, C.J.A. Furtado, and S.A. Petrobras (2005), The impact of injection with fracture propagation during waterflooding process, SPE 94704, paper presented at *the SPE Latin American and Caribbean Petroleum Engineering Conference*, Rio de Janeiro, Brazil, 20-23 June.

Wang, H.F. (2000), *Theory of Linear Poroelasticity: with Applications to Geomechanics and Hydrogeology*, Princeton University Press, Princeton, NJ, 287pp.

Zhao, Z., D. Liu, W. Liu, L. Chai, and H. Zhou (2005), Development of systematic hydraulic fracturing technology for a natrally fractured reservoir, SPE 94101, paper

presented at *the SPE Europec/EAGE Annual Conference*, Madrid, Spain, 13-16 June.

CHAPTER 7
CONCLUSIONS AND RECOMMENDATIONS

7.1 Conclusions

This dissertation addresses three important topics in the mechanics of hydraulic fracturing: (1) hydraulic fracture branching and segmentation in quasi-brittle materials, (2) hydraulic fracturing in particulate materials, and (3) hydraulic fracturing in water flooding conditions.

Our main results can be summarized as follows:

1. We introduced a simple technique to control the orientation and size of hydraulic fractures in laboratory samples. This is achieved by heating or cooling samples prior to injecting the fracturing liquid, so that the induced thermal stresses control the fracture orientation. We developed a simple theoretical model to parameterize experiments in laboratory settings and for materials that are different from ours. We illustrated the utility of the technique with two examples: (i) mixed mode I+III hydraulic fracture propagation, and (ii) visualization of the fluid flow in the created fracture.
2. In quasi-brittle materials, even a small mode III component may cause fracture segmentation due to the creation of a tensile stresses near the fracture front. We experimentally studied not only the effect of mode III loading on the onset of fracture segmentation but also the effect of segmentation on the subsequent

fracture growth when the K_{III}/K_I ratio was rather small (1-10%). We used transparent, cylindrical PMMA samples with circular internal fractures perpendicular to the sample axis. Fracture orientation was controlled by thermoelastic stresses induced in each sample by preheating it before creating a fracture. In order to apply mode III loading to the initial fracture, a constant torque was applied to the specimen while fluid was injected into the fracture at a constant rate to pressurize it and to induce mode I loading. In spite of a small magnitude of the mode III component, we observed segmented fracture fronts in all the tested samples. The segments had similar dimensions and an elongated shape. When the fractures were further pressurized by injecting additional fluid into the sample, second-order segments developed along the fronts of the first-order segments.

3. We developed a simple asymptotic model of a multi-segmented mode I+III fracture propagating in conditions of a low level mode III loading. The model takes into account mechanical interaction between the segments and the parent fracture and shows good agreement with the experimental observations.
4. The obtained results indicate that a K_{III}/K_I ratio as small as a few percent is sufficient for fracture front segmentation even in materials as homogeneous and fracture resistant as PMMA. In reality, a small component of mode III is always expected, for example, due to slight deviations of a three-dimensional fracture from a planar shape or interaction with boundaries or other fractures. As a result, front segmentation (at an appropriate scale) is likely to accompany the growth of most (if not all) real fractures, at least in quasi-brittle materials.

5. We developed a model of a simple localized plastic band to describe the process zone at the tip of a fracture in cohesionless particulate material in the Dugdale-Barenblatt manner. Even though the physical nature of the localized plastic zone appearing in compression and the mechanism of localized fluid flow into cohesionless materials are unclear, the model still results in a stress state that is compressive everywhere, including the fracture tip zone. Since cohesionless materials cannot bear tensile stress, this model is appealing and yields a simple and convenient approach for modeling fracture propagation.
6. Based on the physical mechanism of shear banding, which is characteristic for particulate materials with strain-softening behaviour, we introduced a hydraulic fracturing model that explicitly describes the fracture front and the fluid flow mechanism. The model is consistent with experimental observations and is based on modeling the shear bands by properly oriented and positioned dislocations. To test the shear band hypothesis, we also conducted numerical simulations of the localized plastic deformation at the tip of a fracture in the particulate material with strain softening.
7. Since the super-dislocation model is an important tool to model crack-tip plasticity in different settings, we reassessed the super-dislocation model recently developed by *Papanastasiou and Atkinson* [2000] for simple representation of plastic deformation at the tip of hydraulic fractures in such pressure sensitive materials as soft sediments in hydrocarbon reservoirs. We showed that in the case of the small scale yielding, the conventional approach of determining the dislocation angle by maximizing the crack opening displacement, dislocation

strength, or dislocation length is only effective for frictionless materials as originally suggested by *Atkinson and Kanninen* [1977]. As an alternative, we proposed a criterion based on the maximum shear stress at the dislocation position. We showed that maximizing the shear stress on the dislocation makes the super-dislocation model consistent for a wide range of pressure sensitive cohesive-frictional materials.

8. To investigate the fracture initiation mechanism in water flooding conditions, we conducted a numerical simulation of fluid injection into particulate material using the discrete element method. We observed three distinct stages in the cavity evolution as the injection velocity increases: (1) cavity initiation in the vicinity of the injection point when the velocity of fluid reaches a certain critical value; (2) stable cavity development when the cavity propagates incrementally in response to each increment of velocity increase; and (3) unstable cavity propagation after the injection velocity reaches a second critical value (usually much higher than the critical velocity of cavity initiation). These stages can be explained by considering the drag forces applied to the particles by the fluid continuously seeping through the particle assembly. Due to the drag forces, particles tend to move away from the injection point. As a result, the particulate material is unloaded near the injection point, which causes a positive volumetric strain in its vicinity. Once the strain reaches a critical value corresponding to the loss of contact between the particles in all directions, a cavity forms. This critical strain value corresponds to the "fluidization" of the particle-fluid mixture. When the injection velocity increases, the cavity begins propagating until it reaches the stable state. Once the

resultant magnitude of the drag forces exceeds the reaction on the boundary of the entire particle assembly (at the second critical velocity), the body equilibrium is not possible any more and the cavity begins developing in an unstable manner, that is, without further increase in the injection velocity.

9. We considered a poroelastic model of cavity initiation based on the fluidization mechanism. This model suggests that the critical fluid velocity is *proportional* to the fluid viscosity if the latter is not too high. However, if the fluid viscosity is sufficiently large, the critical velocity is *inversely proportional* to the fluid viscosity. From the physical standpoint, such dependence of the injection velocity on the fluid viscosity corresponds to two different flow regimes: inertial governing regime and viscosity governing regime. The inertial governing regime occurs with low fluid viscosity when the energy dissipation is mainly due to the second term in the nonlinear Darcy law. When fluid viscosity increases, the first linear term gradually becomes dominant, and the energy dissipates mainly through the fluid viscosity. Even though the developed model is oversimplified and does not result in the correct state of stress near the injection point, the critical velocity, estimated based on this model, fits remarkably well the values obtained from numerical simulations with PFC^{2D}.

7.2 Recommendations for Future Work

Our recommendations for future work on hydraulic fracture branching and segmentation in brittle materials include:

- Performing more experiments with the developed setup to obtain more

comprehensive statistical data on the occurrence of the observed types of fracture geometry and injection pressure curve.

- Conducting experiments on mode I+III hydraulic fracture propagation in transparent materials with larger size of test samples (i.e., with diameters two to four times as large). This will further allow investigating fracture propagation geometry and, possibly, scale effect.
- Performing similar experiments with different transparent (e.g., non-organic glass) and non-transparent (e.g., rock, cement, and ceramic) materials.
- Performing further theoretical modeling of fracture segmentation in mode I+III loading conditions by taking into account three-dimensional features of segment geometry.
- Incorporating mixed mode I+III fracture propagation and segmentation in numerical codes.

Our recommendations for future work on hydraulic fracturing in particulate materials include:

- Continuing efforts on the development of consistent criteria of hydraulic fracture propagation in particulate materials. Current work presented in this dissertation is only the initial step in this direction.
- Considering the super-dislocation model based on the dislocation inclined to the fracture plane at the angle that does not create shear strain singularity on the parent fracture (i.e., 70.5º).
- Incorporating the shear-band (particulate material) dilatancy into the super-

dislocation model.

- Studying the possibility of replacing the super-dislocation model with the shear-band model, when the distribution of displacement discontinuity changes along the shear band.

Our recommendations for future work on hydraulic fracturing in water flooding conditions include:

- Performing numerical simulations of fluid injection into particulate materials by using discrete element method with a number of particles considerably large (at least, two or three orders of magnitude greater). This may involve employing high-performance or super computing but will allow studying the main effects associated with sample, grid (cell), and particle dimensions.
- Performing numerical simulations of fluid injection into particulate materials in domains of different geometries.
- Performing 3-D numerical simulations of hydraulic fracturing in water flooding conditions with a particle flow code.
- Explicitly incorporating plastic material properties into the theoretical model of cavity initiation as a result of localized fluid injection into cohesionless particulate material.

APPENDIX A DESIGN OF THE SYRINGE PUMP

Any reasonably stiff pump is well suited for the type of experiments described in this work. Due to the small volume of hydraulic fractures in our experiments, chromatography pumps appear to be particularly useful since they provide low but stable flow rate. For example, Eldex Laboratories, Inc. (http://eldex.com) manufactures commercial chromatography pump with the range of parameters sufficient for conducting experiments reported in this paper.

The design of the pump employed in our experiments is shown in Figure A.1a. It acts as a single stroke syringe pump and is essentially a simplified conventional chromatography pump. While less accurate, it is cost effective and serves our purposes. It consists of a stainless steel, thick-wall tubing (threaded on the inside face) and a stainless steel hex-head bolt (Figure A.1b). Similar to the "screw" pump employed of *Chenov and Kyu* [1996] and *Kyu and Tsyganov* [2003], our pump (Figure A.1) is driven by rotating the bolt, and two strain gauges are attached to the threaded tubing to measure its deformation during pumping. The measured deformation of the tubing is calibrated to the internal pressure in the tubing prior to each experiment. The strain gauges are measured with a data acquisition system so the entire pressure curve for the test can be recorded.

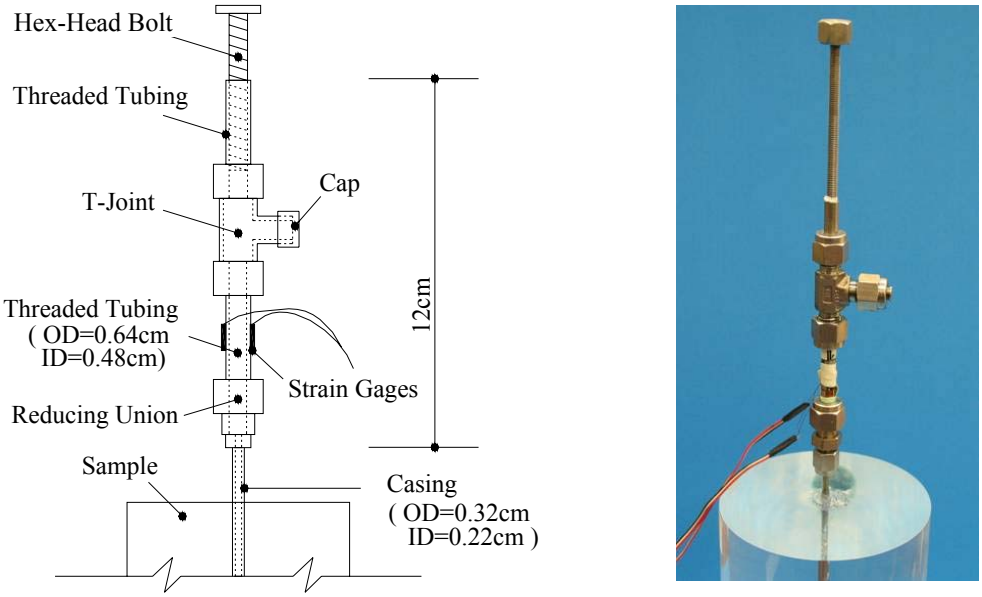

(a) (b)

Figure A.1. Pump used in our experiments: (a) schematics of the design and (b) actual pump.

Before each experiment, the pump-tubing system is completely filled with fracturing liquid. To minimize the existence of air bubbles, we used a T-joint to connect two pieces of threaded tubing while the third end of the T-joint (the cap end) acts as an outlet for the liquid and air. After carefully filling the system with the cap closed, and immediately before we place the hex-head bolt into the threaded tubing to start pumping, we loosen the cap, so that the any remaining air could leak out through the opened end of the T-joint. A few full turns of the bolt are usually sufficient to complete this process. Then, we tighten the cap and begin pressurizing the fracture.

A stepping gear motor is used to turn the threaded rod (hex-head bolt) in the mini pump. This method allows for easy control of the fluid injection rate (between 0.0021

ml/min to 0.10 ml/min). Recognizing that the injection rate may affect the hydraulic fracture propagation, we kept the injection rate sufficiently low to avoid unstable fracture propagation and to reduce the fluid lag at the fracture front. Slow injection rate also makes the pressure distribution inside the fracture more uniform, which is helpful for the subsequent theoretical analysis.

While this type of pump was convenient for our purposes, it is not a unique device for controlling fracture size and orientation as presented in Chapter 2. For example, *Bunger et al.* [2004] used a stepping motor pump with a flow control valve to create hydraulic fractures in PMMA samples. The valve is placed upstream of the injection tube to dissipate elastic energy stored in the fluid and pump prior to breakdown. This setup can also be adopted for our technique.

APPENDIX B UPPER ESTIMATE OF THE VOLUME CHANGE DUE TO TUBING DEFORMATION

For the fully cased drill hole, the *upper* estimate of the volume change due to the tubing deformation corresponds to the free outer surface of the casing tube (i.e., to zero pressure at the outer surface). In this case, the radial displacement of the inner surface is given by [*Timoshenko and Goodier*, 1970]

$$u(p) = p\frac{1+\nu_s}{E_s}\frac{r_1[r_2^2+(1-2\nu_s)r_1^2]}{r_2^2-r_1^2} \tag{B.1}$$

where p is the fluid pressure inside the tube, E_s and ν_s are the Young's Modulus and Poisson's ratio of the tubing material, and r_1 and r_2 are the inner and outer tube radii at $p = 0$, respectively. Under the fluid pressure, p, the deformed inner radius of the tubing becomes $r(p) = r_1 + u(p)$, so that the volume change due to the tubing deformation between the peak, p_1, and residual, p_2, fluid pressures is

$$\Delta V_t = \pi[(r_1+u(p_1))^2-(r_1+u(p_2))^2]L_t \tag{B.2}$$

where L_t is the tube length. Note that $r(p_2) < r(p_1)$, since the pressure decreases from p_1 to p_2 during the crack growth (i.e., $p_2 < p_1$, and the inner surface of the tube translates inwards). This is why the calculated volume change, ΔV_t, represents an upper estimate.

Expression (2.9) can now be rewritten as

$$p_1 - p_2 = K_f \frac{V_2 - V_1}{V_1} \approx K_f \frac{V(a_2) - V(a_1) - \Delta V_t}{V_0} \tag{B.3}$$

Accordingly, expression (2.10) becomes

$$V(a_2) - V(a_1) - \Delta V_t = V_0 \frac{p_1 - p_2}{K_f} \tag{B.4}$$

Here the fluid compressibility, K_f, can be estimated from (2.12) if coefficient C is determined from a trial test:

$$K_f = \frac{3EC}{16(1-\nu^2)} \tag{B.5}$$

For example, in the test shown in Figure 2.7, we had V_0 = 2.46 ml, r_1 = 0.11 cm, r_2 = 0.16 cm, L_t = 10.16 cm, p_1 = 20.7 MPa, p_2 = 4.8 MPa, and C = 0.80. Type 304 stainless steel tubing was used as casing, so that E_s = 200 GPa, and ν_s = 0.29 [www.matweb.com]. Taking E = 3.3 GPa ν = 0.38 for PMMA [*Bunger et al.*, 2004], we find that ΔV_t is only 0.3% of the right hand side in (B.4) and can be omitted, which makes (B.4) identical to (2.10). In other words, for the fully cased drill hole, the upper estimate of the volume change due to the tubing deformation is only 0.3% of that developed due to the crack growth. Hence, ignoring the tubing deformation in the theoretical model does not result in any significant error.

APPENDIX C DISCUSSION ON FRACTURE SIZE CONTROLLING

In our experiments, a_1 was roughly a factor of two greater than the drill hole diameter. The starter fracture first propagates dynamically due to the stress concentration around the drill hole. Then, its growth becomes stable, which can be understood by considering a crack loaded on one side (Figure C.1) that simulates pressing the rod inside the hole with a loading machine (section 2.4). In this case, the stress intensity factor can be expressed from that given by *Tada et al.* [1985]:

$$K_I = \frac{F}{\pi c^2}\left[\sqrt{\frac{a_1}{c}} - \sqrt{\frac{a_1}{c} - \frac{c}{a_1}}\right]\sqrt{\frac{c}{\pi}} \qquad \text{(C.1)}$$

where $F = \pi c^2 p_0$ is the force applied the to the rod, and p_0 is the equivalent, homogeneous stress applied by the rod to the bottom of the drill hole (Figure C.1).

In (C.1), K_I monotonically decreases with increasing a_1. Therefore, criterion (2.3) can only be maintained if the pushing force, F, increases. This increase, however, is limited by the non-elastic deformation on the contact between the rod and the PMMA surface at the tip of the drill hole.

Expression (C.1) suggests that this difficulty can be overcome by employing a drill hole of a larger diameter, $2c$, which allows one to obtain a greater ratio a_1/c at a smaller stress, $p_0 \sim F/c^2$, acting at the bottom of the drill hole. For the drill hole diameters used in our experiments, we could only obtain $a_1/c \approx 2$. In general, a considerable increase of $2c$ also requires changing the sample radius, R. This is why, for a given R, it

may be simpler to change V_0 in order to control fracture size, a_2.

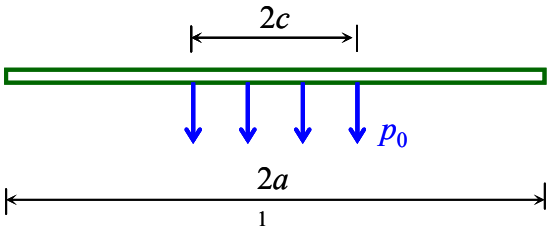

Figure C.1. A crack loaded on one side, which simulates creating a starter fracture by pushing a rod inside the drill hole (section 2.4).

APPENDIX D LABORATORY SETUP FOR MODE I+III FRACTURE PROPAGATION

The transparent PMMA cylinder is positioned horizontally inside a loading frame (Figure D.1a). Clamped to the plate at the end of the frame, one end of the specimen (right sample end in Figure D.1b) is fixed against the lateral movements as well as torsion. The other end of the specimen (left end in Figure D.1b) is pinned against lateral movement but is free to rotate. This end is also connected to a level-weight system. Through this level-weight system, a torsion moment is applied to the specimen (Figure D.1c). This set-up has been designed for sample diameters varying from 2.54 cm to 20.32 cm, which is achieved by using adjustable clamps. In all of our experiments, the ratio of sample length to diameter was larger than 3. The pump used to inject the fluid is described by *Wu et al.* [2006] (Appendix A).

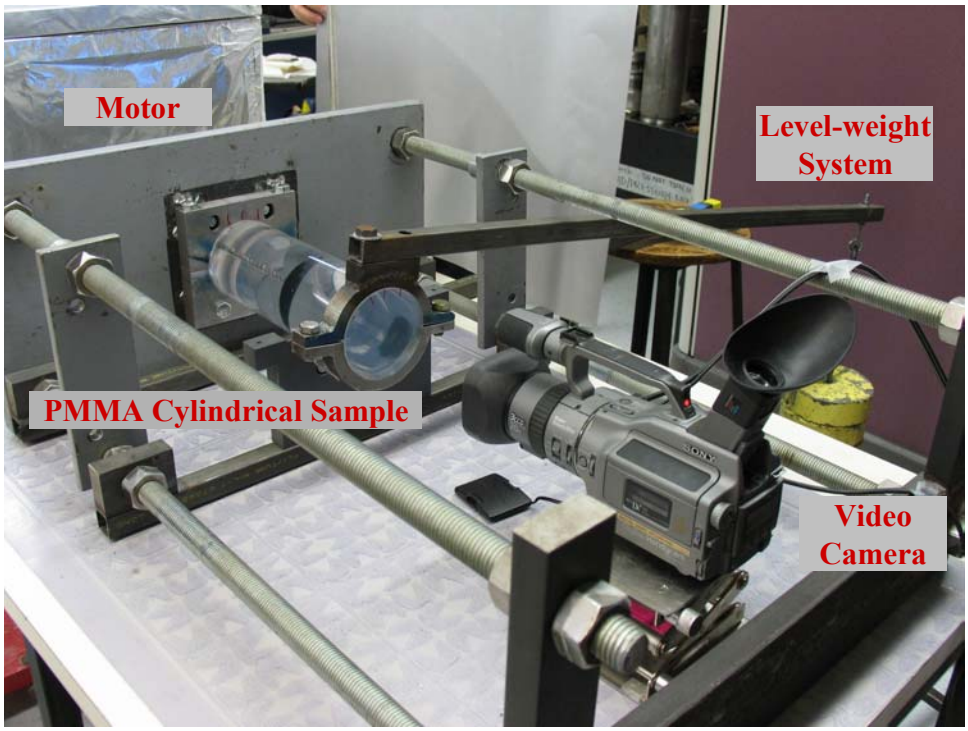

(a)

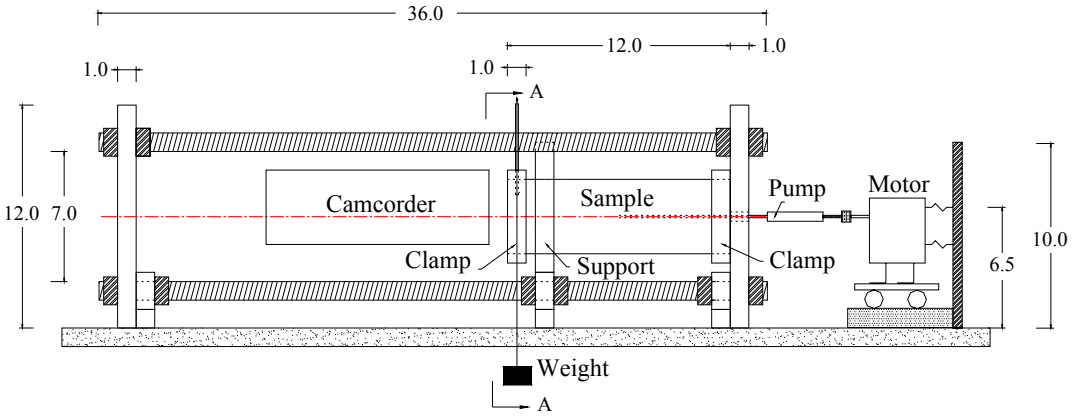

(b)

Figure D.1. Laboratory set-up: (a) general view, (b) sketch of back-view, and (c) sketch of the level-weight system in the cross section A-A in (b) (the dashed line and solid line are the positions of the level before and after hanging the weights, respectively). In photograph (a), the stepping gear motor, which is used to drive the hex-head bolt (Figure A.1), is placed inside an aluminum box to eliminate the effect of electromagnetic radiation.

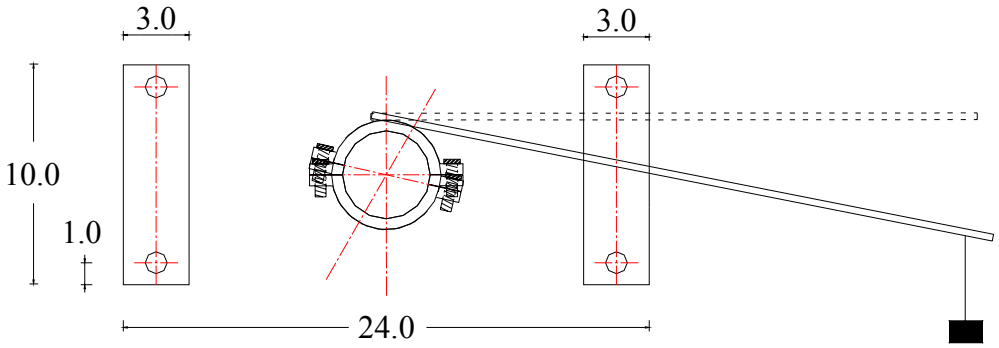

(c)